Porphyrin-Based Nanorings and Helices

Jake Holmes

St. Peter's College

University of Oxford

A thesis submitted for the degree of

Doctor of Philosophy

Trinity 2025

Acknowledgements

Firstly, I would like to thank Professor Harry Anderson for his conscientious supervison of my doctoral studies. Harry's consistent presence throughout my time in the laboratory ensured that I always felt supported and remained on track to achieve our shared research goals, even through some particularly challenging times. I am proud of the work we have achieved together and will look back fondly on my time in your research group. Thank you.

I would also like to thank Dr. Jie-Ren Deng (Kenny) and Dr. Henrik Gotfredsen for kindly taking the time to help me become a better chemist. Kenny, your sage like advice at the start of my studies really set me on the right path. The lab was never the same after you graduated, but I have very much enjoyed our spontaneous chats in the CRL since then. Henrik – your patient support and guidance at a particularly difficult time in my studies was incredibly meaningful. I look forward to catching up during my next visit to Copengahen.

A special thanks goes to Dr Arnau Rubio, not only for his help proof reading parts of this thesis and for his day to day support of my research, but also for making my time in Oxford so enjoyable. I always felt so welcomed when visiting yourself, Ori, Cosi and Pruna, and have thoroughly enjoyed our many game nights. I look forward to seeing what the future holds for you and your family. I am very optimistic and can't wait for my first visit to Spain.

Thanks also goes to all those I have collaborated with during my studies. Janko, Lene, Kavita, Robert, Natalie and Keigo – thank you for your hard work and dedication to our projects.

I have been fortunate to be surrounded by a group of exceptionally motivated and passionate chemists during my studies. Andrew, Bobby, Chiara, Edward, Freddie, Gao, Ka-man, Kate, Kavita, Keith, Lene, Leonard, Michael, Owen, Prakhar, Robert, Sam, Sara, Théa and Wojtek – thank you for making my time in the group so fun and for being a constant source of inspiration during my studies. A special thanks additonally goes to Connor, He and Josh for our many out-of-lab outings, which I hope will continue long into the future.

The PhD was intense, but has been made significantly more enjoyable thanks to the friends I have made during my time in Oxford. Thanks firstly go to Vik and Joe for putting up with me as a flatmate for almost 4 years and for the many memories we have made together. Additionally, I would like to thank a whole bunch from the Peter's MCR – Alice, Alex, Colin, Devon, Julia G., Julia K., Katie, Rana, Rhea and Zeynep.

Thanks also go to Aidan and Dylan – Bath freshers feels like a lifetime ago, but look where we are now. Can't wait for our first Dr. Dr. Dr. meetup after we have all graduated.

Finally, a very special thanks goes to all of my family, but in particular my Mum, Dad and brother, Ben. Your unwavering support throughout all of my studies, from the very beginning, has been incredibly meaningful and has helped me to achieve my goals. At the most intense parts of the PhD, my weekend trips home and long walks with Pepper provided much needed perspective. Thank you for always being there for me and for keeping me grounded, I could not have done this without you. I love you all very much.

Abstract

Chapter 1 discusses the background information and key publications relevant to the work described in Chapters 2-5. It first covers the synthesis of porphyrin-based molecular wires and nanorings, along with their properties. It then provides background information on aromaticity and gives examples of how aromaticity can be observed in large molecular systems. Finally, it discusses how chirality effects the properties of organic π-conjugated materials and how this can be investigated experimentally.

Chapter 2 presents the synthesis of a butadiyne-linked 18-porphyrin nanoring (***c*-P18**) and of two snowflake-shaped templates (**T18$_A$** and **T18$_B$**). I discuss the computational design of the snowflake-shaped templates, then outline the successful synthetic routes to both versions. The synthesis of various linear butadiyne-linked porphyrin wires is then summarised along with the use of these oligomers in the template-directed synthesis of the 18-porphyrin nanoring. Finally, the characterisation data for the various nanoring·template complexes is presented.

Chapter 3 covers our in-depth study of the ***c*-P18·T18$_{A/B}$** complexes, which includes; our computational analysis of the conformations each complex explores in solution, the binding of each template variant to the **c-P18** nanoring, and our computational predictions and experimental evidence for globally aromaticity in ***c*-P18**.

Chapter 4 presents the current progress of our collaboration with Natalie Miller and Dr Gordon Hedley at the University of Glasgow, which aims to explore exciton size and motion in the ***c*-P18·T18$_{A/B}$** complexes.

Chapter 5 summarises the design, synthesis and purification of a chiral template which is capable of holding a butadiyne-linked porphyrin oligomer in a helical geometry. The binding between this chiral template and the oligomer is quantified and the chiroptical properties of the resulting helices are explored.

Supplement to Statement of Authorship

Chapter 2 - Compound **2.15** was synthesised by Keigo Yamada, a visiting student that I supervised over the summer of 2022. I designed and modelled Compound **$T3_B$**, which was then synthesised by Lene Gödde for her 9-porphyrin nanoring project. Dr. Henrik Gotfredsen, Dr. Kavita Rani and I collaborated to produce batches of **$P9_{OOct}(C_2THS)_2$** and **$P9_{THS}(C_2CPDIPS)_2$.** STM analysis of **c-$P18_{OOct}$** was completed by the group of Dr Alex Saywell at the University of Nottingham.

Chapter 3 - Janko Hergenhahn completed all molecular dynamics simulations and Lene Gödde conducted the competition binding titrations.

Chapter 4 - All single molecule measurements discussed in Chapter 4 were completed by Natalie Miller, a PhD student in the group of Dr Gordon Hedley at the University of Glasgow as part of our ongoing collaboration.

Contents

List of Publications

1. J. Hergenhahn, **J. M. Holmes**, J. Deng, H. Gotfredsen, R. M. J. Jacobs, S. M. Kopp, C. R. Timmel and H. L. Anderson, "Radical Anions of Porphyrin Molecular Wires: Delocalization and Dynamics", *J. Am. Chem. Soc.*, 2025, 147, 1, 978–987.
2. **J. M. Holmes**, H. Gotfredsen, L. Gödde, J. Hergenhahn, K. Rani, K. E. Yamada, J. Deng, L. Warwick, M. Clarke, M. Edmondson, J. N. O'Shea, A. Saywell and H. L. Anderson, "An 18-Porphyrin Nanoring at the Size Limit of Global Aromaticity", manuscript under review.

List of Abbreviations

Ar	Aryl	NMR	Nuclear Magnetic Resonance
BPin	Pinacolborane	NOESY	Nuclear Overhauser Effect Spectroscopy
Bu	Butyl	NICS	Nucleus Independent Chemical Shift
CISS	Chiral Induced Spin Selectivity	PIFA	(Bis(trifluoroacetoxy)iodo) benzene
COD	1,5-Cyclooctadiene	SEC	Size Exclusion Chromatography
COSY	Homonuclear Correlation Spectroscopy	STM	Scanning Tunneling Microscopy
DIPA	Diisopropylamine	PF_6^-	Hexafluorophosphate
DDQ	2,3-Dichloro-5,6-dicyano-1,4-benzoquinone	PIFA	(Bis(trifluoroacetoxy)iodo) benzene
DFT	Density Functional Theory	TBAF	Tetrabutylammonium fluoride
DMF	*N*,*N*-Dimethylformamide	TD-DFT	Time-Dependant Density Functional Theory
DMSO	Dimethylsulfoxide	TEA	Triethylamine
ESI	Electrospray Ionisation	TFA	Trifluoroacetic acid
GPC	Gel Permeation Chromatography	THF	Tetrahydrofuran
HMBC	Heteronuclear Multiple Bond Correlation Spectrometry	THS	Tri-*n*-hexylsilyl
HRMS	High-Res Mass Spectrometry	TMS	Trimethylsilyl
HSQC	Heteronuclear Single Quantum Corelation Spectroscopy	TLC	Thin Layer Chromatography
MALDI	Matrix Assisted Laser Desorption/Ionisation	UV-vis	Ultraviolet-visible
MS	Mass Spectrometry		
NBS	*N*-Bromosuccinimide		
NIR	Near-Infrared		

1 Introduction

Contents

Chapter 1 - Introduction

1.1 Porphyrin-based Molecular Wires and Nanorings

1.1.1 Porphyrin

The term porphyrin is used to describe a diverse family of molecules which contain the core framework of the parent structure porphine (**1**, Figure 1.1a).[1] This core framework is comprised of four pyrrole-like heterocycles that are joined together into a cyclic structure by four methine bridging units. This specific arrangement of atoms leads to a planar molecular framework, possessing a fully conjugated circuit of 18 π-electrons. Nature has utilized many variants of this framework for a broad range of functions, such as the use of heme B (**2**, Figure 1.1) in red blood cells for O_2 transport, which utilizes the ability of the porphyrin framework to bind metal atoms in the centre of the ring.

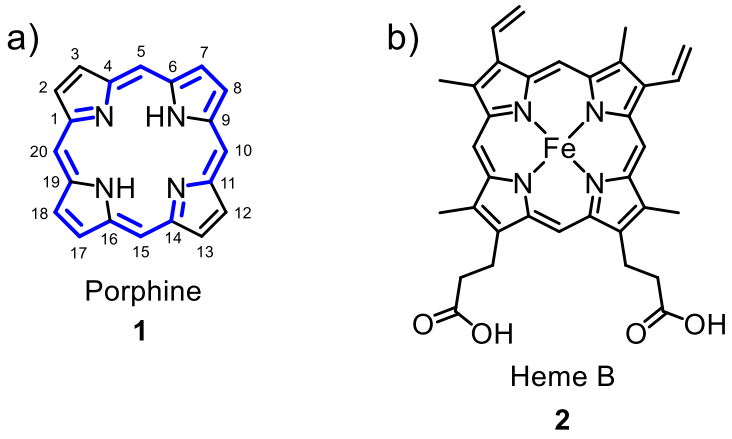

Figure 1.1. (a) Chemical structure of porphine, the parent compound to all porphyrins, with the 18 electron π-circuit highlighted in blue (b) Chemical structure of heme B – an important natural porphyrin that facilitates O_2 uptake by hemoglobin in red blood cells.

The high degree of π-conjugation in the porphyrin framework leads to perhaps the most important property of these molecules; their strong absorbance of UV-visible light. So long as the conjugated π-circuit is maintained, structural modifications can be applied to the porphyrin framework without significantly disrupting this property. Nature has taken advantage of this by incorporating reduced porphyrins (e.g. the chlorin - chlorophyll a, or the bacteriochlorin - bacteriochlorophyll a (Bchl a), Figure 1.2) into the light harvesting systems found in many

plants and photosynthetic bacteria (see LHII found in purple bacteria, Figure 1.3).[2] The chromophores in these systems are held in close proximity by large proteins, which facilitates excitonic coupling of the chromophores, enhancing their ability to harvest incoming light and efficiently funnel this absorbed energy to adjacent reaction centers.[3] The specific cyclic arrangement of Bchl a in LHII has been the inspiration for many synthetic porphyrin arrays, which will be discussed later in this chapter.

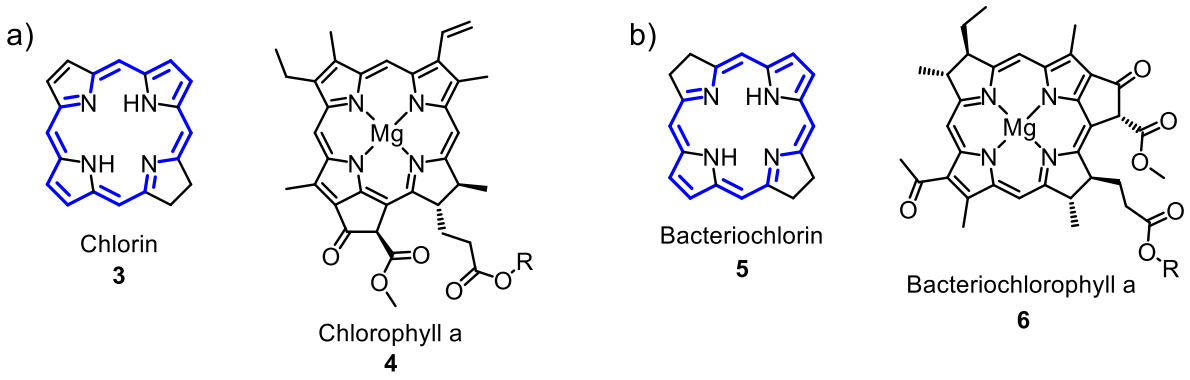

Figure 1.2. (a) Chemical structure of chlorin and chlorophyll a. (b) Chemical structure of bacteriochlorin and bacteriochlorophyll a (Bchl a).

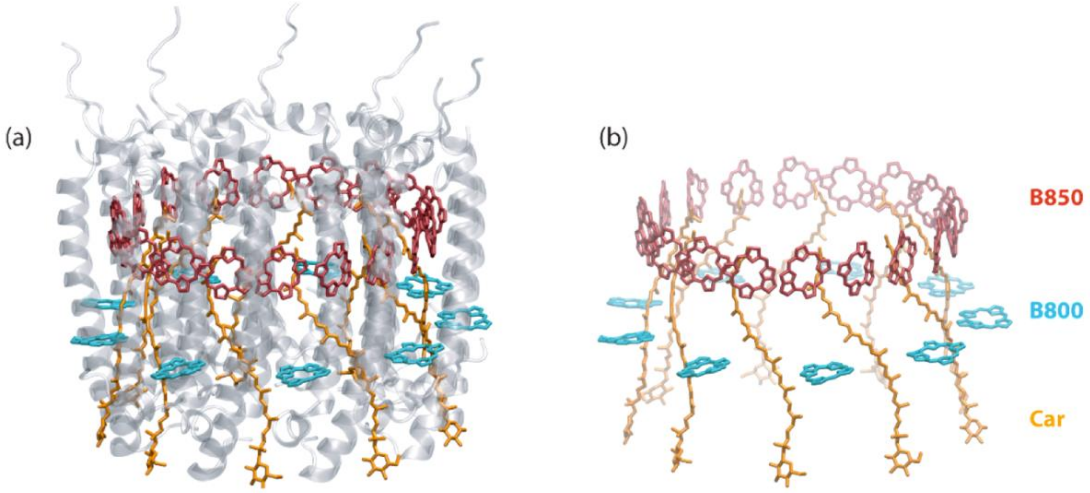

Figure 1.3. (a) Model of LHII. (b) Model of LHII with protein removed for clarity. Bchl a (red/cyan), carotenoid (orange). Reproduced from reference.[2]

In nature, the synthesis of porphyrins, chlorins and bacteriochlorins is achieved through the use of many different enzymes, which work in sequence to form and functionalise these molecular frameworks. Synthetic chemists have long admired these structures, which has resulted in

considerable time and resources being spent to expand upon the approaches to their synthesis.[4] Because of this, the synthetic chemist is now able to prepare and modify the porphyrin framework at any position, with a very broad range of functional groups, which has enabled the study of many novel porphyrin structures with fascinating properties and applications. Much of this work is outside the scope of this thesis, which will focus specifically on the use of porphyrin in novel molecular electronic materials, however, numerous reviews have been written on the applications of porphyrin derivatives in the fields of; photocatalysis,[5] photodynamic therapy,[6] photovoltaics[7] and sensing.[8]

1.1.2 The Porphyrin π-System

The delocalised π-system in porphyrin is of paramount importance to almost all of its applications, as this system is the reason the framework can absorb so strongly in the UV-Visible region. The absorbance of light by this π-system is described well by the Gouterman 4-orbital model (Figure 1.4),[9, 10] which states that both the high energy Soret band ($S_0 \rightarrow S_2$, ~400 nm) and lower energy Q-band ($S_0 \rightarrow S_1$, ~550 nm) arise from transitions between the π and π* molecular orbitals. The difference in absorption intensity of these two transitions is attributed to the configurational interaction of the four potential transitions that can occur between the two occupied π orbitals, and two unoccupied π* orbitals,[11] with constructive interference leading to the intense Soret band, and destructive interference producing the weaker Q-band.

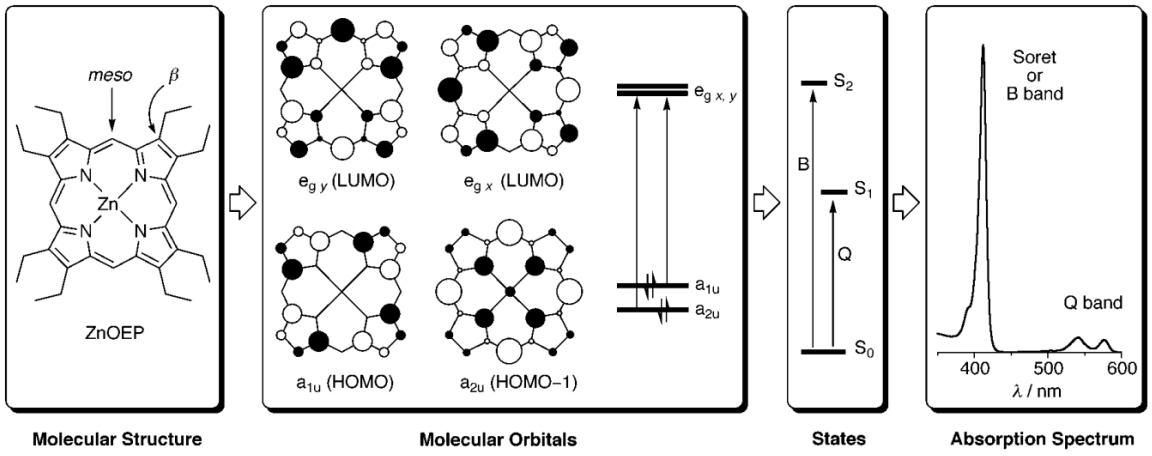

Figure 1.4. The Gouterman 4-orbital model applied to a zinc porphyrin. Reproduced from reference.[11]

The conjugated 18-electron circuit present in the π-system also obeys Hückel's 4n + 2 π-electron rule which results in all porphyrin monomers exhibiting aromaticity. This behaviour means that in the presence of an external magnetic field, a ring current is generated through the 18-electron circuit which generates a magnetic field antiparallel to the external field inside the π-circuit, but parallel outside (Figure 1.5). This increases the magnetic field experienced by the meso protons, which increases the energy gap between the spin states of these nuclei, therefore increasing the ppm value at which these protons are observed (Figure 1.6, H_{meso} at 10.30 ppm) relative to a typical methine proton (5.50 and 6.00 ppm in hexa-2,4-diene[12]). This locally aromatic behaviour is introduced here as it is of particular importance to the global aromaticity of porphyrin based nanorings discussed later in this chapter.

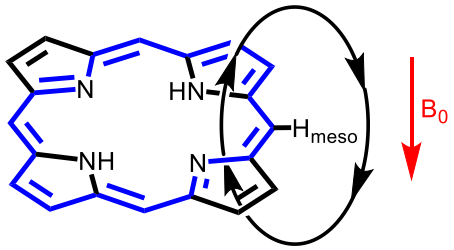

Figure 1.5. Magnetic field generated by aromatic ring currents in the porphyrin molecular framework in the presence of an external magnetic field B_0.

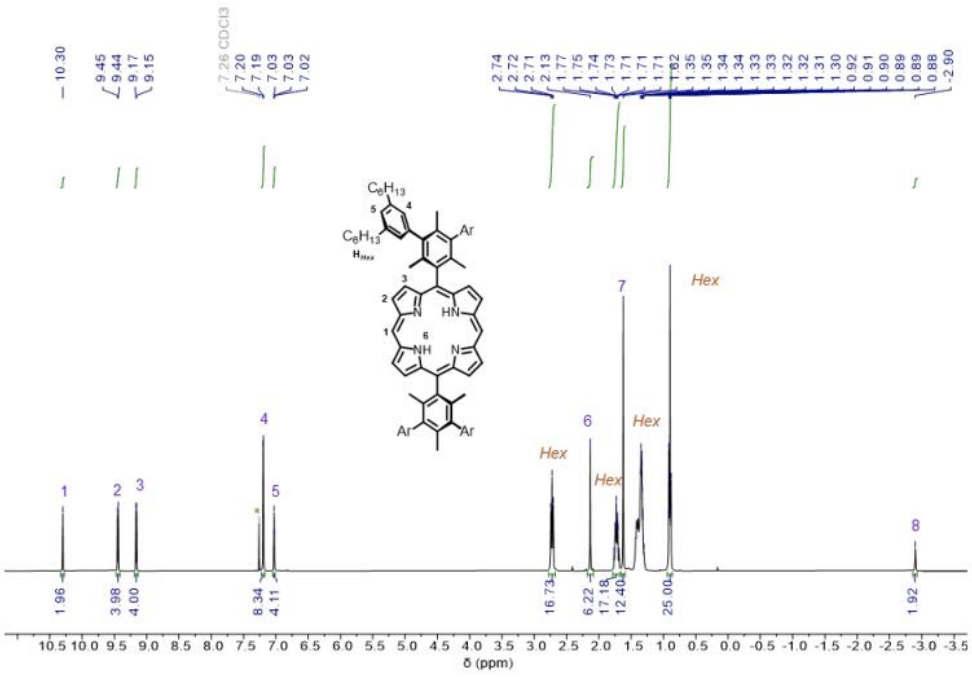

Figure 1.6. ^{1}H NMR of a porphyrin monomer demonstrating the high ppm value at which the meso proton is observed. (400 MHz, $CDCl_3$, 298 K) Reproduced from reference.[13]

1.1.3 Porphyrin-based Molecular Wires

To mimic the porphyrin-porphyrin electronic coupling observed in natural light harvesting systems, such as LHII, chemists have synthesized and studied a range of porphyrin oligomers with various interporphyrin linkers that connect at the porphyrin meso-positions.[14-18] Figure 1.7 summarises a few key linkers. Synthetically, all of these oligomers can be derived from 5,15 aryl substituted porphyrin monomers that are brominated at the 10 and 20 positions.

In the meso-meso linked oligomers, the 90° dihedral angles between units result in very poor π-conjugation between adjacent porphyrin units. As a result, these oligomers have UV-Vis spectra relatively similar to that of the porphyrin monomer (Figure 1.8). In contrast, the ethyne and butadiyne linkers (Figure 1.10) facilitate electronic communication between the porphyrin units well, resulting in significantly more intense, red shifted Q-bands in these oligomers, which correspond to a transition dipole moment aligned down the length of the oligomer.[11] The charge delocalisation properties of the radial cations and anions of a family of butadiyne linked porphyrin oligomers of varying length have been studied by EPR, which show that a single positive charge is delocalised over 2-3 porphyrin units[19] and a single negative charge over 2 units.[20] These studies provide further evidence of the good electronic communication between porphyrin units in these types of oligomers.

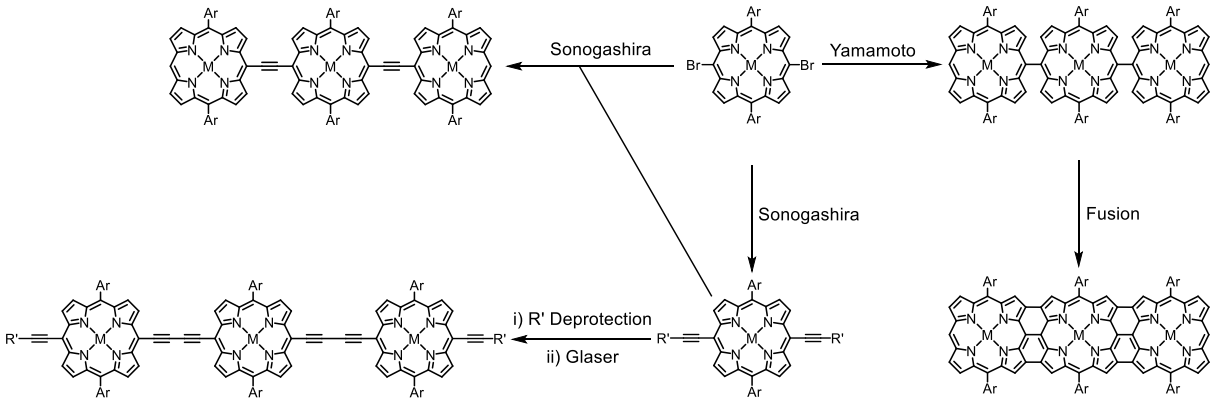

Figure 1.7: Porphyrin oligomers with various meso-meso connecting groups. (Top left) Ethyne linked porphyrin wire. (Bottom left) Butadiyne linked porphyrin wire. (Top right) Meso-meso linked porphyrin wire. (Bottom right) Fused porphyrin nanoribbon.

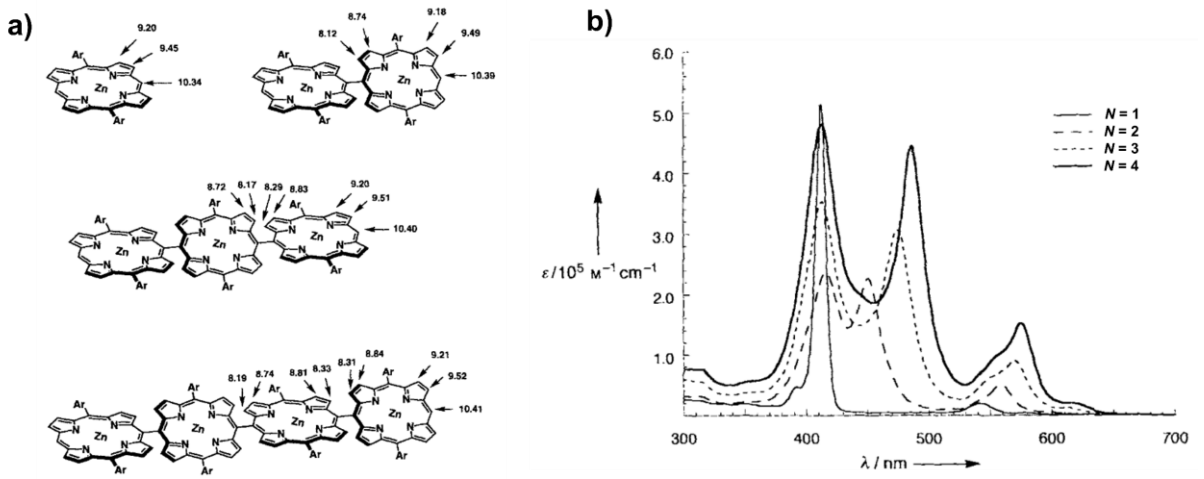

Figure 1.8. (a) Chemical structure and (b) UV-Vis spectrum of meso-meso linked porphyrin oligomers produced by Osuka. Ar = 3,5-^{t}Butylphenyl. Reproduced from reference.[14]

The fusion of meso-meso linked oligomers produces porphyrin nanoribbons with exceptional properties, resulting from the increased π-conjugation between porphyrin units in these materials. This is evidenced by the UV-Visible-IR spectroscopy of these oligomers, which exhibit intense, highly red shifted Q-bands upon fusion, that lie in the IR region for oligomers longer than the monomer (Figure 1.9). Additionally, similar EPR measurements to those on the butadiyne linked oligomers show that the fused tapes are able to delocalise a single positive charge over 10-14 units,[21] and STM break junction measurements have shown that the fused tapes exhibit ballistic conductance, where the transport of electrons is not impeded by scattering events, leading to exceptional conductance, for tape lengths from 1 – 7 nm.[16] This is particularly impressive as less well conjugated molecular wires exhibit poor conductance at lengths > 2 nm, which is significantly hindering the implementation of these molecules in molecular electronic devices.

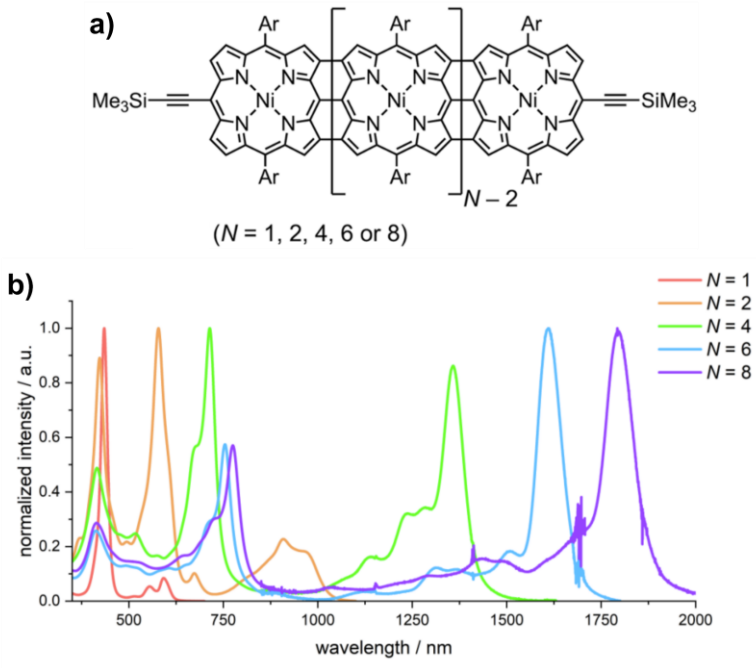

Figure 1.9. (a) Chemical structure and (b) UV-Vis-IR spectrum of fused porphyrin tapes produced by Anderson. Ar = 3,5-bis(tri-n-hexylsilyl)phenyl. ($CHCl_3$, 298 K) Reproduced from reference.[16]

In addition to facilitating stronger electronic communication between porphyrin units, fusing the meso-meso linked linear oligomers also locks the geometry of the structure into a flat linear belt. In contrast, the butadiyne link is significantly unrestricted, which enables completely free rotation of porphyrin units bound by this link.[22] As a result, the Q-band of linear butadiyne-linked oligomers is typically broad, due to the many conformations the oligomers can adopt in solution. Figure 1.10 presents the UV-Vis-NIR spectra of a range of butadiyne linked porphyrin oligomers (green) and the same oligomers bound to ligands designed to constrain the dihedral angles of adjacent porphyrin units to ~ 0° (black). This ligand binding is possible as the zinc metal in each porphyrin is able to bind an additional axial ligand, which in the case of pyridine, typically binds with a formation constant of 1.5 x 10^4 M^{-1} (Experimental section - Chapter 3). The sharper and more red shifted Q-bands of the oligomer·ligand complexes in Figure 1.10 demonstrates that constraining the porphyrin-porphyrin dihedral angles to ~ 0° dramatically increases the coupling between adjacent porphyrin units and limits the conformational freedom of the oligomer.

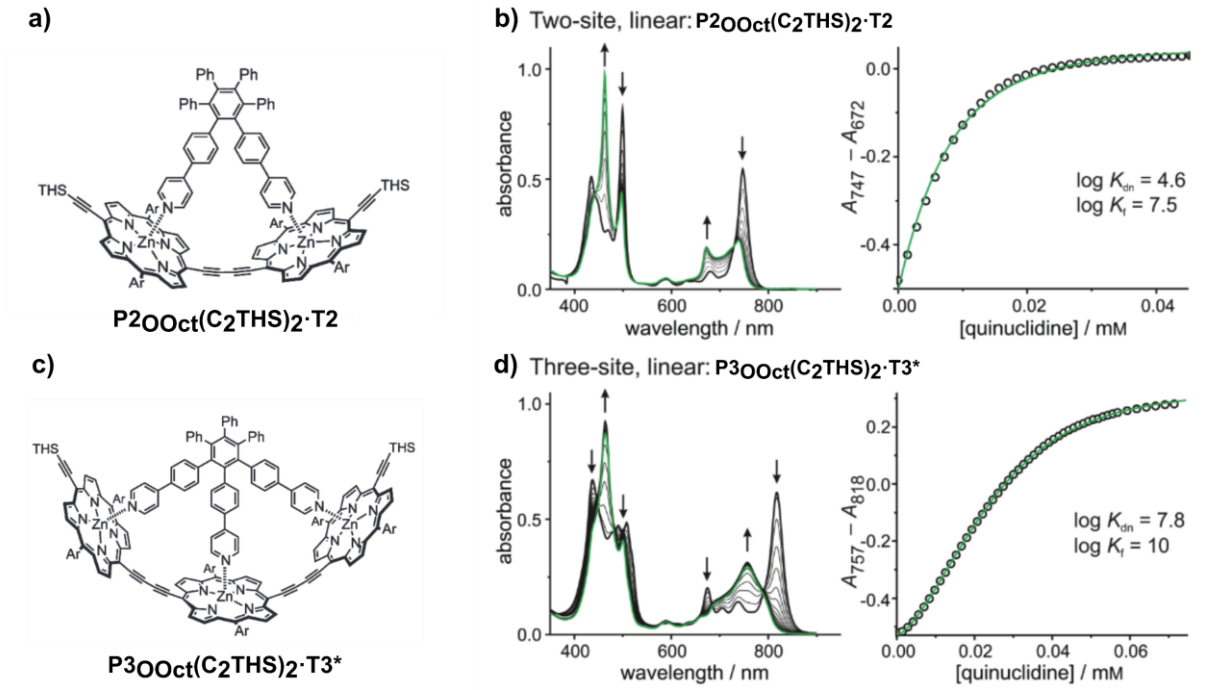

Figure 1.10. (a) Chemical structure of a butadiyne linked porphyrin dimer bound to the **T2** template. (b) UV-Vis spectrum of (a) (black) with varying concentrations of quinuclidine (Endpoint at green trace). (c) Chemical structure of a butadiyne linked porphyrin trimer bound to the **T3** template. (d) UV-Vis spectrum of (c) (black) with varying concentrations of quinuclidine (Saturated at green trace). ($CHCl_3$, 298 K). Reproduced from reference.[23]

1.1.4 Template-directed Synthesis of Porphyrin Nanorings

The ligand binding discussed in Section 1.1.3 has been significantly expanded over the past two decades to facilitate the synthesis of a range of supramolecular porphyrin-based materials.[24] Of specific interest to the work in this thesis is the application of this methodology to the synthesis of porphyrin nanorings. Figure 1.11 presents the archetypal synthesis of a porphyrin nanoring; the synthesis of a butadiyne linked 6-porphyrin nanoring using the T6 template. The butadiyne link is particularly compatible with template-directed synthesis as it is more easily distorted from the ideal linear geometry in comparison to the ethynyl, meso-meso or fused linkages previously discussed.

Though **c-P6** can be prepared from the monomer **P1$_{tBu}$(C$_2$)$_2$** (5% yield), under identical conditions using the dimer **P2$_{tBu}$(C$_2$)$_2$** results in higher yields (33-44 % yield).[25] This increased yield and higher selectivity for **c-P6** is probably a consequence of the exceptional cooperative binding that is exhibited between **T6** and the longer oligomers. As an example, **T6** binds to

P6$_{OOct}$(C$_2$THS)$_2$ with a formation constant K_f of 1 x 10^{20} M^{-1}, which increases to 1 x 10^{36} M^{-1} when using the nanoring **c-P6$_{tBu}$.**[23] The strong binding between the longer oligomers leads to rapid formation of the oligomer·template complexes in which the terminal acetylene groups are pre-organised in the position required for coupling to form **c-P6**, leading to a more selective synthesis.

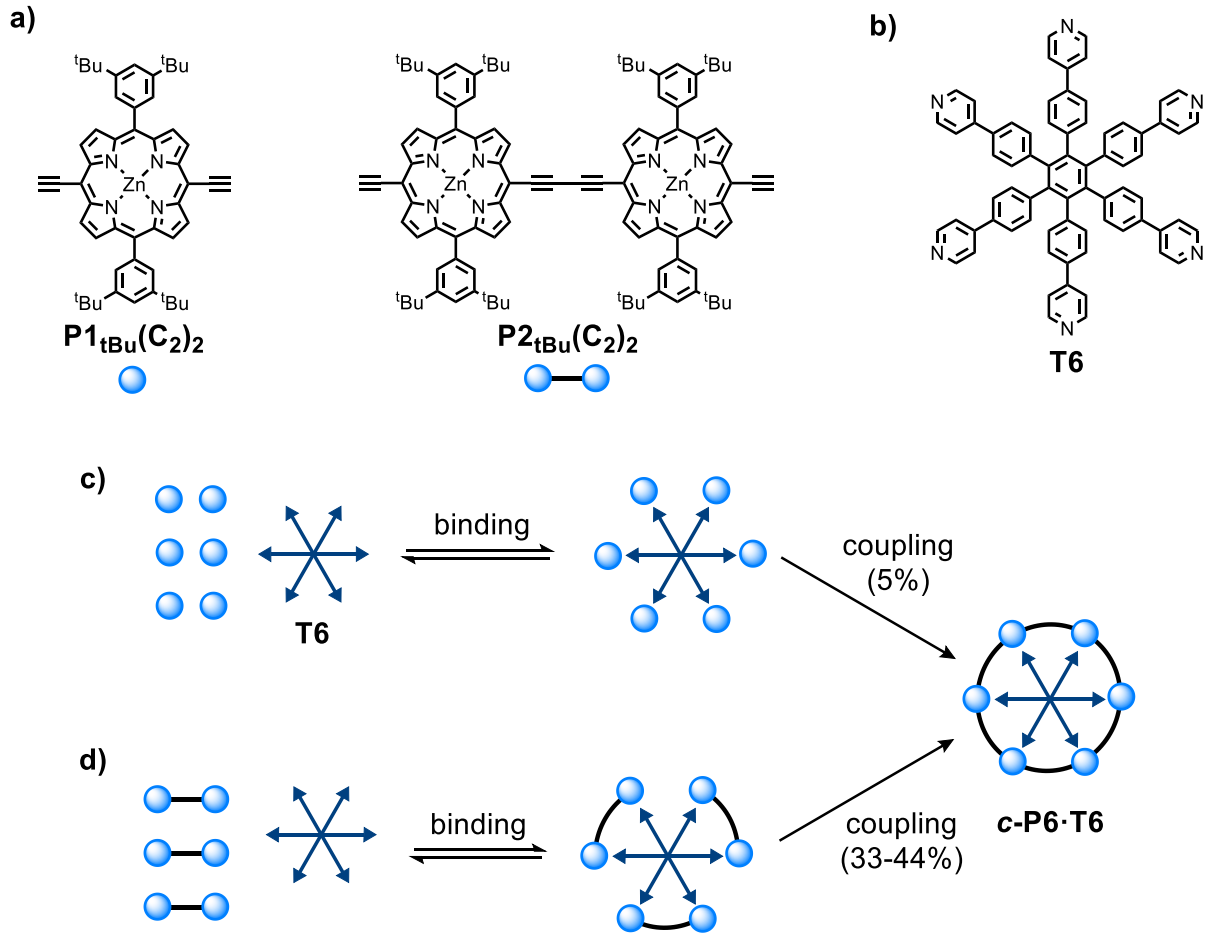

Figure 1.11. (a) Chemical structures of a porphyrin monomer and porphyrin dimer with terminal acetylene groups. (b) Chemical structure of the **T6** template. (c) Template directed synthesis of **c-P6·T6** from monomer. (d) Template directed synthesis of **c-P6·T6** from dimer.

By selecting an oligomer that cannot form an exact 1:1, 2:1 … N:1 (where N is an integer) complex with a given template, larger nanorings can be formed which typically contain a number of porphyrin units equal to the lowest common multiple of the template binding sites and porphyrin units in the selected oligomer. The simplest example of this is the synthesis of the **c-P12** nanoring from **P4** and **T6** (Figure 1.12, 35% yield).[26]

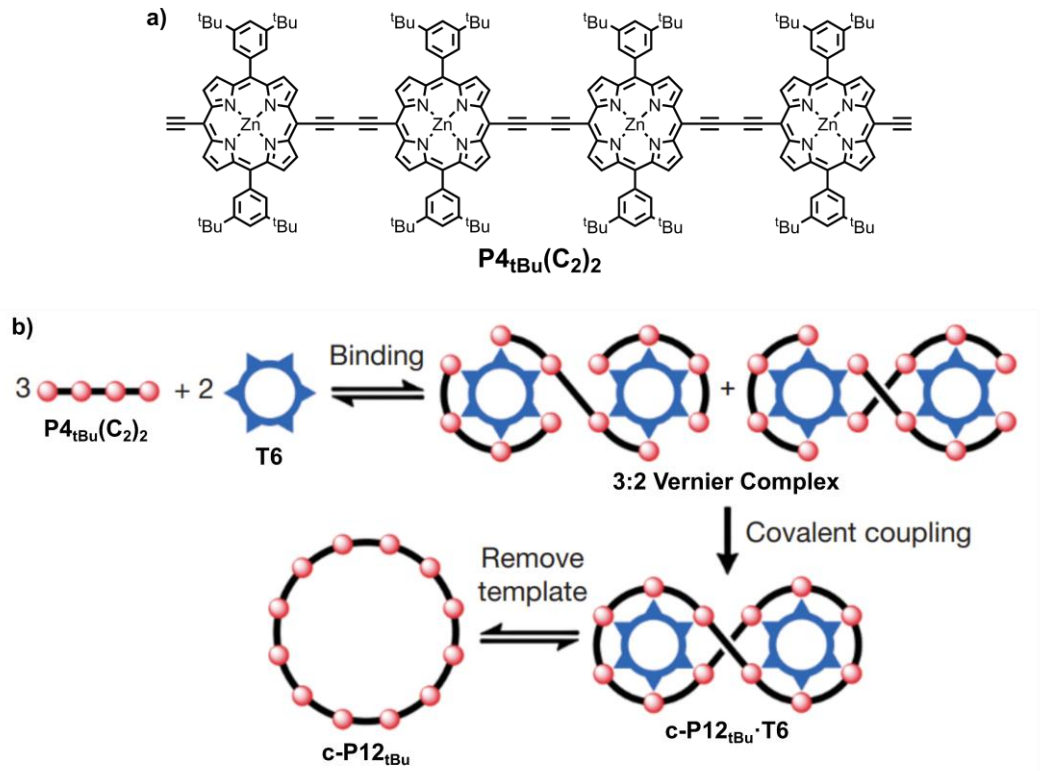

Figure 1.12. (a) Chemical structure of **$P4_{tBu}(C_2)_2$**. (b) Vernier template-directed synthesis of ***c*-$P12_{tBu}$**. Scheme (b) adapted from reference.[26]

Here, 12 is the lowest common multiple of 4 and 6, which corresponds to a 3:2 complex of **$(P4)_3$:$(T6)_2$**. The Vernier route has so far been used to prepare the largest porphyrin based nanoring ***c*-P50**, from a 10-porphyrin oligomer and an 8-legged template.[27] These synthetic routes have been termed Vernier template-directed synthesis, after the French mathematician Pierre Vernier.

Using both the standard and Vernier template-directed approaches, many different sized porphyrin nanorings have been syntheised, with a range of inter-porphyrin connections. It is understood that the smallest rings, such as ***c*-P6**, have relatively more constrained geometries, which is a consequence of the size of the porphyrin units and narrow nanoring cavity slowing the inversion of porphyrin units.[28] In contrast, large porphyrin nanorings, such as ***c*-P50** are considerably more flexible and capable of adopting a wider range of geometries, as evidenced by STM imaging of ***c*-P50**.[27] This behaviour highlights an additional function of the template molecules which is their ability to control and define the precise conformation of porphyrin

nanorings. There are many examples of this functionality in the literature,[24] however one particularly informative example is that of **c-P12**. This particular nanoring is most easily synthesised via the Vernier template-directed route shown in Figure 1.12, which can yield the free nanoring or the 2:1 figure-8 complex **c-P12·(T6)$_2$**. By binding two equivalents of the extended **T6** template, **T6$_e$**, a perfectly cyclic complex can be formed in which the two **T6$_e$** templates are stacked on top of one another in the centre of the nanoring (Figure 1.13). The figure-8 and cyclic geometries of these nanoring complexes are of great importance as to whether global ring currents are observed in ***c*-P12**, which will be discussed later in this chapter.

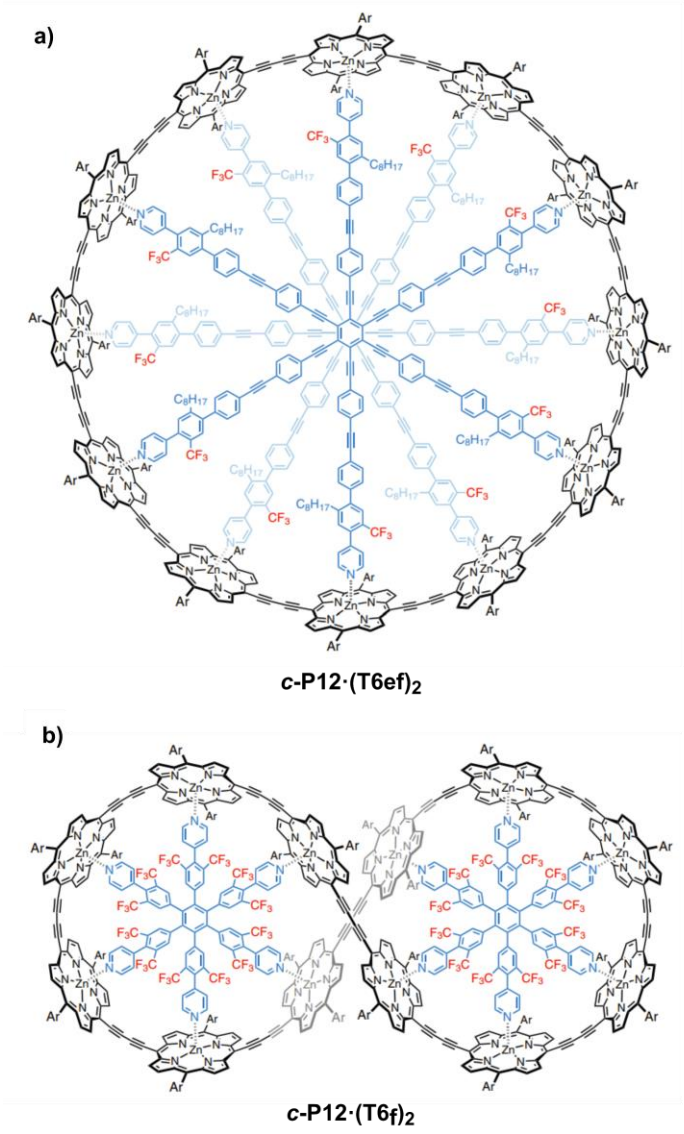

Figure 1.13. (a) Chemical structure of ***c*-P12** in a cyclic geometry when bound to two equivalents of the extended **T6** template – **T6e**. (b) Chemical structure of ***c*-P12** in a figure of 8 geometry when bound to two equivalents of the extended **T6$_{CF3}$**. Reproduced from reference.[29]

The butadiyne-linked porphyrin nanorings are of particular relevance to the work presented in this thesis, however it is important to note that many other nanorings and templates have been synthesised and studied, specifically by the Anderson group as part of a long and systematic study of this class of supramolecular complexes.[24] Figure 1.14 presents a summary of some key structures produced from this study to demonstrate the diversity of nanorings that have so far been produced.

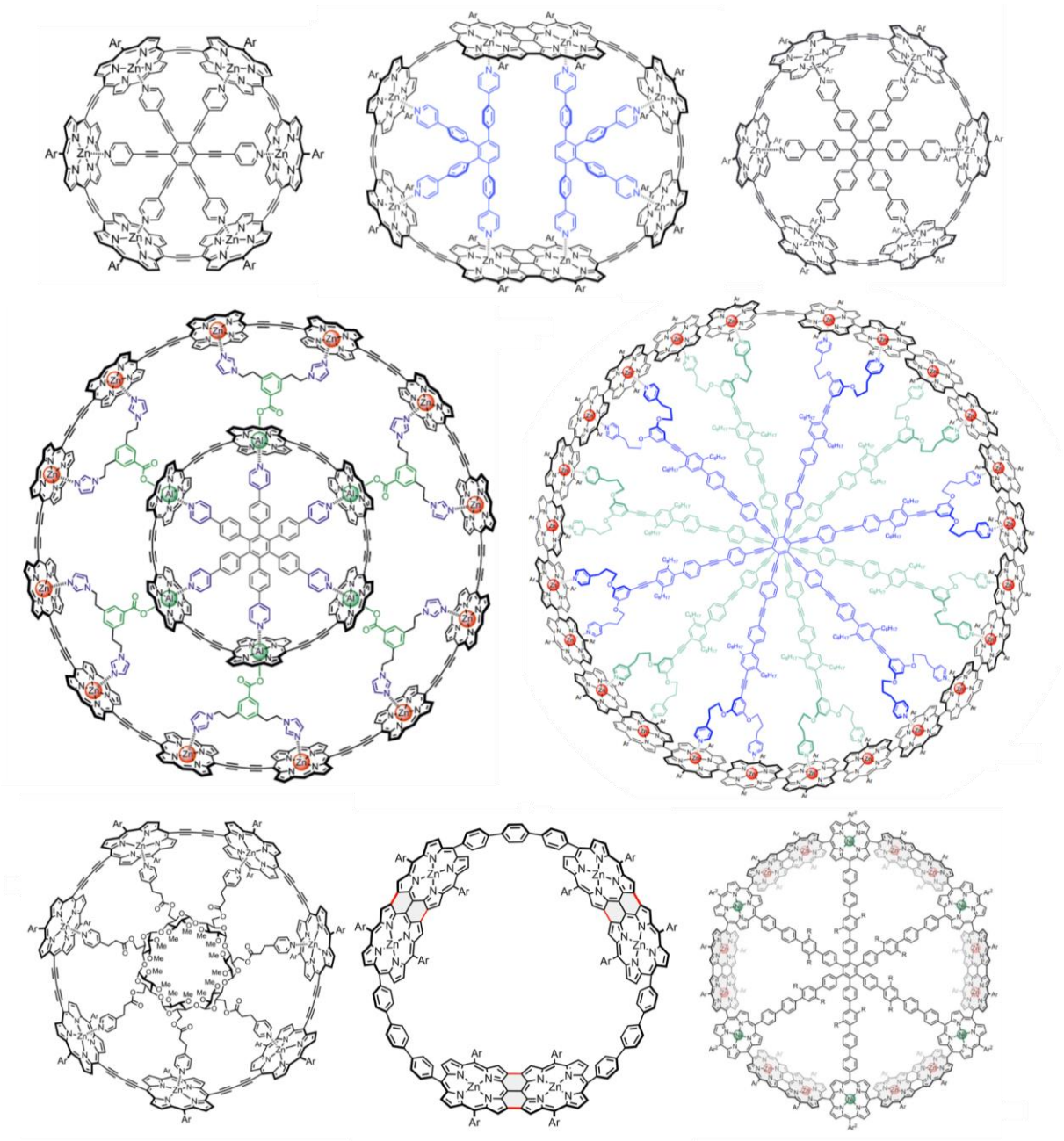

Figure 1.14. Chemical structures of a range of porphyrin nanoring complexes. Reproduced from references.[25, 30-36]

One notable exception from Figure 1.14 is the all meso-meso linked nanoring, which would serve as a precursor to the fully fused belt presented in Figure 1.15. Such structures are of great interest to those in the field of molecular electronics as they are predicted to have exceptional properties, much like those observed in the fused tapes presented in Section 1.1.3.[37] However, the closure of meso-meso linked linear oligomers into rings has proven to be exceptionally challenging, which has been attributed to the high amounts of strain generated by bending these oligomers. Figure 1.14 (middle right) presents the closest published attempt to this ring closure, which require the use of a butadiyne link to finally close the nanoring.

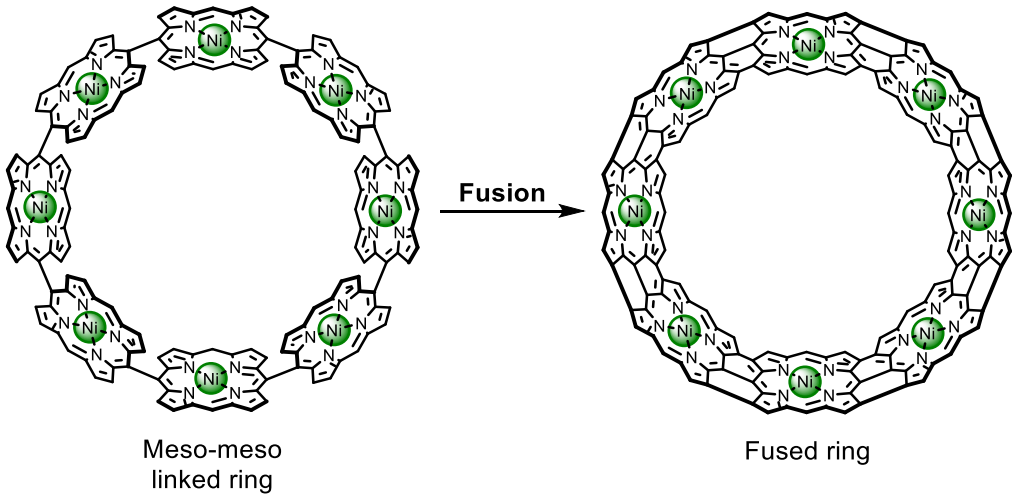

Figure 1.15. Chemical structures of a meso-meso linked 8-porphyrin nanoring and fused belt. Recently synthesised in the Anderson group but not yet published.

One key property of interest in these porphyrin-based nanorings is their ability to sustain global ring currents. The experimental evidence for the presence of these ring currents confirms that the nanorings are globally anti/aromatic, which in the specific case of ***c*-P12·(T6e)$_2$** (Figure 1.13a) marks the largest π-system to exhibit this property (162 π-electrons). The study of global aromaticity in these porphyrin-based nanorings has been a strong source of motivation for their challenging synthesis and for the project outlined in Chapters 2 and 3 of this thesis. Therefore, the next section of this chapter will provide some background to aromaticity and summarise what has been learned so far from studying this phenomenon in porphyrin-based nanorings.

1.2 Aromaticity

1.2.1 A Definition of Aromaticity

Prior to any discussion of aromaticity, it is important to state that the phenomenon termed "aromaticity" encompasses a broad range of emergent properties that are observed across a wide range of chemical species. These properties vary greatly across the species classified as aromatic, with some possessing many of the defining properties whilst others possess very few.[38] Because of this wide diversity of properties and chemical make-up, experts in the field have yet to agree on what precisely defines aromaticity.

To focus this introduction on the type of aromaticity relevant to the work in this thesis, I will limit the following discussion to the effects of aromaticity in π-conjugated organic molecules which obey Hückel's 4n + 2 π-electron rule (In the singlet ground state molecules with 4n + 2 π-electrons are aromatic and 4n π-electrons are antiaromatic). However, it is important to note that various other forms of aromaticity have been identified, for example; Baird aromaticity (4n π-electrons are aromatic in the first electronically excited triplet state),[39] Möbius aromaticity (4n π-electrons are aromatic when in a Möbius geometry),[40, 41] 3D aromaticity (e.g. in *closo*-borane ($B_6H_6^{2-}$)),[42] spherical aromaticity (e.g. in fullerene),[43] or σ-aromaticity (e.g. in $[Ph(SePh)_6]^{2+}$).[44]

For molecules obeying Hückel's rule there are 3 experimentally observable (and computationally predictable) criteria that are frequently used to assign their anti/aromaticity.[45] These are as follows:

1- The Energetic Criterion

This criterion states that the total energy of a given aromatic species is reduced by a contribution from its aromatic stabilisation energy (ASE). Schleyer defines ASE as the "extra stabilisation in excess of the resonance energy", where resonance energy refers to the stabilising effects solely attributable to conjugation.[46] Precisely determining ASE requires

the use of homodesmotic equations (Figure 1.16) which for benzene outputs an ASE value of 28.8 kcal mol^{-1}.[46] With careful selection of the components of the homodesmotic equation, ASU can therefore be calculated, however, this becomes particularly challenging with larger and more complex chemical systems, as all other forms of de/stabilising interactions must be precisely accounted for (e.g. hyperconjugation, strain, van der Waals forces, Coulomb interactions).[46]

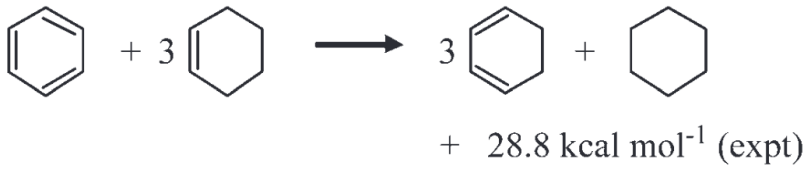

Figure 1.16. A homodesmotic equation used to calculate the ASU for benzene. Reproduced from reference.[46]

2- The Structural Criterion

A key concept in aromaticity is that the strong delocalisation of electrons over the molecule homogenises the lengths of all bonds that facilitate the electron delocalisation. As the simplest example, we can consider benzene verses its theoretical isomer in which all 3 π-bonds are completely localised. The presence of aromaticity in benzene means that the π component of these bonds are actually evenly distributed across all six C-C bonds, so they are of equal length (1.39 Å) when observed experimentally by neutron diffraction.[47] The molecule therefore possesses no bond length alternation (BLA). As precise and indisputable experimental data for bond lengths can be obtained from crystal structures, the concept of BLA has proven to be particularly useful for defining aromaticity. Finally, direct comparison between crystallographic data and computationally optimised geometries allows for finer analysis of how well particular computational methods model aromaticity, and therefore how accurate their predictions of the properties of these molecules may be.

3- The Magnetic Criterion

The magnetic criterion considers the fact that ring currents are induced in circuits of delocalised electrons, when the circuit is in the presence of a magnetic field.[48] For aromatic

molecules (4n+2 π-electrons) the induced current generates a magnetic field which is parallel to the external field outside of the circuit, but anti-parallel inside the circuit. An example of this phenomenon in porphyrin was presented in Figure 1.5, but a simpler example is that of benzene in Figure 1.17.

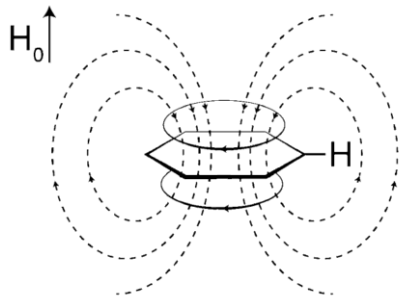

Figure 1.17. Induced ring current and magnetic field in a benzene molecule when exposed to external magnetic field H_0. Reproduced from reference.[48]

The presence of the induced magnetic field means that the proton environments in benzene are exposed to a stronger magnetic field than would be the case if aromaticity did not exist, so appear at a larger ppm value (7.26 ppm[45]) by ^{1}H NMR compared to the vinyl protons in cyclohexene (5.60 ppm[45]). As the direction of the induced magnetic fields is reversed in antiaromatic molecules (4n π-electrons), the difference in shielding/deshielding behaviour inside/outside of the circuit can be used to definitively assign the presence of anti/aromaticity. These assignments are based on experimental NMR evidence from probe nuclei, so are a robust method of assigning anti/aromaticity. However, these assertions can also be supported by computational studies, such as NICS calculations, which will be discussed later in this chapter.

Of these three criteria, the Magnetic Criterion is particularly useful as it can be applied simply to complex molecular systems, for which the precise determination of ASE or collection of x-ray crystallographic data would be challenging. This particular criterion has therefore seen widespread use in recent years, which has generated a wealth of experimental and computational evidence of anti/aromaticity in a wide range of novel compounds. This criterion

is the primary method we used to determine the global anti/aromaticity of the work presented in Chapters 2 and 3, therefore, the following section will explore the origin of the ring current effect and demonstrate how NMR data alongside NICS calculations can be used to assign anti/aromaticity.

1.2.2 The Ipsocentric Approach to Predicting Ring Currents in Aromatic Molecules

Before discussing the experimental and computational methods used to probe the presence of ring currents in molecular systems, I will give a brief overview of the ipsocentric approach to aromaticity, formulated by Stiner and Fowler.[49-51] This approach considers how the translational (change in parity) and rotational (conservation of parity) symmetry of molecular orbital transitions influences the aromaticity of a molecule. Figure 1.18 demonstrates this by analysing the frontier molecular orbitals of benzene.[52]

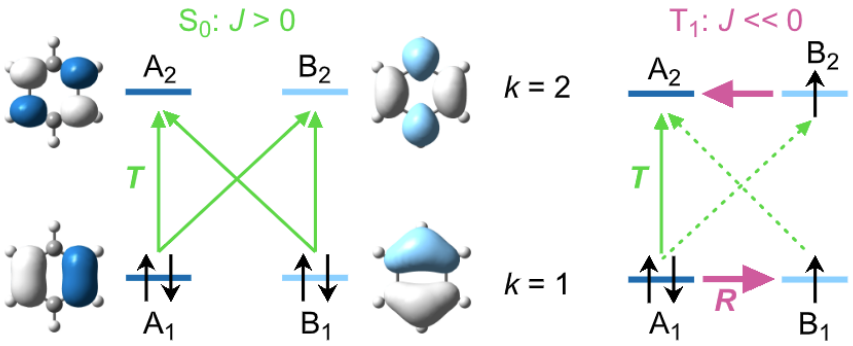

Figure 1.18. Transitions between the frontier molecular orbitals of benzene in the S_0 (left) and T_1 (right) state. Reproduced from reference.[52]

The ipsocentric approach postulates that it is the strengths of the various spin allowed transitions between the frontier molecular orbitals that determine the tropicity of the overall ring current as either diatropic (aromatic) or paratropic (antiaromatic). Transitions between "spatially similar orbitals differing in the number of nodal planes by one" **(T)**, such as a transition from A_1 to A_2 in Figure 1.18, contribute to diatropic ring currents. Whereas transitions which are related by rotations between molecular orbitals **(R)**, such as A_1 to B_1 in Figure 1.18, contribute to paratropic ring currents. By summing these various contributions (computationally) the overall tropicity, and therefore anti/aromaticity, of the ring current can be predicted.

Figure 1.18 demonstrates how the only spin allowed transitions in benzene in the neutral S_0 state are those related by translations **(T)**. This results in a strong diatropic ring current, which matches the known aromaticity of benzene. Conversely, in the first excited triplet state some of the previously allowed translational transitions are spin forbidden and there is now the possibility of spin allowed rotational transitions. When summed, the allowed transitions result in an overall paratropic ring current, which matches the prediction from Baird's rules of aromaticity in triplet excited states.[39]

1.2.3 Using NMR as Experimental Evidence of Aromaticity

As previously discussed, diatropic (aromatic) ring currents generate a magnetic field which opposes the external field inside the circuit but is aligned with the external field outside of the circuit. The magnetic fields generated by paratropic (antiaromatic) ring currents are the opposite of this. For clarity, Figure 1.19 presents the magnetic fields generated by each type of ring current, colour-coded with red regions in which the induced field enhances the external field, and blue regions where the induced field diminishes the external field.

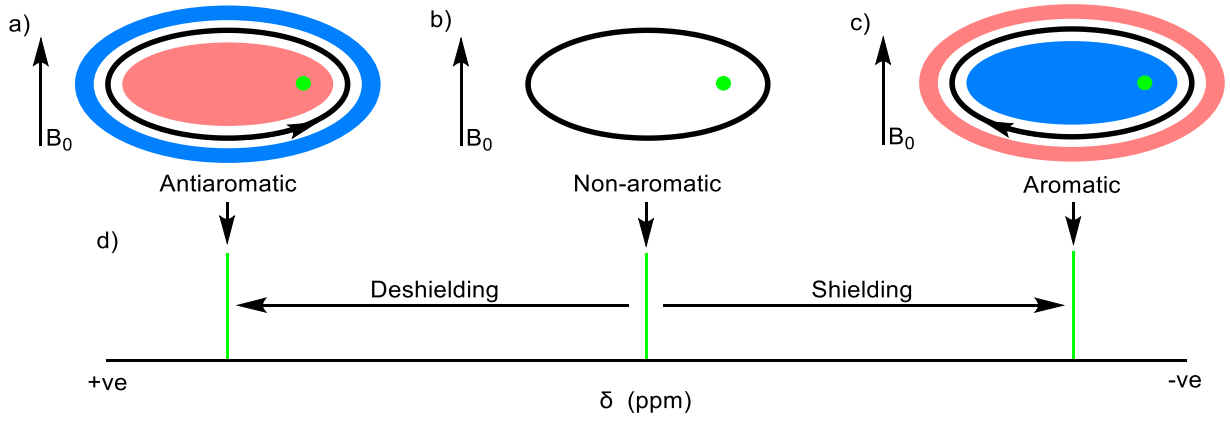

Figure 1.19. A cyclic molecule in the XY plane with magnetic field B_0 applied along the z-axis. (a) The antiaromatic state, with paratropic ring current. (b) The non-aromatic state, with no ring current. (c) The aromatic state, with diatropic ring current. (d) An example of how the NMR signal of a probe nuclei (green) would be expected to shift in each of the different states in (a-c).

If probe nuclei are positioned in these regions they can report on the induced magnetic field and therefore the aromaticity of the molecule. This is particularly useful when the aromaticity of a

molecule can be switched on and off or converted between aromatic and antiaromatic states by an external stimulus (e.g. by a $\pm 2e^-$ oxidation/reduction), as the change in shielding (decrease in external magnetic field)/deshielding (increase in external magnetic field) effect of the ring current can be compared between the different states.

1.2.4 Predicting Aromaticity with NICS Calculations

The shielding/deshielding of probe nuclei (e.g. in Figure 1.19) can be modelled computationally using Nucleus Independent Chemical Shift (NICS) calculations. This methodology was developed by Schleyer in 1996[53] and has since seen widespread adoption in the field of aromaticity. Briefly, the methodology relies on first optimising the geometry of a molecule of interest, to which probe nuclei are overlayed that simply spectate the electronics of the molecule. In Gaussian16, atom type Bq is used for these spectator atoms, which are typically overlayed as an evenly spaced grid through the plane of the molecule of interest. Running an NMR calculation on the molecule + probe nuclei grid structure generates shielding tensors for each atom. Typically, for a ring in the XY plane, either the negative of the shielding tensor's ZZ or isotropic component is plotted for each Bq atom, as a representation of the shielding/deshielding at each Bq atom's position. In doing this, plots such as those in Figure 1.20 can be constructed, which for ***c*-P6** predict no global ring current in the neutral state, but global antiaromaticity for the +4 state and global aromaticity for the +6 state.

Numerous improvements to the initial NICS methodology have been explored over the past three decades which primarily aim to isolate the π-contributions to the NICS values from other contributing factors.[48] Two of the simplest improvements that can be used for planar molecules in the XY plane are: (1) to raise the Bq atom grid 1 Å above the plane of the molecule. (2) plot only the ZZ component of the shielding tensor. Implementing these two changes has been shown to reduce σ-contributions to the NICS values, therefore giving a more accurate representation of the ring current effect for molecules where the ring current arises only from π-contributions.[48]

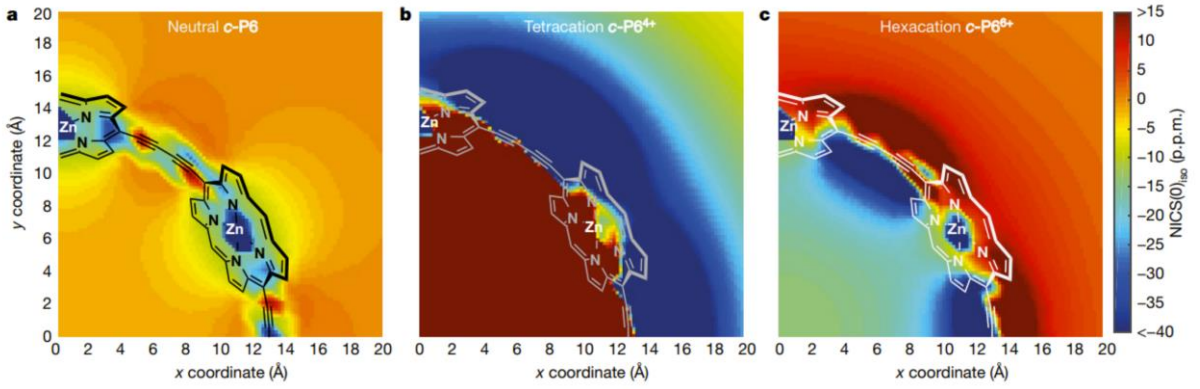

Figure 1.20. $NICS_{iso}$ plots of ***c*-P6** presented as a map of ¼ of the nanoring. (a) Non-aromatic neutral state. (b) Antiaromatic +4 state. (c) Aromatic +6 state. Red = deshielding, blue = shielding. Reproduced from reference.[54]

1.2.5 Experimental Evidence of Global Aromaticity in a 6-Porphyrin Nanoring

To demonstrate the assignment of aromaticity using the magnetic criterion described in Sections 1.2.1.–1.2.4. let us consider the global aromaticity predicted for the butadiyne linked 6-porphyrin nanoring ***c*-P6** (Figure 1.20 and 1.21) in the neutral, +4 and +6 oxidation states.[54]

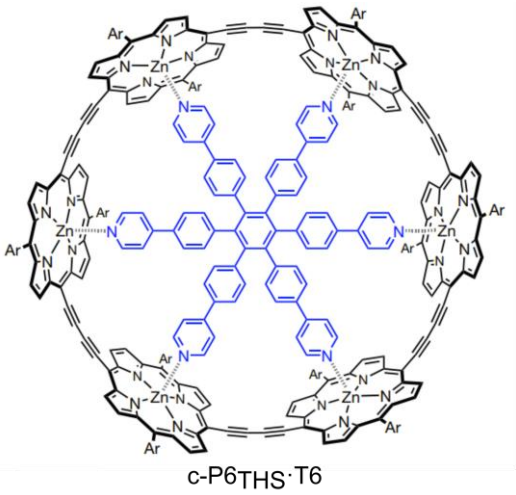

Figure 1.21. Chemical structure of the butadiyne linked 6-porphyrin nanoring ***c*-P6$_{THS}$·T6**. (Ar = (3,5-bis(trihexylsilyl))phenyl. Figure reproduced from reference.[54]

In order to define the structure of the nanoring and to ensure there were probe nuclei positioned on the inside of the ring, the **T6** template was bound to ***c*-P6$_{THS}$**. This binding crucially prevents the porphyrin units from rotating, which would reverse the position of the two aryl groups. Peeks, Claridge and Anderson report that the rotation of these aryl groups is slow on the NMR timescale, so NOESY correlations between the **THS$_{in}$** group (**THS'** in Figure 1.22) and protons

on the **T6** template can be observed.[54] Because of this, the **THS$_{in}$** and **THS$_{out}$** groups can be used as probe nuclei for measuring the effect of a global ring current.

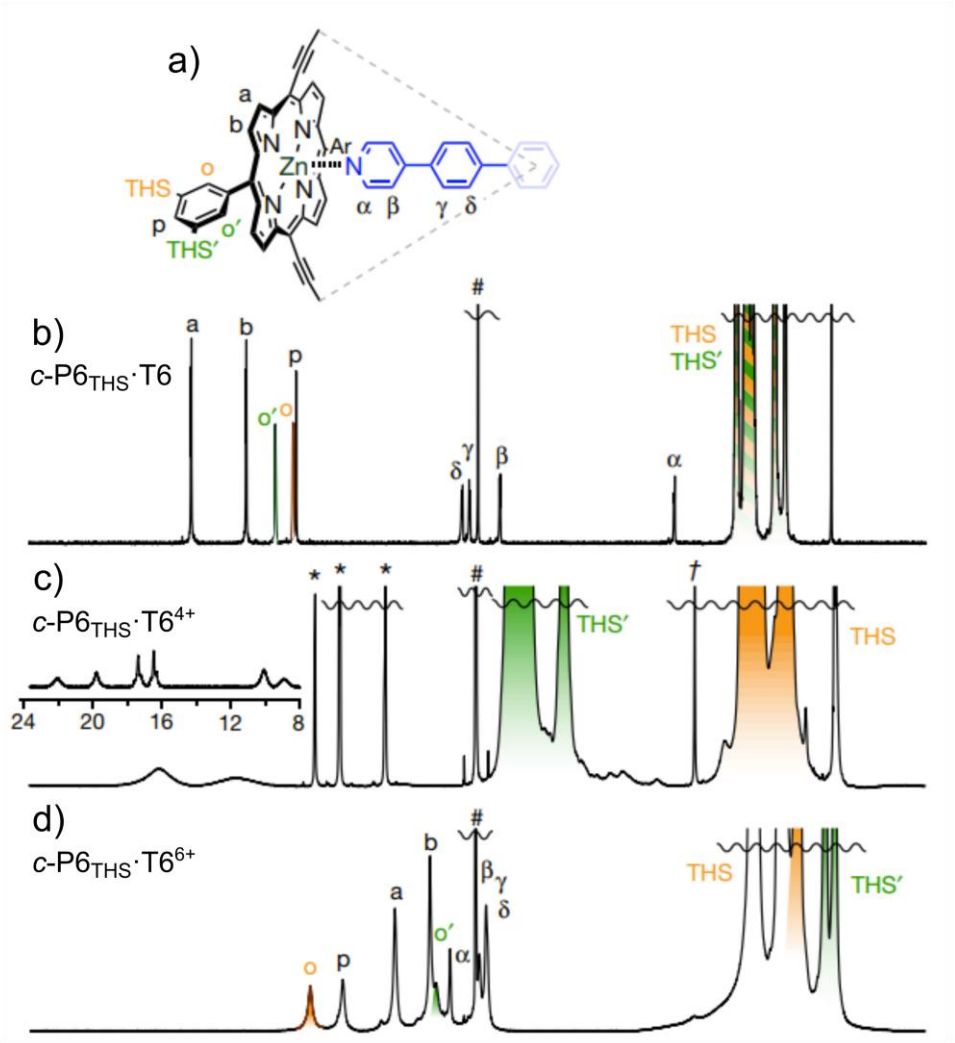

Figure 1.22. (a) Assignment of proton environments in *c*-P6$_{THS}$·T6. (b-d) ^{1}H NMR spectra of *c*-P6$_{THS}$·T6 in the neutral, +4 and +6 oxidation states. Reproduced from reference.[54]

In the neutral state (84 π-electrons – 4n)(Figure 1.22b) no global ring current is observed as **THS$_{in}$** and **THS$_{out}$** are coincident with one another. It is noted that the **T6** template protons are significantly more shielded upon binding to ***c*-P6$_{THS}$**, which is attributed to the local aromatic ring current of the porphyrin units. However, upon oxidation to the +4 state (80 π-electrons – 4n)(Figure 1.22c) a shift in the **THS$_{in}$** group is observed. Here **THS$_{in}$** is assigned by NOESY correlations to the group of very deshielded resonances at 24 – 8 ppm which come from **T6**. The deshielding of both **THS$_{in}$** and **T6** indicates that those environments inside the ring are

experiencing a stronger magnetic field, which is expected for a globally antiaromatic molecule with 80 π-electrons (4n, n = 20).

By further oxidising the nanoring to the +6 state (78 π-electrons, 4n + 2, n = 19) a negative shift in the **THS$_{in}$** peaks is observed, relative to the neutral compound. These shifts are consistent with the centre of the ring experiencing a diminished magnetic field, as a result of the aromatic global ring current present in the nanoring.

1.2.6 Global Aromaticity in Large Porphyrin Nanorings

To further probe the size limit of global aromaticity, Anderson has reported similar oxidative NMR studies on a wide range of nanoring·template complexes. The results of this systematic study are presented in Figure 1.23, which demonstrates how the presence of global aromaticity has been confirmed in π-circuits of up to 162 π-electrons (**[*c*-P12$_{THS}$·(T6$_{ef}$)$_2$]$^{+6}$**).

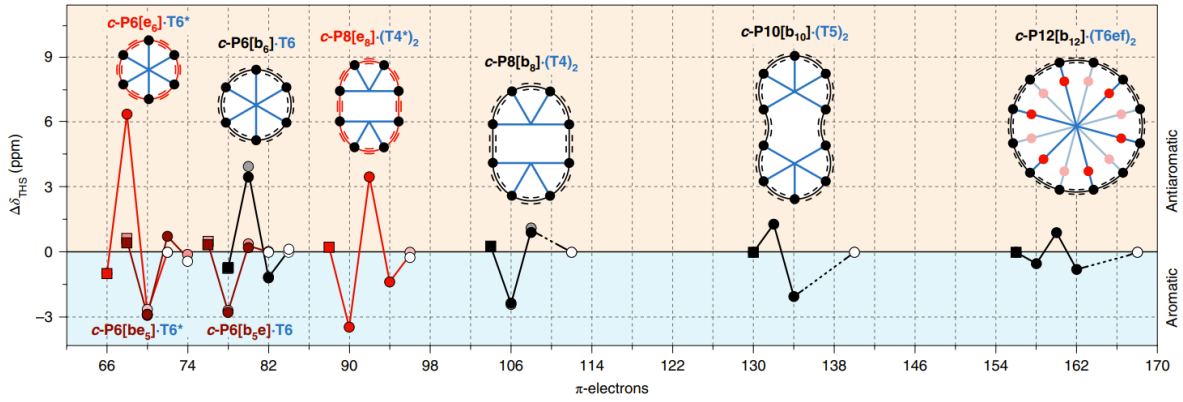

Figure 1.23. The difference between **THS$_{in}$** and **THS$_{out}$** ($\Delta\delta_{THS}$) for a range of nanorings with different π-electron counts. **THS$_{in}$** experiences a larger magnitude change in shielding/deshielding, so negative $\Delta\delta_{THS}$ values indicate global aromaticity, whereas positive $\Delta\delta_{THS}$ values indicate global antiaromaticity. Reproduced from reference.[29]

As discussed in Section 1.1.4, the geometry of ***c*-P12$_{THS}$** can be controlled by the choice of the template that it is bound to, giving either a cyclic geometry with two equivalents of **T6ef**, or a figure-of-8 geometry with two equivalents of **T6f** (Figure 1.13).[29] Oxidative NMR titrations on these two geometries reveal that only the cyclic geometry displays evidence of global aromaticity. It is suggested that ring currents generated in the two lobes of the figure-8 geometry cancel each other at the centre of the structure (Figure 1.24), which rationalises why no aromatic

or antiaromatic states are observed for this particular geometry.[29] This conclusion is supported by NICS calculations.

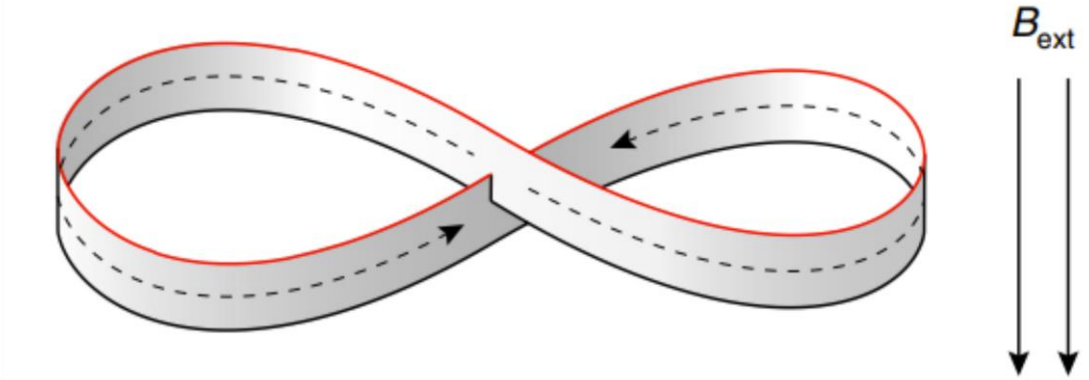

Figure 1.24. Example of how anticlockwise ring currents induced in the two loops of a figure 8 structure cancel out at the centre of the structure. Reproduced from reference.[29]

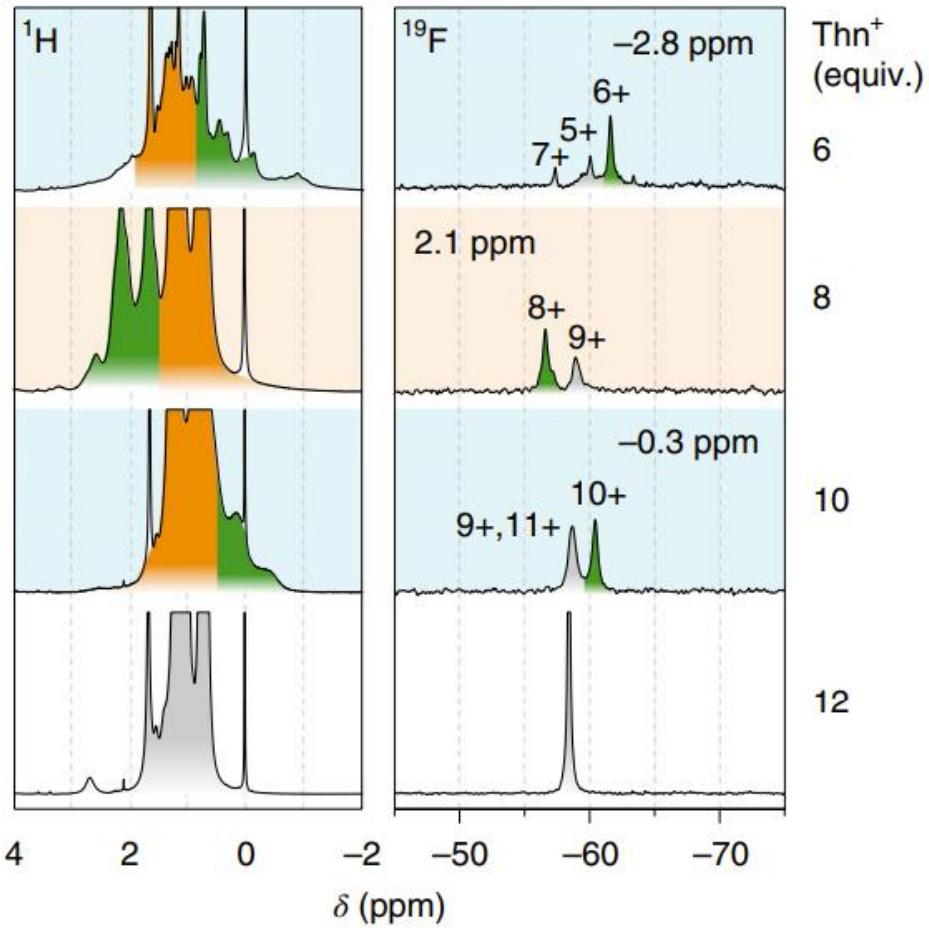

Figure 1.25. Experimental ^{1}H and ^{19}F peaks from the THS_{in} and CF_3 group of ***c*-P12$_{THS}$·(T6$_{ef}$)$_2$** shaded in green with varying equivalents of the oxidant thianthrenium (Thn^+). Reproduced from reference.[29]

Finally, the oxidative titrations on ***c*-P12$_{THS}$·(T6$_{ef}$)$_2$** demonstrate a key design choice that has enabled the study of ring currents in large porphyrin nanorings. In these large nanorings (e.g. *c*-P12) the ^{1}H signals from the template protons become very broad as soon as oxidant is added to the NMR sample. Though the THS groups still shift during the titration (Figure 1.25) these groups cannot be unambiguously assigned to either **THS$_{in}$** or **THS$_{out}$** as there are no observable NOESY correlations to the template. However, by installing CF_3 groups on the template, which are permanently on the inside of the nanoring, the shift of both the CF_3 ^{19}F peak and THS ^{1}H peaks can be correlated, to assign the various aromatic and antiaromatic states. Figure 1.25 presents the ^{19}F and ^{1}H NMR data from a titration of ***c*-P12$_{THS}$·(T6$_{ef}$)$_2$** to demonstrate these shifts.

1.2.7 Thesis Aim 1: The Size Limit of Aromaticity

To continue the systematic study of global aromaticity in porphyrin-based nanorings, the first objective of this thesis was to design and synthesise a template suitable for holding a butadiyne-linked 18 porphyrin nanoring (***c*-P18**) in a circular geometry. This primarily synthetic work is reported in Chapter 2, along with the use of this template to direct the synthesis of ***c*-P18**.

Following this I aimed to investigate the extent of π-delocalisation in the template·nanoring complex and identify any globally aromatic and antiaromatic states of the nanoring, through the previously described oxidative NMR titrations. This work, along with computational studies on the template·nanoring complex is reported in Chapter 3.

1.3 Chiral π-Conjugated Materials

1.3.1 Applications of Achiral Organic Electronic Materials

Due to their unique optical and semiconducting properties, π-conjugated materials (such as porphyrin oligomers) have been of interest to the field of organic electronics, which has grown over the past few decades, inspired by the successful commercialisation of the OLED display.[55] However, many of the applications of organic electronic materials overlap significantly with

the well-established inorganic materials that currently see widespread use in our electronic devices. The processing and manufacturing of these inorganic based devices has been exceptionally well optimised, which reduces the costs associated with this technology and presents a challenge for competing alternative technologies. As a result, for organic electronic materials to see commercial success, they need to either significantly outperform the current inorganic based devices, be substantially cheaper, or be applied to a problem that, as a result of their unique properties, only they can solve.[56]

In terms of the OLED display, this specific technology initially demonstrated many superior properties such as; an increased efficiency, true black colour, higher contrast colours, thinner displays, and faster response times.[55] Optimism for the development of even more commercially viable properties such as transparent or flexible OLED displays increased the appeal for investing in this technology,[57] inevitably leading to its adoption into commercial devices.[55] The example of the OLED display demonstrates one example of how organic electronic devices can compete with well-established technologies. Many additional applications of interest specifically take advantage of the tunability of organic based devices, the low cost of device fabrication, their solution processability and the flexibility of the device architectures. Those in the field hope to utilise these properties for applications as organic photovoltaic cells (OPV)[58], flexible biological sensors[59] and organic field-effect transistors (OFET).[60]

1.3.2 Chiral Organic Electronic Materials

The applications mentioned in Section 1.3.1. rely primarily on the interaction of the organic electronic device with either light, the electrical currents carried by electrons, or both. These can both possess chirality, in the form of circularly polarised light or by the spin quantum number of a given electron. Introducing chirality into organic electronic devices allows chemists to differentiate between these chiral forms of matter, as their interactions with the device will be dependent on their own chirality and that of the device. This opens the door to

an array of interesting applications such chiral sensing,[61] electron spin filtering,[62] spin controlled photoredox catalysis[63] and applications which require the absorption or emission of circularly polarised light, such as display technologies.[64]

To quantify, and therefore compare, the chiroptical activity of novel organic materials for use in these applications, experiments are performed to measure how well the material can differentially absorb/emit left and right circularly polarised light; in addition to measuring the intensity and quantum yields of these processes.

The following section aims to provide some background as to how circularly polarised light interacts with chiral absorbative/emissive materials, as an understanding of this enables us to rationalise the observed chiroptical activities of our materials and direct the rational design of materials with improved properties.

1.3.3 Fundamentals of Chiroptical Spectroscopy

1.3.3.1 Electric Transition Dipole Moment

Electromagnetic radiation is comprised of propagating electric and magnetic fields. In linear polarised light (Figure 1.26, middle) the electric and magnetic field vectors are confined to perpendicular planes and have oscillating amplitude. Circularly polarised (CP) light (Figure 1.26, left) is also comprised of electric and magnetic field vectors which are aligned perpendicularly to one another; however, these vectors are of constant magnitude and rotate either clockwise (righthanded circular polarisation, RCP) or anticlockwise (lefthanded circular polarisation, LCP) about the axis of propagation. The handedness of CP light makes it chiral and as a result carries angular momentum which must be conserved upon absorption or emission from a molecule.

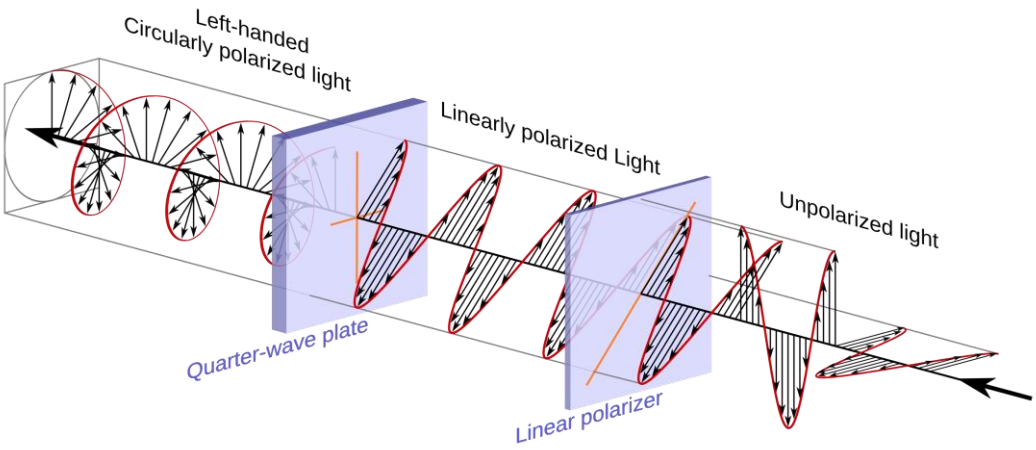

Figure 1.26. Movement of an unpolarised wave of light from right to left through a linear polariser, to form linearly polarised light, then a quarter-wave plate, to form circularly polarised light. The arrows and red lines shown represent the electric field component of the light.

The ability of a material to absorb or emit light is a consequence of how the change in charge distribution of a material, due to an electronic transition, interacts with the electric field component of electromagnetic radiation. The charge distribution of a molecule is defined by its electric dipole moment (**μ**), which for a molecule with **j** point charges is defined as the sum of the product of these point charges (**q**) with their position vectors (**r**), as in Equation 1.1.

$$\mu = \sum_j q_j r_j \qquad \text{Eq 1.1}$$

Using excitation as an example, when a photon of light is absorbed by a molecule it excites an electron from a lower energy molecular orbital into a higher energy molecular orbital. This transition induces a change in the charge distribution of the molecule which means that the electric dipole moment of the final excited state (**f**) differs from that of the initial ground state (**i**). For any given transition, this change in charge distribution is described by the electric transition dipole moment (ETDM), which depends on the wavefunction of the initial (ψ_i) and final (ψ_f) states, along with the position operator (**r**^) and charge **q** (Equation 1.2).[65]

$$\mu_{if} = -q\langle\psi_f|\hat{r}|\psi_i\rangle \qquad \text{Eq 1.2}$$

The intensity of a given transition (oscillator strength, O) is then proportional to the square of the electric transition dipole moment ($\boldsymbol{\mu_{if}}$) between the initial (**i**) and final (**f**) states (Equation 1.3). In summary, this qualitatively means transitions that cause a large change in the polarisation of a molecule during the transition are intense. These transitions can be observed experimentally by optical spectroscopy or calculated using time-dependent DFT (TD DFT).

$$O \propto \left|\mu_{if}\right|^2 \qquad \text{Eq 1.3}$$

Selection rules have been derived which allow us to predict whether a transition will have a large $\boldsymbol{\mu_{if}}$ and therefore be intense, without having to consider the above-described maths. For electric dipole transitions to be allowed they must be between orbitals with opposing parity. For example, a transition from an s orbital, which possesses inversion symmetry (gerade), to a p orbital, which does not possess inversion symmetry (ungerade), would be allowed. However, an s-s transition would not be allowed, so is therefore weak in intensity. This selection rule draws an interesting parallel to the translational transitions in benzene from Figure 1.18 for which the ipsocentric approach states leads to diatropic ring currents.

A final consideration to the above-described mathematical relationships is the assumption that, due to the small size of a typical molecule relative to the wavelength of light that it absorbs, the magnitude of the electric field the molecule experiences is assumed to be constant over the length of the molecule. This is known as the electric dipole approximation.[66] However, for polymers or supramolecular assemblies with lengths approaching the wavelength of light they absorb, the variance of the electric field must be considered as it significantly influences the optical properties of the molecule.[67]

1.3.3.2 Magnetic Transition Dipole Moment

Circularly polarised light, due to its chirality, possesses angular momentum.[68] As a result of this, the magnetic field component of circularly polarised light can interact with the magnetic dipole moments in chiral molecules, which influences the intensity of the electronic transitions in these molecules between states with different magnetic dipole moments.[69] For a given transition from initial state **i** to final state **f**, the magnetic transition dipole moment (MTDM)($\mathbf{m_{ij}}$) depends on the wavefunction of the initial ($\boldsymbol{\psi_i}$) and final ($\boldsymbol{\psi_f}$) states, along with the angular momentum operator (**L**^), charge (**q**), electron mass ($\mathbf{m_e}$) and the velocity of light (**c**) (Equation 1.4).[65] The MTDM is therefore associated with a change in the angular momentum of a molecule due to the movement of an individual electron.[70] In contrast to electric dipole transitions, the selection rules for magnetic dipole transitions require parity to be conserved during the transition, which draws an interesting parallel to the rotational transitions in benzene from Figure 1.18 which the ipsocentric approach states leads to paratropic ring currents. Finally, it is noted that MTDMs are typically significantly weaker than ETDMs.

$$m_{if} = -\frac{q}{2m_e c}\langle\psi_f|\hat{L}|\psi_i\rangle \qquad \text{Eq 1.4}$$

The intensity of a given chiroptical transition (rotary strength) is dependent on both the ETDM and MTDM, along with the cosine of the angle between these two vector quantities (Equation 1.5). The contrasting selection rules for electric and magnetic dipole transitions naturally hinder intense chiroptical transitions and the cosine dependency of the alignment of the ETDM and MTDM means that the orientation of the two vectors is of great importance.

$$R = |\mu_{if}||m_{if}|cos\theta \qquad \text{Eq 1.5}$$

1.3.3.3 Quantifying the Chiroptical Response

For chiroptical applications, chemists strive to develop materials that strongly differentiate between right and left circularly polarised light. To quantify a materials ability to do this, a

simple circular dichroism spectrum can be taken, in which the difference in absorbance of LCP and RCP light is measured across a selected wavelength range. From this the dissymmetry factor (**g**) can be obtained through Equation 1.6, where $\mathbf{I_{LH}}$ and $\mathbf{I_{RH}}$ are the absorbances of LCP and RCP light respectively. This equation can equally be applied to emission of circularly polarised light (Circularly polarised luminescence) where **I** instead refers to the intensity of emission.

$$g = \frac{2\times(I_{LH}-I_{RH})}{I_{LH}+I_{RH}} \qquad \text{Eq 1.6}$$

The dissymmetry factor (**g**) can also be expressed in terms of the ETDM and MTDM by substituting Equations 1.7 and 1.8 into 1.6 to give 1.9.[71]

$$2(I_{LH} - I_{RH}) = \frac{32v^3p}{3c^3\hbar^4}R \qquad \text{Eq 1.7}$$

$$I_{LH} - I_{RH} = \frac{8v^3p}{3c^3\hbar^4}D \qquad \text{Eq 1.8}$$

$$g = 4\frac{R}{D} \qquad \text{Eq 1.9}$$

Where D is the dipole strength, defined as in Equation 1.10.[70]

$$D = \left|\mu_{if}\right|^2 + \left|m_{if}\right|^2 \qquad \text{Eq 1.10}$$

Typically, $\boldsymbol{\mu_{if}}$ is far larger in magnitude than $\mathbf{m_{if}}$, therefore we can remove the $\mathbf{m_{if}}$ component from Equation 1.10, then substitute **D** and **R** into Equation 1.9 as:

$$g = 4\frac{|\mu_{if}||m_{if}|cos\theta}{\left|\mu_{if}\right|^2} \qquad \text{Eq 1.11}$$

Which simplifies to:

$$g \approx 4\frac{|m_{if}|}{|\mu_{if}|}cos\theta \qquad \text{Eq 1.12}$$

Equation 1.12 again demonstrates how the angle between $\boldsymbol{\mu_{if}}$ and $\mathbf{m_{if}}$ has a large impact on the observed dissymmetry, with optimal values when the two vectors are aligned parallel or antiparallel. In addition to this, large g values will be obtained with large $\mathbf{m_{ij}}$ or small $\boldsymbol{\mu_{if}}$, however, as previously discussed, small $\boldsymbol{\mu_{if}}$ values will lead to weak intensity transitions, which are not suitable for chiroptical applications. As a result, strategies to optimise the chiroptical properties of chiral materials are generally focused on aligning the transition dipole vectors and maximising $\mathbf{m_{ij}}$ without sacrificing $\boldsymbol{\mu_{if}}$. This is challenging considering the paradoxical selection rules for electronic and magnetic dipole transitions, however, there are successful examples in the literature of materials with large $\mathbf{g_{abs}}$ or $\mathbf{g_{lum}}$.

1.3.4 π-Conjugated Molecules with Chiroptical Activity

From Section 1.3.3 it is clear that large chiroptical responses require well aligned and large magnitude ETDM and MTDM. In the following section, I will give a few examples of how this has been achieved in organic π-conjugated molecules. However, it is worth noting that strong chiroptical activity has been achieved in a range of materials. In particular, transition metal and lanthanide antenna complexes are capable of reaching g_{lum} values of the order 10^{-2}-10^{-1} with careful selection of appropriate chiral ligands.[72, 73]

Alternatively, the coupling of multiple EDTMs or MTDMs in aggregated or solid-state samples of chiral molecules has been shown to increase their observed chiroptical responses.[70] As an example, Nakano and Fujiki report large g_{lum} values of -0.7 when polysilane **1-S** (M_w = 88,500, PDI = 1.22, Figure 1.27) is aggregated in the presence of the chiral directing solvent R/S-limonene.[74] g_{lum} of monomeric **1-S** was not able to be measured, however, a g_{abs} value of ~2×10^{-4} was obtained, which is 5 orders of magnitude lower than the g_{lum} of the chiral aggregate.

Notably, the chiral aggregates of **1-S** maintain a large photoluminescence quantum yield of 53%, which in combination with the large g_{lum} value mean that the aggregates are highly chiroptically active. The authors propose that the origin of this large g_{lum} comes from the long-range order of the chiral aggregates, which enables the coupling of many weak ETDM across the chiral structure, leading to an overall large oscillator strength for the transition. This transition presumably relates to a strong magnetically allowed transition (hence the weak ETDM), which therefore results in a large dissymmetry factor.

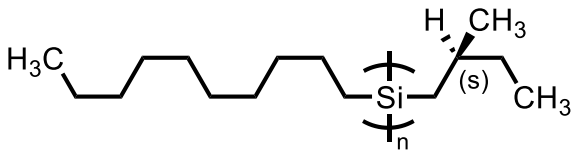

1-S

Figure 1.27. Chemical structure of **1-S**.

1.3.4.1 Chiral Nanoring

An elegant example demonstrating the importance of aligning the EDTM and MTDM is the synthesis and chiral resolution of the nanorings presented in Figure 1.28, which have large g_{abs} and g_{lum} values on the order of 10^{-1}.[75] The impressive chiroptical activity of these molecules has been attributed to the unique symmetry of molecular nanorings. Specifically, their symmetry in the plane of the nanoring, which in the context of the ETDM and MTDM means that the x and y components of these vectors perfectly cancel, leaving only the z component. As a result, in a perfectly symmetric nanoring, the ETDM and MTDM are aligned either exactly parallel or antiparallel, maximising the cos(θ) contribution to the rotary strength (Equation 1.5). Computational studies of the structures in Figure 1.28 reveal this to be precisely the case for the highly symmetric **(P)-(12,8)-4[CC]**, which has exactly antiparallel ETDM and MTDM (Figure 1.29). This, in combination with reasonable magnitude ETDM and MTDM lead to the large g_{abs} (-0.167) and g_{lum} (-0.152).

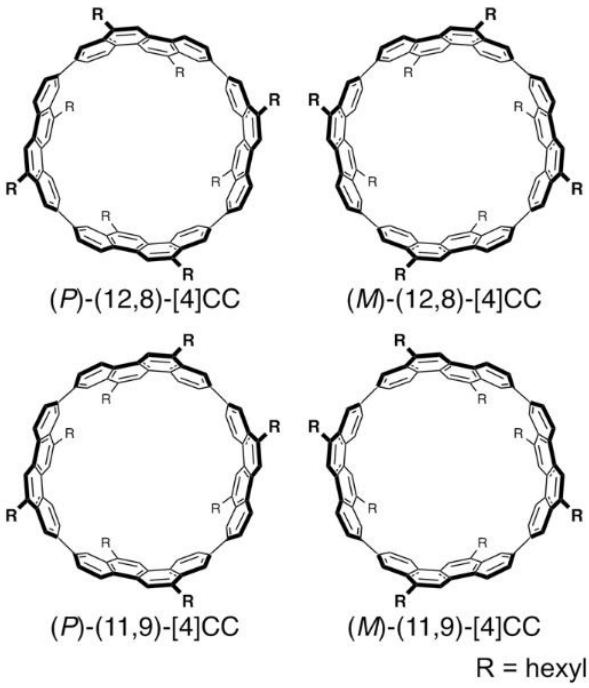

Figure 1.28. Chemical structures of chiral nanorings which demostrate strong alignment of ETDM and MTDM. Reproduced from reference.[75]

(P)-(11,9)-[4]CC is slightly less symmetric than **(P)-(12,8)-4[CC]**, which results in smaller values of both g_{abs} (-0.111) and g_{lum} (-0.101). As expected the ETDM and MTDM of **(P)-(11,9)-[4]CC** are less well aligned (θ = 152°), which contributes to the reduced dissymmetry. However, while the two nanorings have almost identical MTDM, the ETDM of **(P)-(11,9)-[4]CC** is notably smaller (roughly half as large). Both the change in θ and of the ETDM can be attributed to the reduced symmetry of **(P)-(11,9)-[4]CC**, which has a large impact on the molecules chiroptical properties.

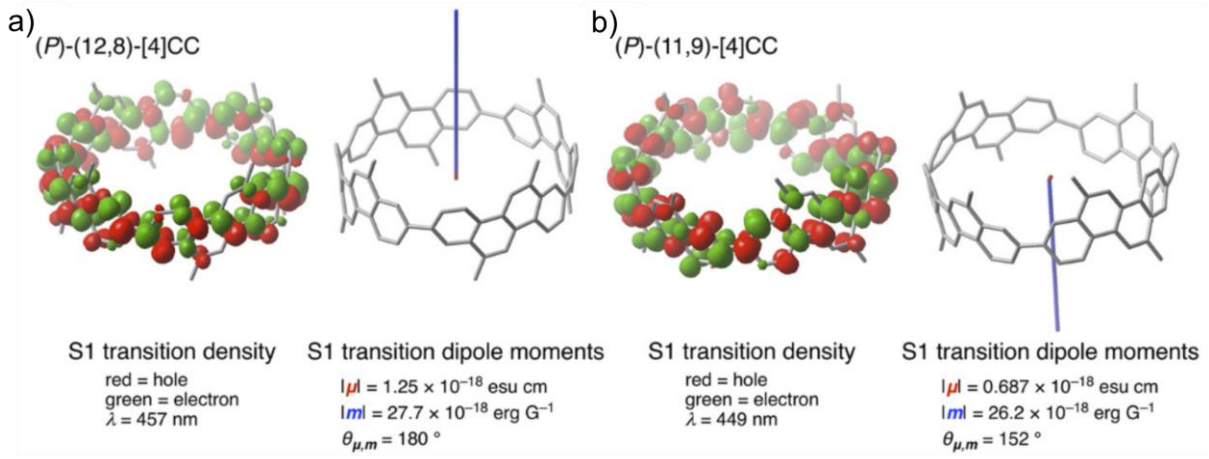

Figure 1.29. Calculated valued of ETDM, MTDM and θ for two chiral nanorings. Reproduced from reference.[75]

1.3.4.2 Geländer Oligomers

Another example is that of the Geländer Oligomers reported by Professor Marcel Mayor.[76, 77] In a very recent publication, Mayor and colleagues report the synthesis and chiroptical properties of a series of helical oligomers with varying lengths, from which they are able to extract some interesting structure property relationships.[76]

The oligomers in these reports are prepared from an axle comprised of phthalimide units, each of which possesses a nitrogen atom that can form a covalent bond orientated orthogonally to the axis of the phthalimide oligomer. This allows them to position groups of interest radially from the main axis, which once connected, form a helical oligomer that wraps around the linear phthalimide oligomer (tetramer example, Figure 1.30). These are termed Geländer oligomers after the German word for banister.

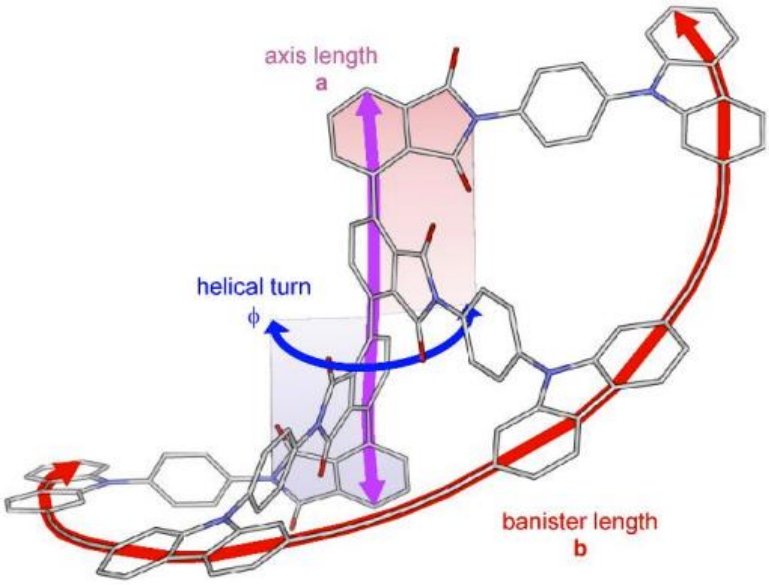

Figure 1.30. A Geländer oligomer with important geometric values highlighted. Reproduced from reference.[76]

Dimer (**G$_{BD}$[2]**), trimer (**G$_{BD}$[3]**) and tetramer (**G$_{BD}$[4]**) length Geländer oligomers with the structure shown in Figure 1.30 are slow to racemise, so were separable by chiral HPLC. ECD spectra of the enantiomers reveal a trend of increasing molar ellipticity ($(\Delta\varepsilon / M^{-1} cm^{-1})$ extinction coefficient value for the ECD data, Table 1.1) with oligomer length for the lowest energy excitation of each molecule. Interestingly the extinction coefficient obtained for each

oligomers lowest energy excitation is roughly consistent, regardless of oligomer length (~ 6 x 10^4 M^{-1} cm^{-1}), indicating that it is a change in the MTDM or angle between ETDM and MTDM that is causing the change in molar ellipticity.

	λ_{abs}[a]	λ_{em}[a] max	ϕ	$E_{0\text{-}0}$[b]	ε[c]	$\Delta\varepsilon$[c]	g_{abs}[c]
G_{BD}[2]	386	395	0.5%	3.20	$60 \cdot 10^3$	14	$2.4*10^{-4}$
G_{BD}[3]	410	417	1.5%	3.00	$59 \cdot 10^3$	44	$1.1*10^{-3}$
G_{BD}[4]	420	427	1.5%	2.93	$57 \cdot 10^3$	309	$6.1*10^{-3}$

Table 1.1. Optical data for the dimer, trimer and tetramer length Geländer oligomers. Reproduced from reference.[76] [a] wavelength in nm. [b] energy in eV. [c] extinction coefficients in M^{-1} cm^{-1}.

Table 1.2 presents the calculated values of ETDM, MTDM and θ for the dimer, trimer and tetramer length oligomers, along with the direction of these vectors overlayed on the structures in Figure 1.31. From these data we can see that while the ETDM remains mostly constant, MTDM increases and θ decreases with increasing length, which serves to increase the value of the rotational constant (R, Equation 1.5) and therefore the molar ellipticity.

species	state	$\lvert\vec{\mu}\rvert$(au)	$\lvert\vec{m}\rvert$(au)	θ
G_{BD}[2]	14	5.23	6.48	90.47°
G_{BD}[3]	10	5.66	8.79	88.38°
G_{BD}[4]	7	6.11	14.78	83.86°

Table 1.2. Calculated values of ETDM (μ), MTDM (m) and angle between these vectors (θ) for the lowest energy excitations of the dimer (**G_{BD}[2]**), trimer (**G_{BD}[3]**) and tetramer (**G_{BD}[4]**) length Geländer oligomers. Reproduced from reference.[76]

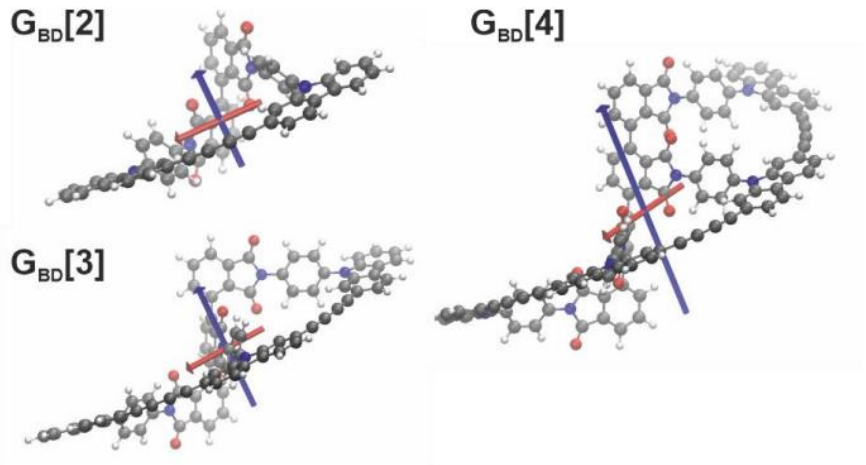

Figure 1.31. Alignment of the ETDM (red) and MTDM (blue) in the various oligomers. Reproduced from reference.[76]

Though these oligomers possess relatively weak g_{abs} (e.g. **G$_{BD}$[4]** has g_{abs} of 6.1 x 10^{-3}) this systematic study demonstrates how increasing the length of helical oligomers towards one full helical pitch can improve the chiroptical properties of molecules, specifically by increasing the MTDM and better aligning it with the ETDM. An interesting threshold to therefore reach and then break through is one full helical turn. Mayor states that the 7-mer length oligomer is predicted to complete one full twist for the framework presented in this section, which they are currently working towards.

1.3.5 Chiral Induced Spin Selectivity

In addition to differentiating between the chiral forms of light, chiral materials are also able to differentiate between electrons of opposing spin.[78] This has contributed to the advancement of the field of spintronics,[79, 80] which aims to develop new technologies by controlling the transport of electron spin. Developments by the spintronics community have already seen commercial application in the form of the magnetic tunnel junctions incorporated into magnetic hard disk drives[81, 82] and in spin transfer torque memory.[83] These applications primarily rely on inorganic materials, however as previously discussed, switching to organic based materials offers unique properties which are of interest to those in the field.[84]

The Chiral Induced Spin Selectivity (CISS) effect describes how electrons of opposing spin scatter asymmetrically when interacting with chiral molecules.[85] This rationalises why spin polarised currents are formed when a current is passed through a chiral molecule; the molecule essentially filters electrons based on their spin. The ability of a molecule to spin polarise electron currents can be measured in numerous ways,[78] one of which is magnetic conductive probe-atomic force microscopy (mc-AFM). This technique has many potential set ups, but as an example, consider Figure 1.32a.[86] Here, chiral peptide (**1N**) containing a thiol functionalised c-terminus, is self-assembled into a monolayer on a gold surface. An AFM tip is then magnetised either parallel or antiparallel to the gold surface and brought into contact with the peptide. The magnetisation of the tip leads to a preference for conducting either spin up or spin

down electrons, which are selected for by the chiral peptide. This results in different currents flowing through the set up for when the magnetisation of the tip is aligned with the spin preference of the peptide. In Figure 1.32b this is shown as higher currents for the south magnetised (blue) over the north magnetised (red) tip.

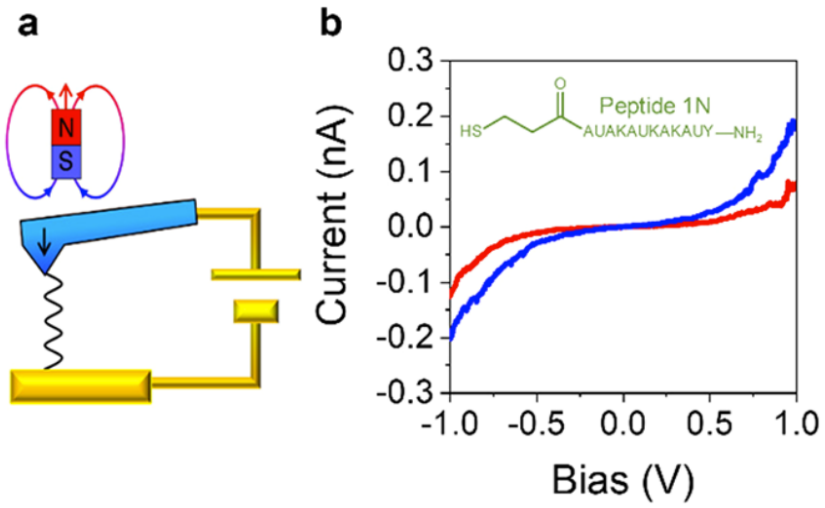

Figure 1.32. (a) Experimental set-up for mc-AFM measurement. (b) Plots of current against voltage when peptide **1N** is positioned between the gold substrate and AFM tip for south (blue) and north (red) magnetised directions. Reproduced from reference.[78]

In addition to spin polarising currents, recent experimental evidence has demonstrated that simply charge-polarising a chiral molecule can lead to spin polarisation. One elegant example of this uses a technique known as spin exchange microscopy (Figure 1.33).[87] Here a chiral polypeptide (AHPA) is bound to an AFM tip. The tip is then brought close to a ferromagnetic surface, which is magnetised either up or down relative to the plane of the surface. By bringing the tip close to the surface a charge polarisation is generated in the molecule that is independent of the direction of magnetisation. The CISS effect predicts that this charge polarisation is also accompanied by a spin polarisation. If this were to be the case, it would be expected that the interaction energy between the chiral molecule and the surface would be dependent on the direction of the magnetisation, as is depicted in Figure 1.33. The experimental evidence confirms that this is true, as significantly different pulling forces between the tip and substrate were observed for the opposing field directions.

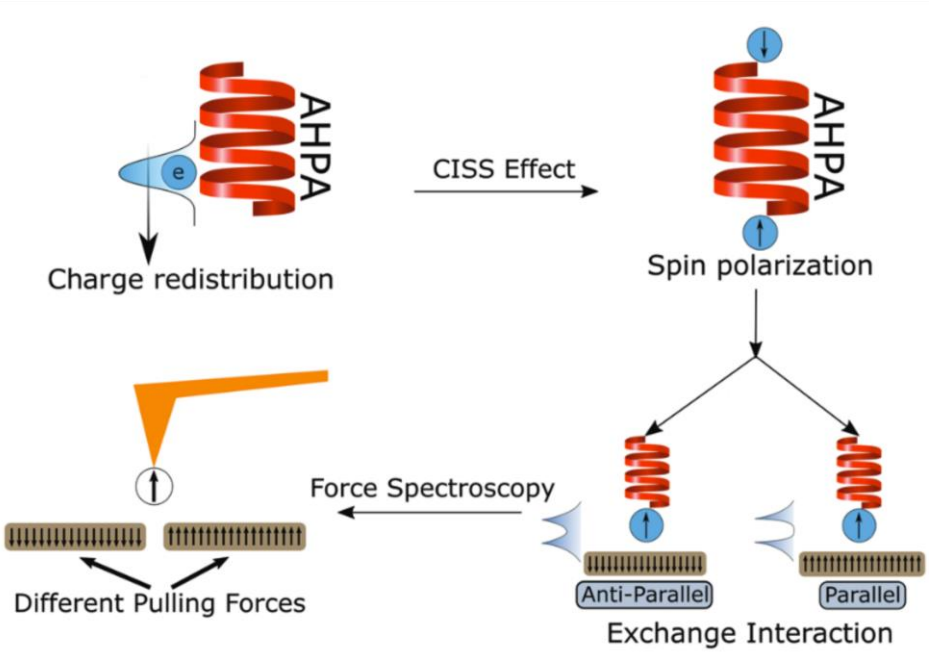

Figure 1.33. A scheme depicting the charge polarisation, spin polarisation and differing interaction energies between a single enantiomer and a surface with parallel and antiparallel magnetisations. Reproduced from reference.[87]

The principle of charge and spin polarisation can also be used to facilitate the separation of enantiomers, as a surface with fixed magnetisation will interact differently with the spin dipoles of each enantiomer, altering how quickly they elute (Figure 1.34).[88]

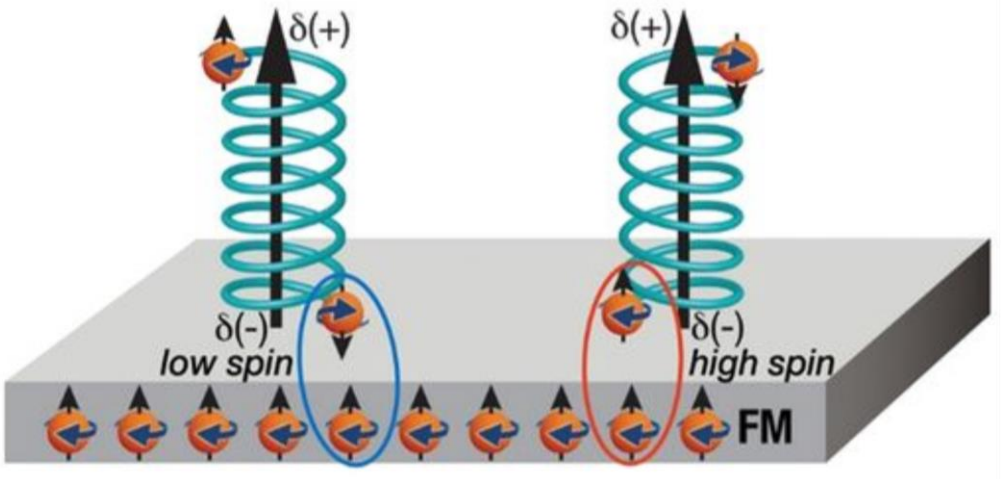

Figure 1.34. Two enantiomers adsorbed onto a magnetised surface. Identical electric dipoles are generated in the molecule; however, the spin dipoles are opposite. The interaction between the spin dipole and magnetisation leads to differing interation energies between the enantiomers and the surface, which can be used to facilitate their separation. Reproduced from reference.[88]

For chiral organic molecules to be commercially applied as spin filters for electron currents, they need to strongly discriminate between the two spin states and demonstrate efficient conduction of the electron current. π-conjugated oligomers, as previously discussed, have high conductivities so are well suited to applications involving charge transport.[89] In particular, they are significantly better conductors than many of the chiral organic molecules studied for the CISS effect (polyeptides). The development of high conductivity and highly spin polarising π-conjugated molecules would therefore be of interest to those in the field of spintronics.

1.3.6 Thesis Aim 2: Helical Porphyrin Oligomers

The second aim of this thesis was to design and synthesise a template capable of holding a butadiyne-linked porphyrin oligomer in a helical conformation (Figure 1.35). As the length of the helix pitch is substantially longer than that of other helical π-conjugated single molecules studied to date,[76, 90] we hope that our complex will exhibit interesting chiroptical properties. In contrast to the well-studied helicenes, the plane of the helical π-system of our target molecule is parallel to the helix axis, which may also affect its chiroptical properties. Furthermore, the low energy Q-band of butadiyne-linked porphyrin oligomers is known to facilitate efficient charge transport.[91] Therefore, we are also interested to study the magnitude and spin polarisation of electron currents passed through the complex. Work towards this goal is presented in Chapter 5.

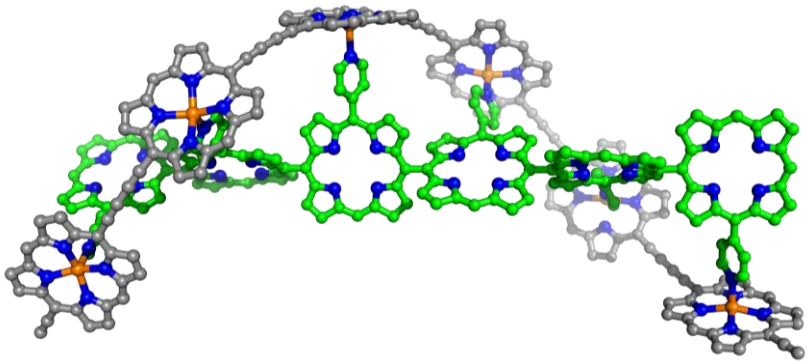

Figure 1.35. A chiral template composed of meso-meso linked porphyrin units bearing pyridyl groups binds a butadiyne-linked porphyrin oligomer in a left-handed helix.

1.4 References

1. M. O. Senge, N. N. Sergeeva and K. J. Hale, *Chemical Society Reviews*, 2021, **50**, 4730-4789.
2. T. Mirkovic, E. E. Ostroumov, J. M. Anna, R. van Grondelle, Govindjee and G. D. Scholes, *Chemical Reviews*, 2017, **117**, 249-293.
3. N. Liguori, X. Periole, S. J. Marrink and R. Croce, *Scientific Reports*, 2015, **5**, 15661.
4. S. Hiroto, Y. Miyake and H. Shinokubo, *Chemical Reviews*, 2017, **117**, 2910-3043.
5. R. Costa e Silva, L. Oliveira da Silva, A. de Andrade Bartolomeu, T. J. Brocksom and K. T. de Oliveira, *Beilstein Journal of Organic Chemistry*, 2020, **16**, 917-955.
6. M. Ethirajan, Y. Chen, P. Joshi and R. K. Pandey, *Chemical Society Reviews*, 2011, **40**, 340-362.
7. J. Min Park, J. H. Lee and W.-D. Jang, *Coordination Chemistry Reviews*, 2020, **407**, 213157.
8. R. Paolesse, S. Nardis, D. Monti, M. Stefanelli and C. Di Natale, *Chemical Reviews*, 2017, **117**, 2517-2583.
9. M. Gouterman, *Journal of Molecular Spectroscopy*, 1961, **6**, 138-163.
10. M. Gouterman, G. H. Wagnière and L. C. Snyder, *Journal of Molecular Spectroscopy*, 1963, **11**, 108-127.
11. H. L. Anderson, *Chemical Communications*, 1999, 2323-2330.
12. G. Erdogan and D. B. Grotjahn, *Organic Letters*, 2014, **16**, 2818-2821.
13. H. Zhu, G. Wen, W. Zheng, N. H. Rees, W. Stawski, H. I. Wang, M. Bonn and H. L. Anderson, *Angewandte Chemie International Edition*, 2025, **64**.
14. A. Osuka and H. Shimidzu, *Angewandte Chemie International Edition in English*, 1997, **36**, 135-137.
15. P. N. Taylor, J. Huuskonen, R. T. Aplin, H. L. Anderson, J. Huuskonen, G. Rumbles and E. Williams, *Chemical Communications*, 1998, 909-910.
16. J.-R. Deng, M. T. González, H. Zhu, H. L. Anderson and E. Leary, *Journal of the American Chemical Society*, 2024, **146**, 3651-3659.
17. M. Pawlicki, M. Morisue, N. K. S. Davis, D. G. McLean, J. E. Haley, E. Beuerman, M. Drobizhev, A. Rebane, A. L. Thompson, S. I. Pascu, G. Accorsi, N. Armaroli and H. L. Anderson, *Chemical Science*, 2012, **3**, 1541-1547.
18. V. S.-Y. Lin, S. G. DiMagno and M. J. Therien, *Science*, 1994, **264**, 1105-1111.
19. M. D. Peeks, C. E. Tait, P. Neuhaus, G. M. Fischer, M. Hoffmann, R. Haver, A. Cnossen, J. R. Harmer, C. R. Timmel and H. L. Anderson, *Journal of the American Chemical Society*, 2017, **139**, 10461-10471.
20. J. Hergenhahn, J. M. Holmes, J.-R. Deng, H. Gotfredsen, R. M. J. Jacobs, S. M. Kopp, C. R. Timmel and H. L. Anderson, *Journal of the American Chemical Society*, 2025, **147**, 978-987.
21. S. M. Kopp, J.-R. Deng, A. J. Redman, H. Gotfredsen, R. M. J. Jacobs, H. L. Anderson and C. R. Timmel, *Chem*, 2024, **10**, 3595-3606.
22. M. D. Peeks, P. Neuhaus and H. L. Anderson, *Physical Chemistry Chemical Physics*, 2016, **18**, 5264-5274.
23. H. J. Hogben, J. K. Sprafke, M. Hoffmann, M. Pawlicki and H. L. Anderson, *Journal of the American Chemical Society*, 2011, **133**, 20962-20969.
24. P. S. Bols and H. L. Anderson, *Accounts of Chemical Research*, 2018, **51**, 2083-2092.
25. J. K. Sprafke, D. V. Kondratuk, M. Wykes, A. L. Thompson, M. Hoffmann, R. Drevinskas, W.-H. Chen, C. K. Yong, J. Kärnbratt, J. E. Bullock, M. Malfois, M. R. Wasielewski, B. Albinsson, L. M. Herz, D. Zigmantas, D. Beljonne and H. L. Anderson, *Journal of the American Chemical Society*, 2011, **133**, 17262-17273.

26. M. C. O'Sullivan, J. K. Sprafke, D. V. Kondratuk, C. Rinfray, T. D. W. Claridge, A. Saywell, M. O. Blunt, J. N. O'Shea, P. H. Beton, M. Malfois and H. L. Anderson, *Nature*, 2011, **469**, 72-75.
27. D. V. Kondratuk, L. M. A. Perdigão, A. M. S. Esmail, J. N. O'Shea, P. H. Beton and H. L. Anderson, *Nature Chemistry*, 2015, **7**, 317-322.
28. M. Jirásek, M. Rickhaus, L. Tejerina and H. L. Anderson, *Journal of the American Chemical Society*, 2021, **143**, 2403-2412.
29. M. Rickhaus, M. Jirasek, L. Tejerina, H. Gotfredsen, M. D. Peeks, R. Haver, H.-W. Jiang, T. D. W. Claridge and H. L. Anderson, *Nature Chemistry*, 2020, **12**, 236-241.
30. S. M. Kopp, H. Gotfredsen, J.-R. Deng, T. D. W. Claridge and H. L. Anderson, *Journal of the American Chemical Society*, 2020, **142**, 19393-19401.
31. W. Stawski, J. M. Van Raden, C. W. Patrick, P. N. Horton, S. J. Coles and H. L. Anderson, *Organic Letters*, 2023, **25**, 378-383.
32. H. Gotfredsen, J.-R. Deng, J. M. Van Raden, M. Righetto, J. Hergenhahn, M. Clarke, A. Bellamy-Carter, J. Hart, J. O'Shea, T. D. W. Claridge, F. Duarte, A. Saywell, L. M. Herz and H. L. Anderson, *Nature Chemistry*, 2022, **14**, 1436-1442.
33. M. A. Majewski, W. Stawski, J. M. Van Raden, M. Clarke, J. Hart, J. N. O'Shea, A. Saywell and H. L. Anderson, *Angewandte Chemie International Edition*, 2023, **62**.
34. P. Liu, P. Neuhaus, D. V. Kondratuk, T. S. Balaban and H. L. Anderson, *Angewandte Chemie International Edition*, 2014, **53**, 7770-7773.
35. S. A. L. Rousseaux, J. Q. Gong, R. Haver, B. Odell, T. D. W. Claridge, L. M. Herz and H. L. Anderson, *Journal of the American Chemical Society*, 2015, **137**, 12713-12718.
36. M. Rickhaus, A. Vargas Jentzsch, L. Tejerina, I. Grübner, M. Jirasek, T. D. W. Claridge and H. L. Anderson, *Journal of the American Chemical Society*, 2017, **139**, 16502-16505.
37. M. Vitek, J.-R. Deng, H. L. Anderson and I. Rončević, *ACS Nano*, 2025, **19**, 1405-1411.
38. P. v. R. Schleyer, *Chemical Reviews*, 2001, **101**, 1115-1118.
39. N. C. Baird, *Journal of the American Chemical Society*, 1972, **94**, 4941-4948.
40. H. S. Rzepa, *Chemical Reviews*, 2005, **105**, 3697-3715.
41. Z. S. Yoon, A. Osuka and D. Kim, *Nature Chemistry*, 2009, **1**, 113-122.
42. R. B. King, *Chem Rev*, 2001, **101**, 1119-1152.
43. M. Bühl and A. Hirsch, *Chemical Reviews*, 2001, **101**, 1153-1184.
44. S. Furukawa, M. Fujita, Y. Kanatomi, M. Minoura, M. Hatanaka, K. Morokuma, K. Ishimura and M. Saito, *Communications Chemistry*, 2018, **1**, 60.
45. Z. Chen, C. S. Wannere, C. Corminboeuf, R. Puchta and P. v. R. Schleyer, *Chemical Reviews*, 2005, **105**, 3842-3888.
46. Y. Mo and P. v. R. Schleyer, *Chemistry – A European Journal*, 2006, **12**, 2009-2020.
47. G. E. Bacon, N. A. Curry, S. A. Wilson and R. Spence, *Proceedings of the Royal Society of London. Series A. Mathematical and Physical Sciences*, 1964, **279**, 98-110.
48. R. Gershoni-Poranne and A. Stanger, *Chemical Society Reviews*, 2015, **44**, 6597-6615.
49. E. Steiner and P. W. Fowler, *Physical Chemistry Chemical Physics*, 2004, **6**, 261-272.
50. E. Steiner and P. W. Fowler, *Chemical Communications*, 2001, DOI: 10.1039/B104847N, 2220-2221.
51. E. Steiner and P. W. Fowler, *The Journal of Physical Chemistry A*, 2001, **105**, 9553-9562.
52. I. Rončević, F. J. Leslie, M. Rossmannek, I. Tavernelli, L. Gross and H. L. Anderson, *Journal of the American Chemical Society*, 2023, **145**, 26962-26972.

53. P. v. R. Schleyer, C. Maerker, A. Dransfeld, H. Jiao and N. J. R. van Eikema Hommes, *Journal of the American Chemical Society*, 1996, **118**, 6317-6318.
54. M. D. Peeks, T. D. W. Claridge and H. L. Anderson, *Nature*, 2017, **541**, 200-203.
55. G. Hong, X. Gan, C. Leonhardt, Z. Zhang, J. Seibert, J. M. Busch and S. Bräse, *Advanced Materials*, 2021, **33**, 2005630.
56. A. Facchetti, *Materials Today*, 2007, **10**, 28-37.
57. M. Y. Wong and E. Zysman-Colman, *Adv Mater*, 2017, **29**.
58. E. K. Solak and E. Irmak, *RSC Advances*, 2023, **13**, 12244-12269.
59. J. B. Kaushal, P. Raut and S. Kumar, *Biosensors*, 2023, **13**, 976.
60. K. Liu, B. Ouyang, X. Guo, Y. Guo and Y. Liu, *npj Flexible Electronics*, 2022, **6**, 1.
61. J. G. Ibanez, M. E. Rincón, S. Gutierrez-Granados, M. Chahma, O. A. Jaramillo-Quintero and B. A. Frontana-Uribe, *Chem Rev*, 2018, **118**, 4731-4816.
62. P. C. Mondal, C. Fontanesi, D. H. Waldeck and R. Naaman, *Accounts of Chemical Research*, 2016, **49**, 2560-2568.
63. S. He, Y. Chen, J. Fang, Y. Liu and Z. Lin, *Chemical Society Reviews*, 2025, **54**, 2154-2187.
64. J. R. Brandt, F. Salerno and M. J. Fuchter, *Nature Reviews Chemistry*, 2017, **1**, 0045.
65. T. Mori, *Chemical Reviews*, 2021, **121**, 2373-2412.
66. N. H. List, T. R. L. Melin, M. van Horn and T. Saue, *The Journal of Chemical Physics*, 2020, **152**.
67. N. H. List, J. Kauczor, T. Saue, H. J. Jensen and P. Norman, *J Chem Phys*, 2015, **142**, 244111.
68. R. I. Khrapko, *Heliyon*, 2024, **10**.
69. J. A. Schellman, *Chemical Reviews*, 1975, **75**, 323-331.
70. J. L. Greenfield, J. Wade, J. R. Brandt, X. Shi, T. J. Penfold and M. J. Fuchter, *Chemical Science*, 2021, **12**, 8589-8602.
71. Y. Nagata and T. Mori, *Frontiers in Chemistry*, 2020, **8**.
72. B.-A. N. Willis, D. Schnable, N. D. Schley and G. Ung, *Journal of the American Chemical Society*, 2022, **144**, 22421-22425.
73. J. L. Lunkley, D. Shirotani, K. Yamanari, S. Kaizaki and G. Muller, *Journal of the American Chemical Society*, 2008, **130**, 13814-13815.
74. Y. Nakano and M. Fujiki, *Macromolecules*, 2011, **44**, 7511-7519.
75. S. Sato, A. Yoshii, S. Takahashi, S. Furumi, M. Takeuchi and H. Isobe, *Proceedings of the National Academy of Sciences*, 2017, **114**, 13097-13101.
76. A. D'Addio, C. C. E. Kroonen, O. Fuhr, D. Fenske, D. Häussinger and M. Mayor, *Chemical Science*, 2025, Advance Article.
77. A. D'Addio, J. Malinčik, O. Fuhr, D. Fenske, D. Häussinger and M. Mayor, *Chemistry – A European Journal*, 2022, **28**.
78. B. P. Bloom, Y. Paltiel, R. Naaman and D. H. Waldeck, *Chemical Reviews*, 2024, **124**, 1950-1991.
79. A. Hirohata, K. Yamada, Y. Nakatani, I.-L. Prejbeanu, B. Diény, P. Pirro and B. Hillebrands, *Journal of Magnetism and Magnetic Materials*, 2020, **509**, 166711.
80. I. Žutić, J. Fabian and S. Das Sarma, *Reviews of Modern Physics*, 2004, **76**, 323-410.
81. S. D. Bader and S. S. P. Parkin, *Annual Review of Condensed Matter Physics*, 2010, **1**, 71-88.
82. J.-G. Zhu and C. Park, *Materials Today*, 2006, **9**, 36-45.
83. T. Kawahara, K. Ito, R. Takemura and H. Ohno, *Microelectronics Reliability*, 2012, **52**, 613-627.
84. Z. Xie, T. Z. Markus, S. R. Cohen, Z. Vager, R. Gutierrez and R. Naaman, *Nano Letters*, 2011, **11**, 4652-4655.

85. K. Ray, S. P. Ananthavel, D. H. Waldeck and R. Naaman, *Science*, 1999, **283**, 814-816.
86. C. Clever, E. Wierzbinski, B. P. Bloom, Y. Lu, H. M. Grimm, S. R. Rao, W. S. Horne and D. H. Waldeck, *Israel Journal of Chemistry*, 2022, **62**, e202200045.
87. A. Ziv, A. Saha, H. Alpern, N. Sukenik, L. T. Baczewski, S. Yochelis, M. Reches and Y. Paltiel, *Adv Mater*, 2019, **31**, e1904206.
88. K. Banerjee-Ghosh, O. Ben Dor, F. Tassinari, E. Capua, S. Yochelis, A. Capua, S.-H. Yang, S. S. P. Parkin, S. Sarkar, L. Kronik, L. T. Baczewski, R. Naaman and Y. Paltiel, *Science*, 2018, **360**, 1331-1334.
89. W. R. Salaneck, R. H. Friend and J. L. Brédas, *Physics Reports*, 1999, **319**, 231-251.
90. Y. Shen and C.-F. Chen, *Chemical Reviews*, 2012, **112**, 1463-1535.
91. P. Zwick, D. Dulić, H. S. J. van der Zant and M. Mayor, *Nanoscale*, 2021, **13**, 15500-15525.

1.5 General Methods

The following general methods are applicable to **all experimental sections** in this thesis (Sections 2.8, 3.8 and 5.7) so will only be listed here and not repeated in each chapter.

DIPA, DCM, THF, DMF and chloroform used in reactions were obtained from an MBraun MBSPS-5-BenchTop solvent purification, which is under a nitrogen atmosphere. $CDCl_3$ used in NMR experiments was stored over K_2CO_3 and filtered through Al_2O_3 prior to addition to any porphyrin species. All other solvents and reagents were used as received from commercial suppliers. Silica gel column chromatography was conducted using SiO_2 with 60 Å pore size and 40−63 μm particle size. Benchtop size exclusion chromatography (SEC) was conducted using columns with a sintered glass filter packed with Bio-Rad Bio-Beads S-X1 (40–80 μm bead size) in either toluene or chloroform, with or without 1% pyridine, as stated in the procedure. Analytical gel permeation chromatography (GPC) was conducted using one JAIGEL-3H-A (8 × 500 mm) and one JAIGEL-4H-A (8 × 500 mm) connected in series and packed in THF + 1% pyridine with a flow rate of 1.0 mL/min. The sequencing and control of analytical GPC traces was achieved using Agilent ChemStation. Semi-preparative GPC was conducted on either: (1) a Shimadzu recycling GPC system equipped with a LC-20 AD pump, SPD-20A UV detector and a set of JAIGEL 3H (20 × 600 mm) and JAIGEL 4H (20 × 600 mm) columns in toluene + 1% pyridine with a flow rate of 3.5 mL/min. Or (2) a JAIGEL LaboACE LC-7080Plus equipped with a P-LA80 pump, UV-Vis 4ch 800LA detector and a set of JAIGEL 3HR (20 x 600 mm) and JAIGEL 4HR (20 x 600 mm) GPC columns in toluene + 1% pyridine with a flow rate of 10 mL/min.

Chiral separation was conducted using an Agilent 1100 HPLC system equipped with a CHIRALPAK IC analytical column (4.6 mm, 250 mm, 5 μm), using varying solvent and flow rates as detailed in the associated procedures.

^{1}H, ^{19}F and ^{13}C spectra were recorded on either a Bruker AVIII HD 400, a Bruker AVIII HD 500, a Bruker AVII 500 with a 13C(1H) dual cryo-probe, or a Bruker AVIII 600 with a broadband cryo-probe. Chemical shift values are quoted in ppm and coupling constants (J) in hertz to the nearest 0.1 Hz. ^{1}H and ^{13}C NMR spectra are referenced against the residual solvent peak ($CHCl_3$ δ_H = 7.26 ppm, $CDCl_3$ δ_C = 77.16 ppm; $CHDCl_2$ δ_H = 5.32 ppm, CD_2Cl_2 δ_C = 53.84 ppm, $C_2H_2Cl_4$ δ_H = 6.00 ppm, $C_2D_2Cl_4$ δ_C = 73.78 ppm). ^{19}F NMR spectra are referenced against hexafluorobenzene (δ_F = –164.8 ppm) which was added to the samples. Unless stated otherwise, NMR spectra were recorded at 298 K.

UV-Vis measurements were conducted on a Perkin Elmer Lambda 20 spectrometer equipped with a Perkin Elmer PTP-1 peltier system. Fluorescence measurements were conducted on an Edinburgh Instruments FS5 spectrofluorometer operating Fluoracle® software, equipped with a xenon arc lamp (providing 230–1000 nm excitation range), a thermostatic sample holder (SC-20) and both an R13456 PMT detector (200–950 nm spectral coverage, Hamamatsu) and an InGaAs analogue NIR detector (850–1650 nm spectral coverage). Both UV-Vis and fluorescence measurements were conducted using a quartz cuvette with 10 mm path length. Circular dichroism spectra were recorded on a Chirascan circular dichroism spectrometer (Applied Photophysics), using a quartz cuvette with 1 mm path length. $CDCl_3$ stored over K_2CO_3 and filtered over Al_2O_3 was used as a solvent in all measurements, which were conducted at 298 K unless otherwise stated.

MALDI-ToF spectra were measured on a Bruker MALDI Autoflex Speed instrument, using dithranol or DCTB as a matrix. ESI spectra were measured on a Thermo Orbitrap Exactive mass spectrometer.

2

Template-directed Synthesis of an 18-porphyrin Nanoring

Contents

Chapter 2 - Template-directed Synthesis of an 18-porphyrin Nanoring

2.1 Introduction

2.1.1 Aromaticity in Porphyrin Nanorings

Aromaticity is an emergent phenomenon that arises in a diverse range of molecules and materials. Its definition has been the source of much debate, from which there is still no definitive consensus.[1, 2] Arguably the most commonly encountered form of aromaticity is that which arises in planar, cyclic organic molecules that possess a fully conjugated chain of p orbitals (π-system) containing 4n+2 π-electrons that are delocalized over the molecular framework. Benzene is often given as the archetypal example of such aromatic molecules, which as a result of aromaticity exhibit high structural symmetry (less bond length alternation), lower energy (aromatic stabilization energy) and lower chemical reactivity, than non-aromatic analogues.[3] Additionally, in the presence of a magnetic field, these molecules are capable of generating ring currents in their π-systems, which strengthen the applied magnetic field inside the ring and weaken it outside the ring.[44] In benzene this is evidenced by the significant deshielding of its protons relative to the alkene protons in cyclohexene.[3]

As a result of these emergent properties, aromaticity has a significant effect on the reactivity and photophysics of such cyclic π-conjugated molecules, in addition to affecting their shape and the type of intermolecular interactions these molecules participate in, which importantly affects the binding interactions of aromatic molecules in biological systems. As will be discussed in section 2.1.2., the ring currents observed in aromatic molecules also share similarities with the persistent ring currents observed in macrocyclic metal rings. Some have proposed that these phenomenon may be manifestations of the same underlying physics,[4] however, further study of these materials will be required to prove these theories. Due to its wide-reaching impact on the chemistry of cyclic π-conjugated molecules, further exploration of the properties and limits of aromaticity is therefore of broad interest to many in the scientific community, as the lessons learned from studying aromaticity may assist in our understanding

of the fundamental laws of physics or inform the design of materials and molecular electronic components with novel properties. The work in Chapters 2 and 3 of this thesis focuses on expanding our knowledge of aromaticity by probing the size limit of this phenomenon.

In Chapter 1 we discussed the origin aromaticity, the effects this phenomenon has on molecular systems and explored examples in the literature of large aromatic molecules, some of which utilized porphyrin as a key building block. These studies demonstrate that aromaticity persists in very large π-conjugated materials, in contradiction to the historical view that Hückel's rule only applies to molecules possessing up to 22 π electrons. Prior to the work presented in this thesis, the largest π-conjugated macrocycle studied for global aromaticity was the butadiyne-linked 12-porphyrin nanoring previously reported by the Anderson group.[5] This macrocycle was held in a rigid circular geometry by two stacked 6-legged templates, which bind to the zinc metal at the center of each porphyrin, ensuring that each porphyrin is orientated perpendicular to the plane of the nanoring. As a result, the ***c*-P12·(T6$_e$)$_2$** complex (Figure 2.1) possesses a π-conjugated circuit of 168 π electrons in the neutral state, which exhibits global aromaticity when oxidized to the +6 state, containing 162 π electrons.[5] Prior to the work in this thesis, this was the largest experimental example of global aromaticity.

To date, no porphyrin-based nanorings have shown evidence of global aromaticity in the neutral state. However, this behavior has been predicted for fully fused belts.[6] Figure 2.2 presents the general structure of a fully fused porphyrin nanobelt and the results of Nuclear Independent Chemical Shift (NICS) calculations on a selection of these structures in the neutral state. The experimental workflow for performing NICS calculations is discussed in detail in Chapter 3, Section 3.3. Briefly, these calculations compute the level of shielding/deshielding that spectator nuclei experience due to the presence of global ring currents. In Figure 2.2, we see that all of the even-numbered fully fused porphyrin nanobelts exhibit regions of deshielding (red) inside the nanoring and shielding (blue) outside of the ring, which implies that they all posess global anti-aromatic ring currents in the neutral state.

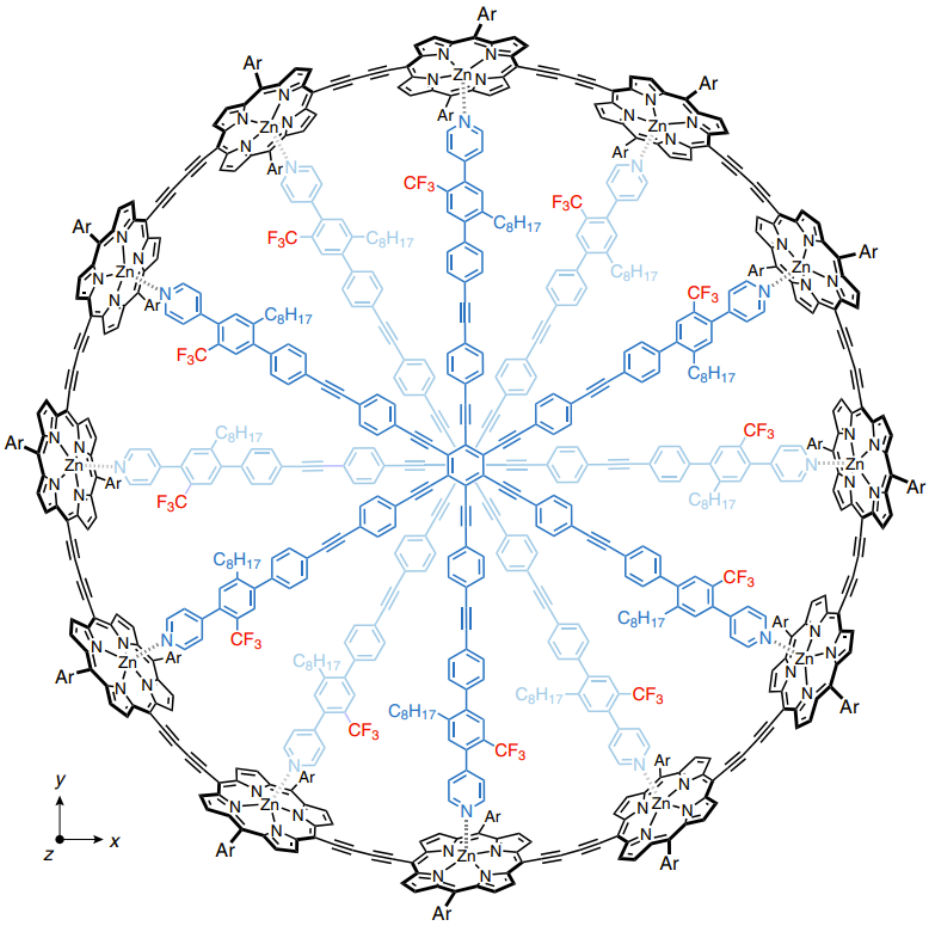

Figure 2.1: Chemical structure of the largest π-conjugated macrocycle confirmed to show global aromaticity. ***c*-P12·(T6e)$_2$** is globally aromatic in the +6 state where it contains 162 electrons in its conjugated π-circuit. Figure reproduced from reference[5].

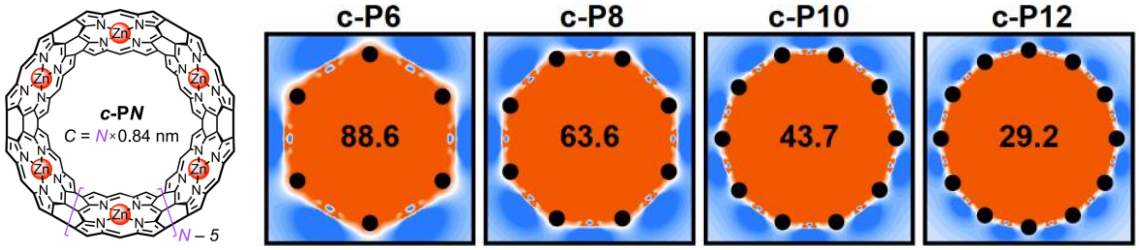

Figure 2.2: NICS plots predicting antiaromaticity in various even sized nanobelts. NICS(0)$_{zz}$ value from the center of the ring is shown in bold. Figures reproduced from reference[6].

As described in Chapter 1, numerous butadiyne-linked nanorings (***c*-P*N***, where *N* is the number of porphyrin units) have been synthesized and studied for the presence of global ring currents (*N* = 6, 8, 10 and 12) as they are synthetically the simplest porphyrin-based macrocycles to prepare and are highly compatible with template binding.[7] In the most extreme comparison, the all meso-meso linked nanorings, which are key precursors to fully fused belts, have proven

exceptionally challenging to prepare. This is primarily due to the high strain of these macrocycles, but additionally, template design for meso-meso linked nanorings is more challenging, due to the orthogonal orientation of adjacent porphyrin units in the nanoring.[8-10] Figure 2.3a presents an assessment of the strain energy in a meso-meso linked 18-porphyrin nanoring, with one butadiyne link. This strain map was computed using the StrainVis protocol,[11] which calculates the strain of a molecular framework by minimizing fragmented geometries that can relax to unstrained linear geometries. Many repeats of this process can be averaged to yield strain contributions for each bond, arising from the bond energy, angle strain and torsional strain, which are summed to produce a plot such as Figure 2.3a, which shows very high values for the meso-meso and butadiyne link.

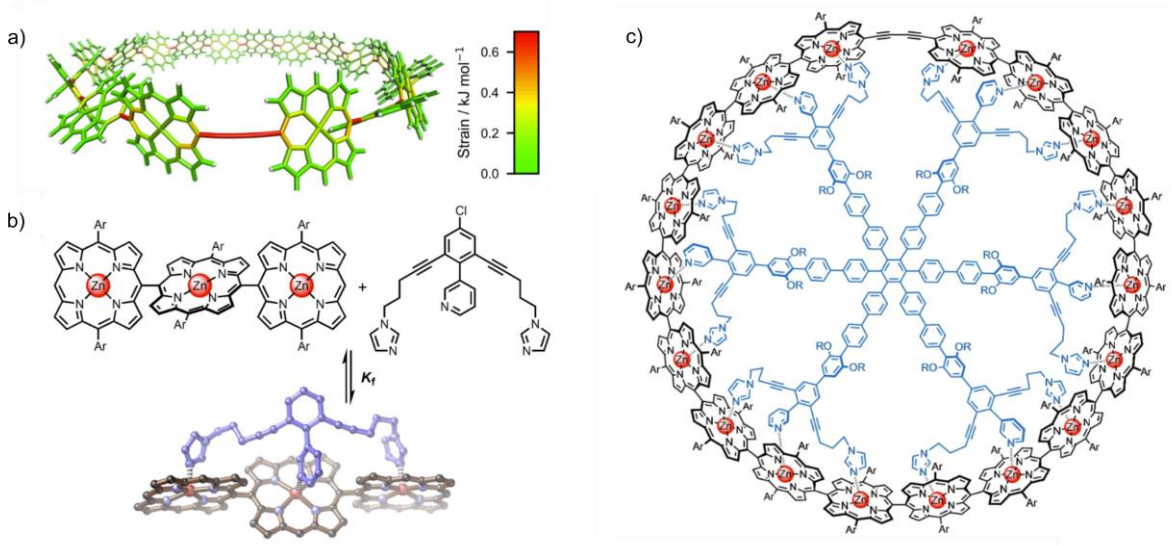

Figure 2.3: (a) Strain energies in a meso-meso linked porphyrin nanoring, containing a single butadiyne link. Computed with Strain-Vis. (b) Binding of a trimeric template to a meso-meso linked porphyrin trimer. (c) ChemDraw of the template design used to bend a liner meso-meso linked, ethynyl terminated, 18-porphyrin oligomer into a ring. Figures reproduced from reference[10].

Butadiyne-linked porphyrin nanorings are now routinely synthesized in good yields using the established template directed methods.[7] Due to the relative ease of their synthesis, it is expected that the strain in these macrocycles is smaller and more evenly distributed than in the meso-meso linked rings. A larger butadiyne-linked nanoring therefore seemed the most rational target for continuing the Anderson group's systematic study of aromaticity in porphyrin-based

nanorings. To this end, Chapters 2 and 3 of this thesis summarize the synthesis and study of a butadiyne-linked 18 porphyrin nanoring.

2.1.2 The Size Limit of Aromaticity

Our specific interest in the size limit of aromaticity is inspired by the studies of persistent current induction in mesoscopic metal rings[12] and the Aharonov-Bohm effect.[13] Lenz's law teaches us that macroscopic ring-shaped conductors, experiencing a change in magnetic flux through their cross-sectional area, produce ring currents that generate a magnetic field opposing the applied field (Figure 2.4). Due to the relatively high resistivity and disorder in macroscopic materials, currents generated in this manner are rapidly dissipated as heat; a process which consequently eliminates the magnetic field generated by the ring in the presence of a static magnetic field.[14]

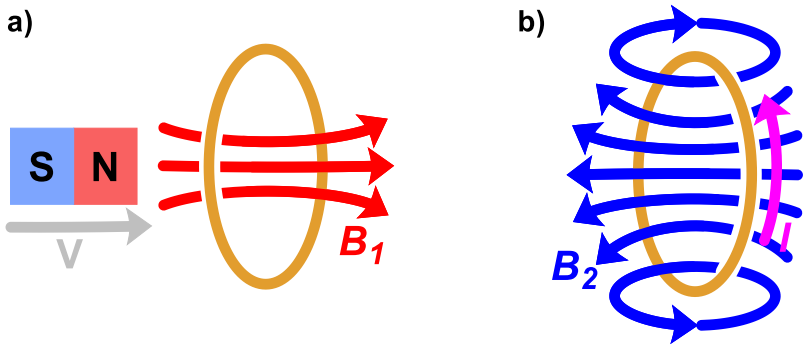

Figure 2.4: (a) A bar magnet with velocity *V* approaches a macroscopic metal ring, imposing magnetic field B_1 on the ring. (b) Diagram showing the current and magnetic field induced in the ring from scenario shown in (a). Current *I* is induced in the ring in an anticlockwise direction, so as to generate magnetic field B_2 that opposes B_1.

The high resistivity of these materials is a result of electron scattering, which can be mitigated in certain cases by cooling the material to low temperatures.[14] Bardeen-Cooper-Schrieffer (BCS) theory[15] states that below the critical temperature (T_c), critical current density (J_c) and critical magnetic field (H_c) of superconducting materials, electrons form Cooper pairs which can travel through the material without scattering and therefore with minimal resistance. Values of T_c, J_c and H_c in these materials are dependent on one another, so together, define the superconducting space of the material. While in this space, the application of a static external

magnetic field through a superconducting ring induces a ring current. As the electrons carrying this current experience close to no resistance, the ring current can persist even in the absence of an external magnetic field and for a significant length of time (experimental evidence for 533 days[16]) as long as $T<T_c$. Bardeen, Cooper and Schrieffer were jointly awarded the Nobel Prize in Physics in 1972 for their development of this theory of superconductivity.[17]

The presence of persistent currents in superconducting mesoscopic rings generates a magnetic field which has opposing directions inside and outside of the ring. Theoretical calculations indicate that the absolute direction of these fields can be predicted using Hückel's rule, based on the number of delocalized electrons in the ring.[18] However, experimental evidence supporting this theory has not yet been produced. One such result would link the phenomenon of molecular aromaticity and persistent ring currents. Our work seeks to approach the question from the other size domain, by probing the existence of aromaticity in large molecular rings.

The direction of ring currents in mesoscopic rings has been shown experimentally to change as a function of applied magnetic field strength (B).[19] This phenomenon is a consequence of the fact that magnetic flux (Φ, where $\Phi = B\pi r^2$) passing through a ring of delocalized electrons shifts the phase of the wavefunctions of the orbitals associated with the delocalized electrons.[4] This concept was first applied by London to calculate ring current effects in benzene,[20] and has since been used by Anderson and coworkers to predict the field dependent aromaticity of benzene (Figure 2.5).[4] From 0 applied field ($B = 0$, $\Phi = 0$), Figure 2.5a presents how the application of a magnetic field is predicted to break the degeneracy of the molecular orbitals in benzene, which regain degeneracy at values of Φ/Φ_0 that are multiples of 0.5. As ring current is proportional to the change in energy of the system with respect to applied magnetic field ($I \propto -\delta E/\delta B$, where negative values represent aromatic currents and positive values represent antiaromatic currents), the shift in occupied orbital energies results in an oscillation of aromaticity with a period of a flux quantum Φ_0 ($\Phi_0 = h/e$, where h = Planck's constant, e = elementary charge).[4] This behavior has been attributed to the Aharonov-Bohm effect.[13]

Eq. 2.1 can be used to calculate the applied magnetic field (B_0) required to reach one flux quantum for a nanoring of known radius r.

$$B_0 = \frac{\Phi_0}{\pi r^2} \qquad \text{Eq 2.1}$$

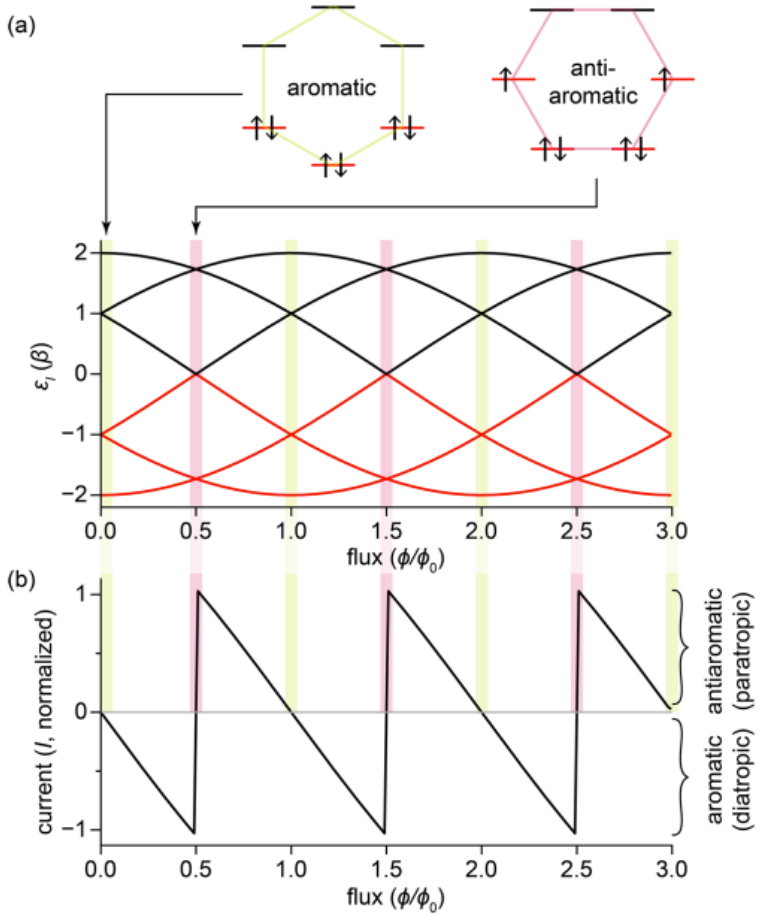

Figure 2.5: Properties of benzene as a function of magnetic field strength, calculated by reference[4] using the Hückel–London model. (a) Electronic structure (Occuped states – red, unoccupied states – black). (b) Ring current as a function of Φ/Φ_0 . Reproduced from reference[4].

Due to the large size of mesoscopic metal rings, magnetic field strengths encompassing multiple flux quantum can be achieved, and therefore studied, with current instrumentation.[19] However, the relatively small size of organic macrocycles require phenomenally large fields to achieve only a single flux quantum. As an example, the butadiyne-linked 12-porphyrin nanoring (***c*-P12·(T6$_e$)$_2$**), with an estimated radius of 25.8 Å, requires a magnetic field of 197 T to reach one flux quantum. For context, a 600 MHz NMR spectrometer has a field of 14.1 T. This size limitation is the primary reason for the absence of experimental evidence of field dependent

aromaticity in organic molecules to date. Our work to produce and study larger π-conjugated macrocycles contributes to reaching the minimum size limit for one such experiment. The butadiyne-linked 18-porphyrin nanoring discussed in Chapters 2 and 3 would require 88 T for one flux quantum, which with current NMR field strengths is still too small to observe flipping of the ring current direction. However, expansion to 36 porphyrin units would result in a ring of radius 77.5 Å, that requires 22 T for one oscillation; a target that is certainly achievable with the most advanced 1,200 MHz, 28 T, NMR spectrometers. In fact, confirmation of magnetic field dependent aromaticity only requires observation of the flipping aromaticity, which is predicted to occur at $\Phi = \Phi_0/2$. For a butadiyne linked 36-porphyrin nanoring this should require a field slightly stronger than 11T, which is achievable on a 500 MHz (11.7 T) or 600 MHz (14.1 T) spectrometer.

With the motivation for exploring the limits of aromaticity in larger π-conjugated macrocycles now laid out, the following sections of this chapter will focus on the synthetic work carried out to prepare the butadiyne-linked 18-porphyrin nanoring (***c*-P18**), and the template (**T18**) required for ring current studies.

2.2 Design of Template Candidates

2.2.1 Design and Computational Modelling of Template Candidates

When considering template candidates for ***c*-P18** we decided that the simplest design would be a template with 6-fold symmetry that branches at the end of each arm into three binding sites, much like the archetypal depiction of a snowflake. We expect that the higher rigidity and more defined conformation of an 18-fold symmetric template would have led to stronger binding, however, as we could not find any reasonable template cores with 18-fold symmetry, the 6-fold symmetric approach seemed the most reasonable (Figure 2.7, b and c).

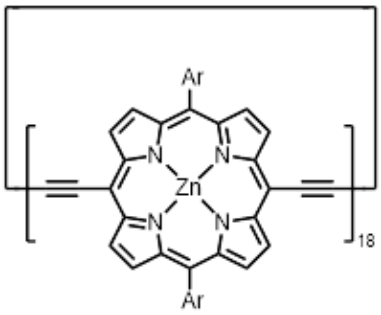

Figure 2.6. Chemical structure of ***c*-P18**

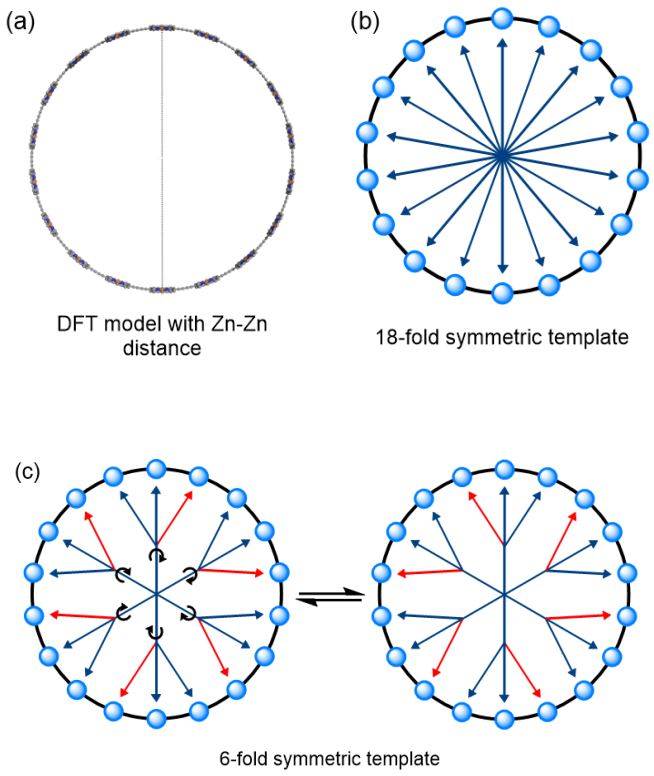

Figure 2.7: (a) DFT (B3LYP/6-31g(d)) model of ***c*-P18** with Zn-Zn distance highlighted. (b) 18-fold symmetric template in ***c*-P18**. (c) Branched 6-fold symmetric template in ***c*-P18**.

To begin the design process, I first optimised a model of ***c*-P18** using DFT (B3LYP/6-31g(d)) in Gaussian16[21] and measured the diameter from opposing Zn atoms, which gave a value of 77.7 Å (Figure 2.7a). From previous work, we understand that binding a pyridyl unit to a zinc porphyrin displaces the Zn 0.37 Å out of the plane of the porphyrin, and that the N-Zn bond length is 2.15 Å.[22] Considering all these factors, we calculate an optimal template diameter (N-N) of 72.69 Å. After considering many combinations of phenyl, ethynyl and pyridyl combinations, I determined that from the central benzene core to the terminal pyridyl at the end of one arm, there should be 5 phenyl units and 4 ethynyl units to reach the target diameter.

With the main structure of the template established, I then considered how to branch the template to enable binding of the remaining 12 porphyrin units. A good template would ideally point the pyridyl/imidazole nitrogen lone pair directly at the zinc atom of the target porphyrin, whilst also positioning this group close to the porphyrin to minimize conformational change

upon binding. Figure 2.8 shows the DFT (B3LYP/6-31g(d)) optimized models of the template candidates considered at this stage, bound to a linear butadiyne-linked porphyrin trimer (**P3**).

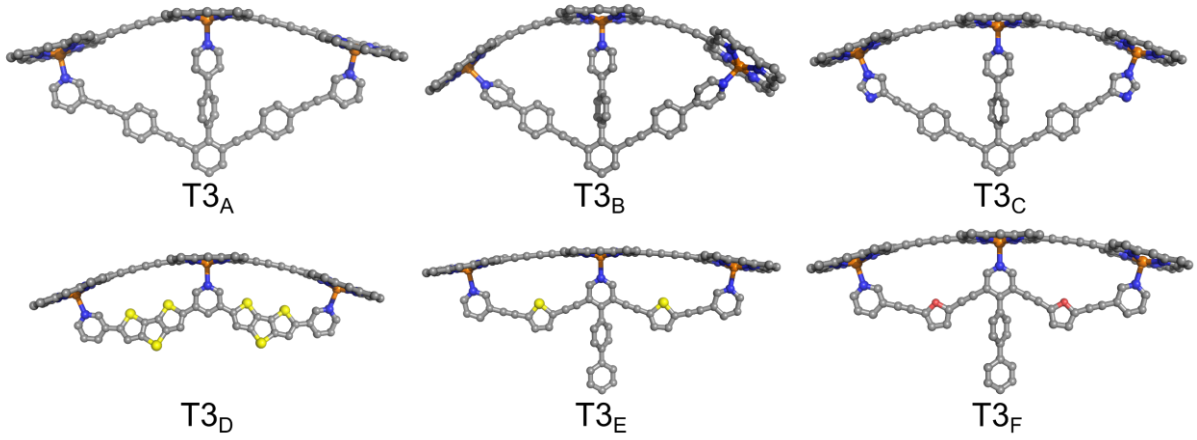

Figure 2.8: DFT (B3LYP/6-31g(d)) optimized models of various **T3** candidates bound to a linear butadiyne-linked porphyrin trimer (**P3**). C = Grey, N = Blue, O = Red, S = Yellow and Zn = Orange.

Of the templates considered in Figure 2.8, **T3B** is the only candidate which has no internal rotations that would create an entropic cost to binding T3. For example, in **T3A** the meta pyridyl unit can rotate, which changes the direction of the pyridyl nitrogen lone pair and points it away from **P3**. We expected that this would lead to poorer binding. There are considerably more unfavorable internal rotations in **T3D**, **T3E** and **T3F**, so these designs were discarded. Despite the added internal rotation **T3A** and **T3C** warp the **P3** unit considerably less than **T3B** and form a curvature more like that of **c-P18**. We therefore decided to investigate the geometries of the full template nanoring complexes using **T3A-C** and the combination of phenyl and ethynyl units determined earlier in this section.

Due to the large size of the full complexes, geometry optimizations using DFT were impractical, so I instead used the PM7 semi-empirical method in MOPAC[23] to optimize the geometries. Figure 2.9 presents the results of these calculations, which confirm that the warping seen in the **P3·T3B** does translate into **T18B** significantly warping the geometry of ***c*-P18**. Both **T18A** and **T18C** result in very reasonable cyclic geometries, with **T18A** showing that some slight bending

is required in the branched arms to properly bind ***c*-P18**. Finally, all **T18** candidates lie perfectly planar inside the nanoring, as seen in the vertical profile images of the models.

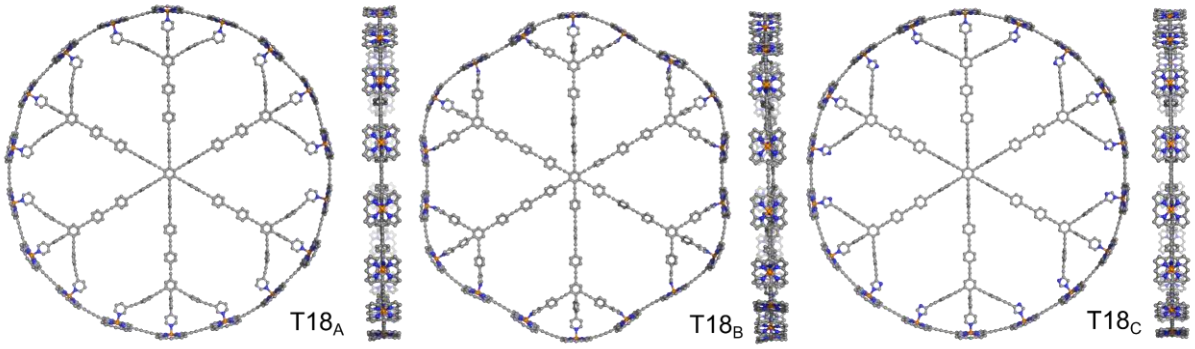

Figure 2.9: Semi-empirical (PM7) optimized models of various **T18** candidates bound to a cyclic butadiyne-linked 18-porphyrin nanoring (***c*-P18**).

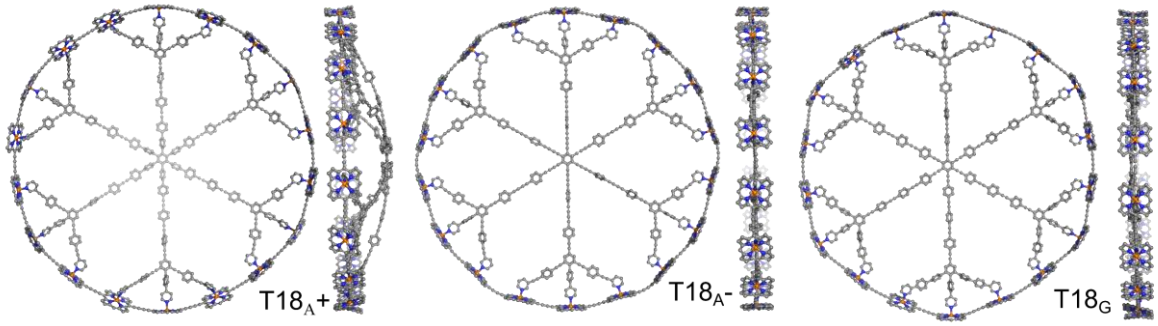

Figure 2.10: Semi-empirical (PM7) optimized models of ***c*-P18·T18** complexes each with slight variations in the total size of **T18**. One acetylene per radius replaced with a para-phenylene group (**T18A+**). One para-phenylene per radius replaced with an acetylene (**T18A-**). Two acetylenes per branch of **T3A** substituted for a para-phenylene group (**T18G**).

These models show that binding **T18B** clearly leads to a less cyclic nanoring geometry, so this design was discarded at this point. Additionally, early in the design process we discussed the challenges associated with incorporating imidazole units into a template design. This was learnt from a previous study (Figure 2.3) that was targeting the template directed synthesis of meso-meso linked nanorings, with imidazole-based templates.[10] The higher basicity of imidazole compared to pyridine made the synthesis and isolation of these templates more challenging, so it was advised to only use imidazole if the design showed a significant improvement over the equivalent pyridyl based design. Although **T18C** clearly has the most pristine model, with almost perfect cyclic geometry of ***c*-P18** and minimal distortion to **T18C** upon binding, we

decided that the **T18$_A$** model was close enough that the minor improvements **T18$_C$** offered would not outweigh the more challenging synthesis.

With **T18$_A$** selected as the most optimal design, I concluded this computational study by investigating the effect of minor changes to the **T18$_A$** design. These changes (Figure 2.10) include lengthening (**T18$_A$+**) or shortening (**T18$_A$-**) the radial arms of the template and replacing both ethynyl group in the branches of **T3$_A$** with a phenyl group (**T18$_G$**). **T18$_A$+** is clearly too large and forms a bowl-shaped complex, while **T18$_A$-** and **T18$_G$** form more distorted complexes than **T18$_A$**. We can therefore conclude that **T18$_A$** is the most synthetically feasible optimal design for ***c*-P18**.

2.2.2 Synthetic Plan for T18$_A$

The design for **T18$_A$** shown in Figure 2.9 requires the addition of CF_3 groups which will be used to probe global aromaticity in the oxidative NMR experiments, as discussed in Chapters 1 and 3 of this thesis. These groups should be close to the ***c*-P18** nanoring as we understand that the induced magnetic field from an (anti)aromatic nanoring gets weaker as you move away from the circumference of the ring to the center. However, the groups should not provide any steric hinderance to binding. We therefore decided to position them on the central phenyl groups in the branched arms. Our retrosynthetic analysis of **T18$_A$** also showed that this position is one of the most reasonable to add CF_3 groups.

A large and planar molecule like **T18$_A$** is also likely to be highly insoluble, so we considered the addition of solubilizing groups to mitigate this. Previously, studies used simple octyl chains to achieve this on smaller templates, so we positioned two of these groups per radial arm.[5] The final design of **T18$_A$** is shown in Figure 2.11 along with the key intermediates that we proposed to prepare it from.

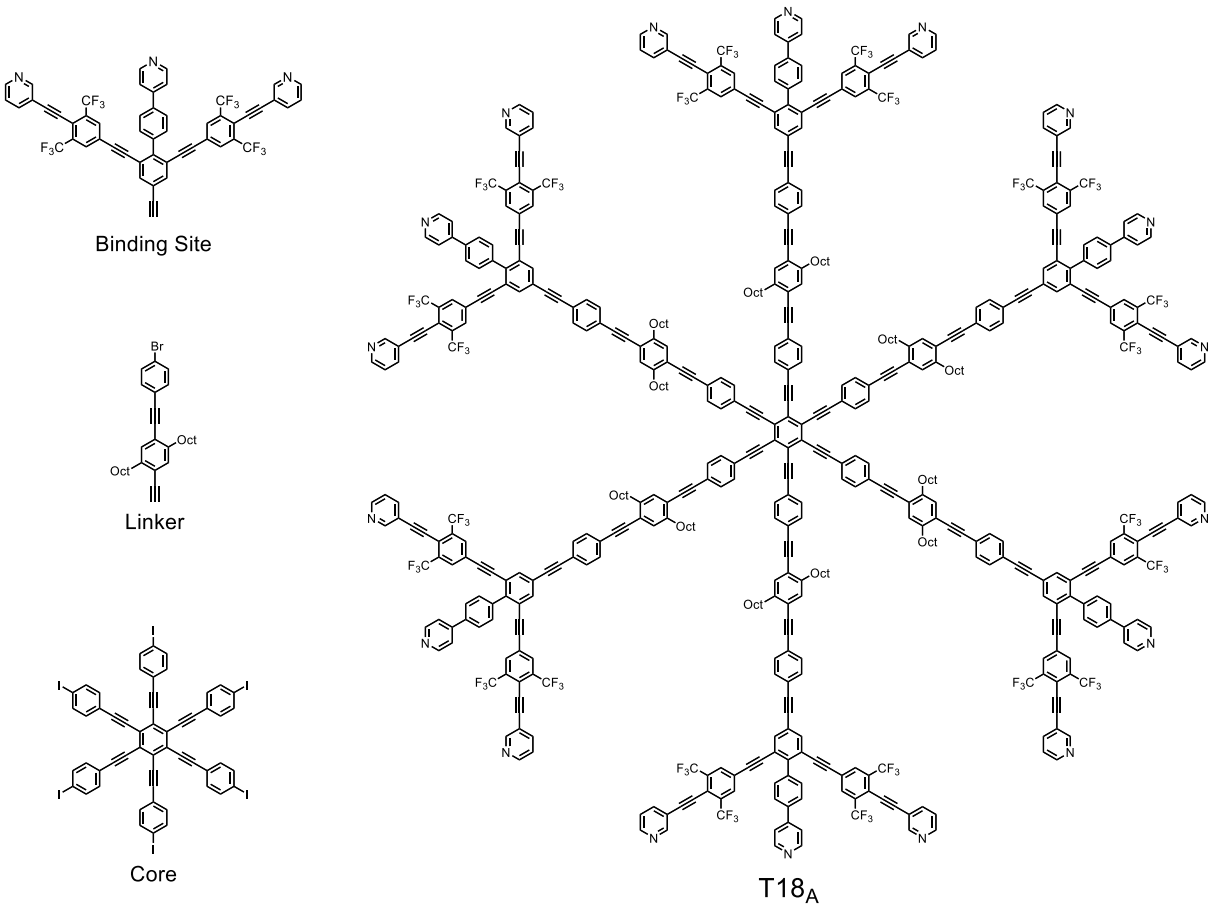

Figure 2.11: (Left) Key intermediates in the proposed synthesis of **T18$_A$**. (Right) Finalized chemical structure of **T18$_A$**.

2.3 Synthesis of T18$_A$ and T18$_B$

2.3.1 Synthesis of T3$_A$ Fragment

My first approach to **T3$_A$** followed the proposed route in Figure 2.12. This route was designed to add the central arm first, as we were concerned that adding the branched arms first would sterically hinder the central position and make coupling the central arm more challenging. Compound **2.4** is therefore key in this route, however I was unable to reproduce the synthesis of **2.3**[24] required to access this intermediate. On every attempt I obtained a significant amount of the tri-brominated product, which was inseparable from the desired dibrominated product. Furthermore, the iridium catalysed borylation/bromination[25] that I planned to use to access **2.2** was unreactive on my substrate (**2.1**), so the synthetic route was redesigned to avoid these steps.

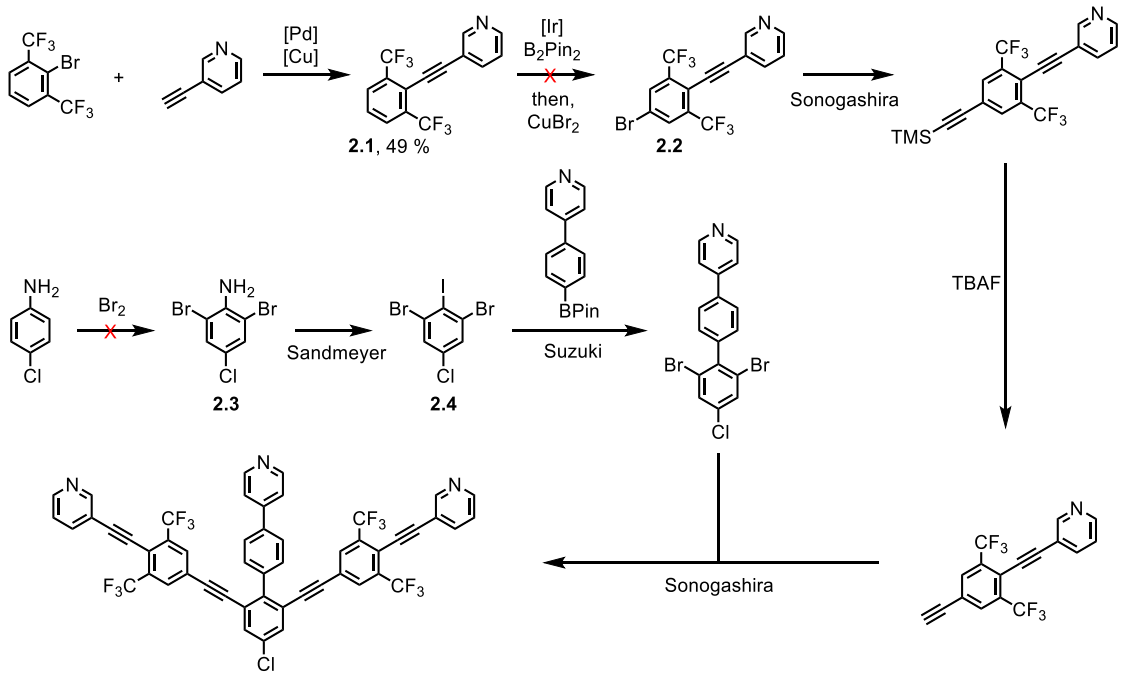

Figure 2.12: First attempted route to **T3A**.

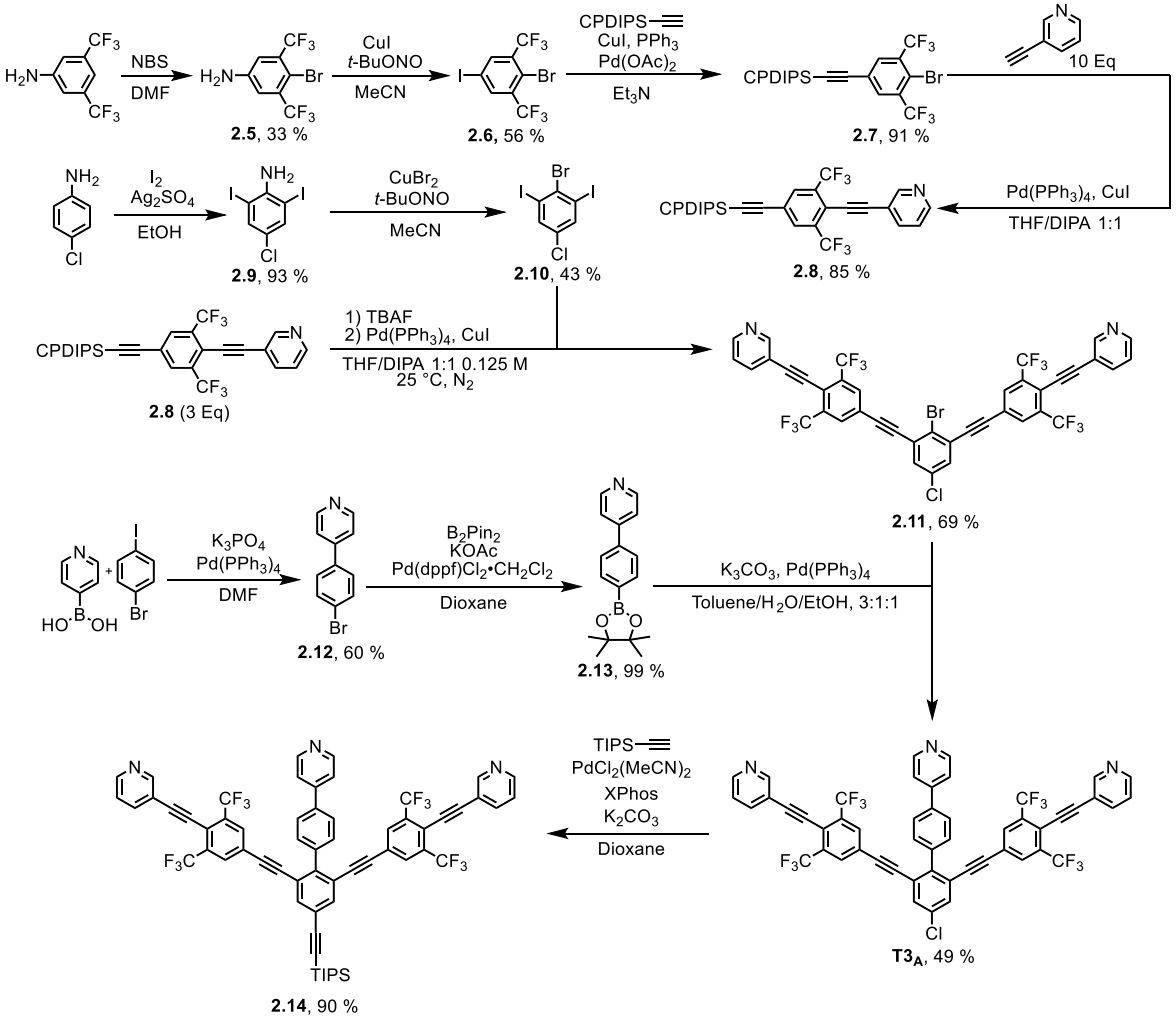

Figure 2.13: Successful route to **T3A**.

The redesigned route to **T3A** (Figure 2.13) follows a reported procedure for the synthesis of the tetrahalogenated core of the fragment **2.10**[26] which requires that the branched arms be installed first, then the central arm, due to the position of the iodine and bromine atoms. This order does not seem to significantly hinder the addition of **2.13** to **2.11**, which is achieved in 49% yield. The new route also builds the branched arm **2.8** in the opposite order to the scheme in Figure 2.12, so the terminal acetylene is installed first, then the pyridyl group is added after via a Sonogashira coupling.

To join **T3A** to the other fragments required to make **T18A** it is necessary to first couple an acetylene to the aryl-chloride group. This group is quite unreactive, however conditions developed by Buchwald[27] can be used to install a TIPS protected acetylene at this position in 90% yield.

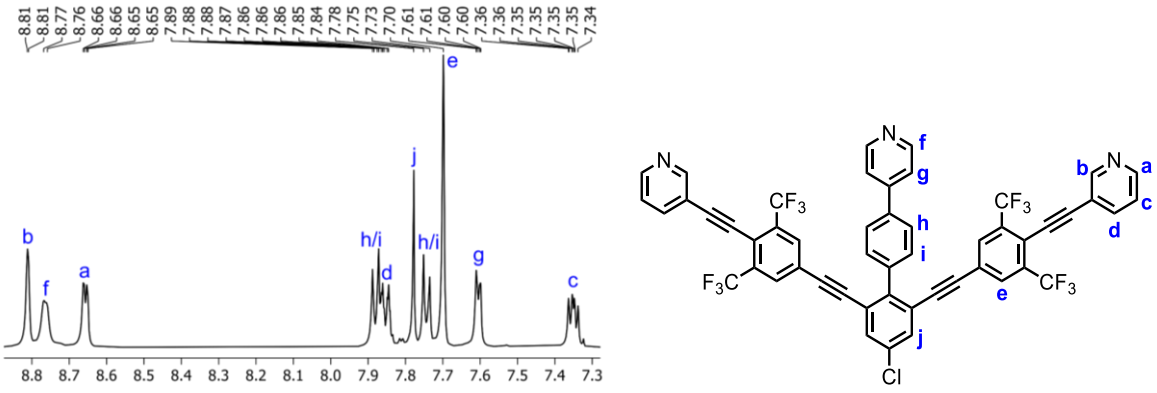

Figure 2.14: (Left) 600 MHz ^{1}H NMR spectrum of **T3A** in $C_2D_2Cl_4$ at 373 K. (Right) **T3A** with protons assigned.

2.3.2 Synthesis of T18A

To continue the synthesis of **T18A**, fragments **2.15** and **2.19** needed to be synthesized. **2.19** is novel (Figure 2.15), however **2.15** has been previously reported through a series of cross coupling reactions, which were repeated to obtain **2.15** for use in this project.[5]

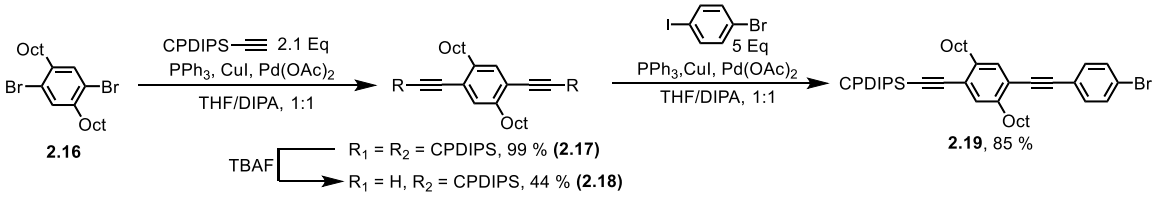

Figure 2.15: Synthetic route to linker **2.19**

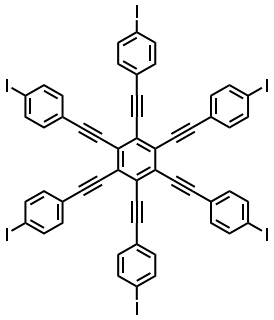

2.15

Figure 2.16. Chemical structure of **2.15**

After the synthesis of **2.15** and **2.19**, I explored how to combine the 3 key fragments to assemble **T18A**. The first approach (Figures 2.17 and 2.18) was designed to minimize the number of 6-fold coupling reactions required to make the template, as these can be challenging to push to full completion. The full radial arm of **T18A** (**2.24**) can be accessed by Sonogashira coupling **2.20** with **2.19**, which proceeds in 31% yield. The homocoupling of **2.20** is observed as a major byproduct of this reaction, which consumes a lot of the precious **T3A**. To minimize this, TMS-acetylene can first be coupled to **2.19** then selectively deprotected with KOH to yield the free acetylene **2.23**. Using a high excess of this material (10 Eq), **2.24** can be obtained by Sonogashira coupling to **T3A** in 55% yield, respective to **T3A.**

Unfortunately, coupling of **2.25** with **2.15** did not yield **T18A**. Instead, the major product observed is the homocoupled **2.26** and unreacted **2.15**. Despite multiple repeats I never observed any coupling between the components, so decided to explore an alternative route to **T18A**.

The alternative route to **T18A** is to build the template from the inside out (Figure 2.19-2.20). This seems counterintuitive, as it requires two subsequent 6-fold Sonogashira reactions, but the experimental evidence indicates it is a slightly better route. Surprisingly, coupling **2.27** to **2.15** (Figure 2.19) is very efficient and proceeds in 98% yield. **2.15** is a very poorly soluble compound, whereas **2.27** is relatively more soluble in most solvents. I believe that this is a key factor in the success of the reaction, because as the reaction proceeds the growing core becomes increasingly more soluble, which assists the coupling of the other units of **2.27**.

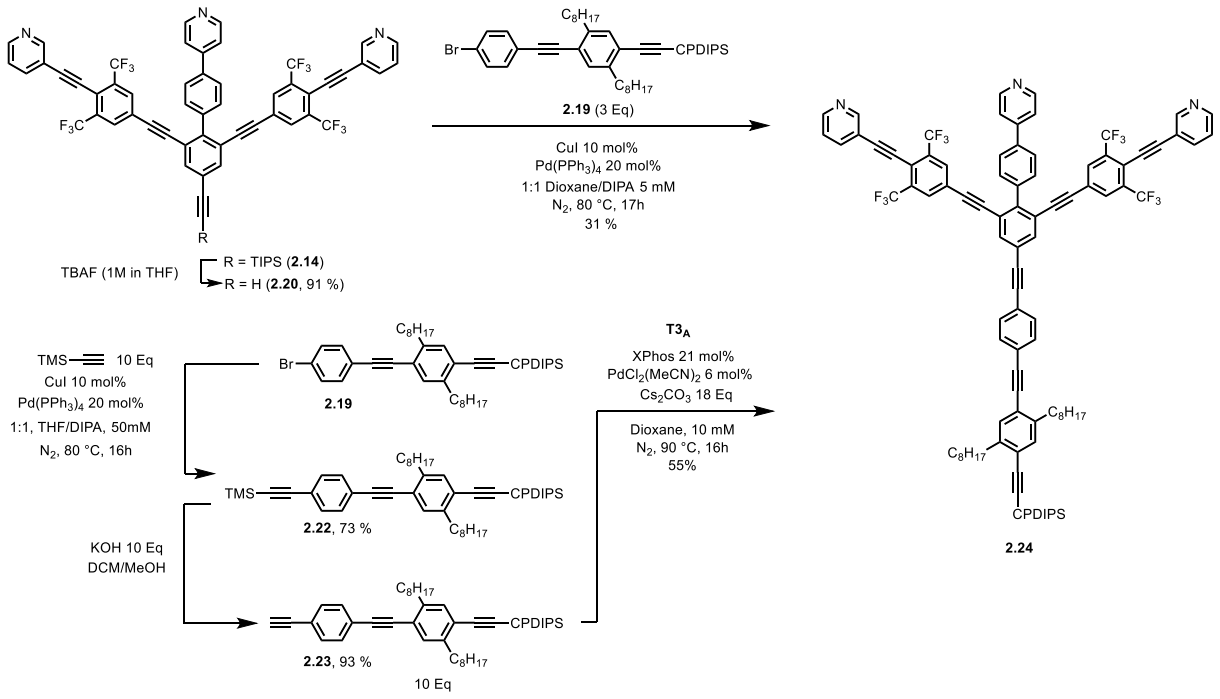

Figure 2.17: Synthetic routes to full radial arm of **T18$_A$ (2.24)**

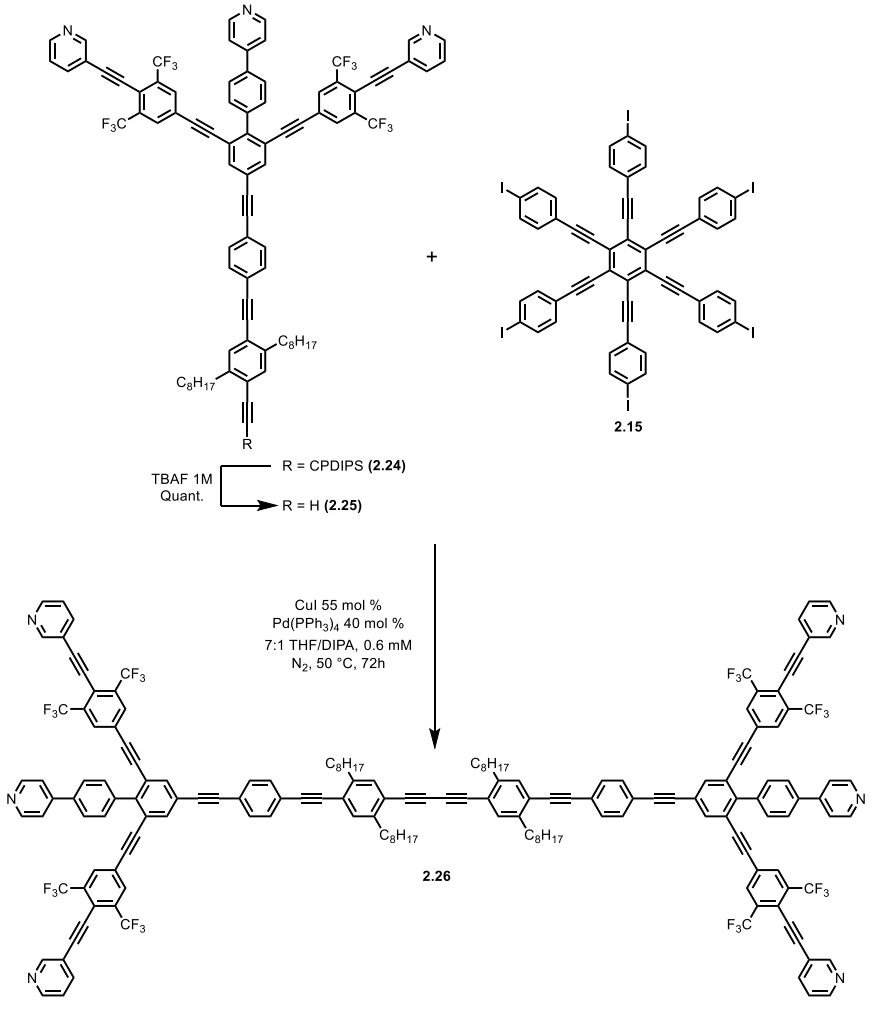

Figure 2.18: Outside-in approach to **T18$_A$**

To reach **T18A**, **2.28** needs to be coupled to **2.20** (Figure 2.20). **2.20** is a poorly soluble component, as highlighted by the need to do all NMR characterization of **T3A** in $C_2D_2Cl_4$ at 373 K. As **2.20** is coupled to **2.28** the solubility of the product decreases and eventually material begins to crash out of the reaction mixture. TLC of the crude reaction mixture shows a bright yellow spot that is more polar than a 12-legged pyridyl template previously made in the group.[28] This indicates some template with 12 or more pyridyl groups has been made, however the crude was too complex to isolate any **T18A** from this route. I was instead able to recover a significant amount of **2.29**. My conclusion from this route is that the inside-out approach is the most promising, however the final step is hindered by the poor reactivity of the terminal aryl-bromides. Changing this group to an aryl-iodide was expected to yield better results, so was attempted next.

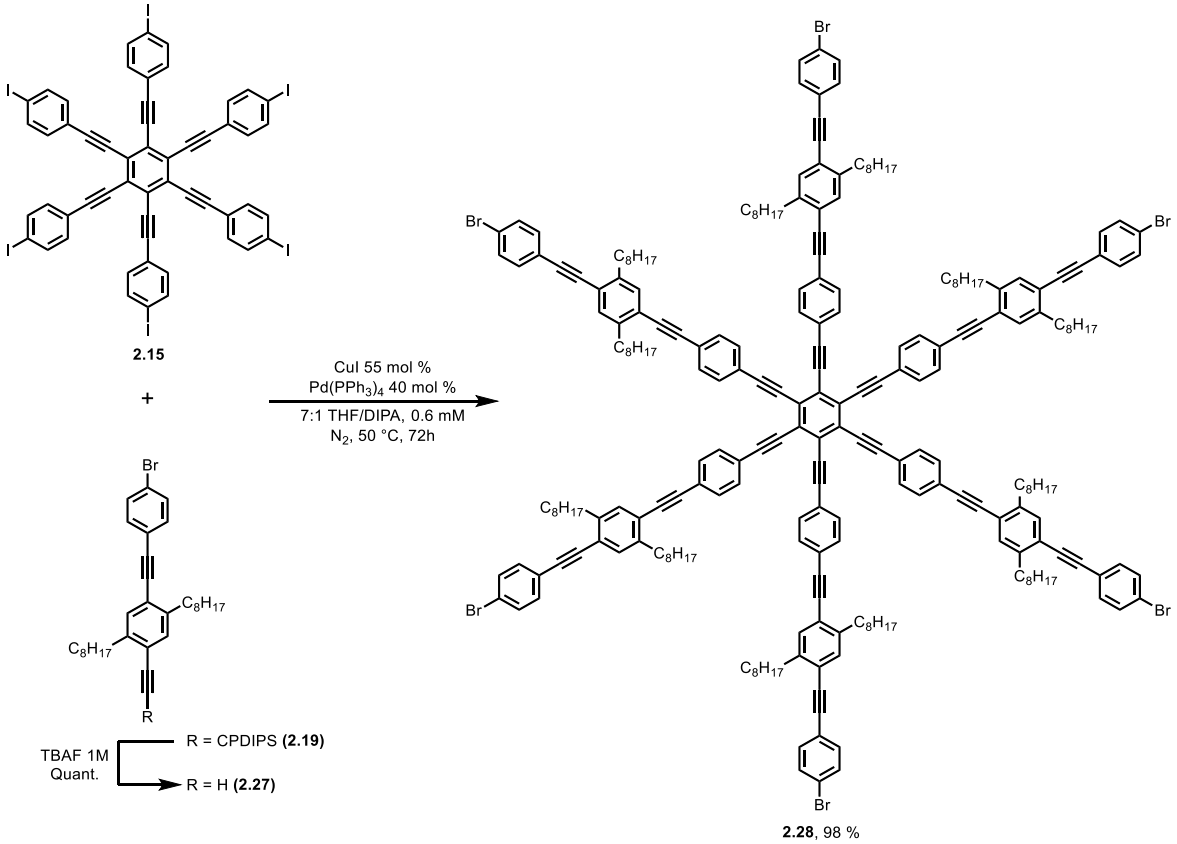

Figure 2.19: Extension of **2.15** with linker **2.27**.

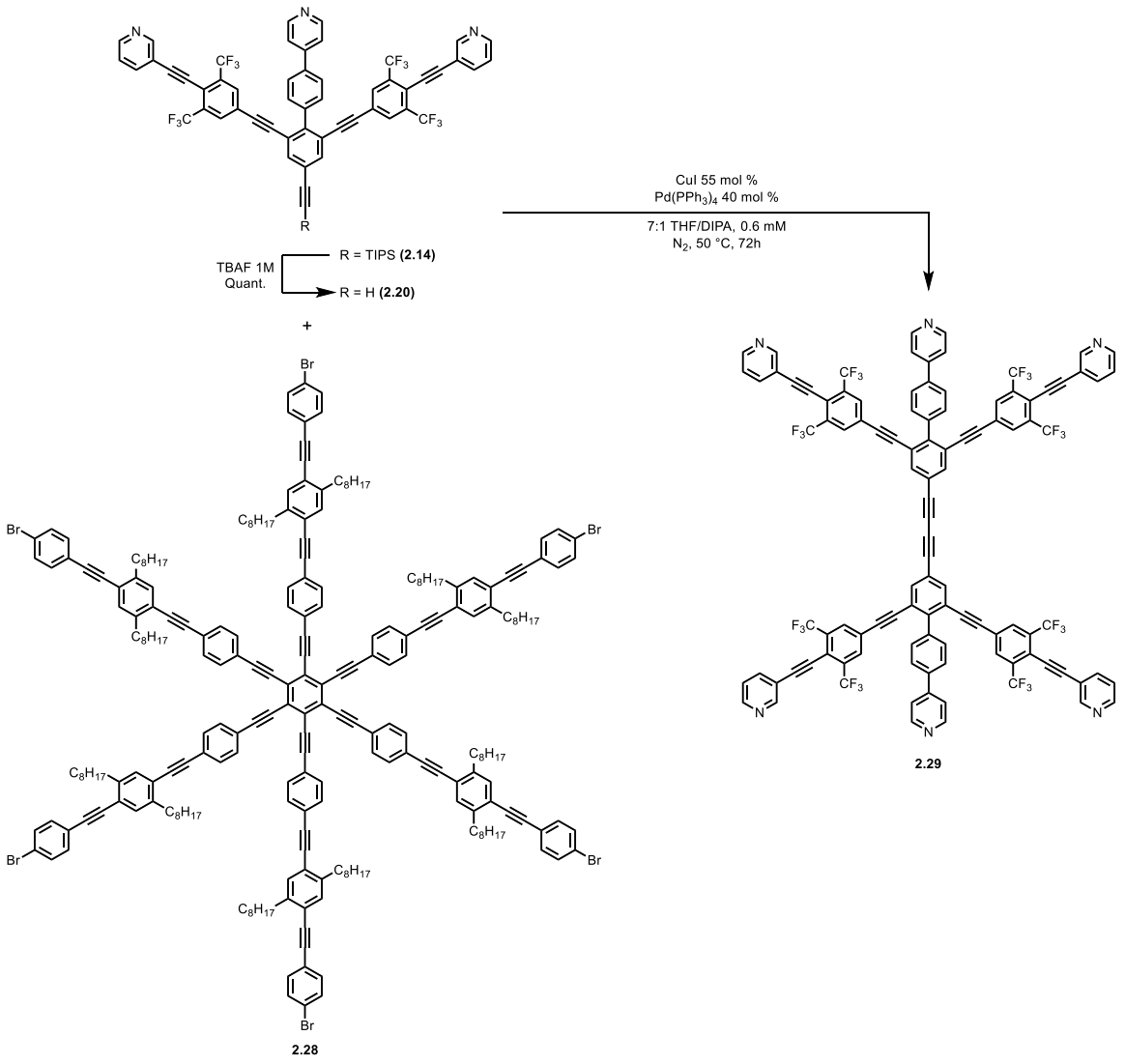

Figure 2.20: Attempted inside-out synthesis of **T18$_A$**

I first attempted an aryl Finkelstein reaction[29] (Figure 2.21) to swap the aryl-bromide to aryl-iodide. This reaction worked on my first attempt, but frustratingly never again after that. Instead, the synthetic route was reworked to utilize a diethyltriazine group as a masked iodide. This route (Figure 2.22-2.23) works well and can deliver the aryl-iodide capped template precursor **2.30** at scale.

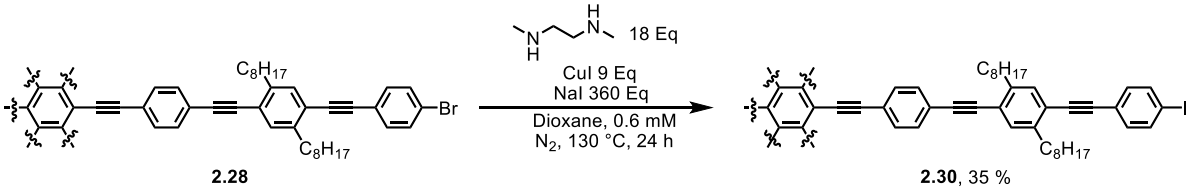

Figure 2.21: Aryl Finkelstein conditions used to swap Br for I

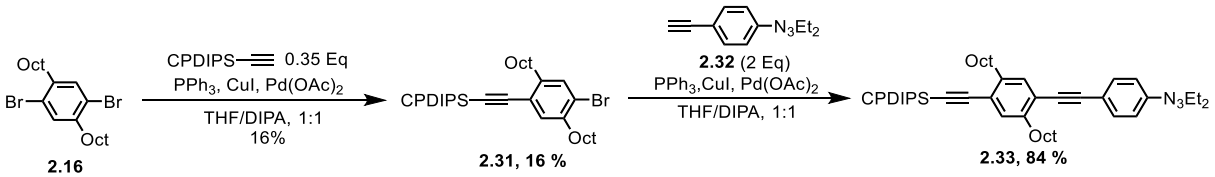

Figure 2.22: Route to diethyltriazine terminated linker

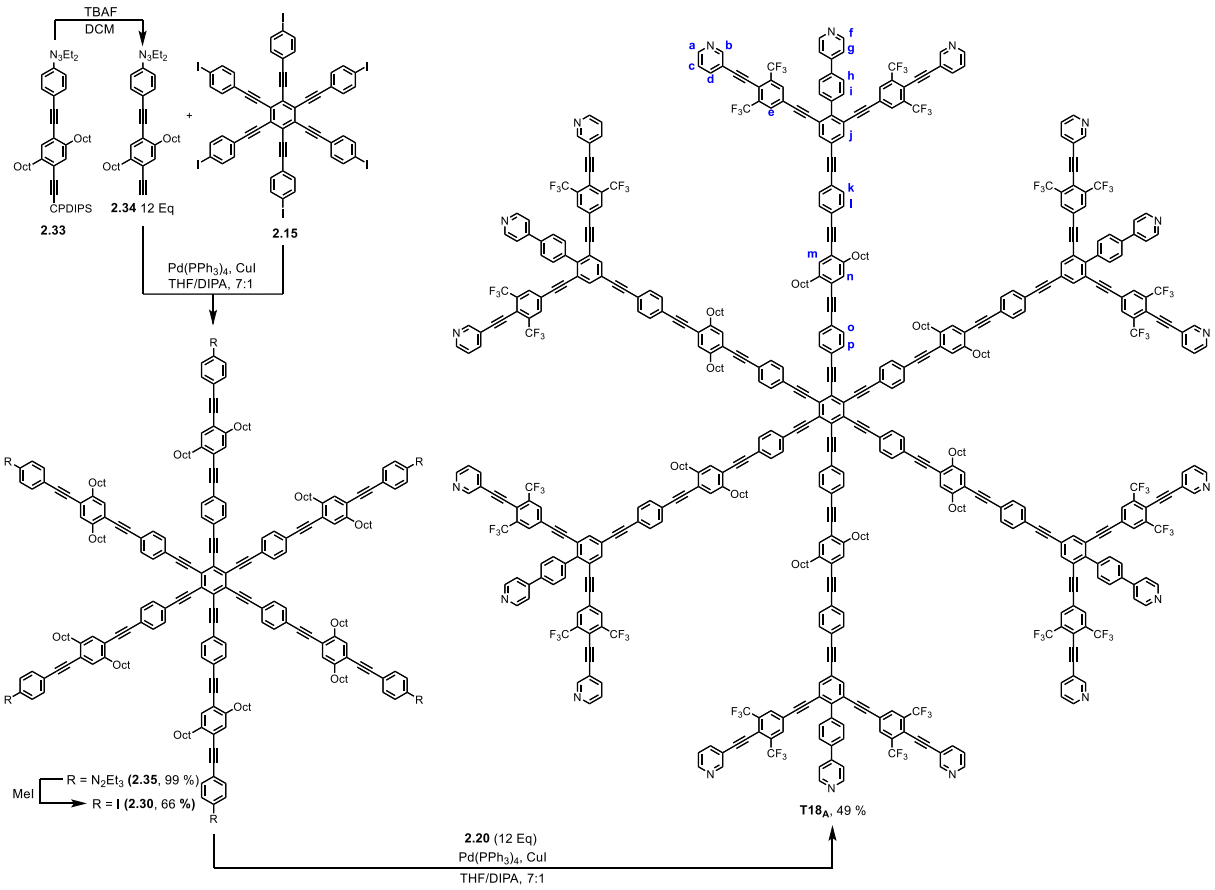

Figure 2.23: Successful route to **T18A**.

T18A was finally prepared by the 6-fold Sonogashira coupling of **2.30** and **2.20**. Despite the high solubility of **2.30**, the poor solubility of **2.20** leads to **T18A** crashing out of the crude reaction mixture. After a column in $CHCl_3$ + 10 % methanol + 0.5 % $^tBuNH_2$, **T18A** can be isolated as a bright yellow powder, which required characterization in $C_2D_2Cl_4$ at 373 K to obtain good NMR data (Figure 2.24). **T18A** is soluble in chloroform but will precipitate out if left in solution for an extended period of time. I expect this precipitated material to be protonated **T18A**. Solubility can be recovered by passing the material through a short silica plug in $CHCl_3$ + 10 % methanol + 0.5 % $^tBuNH_2$. Mass spectrometry of this material proved to be

quite challenging, but some success was had when using dithranol as a matrix for MALDI spectroscopy. This analysis showed a mass peak for **T18A** and no evidence of the 5-fold or 4-fold coupled products.

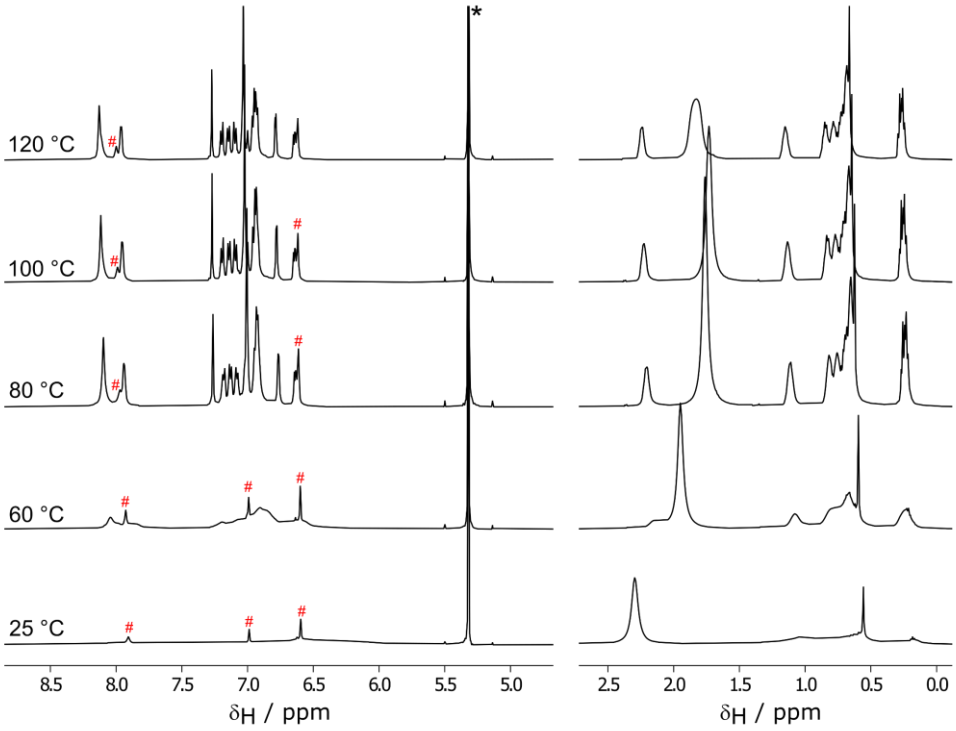

Figure 2.24: ^{1}H NMR spectrum of **T18A** (500 MHz, $C_2D_2Cl_4$, 298 - 393 K). * = $C_2H_2Cl_4$. # = Pyridine

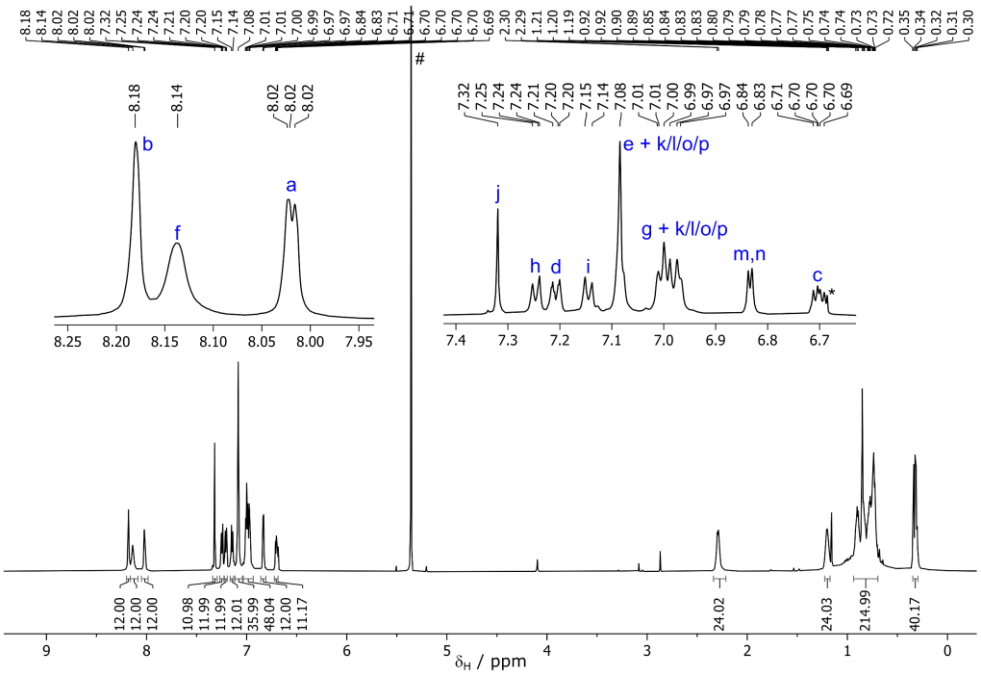

Figure 2.25: ^{1}H NMR spectrum of **T18A** (600 MHz, $C_2D_2Cl_4$, 393 K)(2D data used for the full assignment in experimental). # = $C_2H_2Cl_4$

2.3.3 Design of a Template for *c*-P9 and Synthesis of T18$_B$

At this stage of my thesis, I was exploring new template designs using the skills I developed in Section 2.2. In particular, I was exploring what a 9-legged template using **T3$_A$** would look like inside a ***c*-P9** nanoring (Figure 2.26, left). This template severely buckles the ***c*-P9** nanoring into a triangular shape, so it would not be suitable for studying the ring currents of this nanoring. However, a small modification to the **T3$_A$** structure leads to a template that fits well in ***c*-P9** (Figure 2.26, right). Coincidentally, the trimer unit of this more appropriate template is the **T3$_B$** unit we explored in Section 2.2. Lene Gödde in the Anderson group has since synthesized **T3$_B$** using a modified version of the **T3$_A$** route shown in Figure 2.13, then extended this into the **T9** template shown in Figure 2.26 (right) and investigated the ring currents present in ***c*-P9**.

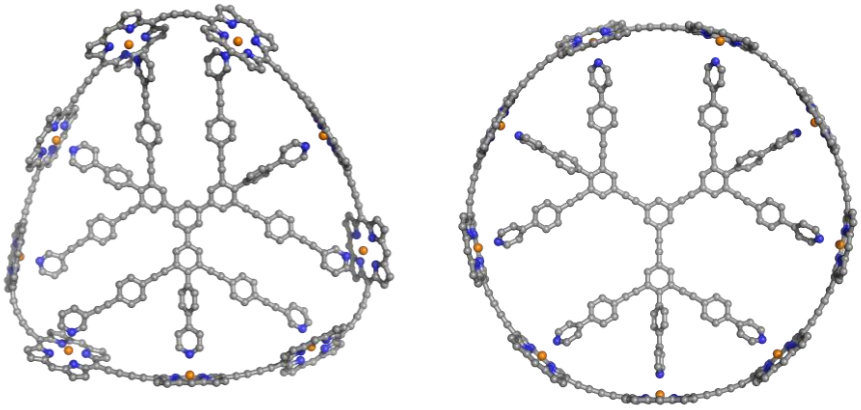

Figure 2.26: DFT (B3LYP/6-31g(d)) optimised geometries of ***c*-P9·T9$_A$** (left) and ***c*-P9·T9$_B$** (right)

The successful route to **T18$_A$** outlined in Figure 2.23 fortunately adds the **T3$_A$** unit as the final step, therefore, I was able to take a small portion of **2.43** that Lene prepared and use it to make **T18$_B$** (Figure 2.28). This reaction worked well, with a yield of 98%. In contrast to **T18$_A$**, **T18$_B$** is readily soluble in $CHCl_3$ and does not crash out of the crude reaction mixture. The column chromatography was also simpler, and all NMR characterization was achievable in $CDCl_3$ at 298 K. I expect the higher solubility of **T18$_B$** to be the key to the improved yield. The limiting factor in the final step of both the **T18$_A$** and **T18$_B$** syntheses is the competing homocoupling of the acetylene terminated **T3** units. The productive reaction of these components with the growing template is dependent on the solubility of both components. In the case of the A

templates, **T18$_A$** is relatively insoluble, so homocoupling of **T3$_A$** is favored as the template precursor gains **T3$_A$** units and crashes out of solution. In contrast the good solubility of **T18$_B$** means the growing template remains in solution, so can better compete for **T3$_B$** units.

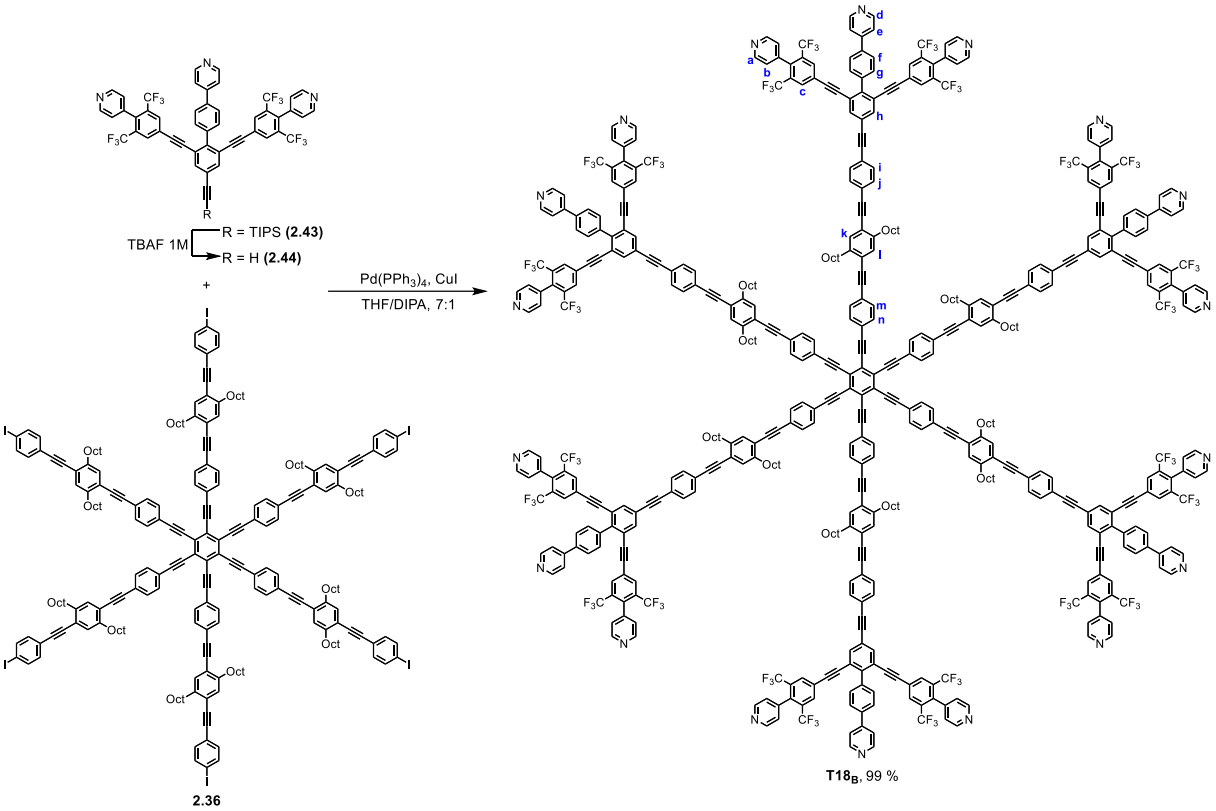

Figure 2.28: Successful route to **T18$_B$**.

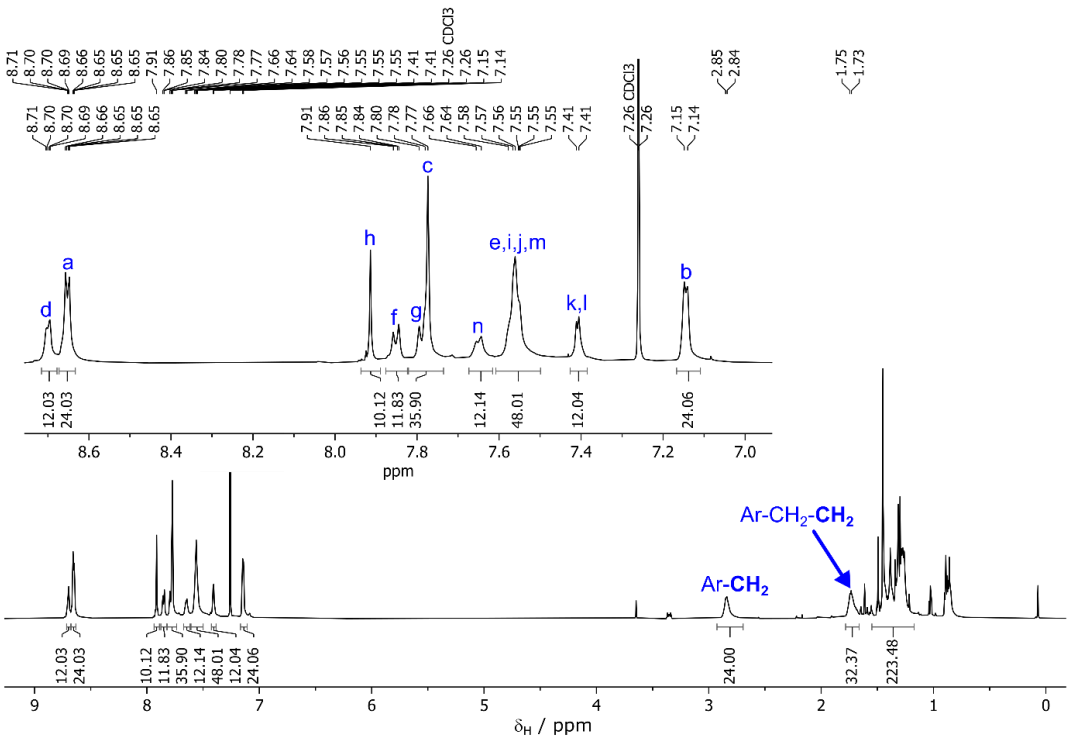

Figure 2.29: ^{1}H NMR spectrum of **T18$_B$** (600 MHz, $CDCl_3$, 298 K)

2.4 Synthesis of Butadiyne-linked Porphyrin Oligomers

2.4.1 Use Cases for OOct and THS Solubilised Oligomers

Advances in porphyrin synthesis mean that a wide variety of functional groups can now be installed on the periphery of porphyrin units.[30, 31] These advances have enabled the synthesis of a diverse range of porphyrin based materials, but of specific interest to this thesis is the preparation of butadiyne-linked porphyrin oligomers, through the installation and subsequent coupling of ethynyl groups at the 5 and 15 positions.[32] To ensure these oligomers remain soluble and do not aggregate, solubilizing aryl groups are installed at the 10 and 20 positions.[33]

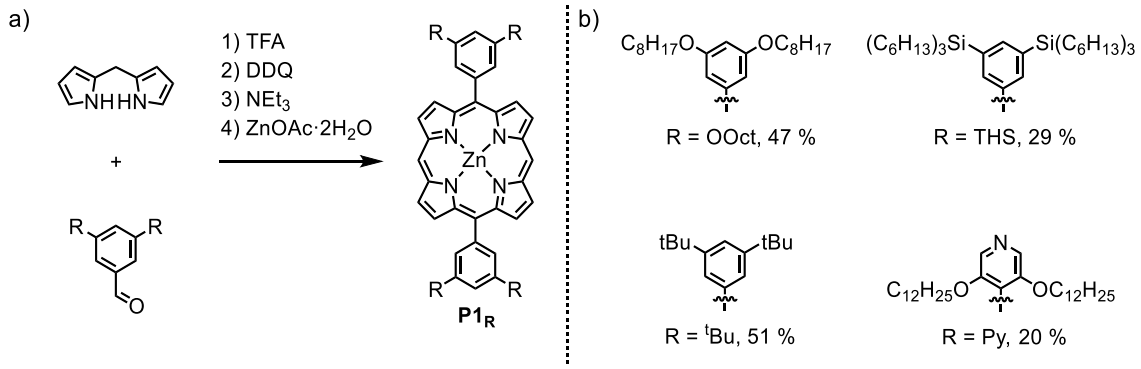

Figure 2.30: (a) General synthesis of porphyrin monomers. (b) Yields of **P1** with different solubilizing groups; OOct, THS[34], ^{t}Bu[35], and Py[36].

A typical synthetic route to various porphyrin monomers is outlined in Figure 2.30. This route can be readily modified to alter the nature of the solubilizing group R, with slight variations in the yield of the porphyrin monomer based on the electronic properties of the required aldehyde.

The 3,5-di(octyloxy)phenyl (OOct) group has been utilized as a solubilizing group in many studies,[32, 37-40] including the first synthesis of a butadiyne-linked porphyrin-based nanoring.[41] This group is relatively easy to prepare, and in addition to improving the solubility of the porphyrin species, is highly compatible with STM analysis of porphrin-based oligomers and nanorings, which is especially useful for confirming and investigating the geometry of these supramolecular materials,[9, 42] as X-ray crystal structures of such large molecules can be challenging to acquire. STM has also been used to probe the electronic structure of porphyrin-

based nanorings,[43] so can be used to supplement the characterization of these materials and explore their photophysical properties.

One drawback to the OOct group is its tendency to aggregate at high concentration and/or low temperature; a behaviour that gets more pronounced as oligomer length increases. This is demonstrated clearly in a study by Hutin and co-workers[44] which shows that OOct-solubilized butadiyne-linked porphyrin tetramers aggregate to form discrete 3-layered stacks. Aggregated oligomers of zinc porphyrins can be disaggregated through coordination of pyridine or a template.[45, 46]

Studying the global aromaticity of porphyrin nanorings requires that each nanoring·template complex is free in solution, as aggregation may cause distortions to the nanoring geometry or encourage charge to localize in the structure, which would impede the precession of global ring currents. As the oxidative titration experiments used to probe global aromaticity of these nanorings are often completed at low temperature (- 40 °C) a bulkier solubilizing group was designed to minimize aggregation of nanoring·template complexes, which has been used for all studies of global aromaticity to date.[5, 47-49] This group is 3,5-bis(trihexylsilyl)phenyl (THS).

For this project we aimed to target both the OOct and THS solubilised nanorings. We planned to use the THS solubilised nanorings for the oxidative NMR titrations to probe global aromaticity and the OOct solubilised nanorings for on surface measurements of free ***c*-P18$_{OOct}$** and the ***c*-P18$_{OOct}$·T18** complex. **T18$_A$** and **T18$_B$** are precious materials, so we planned to produce both nanorings through the Vernier route shown in Figure 2.31, from butadiyne linked porphyrin 9-mers (**P9**) and the **T6** template. Finally, the synthesis of ***l*-P9** will yield other oligomers of interest as side products, for example ***l*-P15$_{OOct}$,** which could be combined with **T18$_{A/B}$** to attempt the Vernier templated synthesis of ***c*-P90.**

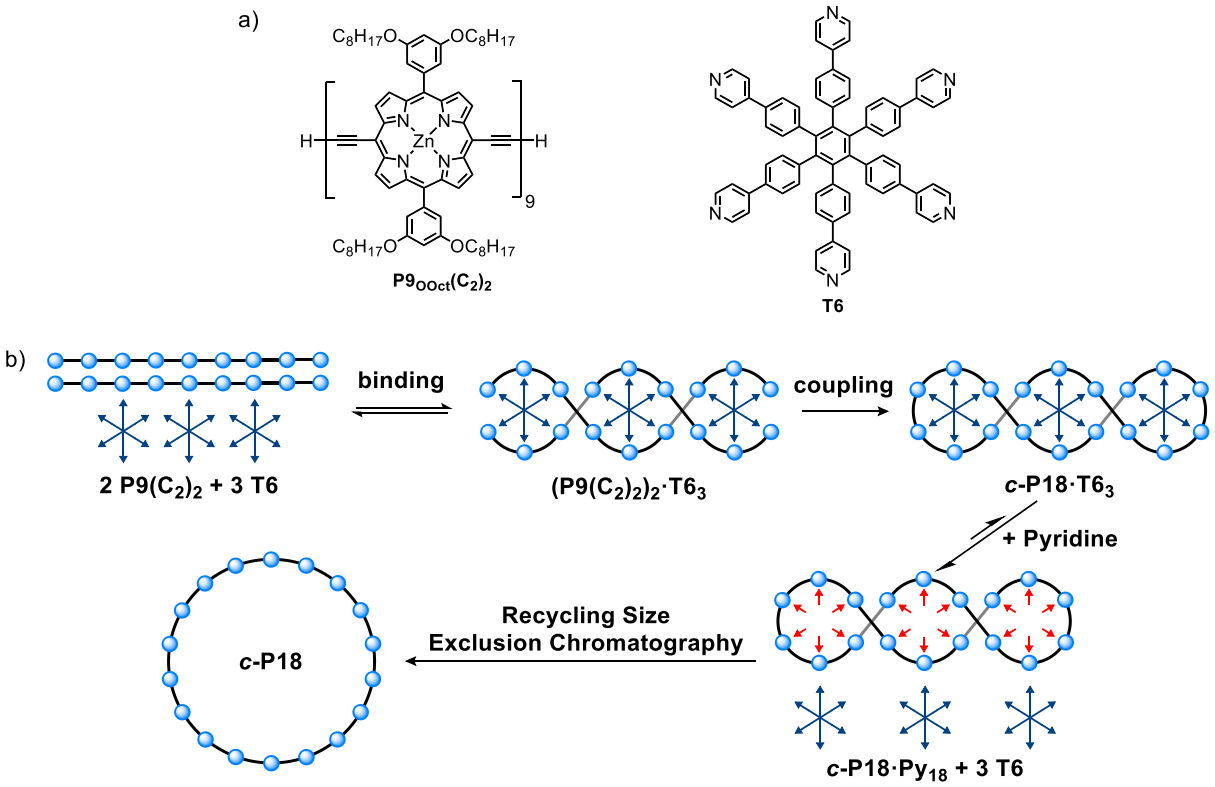

Figure 2.31: (a) ChemDraw structure of OOct-solubilized linear butadiyne-linked 9-mer (**$P9_{OOct}(C_2)_2$**) and the **T6** template. (b) Schematic representation of Vernier template-directed synthesis of ***c*-P18** from **$P9(C_2)_2$** and **T6**.

2.4.2 Synthesis of OOct and THS Solubilised Oligomers

The synthesis of OOct and THS solubilized butadiyne-linked porphyrin oligomers in this project generally followed a literature procedure used to access the butadiyne-linked hexamer **$P6_{tBu}$**.[50] This procedure was followed, with slight modifications, to produce **$P3_{OOct/THS}(C_2THS)_2$** and **$P9_{OOct/THS}(C_2THS)_2$** for this project (Figures 2.32 and 2.33).

In the case of the OOct solubilized oligomers (Figure 2.32), the main change we implemented was the consecutive statistical deprotection and coupling of **$P1_{OOct}(C_2THS)_2$** to access **$P3_{OOct}(C_2THS)_2$**, then of **$P3_{OOct}(C_2THS)_2$** to access **$PN_{OOct}(C_2THS)_2$** where N = 3, 6, 9, 12, 15 … 21. The polarity of the acetylene protecting group must be carefully considered with respect to the solubilizing group, so that TLC analysis can be used to estimate the extent of deprotection in the **$P3_{OOct}(C_2THS)_2$** unit. We have observed that the statistical deprotection of all acetylene protecting groups is rather fiddly and unless properly monitored, can run away, leaving only the fully deprotected oligomer. In the case of OOct solubilised oligomers, THS

protected terminal acetylenes grant enough of a difference in polarity that the ratio between fully protected, mono-deprotected and fully deprotected **P3$_{OOct}$** can be identified by TLC. Generally, we aim for a 1:2:1 ratio. Once deprotected, a Glaser-Hay coupling was used to oligomerize the material, which was later separated by recycling GPC. Using this approach, we were able to synthesize the large quantities of OOct solubilised oligomers required for this project.

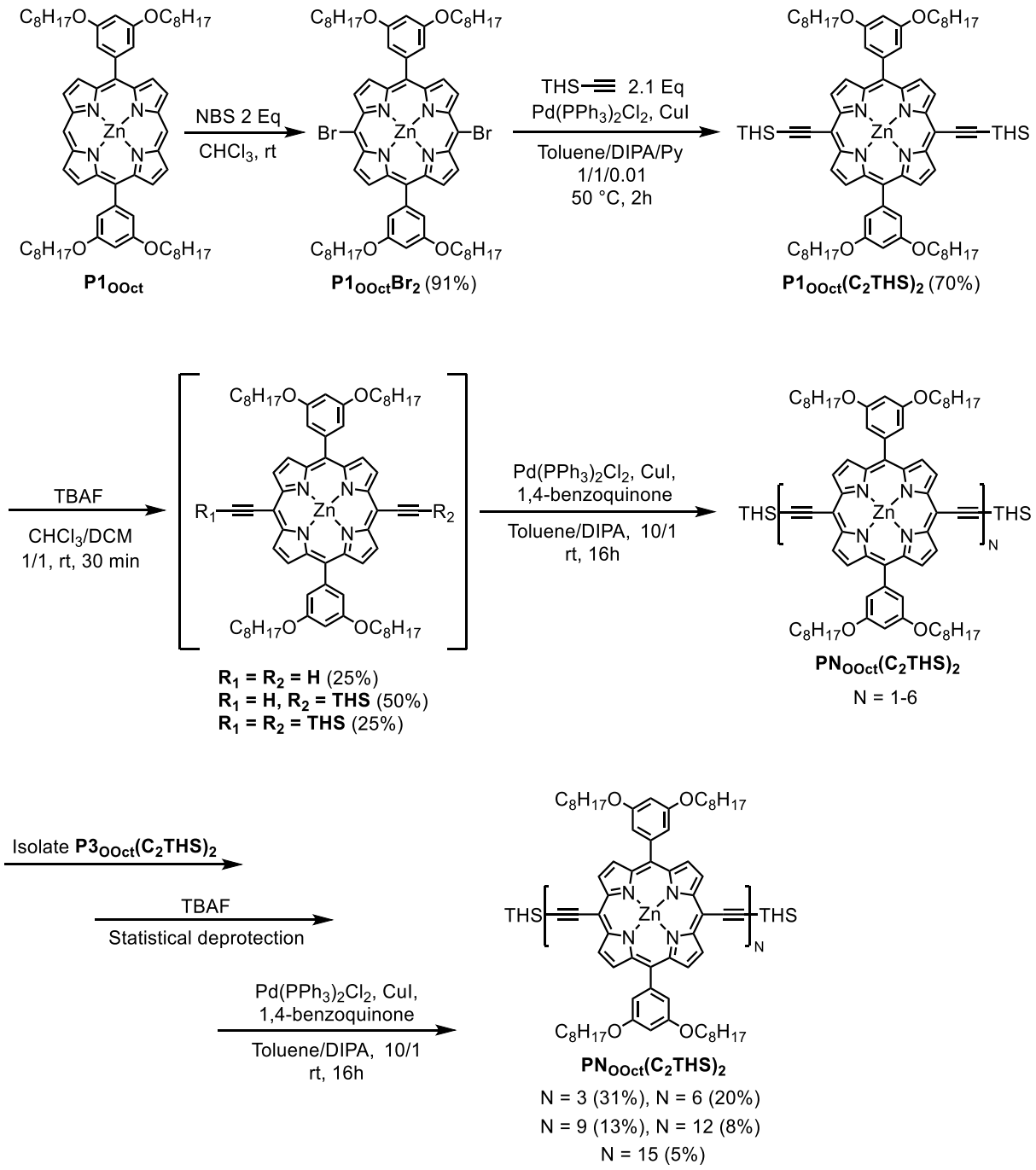

Figure 2.32: Synthetic route used to access **P9$_{OOct}$(C$_2$THS)$_2$**

The synthesis of the THS solubilized oligomers (Figure 2.33) follows the same route as the OOct oligomers, except that the CPDIPS acetylene protecting group is used to give the best resolution between statistically deprotected **P3$_{THS}$**.

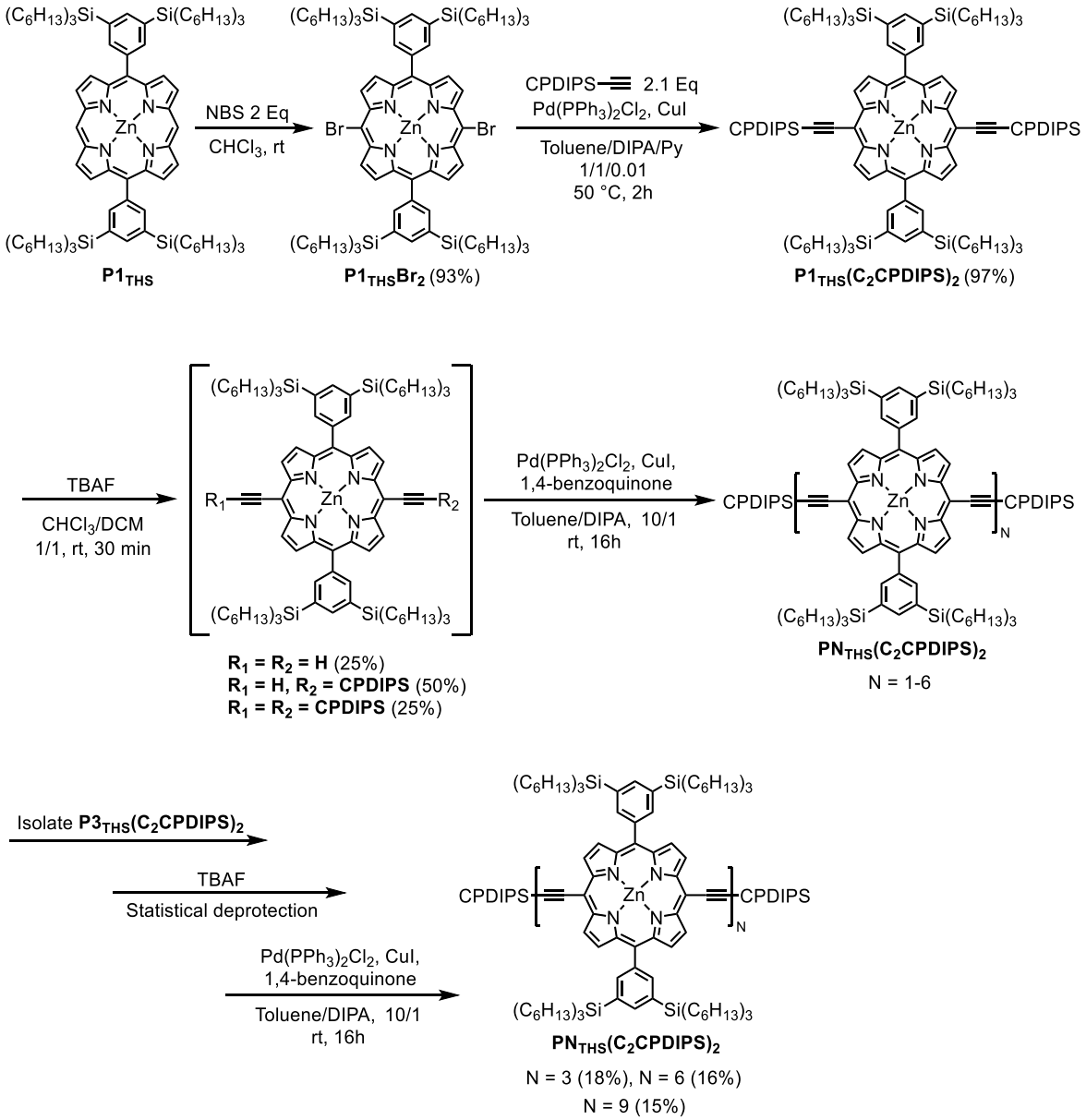

Figure 2.33: Synthetic route used to access **P9$_{THS}$(C$_2$CPDIPS)$_2$**

2.5 Template-directed Synthesis of *c*-P18

2.5.1 Vernier Template-directed Approach with T6

After the successful synthesis of **P9$_{OOct}$(C$_2$THS)$_2$** and **P9$_{THS}$(C$_2$CPDIPS)$_2$** I next turned my attention to examining the Vernier template-directed synthesis of ***c*-P18** using these oligomers and the previously reported **T6** template (Figure 2.34).[50]

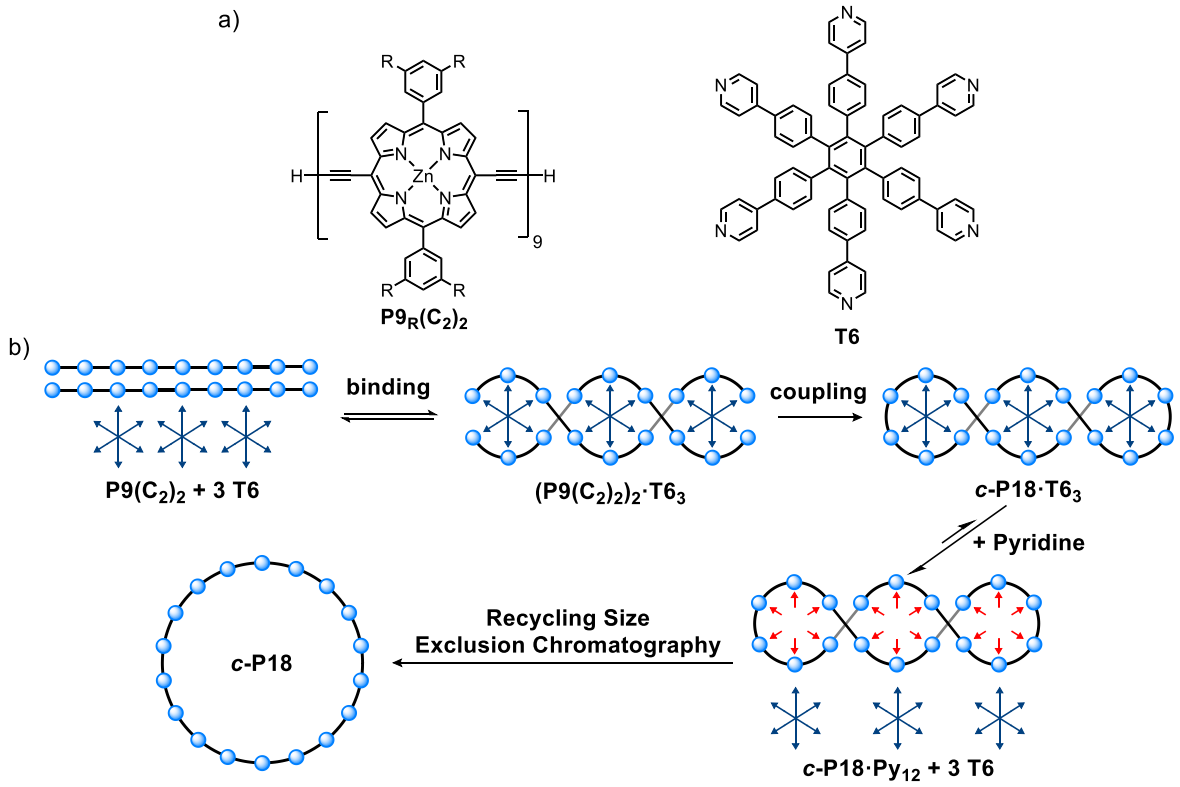

Figure 2.34: (a) Structures of butadiyne-linked porphyrin oligomer with free terminal acetylenes **P9$_{R}$(C$_2$)$_2$** and **T6**. (b) Vernier template-directed synthesis of ***c*-P18**.

***c*-P12$_{tBu}$** has been previously synthesized from **P4$_{tBu}$(C$_2$)$_2$** and **T6** using the Vernier route in 39% yield.[28, 51] However, this work utilised the smaller ^{t}Bu solubilizing group. The larger OOct solubilizing group used in this thesis is also compatible with Vernier template-directed synthesis, as demonstrated by the preparation of ***c*-P24$_{OOct}$** from **P8$_{OOct}$(C$_2$)$_2$** and **T6** in 25% yield.[52] However, it has been observed that the bulky THS group results in lower yields through the Vernier route, presumably due to it sterically inhibiting the formation of the vernier complexes.[7, 53]

Figure 2.35 summarizes the results of the Vernier template-directed synthesis of ***c*-P18$_{OOct}$** and ***c*-P18$_{THS}$** achieved in this study. **P9$_{OOct}$(C$_2$)$_2$** when subjected to the coupling conditions and in the presence of no template rapidly oligomerizes to give a narrow distribution of very long oligomers. With the addition of 1.5 Eq of **T6** the oligomerization is strongly directed towards the formation of ***c*-P18$_{OOct}$.** Interestingly, a small amount ***c*-P9$_{OOct}$** is formed, presumably from the mismatched 1:1 complex of **T6** and **P9$_{OOct}$(C$_2$)$_2$.** In contrast, **P9$_{THS}$(C$_2$)$_2$** in the presence of

no template oligomerizes less well, giving a distribution of oligomers centered at **P56$_{THS}$(C$_2$)$_2$** but with clear amounts of **P9$_{THS}$(C$_2$)$_2$**, **P18$_{THS}$(C$_2$)$_2$** and **P27$_{THS}$(C$_2$)$_2$** present. Furthermore, there is far less selectivity for ***c*-P18$_{THS}$** when **P9$_{THS}$(C$_2$)$_2$** is coupled in the presence of **T6**. Instead, we see ***c*-P9$_{THS}$** as the major product, with significant amounts of the shorter **P9$_{THS}$(C$_2$)$_2$**, **P18$_{THS}$(C$_2$)$_2$** and **P27$_{THS}$(C$_2$)$_2$** linear oligomers. This supports the previous evidence that the THS solubilizing group results in poorer yields of Vernier-templated nanorings, likely due to its large size.

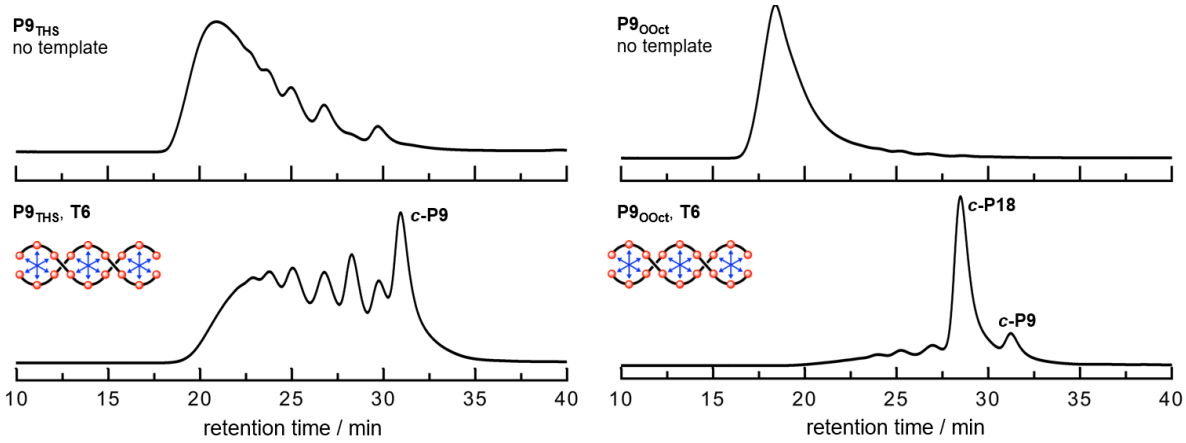

Figure 2.35: Analytical gel permeation chromatography (GPC) traces (500 nm) of crude reaction mixtures from coupling **P9$_{THS}$(C$_2$)$_2$** and **P9$_{OOct}$(C$_2$)$_2$** in the absence of a template (top) and in the presence of **T6** (bottom). Reaction conditions: Pd(PPh$_3$)$_2$Cl$_2$, CuI, 1,4-benzoquinone in CHCl$_3$ 20 °C, 17 h. Analytical GPC analysis performed using JAIGEL-3H-A (8 × 500 mm) and JAIGEL-4H-A (8 × 500 mm) columns in THF + 1% pyridine as eluent with a flow rate of 1.0 mL/min.

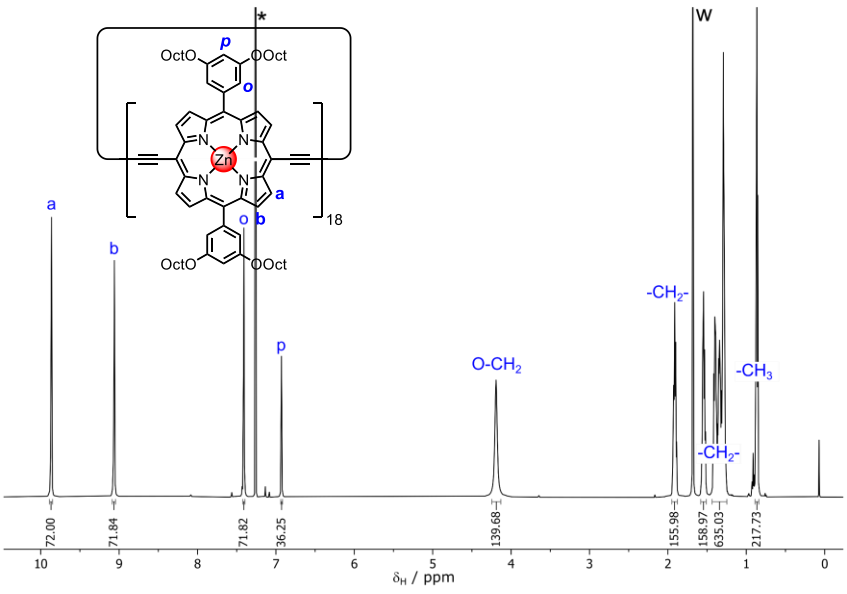

Figure 2.36: ^{1}H NMR spectrum of ***c*-P18$_{OOct}$** (600 MHz, CDCl$_3$ + 1% d$_5$-pyridine 298 K). * = CHCl$_3$; w = water. (right)

The high selectivity for ***c*-P18$_{OOct}$** from **P9$_{OOct}$(C$_2$)$_2$** and **T6** encouraged us to scale this reaction to obtain enough ***c*-P18$_{OOct}$** for on surface measurements. This reaction proceeded well on scale, yielding 4.3 mg ***c*-P18$_{OOct}$** from 10.0 mg **P9$_{OOct}$(C$_2$THS)$_2$**, which corresponds to a 46% yield. Figures 2.36 shows the ^{1}H NMR of this material.

2.5.2 Scanning Tunnelling Microscopy of c-P18$_{OOct}$

Scanning tunnelling microscopy (STM) has been used in numerous publications to investigate the size and geometry of porphyrin nanorings.[8-10, 43] In these studies the 3,5-bisoctyloxy solubilising aryl group was used as it is known to be particularly compatible with STM measurements. A sample of **c-P18$_{OOct}$** and the complex **c-P18$_{OOct}$·T18$_A$** (discussed later in this chapter) was sent to our collaborator Dr Alex Saywell at the University of Nottingham for imaging. The complex **c-P18$_{OOct}$·T18$_A$** unfortunately did not produce any meaningful data, however, images were successfully obtained for **c-P18$_{OOct}$** (Scheme 1).[8, 10]

Scheme 1a presents an STM image of a sample of ***c*-P18$_{OOct}$** in which we observe a single nanoring (white arrow), stack of two nanorings (black arrow) and a linear chain (red arrow). Scheme 1b confirms that the nanoring has exactly 18 porphyrin units. By analysing the height of the ring across the long and short axis (blue and red in Scheme 1c) we can determine the approximate length of these axis. By repeating this measurement over a number of nanorings we can obtain the plot shown in Scheme 1e, which informs us on the ellipticity of the nanoring on the surface. In this figure the blue arc represents combinations of long axis length (a) and short axis length (b) that produce a circumference of 21nm, the average of **c-P18$_{OOct}$.** The solid black line represents a perfectly cyclic nanoring, with the dotted lines representing varying degrees of ellipticity, where f = (a-b)/a. We observe that on surface ***c*-P18$_{OOct}$** predominantly adopts an elliptical geometry with f = 0.2.

STM data from both the nanoring complexes **c-P18$_{OOct}$·T18$_A$** and **c-P18$_{OOct}$·T18$_B$** would have allowed us to draw further comparisons between the geometries of these complexes, in comparison to the information gained from the computational studies discussed earlier in this

chapter and in Chapter 3. Additionally, probing the molecular orbitals of these complexes using STM[43] and comparing the results would have further enriched our study of these materials. Regrettably, the poor data obtained from **c-P18$_{OOct}$·T18$_{A}$** prohibited us from taking these measurements and therefore limits the utility of this STM study on our exploration of the global aromaticity of ***c*-P18$_{OOct}$.**

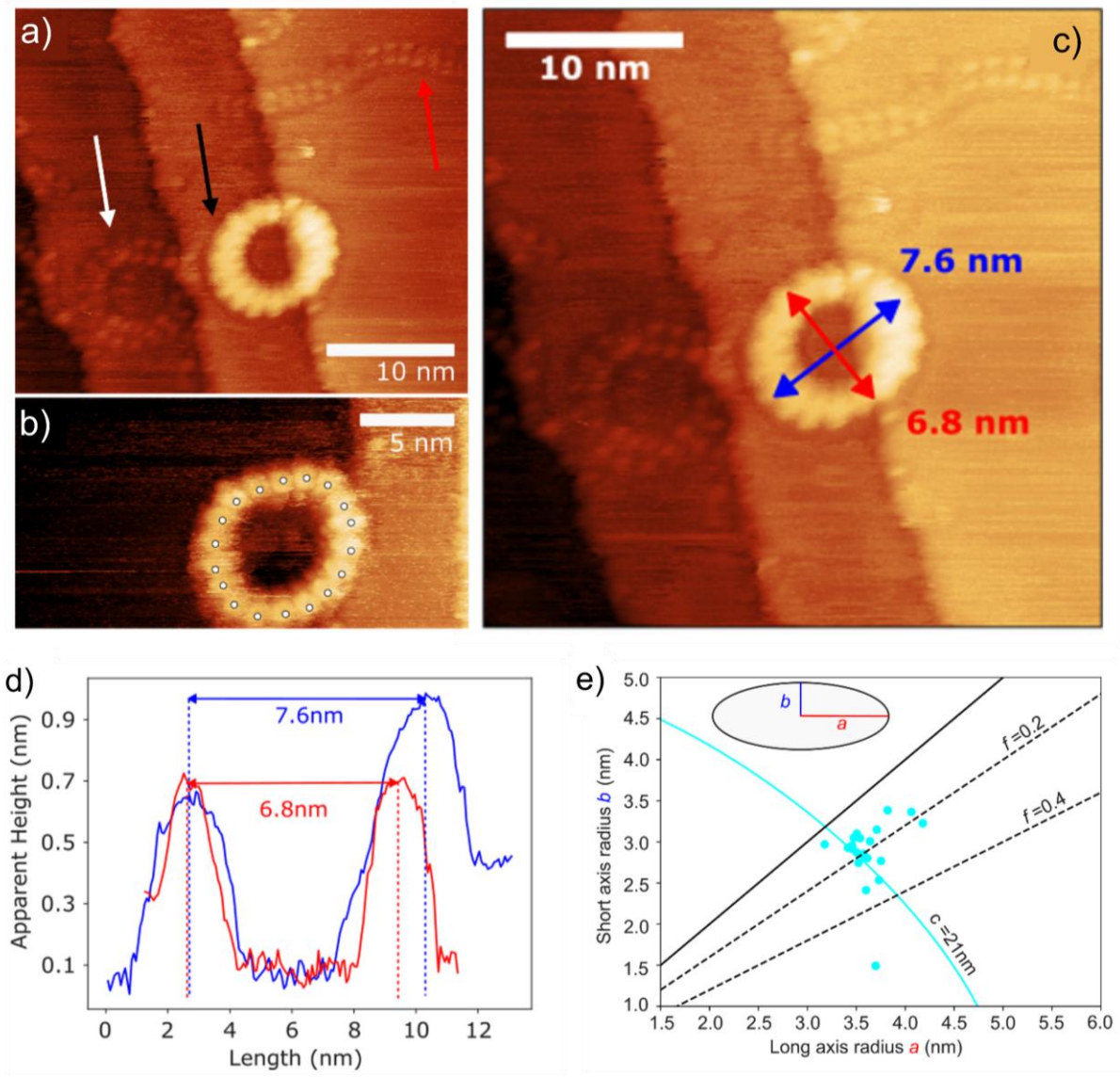

Scheme 1. Collection of STM data obtained from ***c*-P18$_{OOct}$** which was deposited by electrospray ionization onto an Au 111 surface. (a-c) STM images of ***c*-P18$_{OOct}$.** (d) Height profiles of the long and short axis of ***c*-P18$_{OOct}$** shown in (c). (e) Comparison of the short and long axis in a sample of ***c*-P18$_{OOct}$.** The blue line represents length combinations resulting in a diameter of 21nm. The solid black line represents a perfectly circular nanoring. Dotted black lines represent elliptical nanorings where f = (a-b)/a.

2.5.3 Standard Template-directed Approach with $T18_{A/B}$

As discussed in Section 2.3.4, the oxidative NMR experiments used to probe global aromaticity must be conducted on ***c*-P18$_{THS}$**, which is obtained in poor yields from the Vernier-template directed route with **P9$_{THS}$(C$_2$)$_2$** and **T6**. To resolve this, we chose to explore the standard template directed approach using **P9$_{THS}$(C$_2$)$_2$** with both **T18$_A$** and **T18$_B$** (Figure 2.37). Analogous experiments were also performed with **P9$_{OOct}$(C$_2$)$_2$**. The results of these experiments are presented in Figure 2.38.

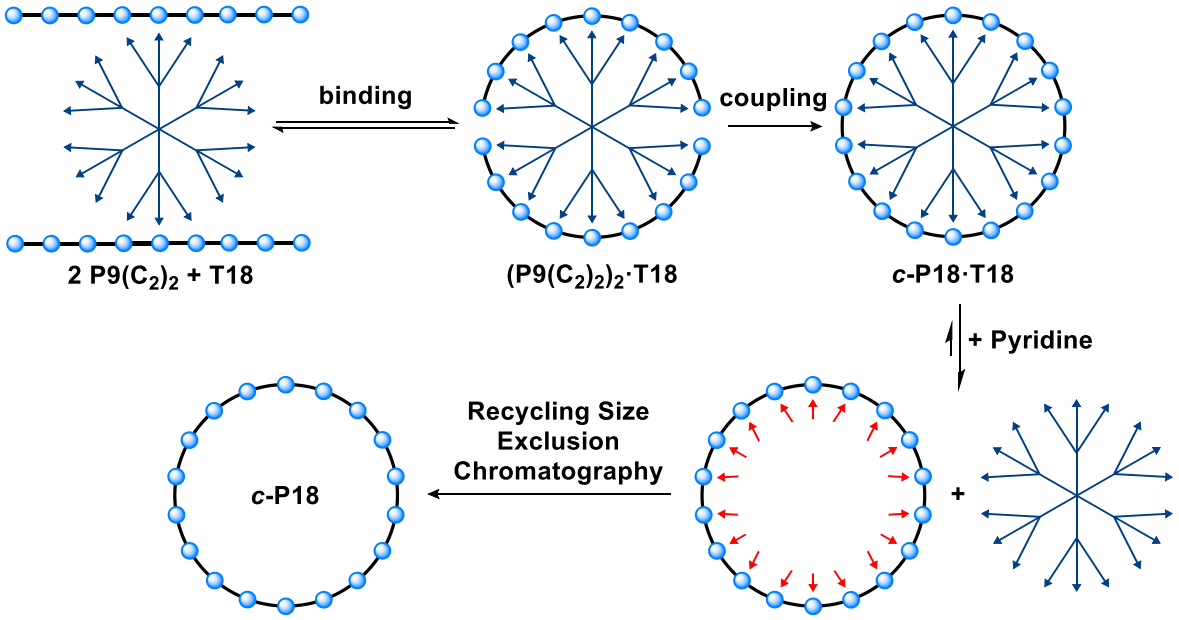

Figure 2.37: Template-directed synthesis of ***c*-P18** using **T18** and **P9(C$_2$)$_2$**.

From these test macrocyclization reactions, we observe that regardless of the solubilizing group, **T18$_A$** and **T18$_B$** are selective for the synthesis of ***c*-P18**. The selectivity for ***c*-P18** appears to be higher with the **OOct** solubilizing group, however, the ***c*-P18$_{THS}$** synthesis is hindered by incomplete coupling of the THS oligomers (as seen in the template free coupling), which we expect is due to degradation or side reactions of the free acetylene groups. A **P9$_{THS}$** or **P18$_{THS}$** oligomer with one end deactivated can still oligomerize at the other end of the chain, but can never form cyclic species, even if fully bound to a **T18** template. This rationale may explain the higher abundance of all linear species in the test macrocyclization reactions using THS oligomers.

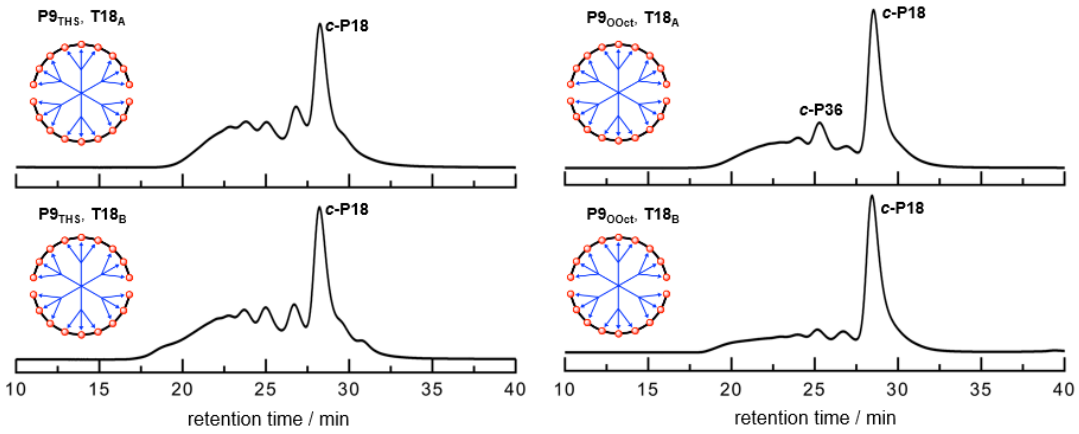

Figure 2.38: Analytical gel permeation chromatography (GPC) traces (500 nm) of crude reaction mixtures from coupling **P9$_{THS}$(C$_2$)$_2$** (left) and **P9$_{OOct}$(C$_2$)$_2$** (right) in the presence of **T18$_A$** (top) or **T18$_B$** (bottom). Reaction conditions: Pd(PPh$_3$)$_2$Cl$_2$, CuI, 1,4-benzoquinone in CHCl$_3$ 20 °C, 17 h. Analytical GPC analysis performed using JAIGEL-3H-A (8 × 500 mm) and JAIGEL-4H-A (8 × 500 mm) columns in THF + 1% pyridine as eluent with a flow rate of 1.0 mL/min

Encouraged by the promising analytical scale macrocyclization reactions, I scaled up the synthesis using 16.5 mg **P9$_{THS}$(C$_2$)$_2$** and 6.1 mg **T18$_A$**, which yielded 4.0 mg ***c*-P18$_{THS}$** corresponding to a yield of 25%. Due to the dramatically higher polarity of **T18$_A$** compared to every other species in the crude reaction mixture, a short silica plug of the crude in CHCl$_3$ + 5% pyridine elutes everything but **T18$_A$**, which is retained on the column. **T18$_A$** can then be recovered by flushing the silica plug with an 84:15:1 mixture of CHCl$_3$:MeOH:^{t}BuNH$_2$. This process yielded 4.9 mg of **T18$_A$**, which is 80% of the material used in the reaction.

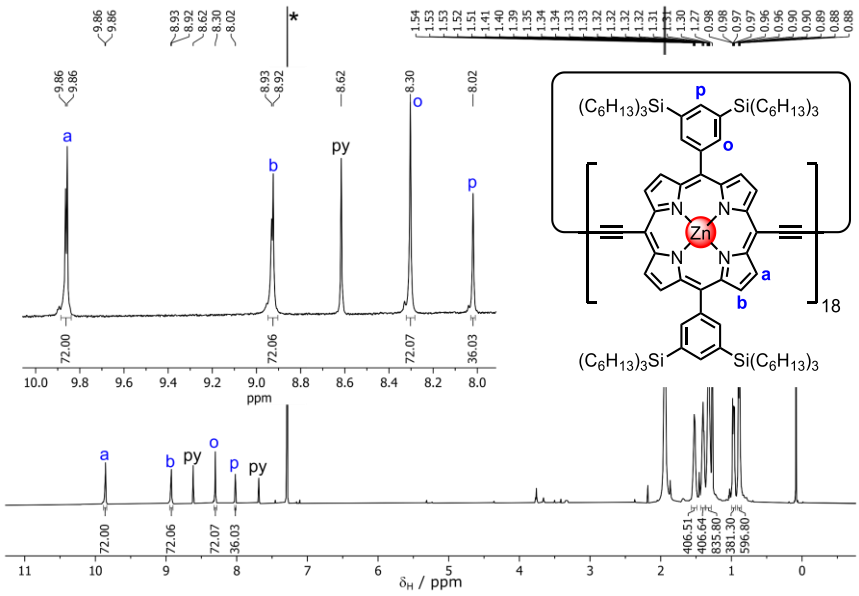

Figure 2.39: ^{1}H NMR spectrum of ***c*-P18$_{THS}$** (600 MHz, CDCl$_3$, 298 K). * = CHCl$_3$; py = pyridine

2.6 Formation and Characterization of c-P18·T18$_{A/B}$

2.6.1 ^{19}F Formation Titration of *c*-P18$_{THS}$·T18$_{A}$

With **T18$_A$**, **T18$_B$**, ***c*-P18$_{OOct}$** and ***c*-P18$_{THS}$** in hand, I next investigated forming the ***c*-P18·T18** complexes by ^{19}F NMR, to ensure that an exact 1:1 stoichiometry was reached. Figure 2.40 shows the ^{19}F NMR data obtained from titrating **T18$_A$** into a sample of ***c*-P18$_{THS}$**, as an example of one of these formation titrations. As expected, free ***c*-P18$_{THS}$** has no ^{19}F signal, but as **T18$_A$** is added a peak grows in representing **T18$_A$** bound inside the ***c*-P18** nanoring. At 1.05 Eq of **T18$_A$** a second peak is observed at exactly the same ppm as free **T18$_A$**. A short silica column of this mixture in 1:1 chloroform:pentane elutes only the 1:1 complex, as excess **T18$_A$** is retained on the column**.** This process was then repeated with ***c*-P18$_{THS}$** + **T18$_B$**, and ***c*-P18$_{OOct}$** + **T18$_A$** to obtain the complexes discussed in the following three sub-sections.

Figure 2.41 demonstrates the shielding effect the local ring current of the porphyrin units has on **T18$_A$** proton environments. Those closest to the porphyrin (Red, α-Pyridyl-N) are most significantly shielded (Δδ>-5 ppm). This extent of shielding decays as a function of distance to the porphyrin as shown in Figure 2.42.

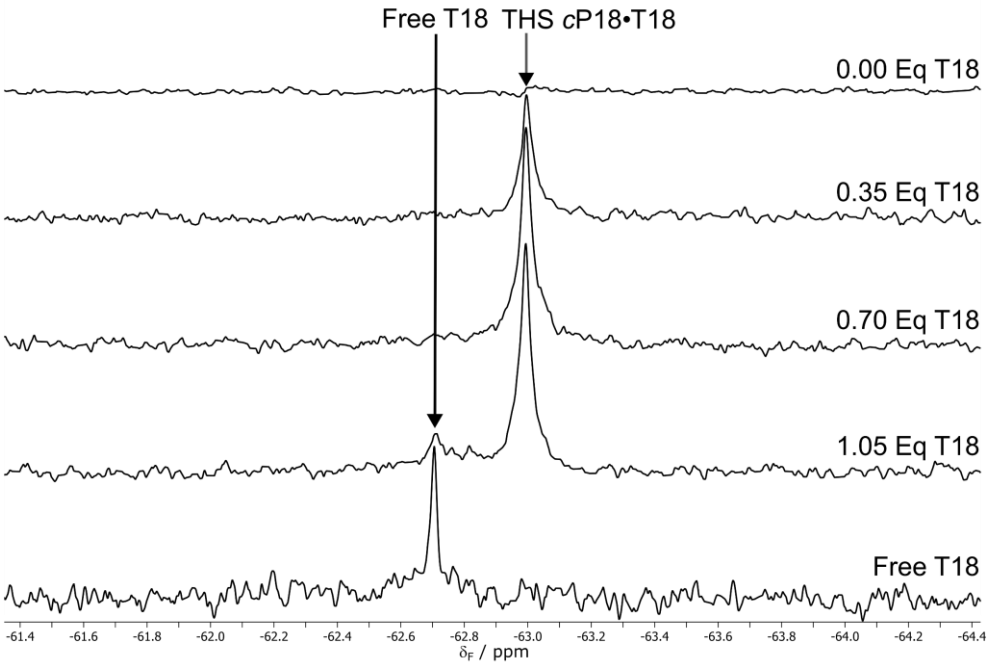

Figure 2.40: ^{19}F NMR spectra of ***c*-P18$_{THS}$** with varying amounts of **T18$_A$** (377 MHz, $CDCl_3$, 298 K).

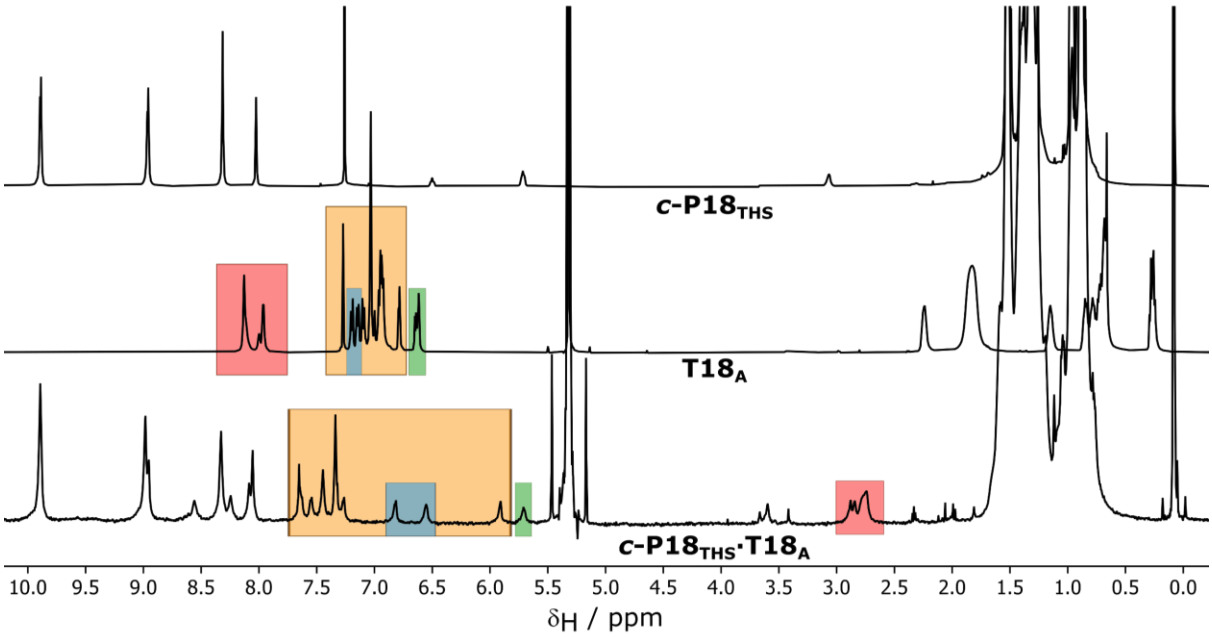

Figure 2.41: ^{1}H NMR spectra of ***c*-P18$_{THS}$** (top, 500 MHz, $CDCl_3$, 298 K), **T18$_A$** (middle, 600 MHz, $C_2D_2Cl_4$, 393 K) and ***c*-P18$_{THS}$·T18$_A$** (bottom, 500 MHz, CD_2Cl_{32}, 298 K).

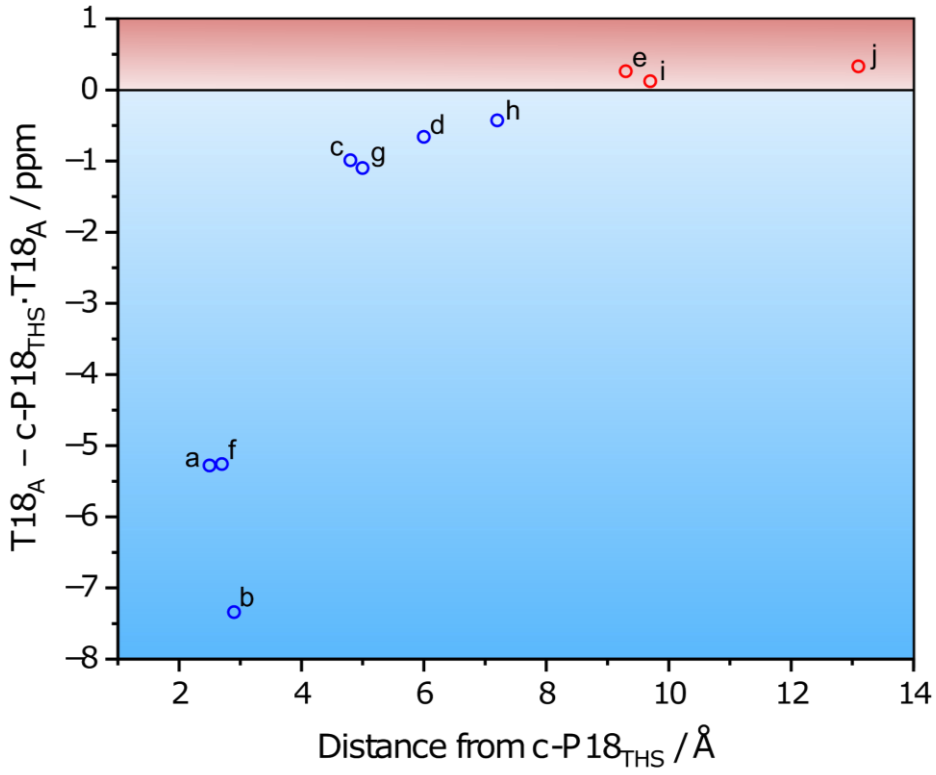

Figure 2.42: Changes in the ppm values of proton environments in **T18$_A$** after binding to the ***c*-P18$_{THS}$** nanoring, shown against their distance from ***c*-P18$_{THS}$** (taken from the PM7 optimised geometry of ***c*-P18$_{THS}$·T18$_A$**)

2.6.2 NMR and MALDI of *c*-P18$_{THS}$·T18$_A$

Presented in Figures 2.44 - 2.47 are the assigned ^{1}H and NOESY spectrum of ***c*-P18$_{THS}$·T18$_A$** along with a MALDI spectrum and chemical structure of the complex**.** Figure 2.43 highlights the important couplings identified from the COSY and NOESY NMR spectra.

The assignment of this complex began from protons a, b and f, which are dramatically shielded when bound inside the ***c*-P18** nanoring, as previously discussed. The COSY spectrum was particularly useful for assigning these protons along with the other protons on the T18$_A$ template. The template protons can also be distinguished from the ***c*-P18** protons as the ***c*-P18** protons do not change much due to binding of **T18$_A$**, as seen in Figure 2.41.

The NOESY spectrum was useful for several environments: (1) identification of proton j by coupling to proton e. (2) identification of α_{in} and α' environments by coupling to either f or a. (3) identification of α_{out} by coupling to $\alpha_{in.}$ (4) identification of protons n and m by strong coupling to Ar-CH_2.

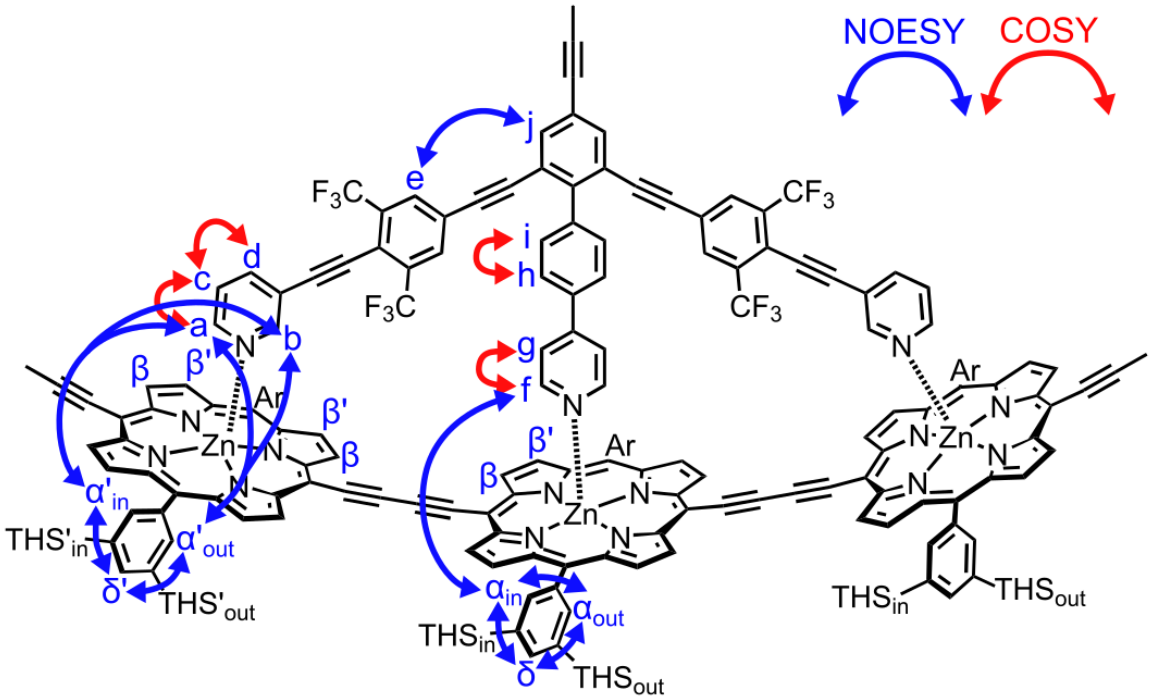

Figure 2.43: Chemical structure of **T3$_A$** fragment of **T18$_A$** in ***c*-P18$_{THS}$·T18$_A$** identifying important COSY and NOESY correlations.

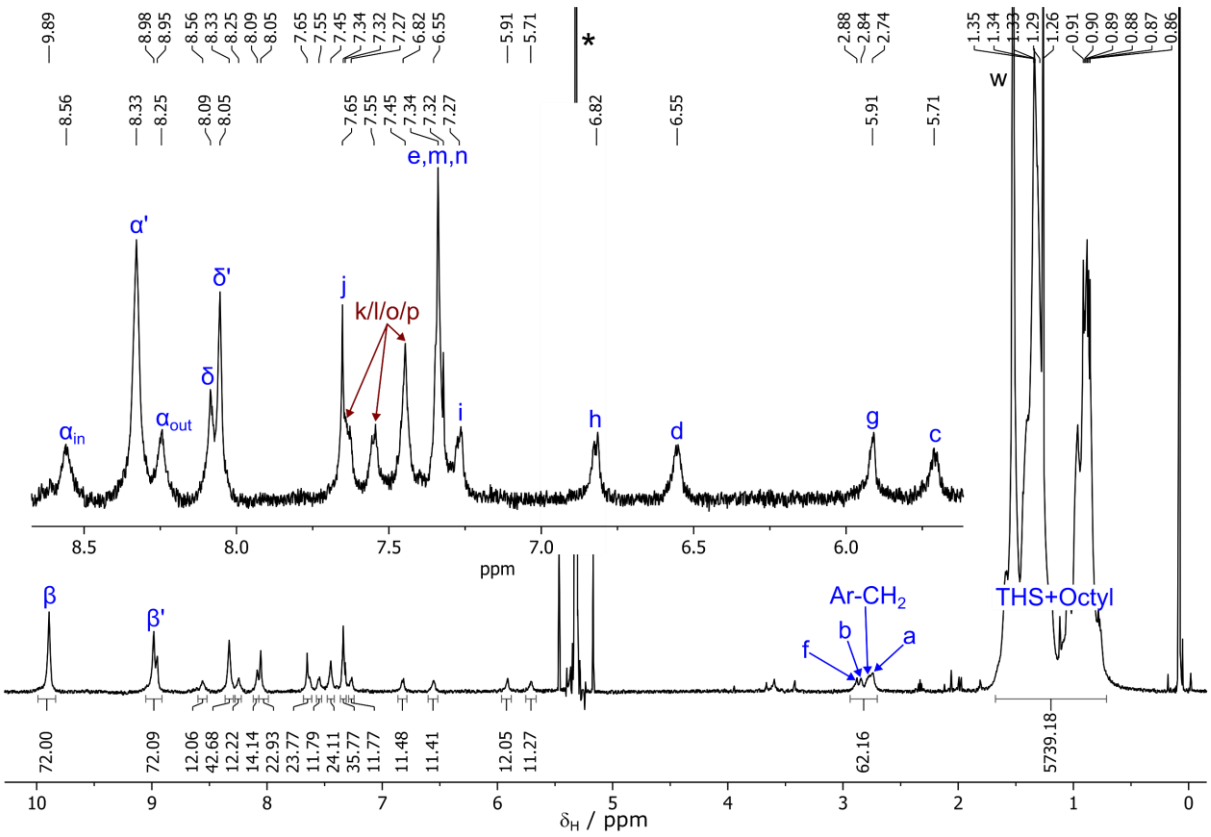

Figure 2.44: ^{1}H NMR spectra of ***c*-P18$_{THS}$·T18$_{A}$** (600 MHz, CD_2Cl_2, 298 K). * = CD_2Cl_2; w = water

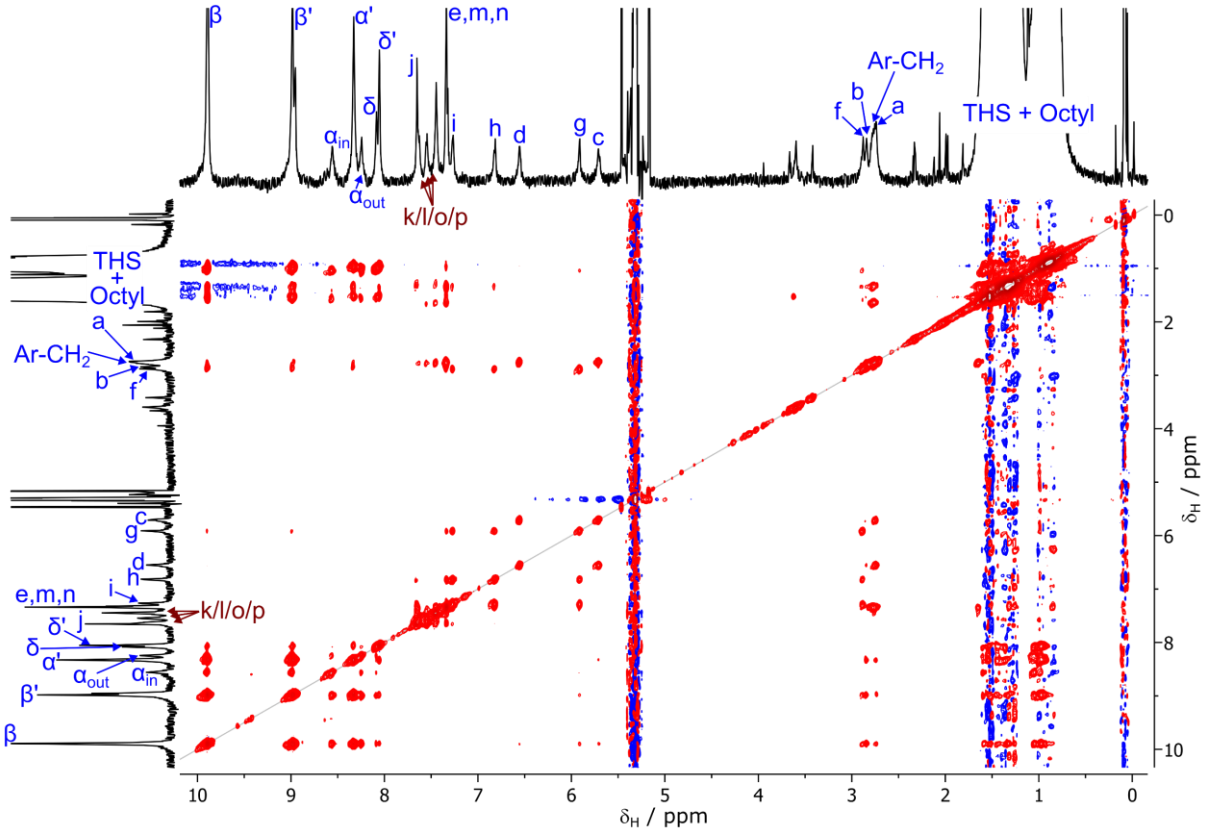

Figure 2.45: ^{1}H NOESY NMR spectra of ***c*-P18$_{THS}$·T18$_{A}$** (600 MHz, CD_2Cl_2, 298 K). * = CD_2Cl_2; w = water

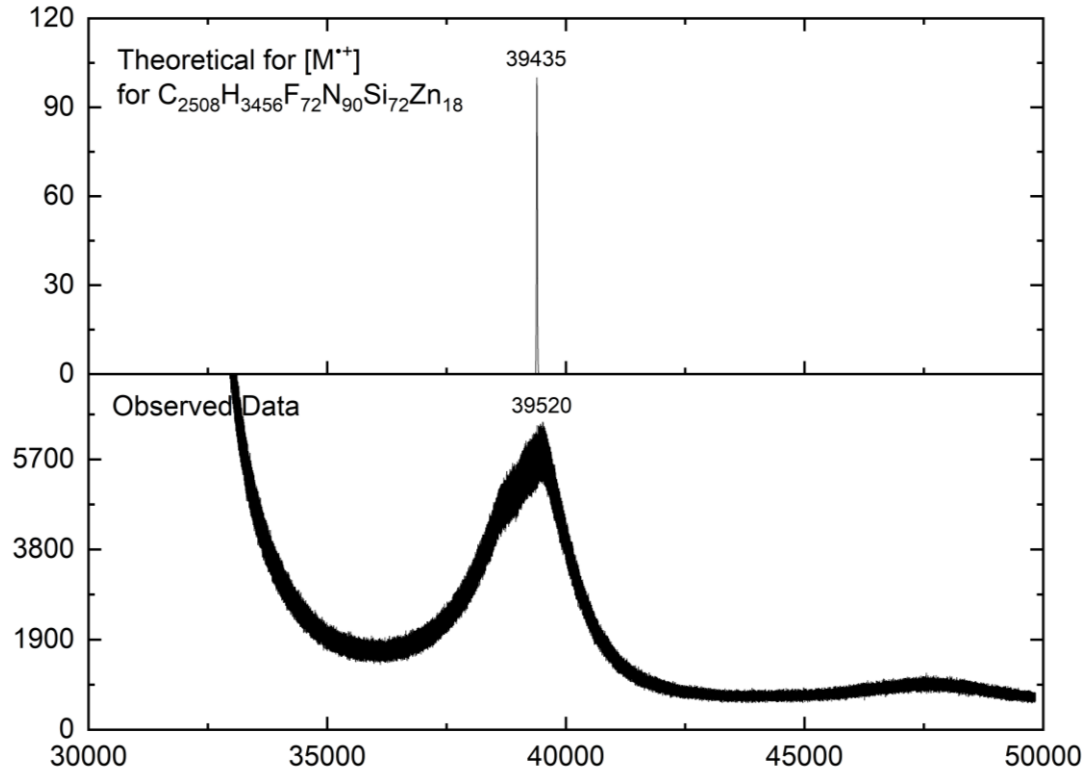

Figure 2.46: MALDI mass spectrum of ***c*-P18$_{THS}$·T18$_{A}$** (Obtained using dithranol as a matrix)

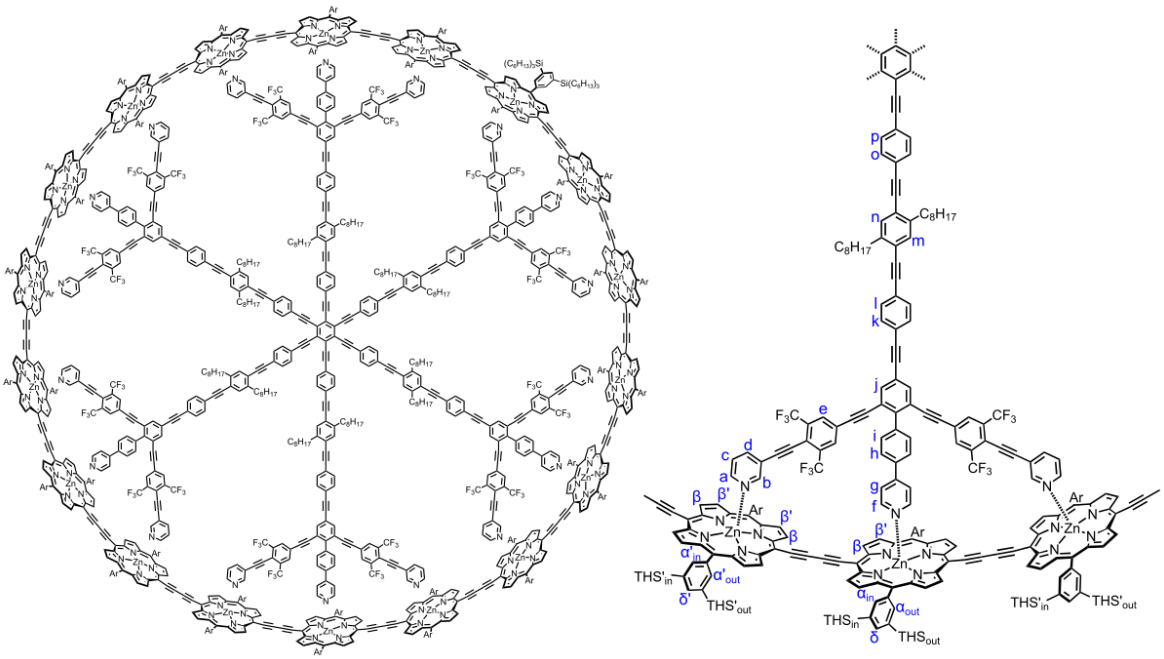

Figure 2.47: Chemical structure of ***c*-P18$_{THS}$·T18$_{A}$**

2.6.3 NMR and MALDI of *c*-P18$_{THS}$·T18$_B$

Presented in Figures 2.49 and 2.52 are the assigned ^{1}H and NOESY spectrum of ***c*-P18$_{THS}$·T18$_A$** along with a MALDI spectrum and chemical structure of the complex. Figure 2.48 highlights the important couplings identified by COSY and NOESY. As with ***c*-P18$_{THS}$·T18$_A$**, COSY was primarily useful for identifying the order of template protons a-b and d-g. NOESY was again particularly useful for identifying several environments: (1) β and β' groups first assigned by comparison to ***c*-P18$_{THS}$·T18$_A$** (β more deshielded due to proximity to acetylene). Next, β, β_{in} and β_{out} distinguished by NOESY as only β_{in} couples to all members of the group (β and β_{out} show no NOESY correlation). Finally, β' group can be assigned by COSY correlations to β group members. (2) identification of α' by NOESY to β_{in}, β'_{in}, β_{out} and β'_{out}. (3) identification of α_{in} and α_{out} by strength of NOESY to proton d. (4) identification of protons l and k by strong coupling to Ar-CH_2. One interesting difference between ***c*-P18$_{THS}$·T18$_A$** and ***c*-P18$_{THS}$·T18$_B$** is the splitting of the β signals present in ***c*-P18$_{THS}$·T18$_B$**. The structure of ***c*-P18$_{THS}$·T18$_B$** in the PM7 optimized model in Figure 2.9 (Section 2.2) show the nanoring to be significantly distorted from the ideal circular geometry. The splitting of the β signals supports this distorted geometry, as the central (β/β') and peripheral (β_{in}/β'_{in}/β_{out}/β'_{out}) porphyrin units are in more unique environments, which leads to β/β'/β_{in}/β'_{in}/β_{out}/β'_{out} all appearing at different ppm values.

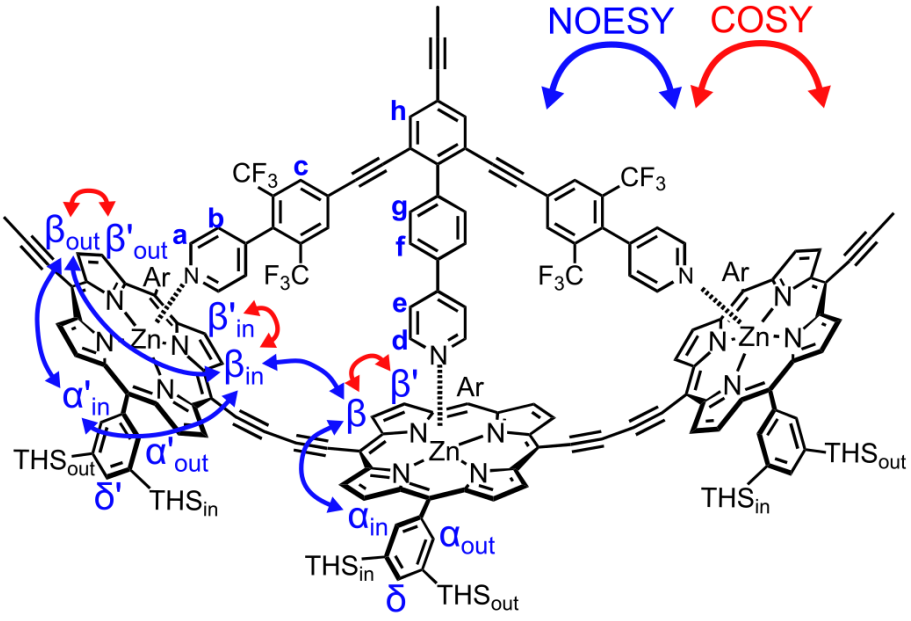

Figure 2.48: Structure of **T3$_B$** fragment of **T18$_B$** in ***c*-P18$_{THS}$·T18$_B$** identifying important COSY and NOESY correlations

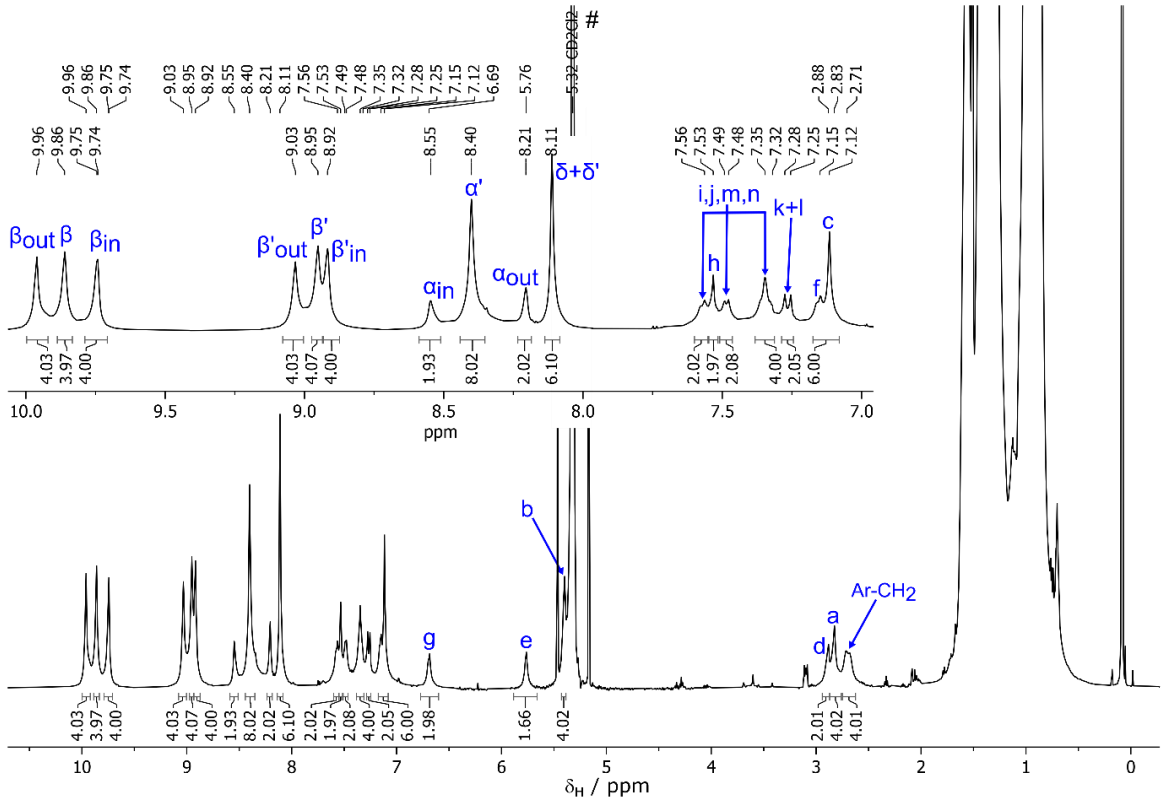

Figure 2.49: ^{1}H NMR spectra of ***c*-P18$_{THS}$·T18$_{B}$** (600 MHz, CD_2Cl_2, 298 K). # = CD_2Cl_2

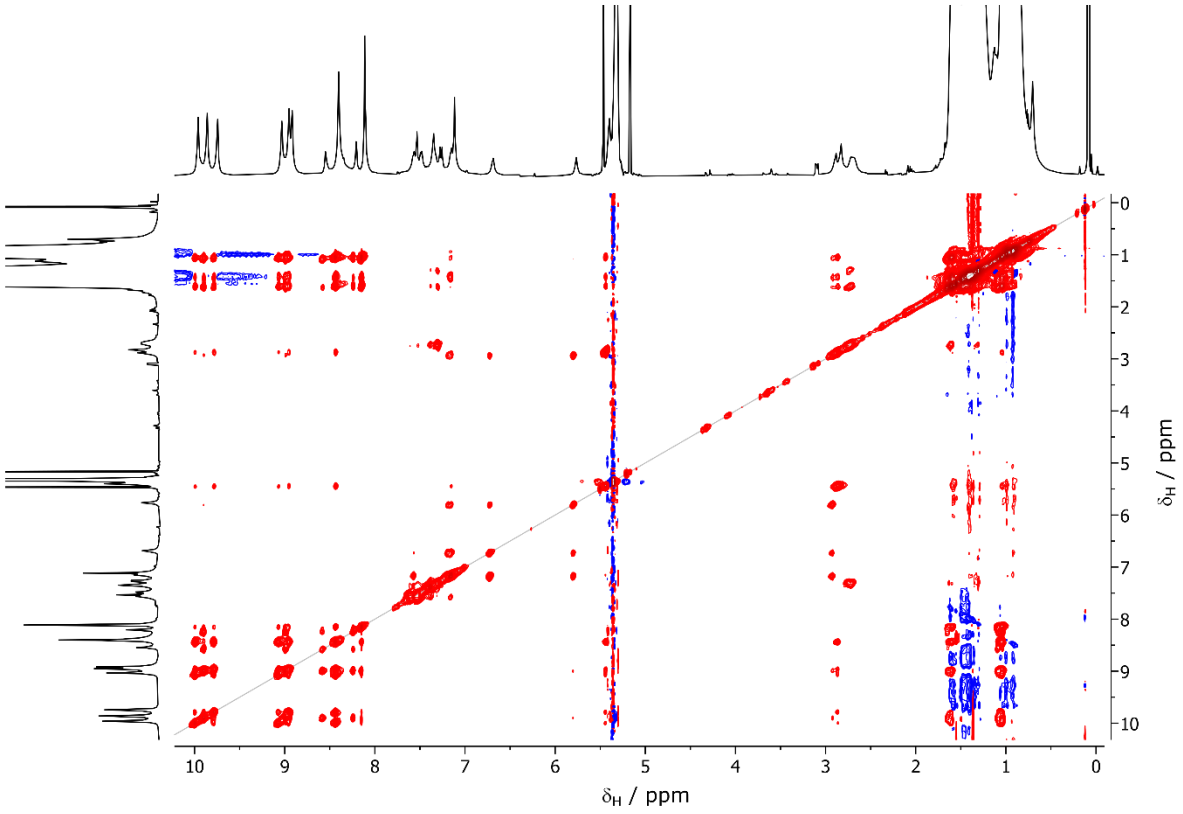

Figure 2.50: ^{1}H NOESY NMR spectra of ***c*-P18$_{THS}$·T18$_{B}$** (600 MHz, CD_2Cl_2, 298 K). # = CD_2Cl_2.

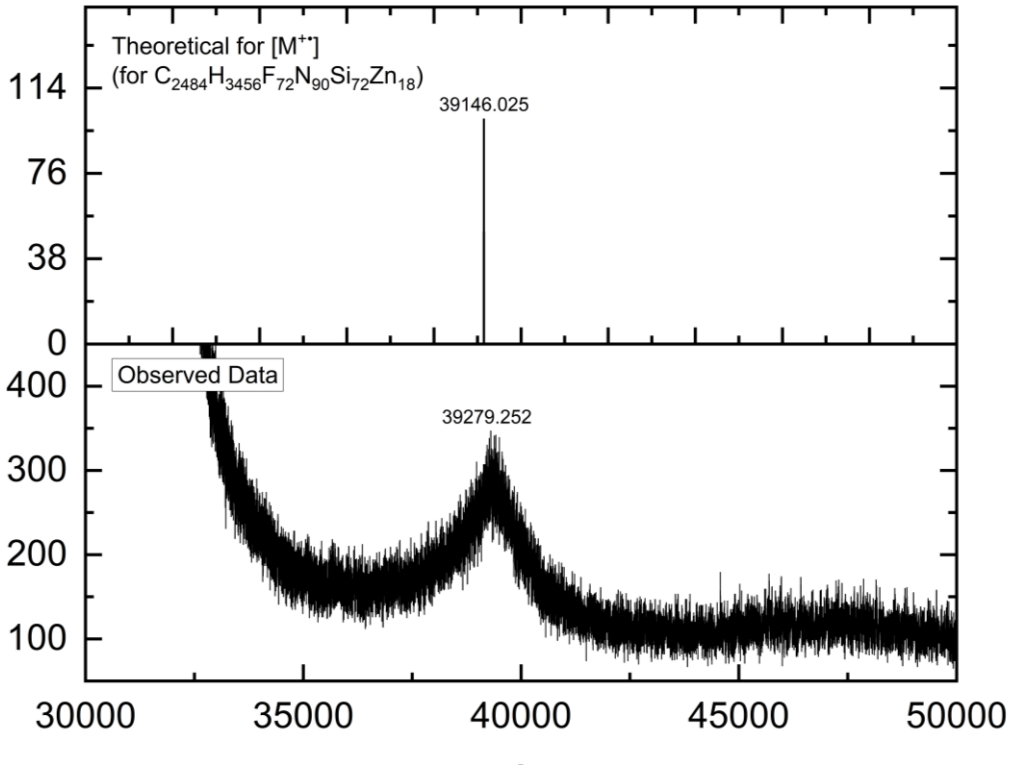

Figure 2.51: MALDI mass spectrum of ***c*-P18$_{THS}$·T18$_{B}$** (Obtained using dithranol as a matrix)

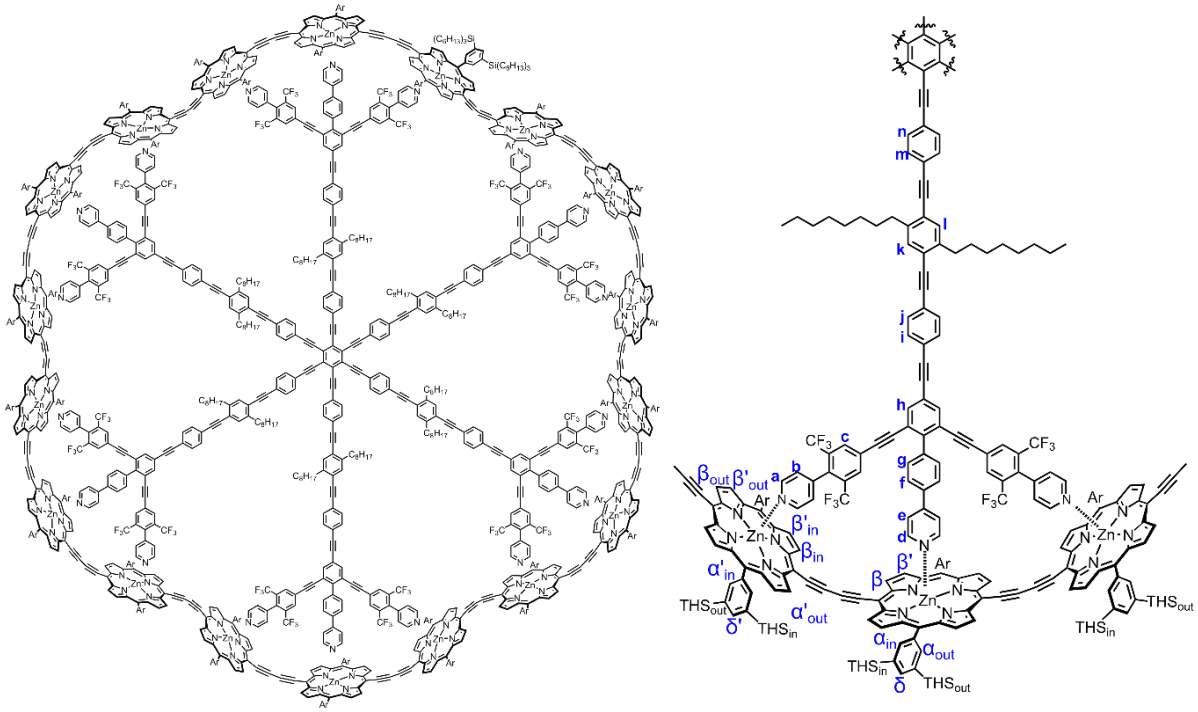

Figure 2.52: Chemical structure of ***c*-P18$_{THS}$·T18$_{B}$**

2.6.4 NMR and MALDI of *c*-P18$_{OOct}$·T18$_A$

Presented in Figures 2.54 and 2.57 are the assigned ^{1}H and NOESY spectrum of ***c*-P18$_{OOct}$·T18$_A$** along with a MALDI spectrum and chemical structure of the complex. Figure 2.53 highlights the important couplings identified by COSY and NOESY. As with ***c*-P18$_{THS}$·T18$_A$** and ***c*-P18$_{THS}$·T18$_B$**, COSY was primarily useful for identifying the order of template protons a-d and f-i. NOESY was yet again particularly useful for identifying several environments, but of particular interest in this specific complex is the assignment of the OCH_{2in} (from $OOct_{in}$) environment, as identified by a NOESY correlation to α_{in}, which itself was assigned through NOESY correlations to both proton f and g (α_{out} only correlates to proton f).

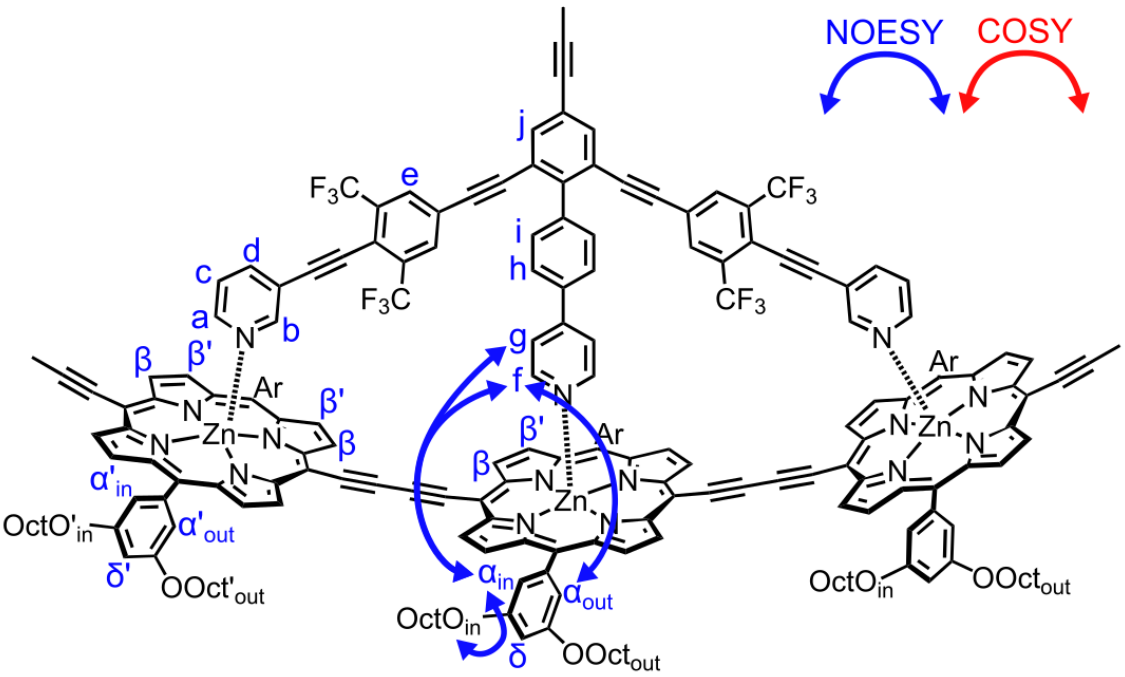

Figure 2.53: Chemical structure of **T3$_A$** fragment of **T18$_A$** in ***c*-P18$_{OOct}$·T18$_A$** identifying important COSY and NOESY correlations

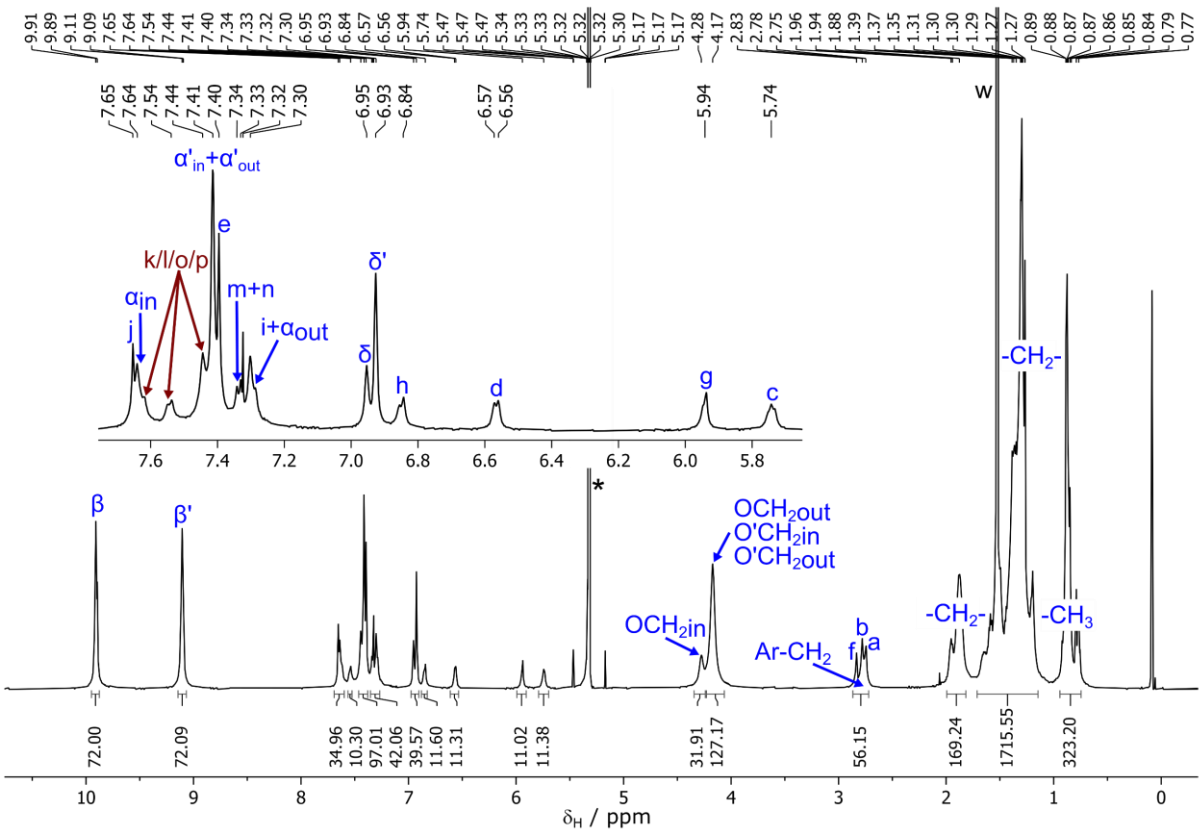

Figure 2.54: ^{1}H NMR spectra of ***c*-P18$_{OOct}$·T18$_{A}$** (600 MHz, CD_2Cl_2, 298 K). * = CD_2Cl_2, w = water.

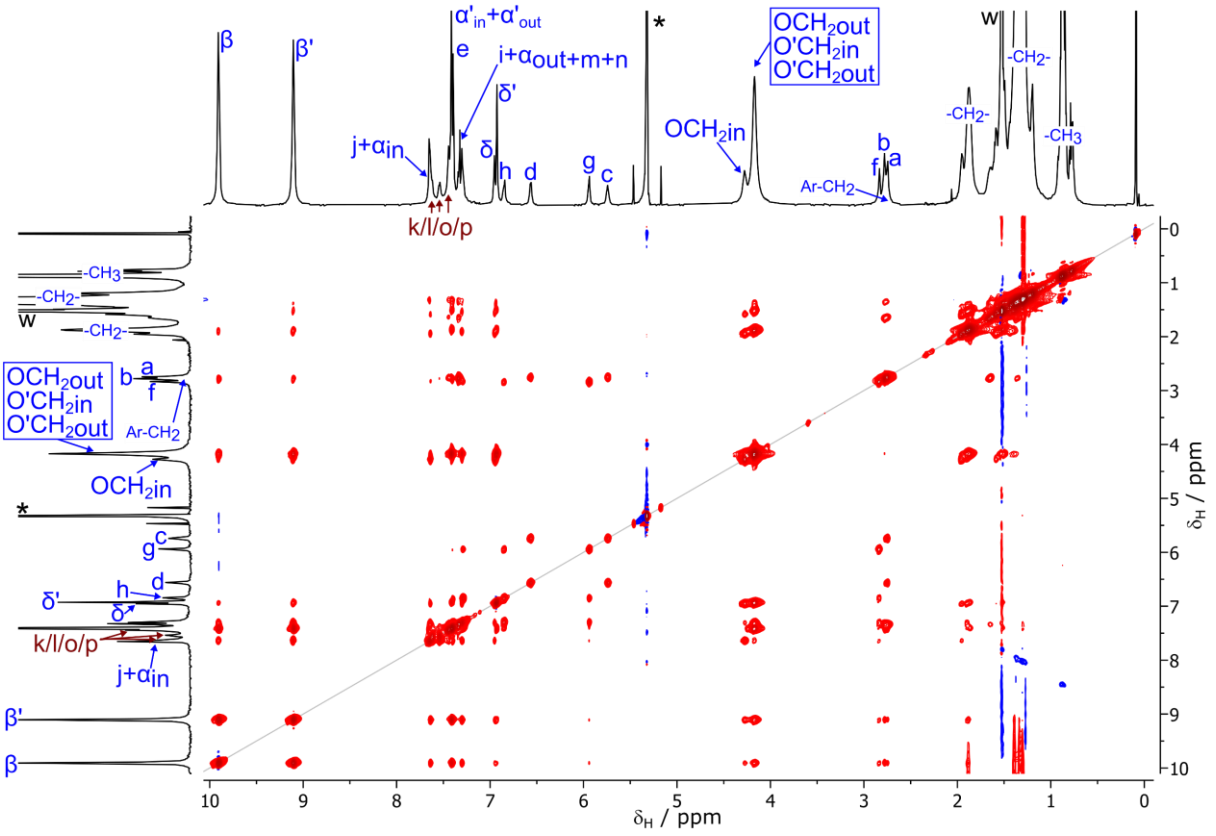

Figure 2.55: ^{1}H NOESY NMR spectra of ***c*-P18$_{OOct}$·T18$_{A}$** (600 MHz, CD_2Cl_2, 298 K). * = CD_2Cl_2, w = water.

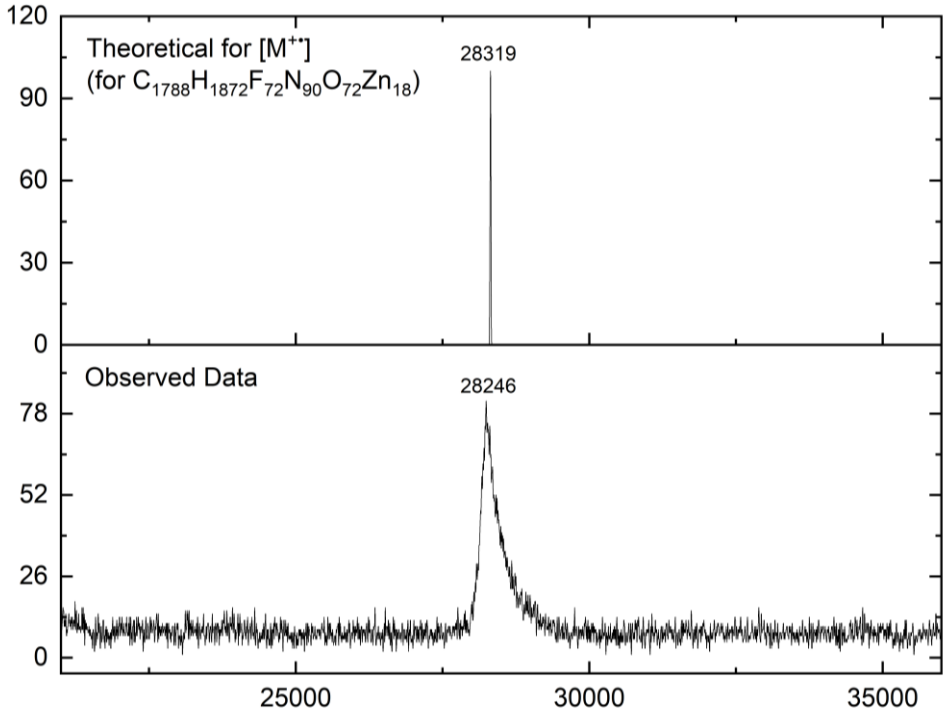

Figure 2.56: MALDI mass spectrum of ***c*-P18$_{OOct}$·T18$_{A}$** (Obtained using dithranol as a matrix)

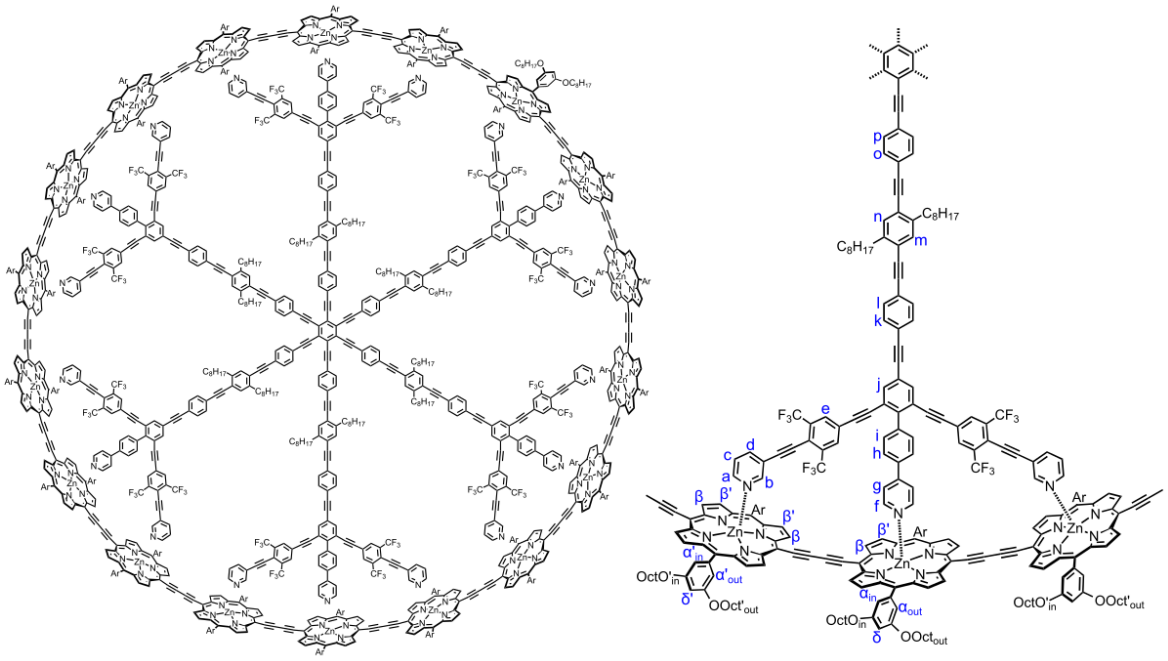

Figure 2.57: Chemical structure of ***c*-P18$_{OOct}$·T18$_{A}$**

2.7 Summary of Results

In this chapter I first outlined our motivation for studying global aromaticity in large π conjugated macrocycles, as this work contributes to our understanding of the link between molecular aromaticity and persistent ring currents in mesoscopic superconducting rings.

I next discussed the rational design process we used to identify the most promising template design for binding **c-P18** in a cyclic geometry, with all porphyrin units parallel to one another. Initial design choices in this process were informed by the structural information obtained from crystal structures of previous template·nanoring complexes. Semi-empirical and DFT methods were then used to obtain the optimised geometries of these designs bound to porphyrin species, which were assessed, and the most suitable template designs selected for synthesis.

Following this, I have outlined the total synthesis of two template designs: **T18$_{A}$** and **T18$_{B}$**. These templates are synthesised from 3 key intermediates: **T3$_{A/B}$**, linker (**2.19**/**2.33**) and core (**2.15**). The combination of these components to deliver clean **T18$_{A/B}$** encountered some difficulties, primarily due to Glaser coupling of the intermediates out-competing the desired Sonogashira coupling. This was resolved by swapping terminal aryl-bromide groups (**2.28**) for more reactive aryl-iodides (**2.36**), which allowed for the syntheses of both **T18$_{A}$** and **T18$_{B}$** in good yields.

With **T18$_{A}$** and **T18$_{B}$** in hand, I then presented the syntheses of both OOct and THS solubilised butadiyne-linked 9-porphyrin oligomers and described the template-directed synthesis of ***c*-P18$_{OOct}$** and ***c*-P18$_{THS}$** using these materials. In summary, synthesis of ***c*-P18$_{OOct}$** can be achieved in good yield using the Vernier-template directed approach with **T6** and **P9$_{OOct}$(C2)$_{2}$**, however, yields of ***c*-P18$_{THS}$** with this method are poor. We attribute this to the bulkiness of the THS group preventing formation of the Vernier-complex. Instead, the standard route using **T18$_{A/B}$** can be used to deliver ***c*-P18$_{THS}$** in good yields.

Finally, I presented the formation of the ***c*-P18$_{THS}$·T18$_{A}$** complex by ^{1}H and ^{19}F NMR and discussed the characterisation of the ***c*-P18$_{THS}$·T18$_{A}$**, ***c*-P18$_{THS}$·T18$_{B}$** and ***c*-P18$_{OOct}$·T18$_{A}$** complexes by NMR.

In the following chapter I will present and analyse the experiments conducted to probe the photophysical properties of these complexes, along with an investigation into the binding between **T18$_{A/B}$** and **c-P18$_{THS}$** and the results of the oxidative NMR titrations used to probe global aromaticity in the ***c*-P18$_{THS}$·T18$_{A/B}$** complexes.

2.8 References

1. H. Ottosson, *Chemical Science*, 2023, **14**, 5542-5544.
2. G. Merino, M. Solà, I. Fernández, C. Foroutan-Nejad, P. Lazzeretti, G. Frenking, H. L. Anderson, D. Sundholm, F. P. Cossío, M. A. Petrukhina, J. Wu, J. I. Wu and A. Restrepo, *Chemical Science*, 2023, **14**, 5569-5576.
3. Z. Chen, C. S. Wannere, C. Corminboeuf, R. Puchta and P. v. R. Schleyer, *Chemical Reviews*, 2005, **105**, 3842-3888.
4. M. Jirásek, H. L. Anderson and M. D. Peeks, *Accounts of Chemical Research*, 2021, **54**, 3241-3251.
5. M. Rickhaus, M. Jirasek, L. Tejerina, H. Gotfredsen, M. D. Peeks, R. Haver, H.-W. Jiang, T. D. W. Claridge and H. L. Anderson, *Nature Chemistry*, 2020, **12**, 236-241.
6. M. Vitek, J.-R. Deng, H. L. Anderson and I. Rončević, *ACS Nano*, 2025, **19**, 1405-1411.
7. P. S. Bols and H. L. Anderson, *Accounts of Chemical Research*, 2018, **51**, 2083-2092.
8. H. Gotfredsen, J.-R. Deng, J. M. Van Raden, M. Righetto, J. Hergenhahn, M. Clarke, A. Bellamy-Carter, J. Hart, J. O'Shea, T. D. W. Claridge, F. Duarte, A. Saywell, L. M. Herz and H. L. Anderson, *Nature Chemistry*, 2022, **14**, 1436-1442.
9. M. A. Majewski, W. Stawski, J. M. Van Raden, M. Clarke, J. Hart, J. N. O'Shea, A. Saywell and H. L. Anderson, *Angewandte Chemie International Edition*, 2023, **62**.
10. J. M. Van Raden, J.-R. Deng, H. Gotfredsen, J. Hergenhahn, M. Clarke, M. Edmondson, J. Hart, J. N. O'Shea, F. Duarte, A. Saywell and H. L. Anderson, *Angewandte Chemie International Edition*, 2024, **63**.
11. C. E. Colwell, T. W. Price, T. Stauch and R. Jasti, *Chemical Science*, 2020, **11**, 3923-3930.
12. A. C. Bleszynski-Jayich, W. E. Shanks, B. Peaudecerf, E. Ginossar, F. von Oppen, L. Glazman and J. G. E. Harris, *Science*, 2009, **326**, 272-275.
13. Y. Aharonov and D. Bohm, *Physical Review*, 1959, **115**, 485-491.
14. R. L. Fagaly, *Review of Scientific Instruments*, 2006, **77**.
15. J. Bardeen, L. N. Cooper and J. R. Schrieffer, *Physical Review*, 1957, **108**, 1175-1204.
16. B. Elsaka, O. Francis and J. Kusche, *Pure and Applied Geophysics*, 2023, **180**, 629-641.
17. D. Pines and C. P. Slichter, *Science*, 1972, **178**, 489-491.
18. D. Loss and P. Goldbart, *Physical Review B*, 1991, **43**, 13762-13765.
19. N. A. J. M. Kleemans, I. M. A. Bominaar-Silkens, V. M. Fomin, V. N. Gladilin, D. Granados, A. G. Taboada, J. M. García, P. Offermans, U. Zeitler, P. C. M. Christianen, J. C. Maan, J. T. Devreese and P. M. Koenraad, *Physical Review Letters*, 2007, **99**, 146808.
20. F. London, *C.R. Acad. Sci*, 1937, **205**, 28-30.
21. M. J. Frisch, G. W. Trucks, H. B. Schlegel, G. E. Scuseria, M. A. Robb, J. R. Cheeseman, G. Scalmani, V. Barone, G. A. Petersson, H. Nakatsuji, X. Li, M. Caricato, A. V. Marenich, J. Bloino, B. G. Janesko, R. Gomperts, B. Mennucci, H. P. Hratchian, J. V. Ortiz, A. F. Izmaylov, J. L. Sonnenberg, Williams, F. Ding, F. Lipparini, F. Egidi, J. Goings, B. Peng, A. Petrone, T. Henderson, D. Ranasinghe, V. G. Zakrzewski, J. Gao, N. Rega, G. Zheng, W. Liang, M. Hada, M. Ehara, K. Toyota, R. Fukuda, J. Hasegawa, M. Ishida, T. Nakajima, Y. Honda, O. Kitao, H. Nakai, T. Vreven, K. Throssell, J. A. Montgomery Jr., J. E. Peralta, F. Ogliaro, M. J. Bearpark, J. J. Heyd, E. N. Brothers, K. N. Kudin, V. N. Staroverov, T. A. Keith, R. Kobayashi, J. Normand, K. Raghavachari, A. P. Rendell, J. C. Burant, S. S. Iyengar, J. Tomasi, M. Cossi, J. M. Millam, M. Klene, C.

Adamo, R. Cammi, J. W. Ochterski, R. L. Martin, K. Morokuma, O. Farkas, J. B. Foresman and D. J. Fox, *Gausian16*, 2016.
22. J. K. Sprafke, D. V. Kondratuk, M. Wykes, A. L. Thompson, M. Hoffmann, R. Drevinskas, W.-H. Chen, C. K. Yong, J. Kärnbratt, J. E. Bullock, M. Malfois, M. R. Wasielewski, B. Albinsson, L. M. Herz, D. Zigmantas, D. Beljonne and H. L. Anderson, *Journal of the American Chemical Society*, 2011, **133**, 17262-17273.
23. J. J. P. Stewart, *MOPAC2016*, 2016.
24. H. Wang, Y. Li, H. Yu, B. Song, S. Lu, X.-Q. Hao, Y. Zhang, M. Wang, S.-W. Hla and X. Li, *Journal of the American Chemical Society*, 2019, **141**, 13187-13195.
25. J. M. Murphy, X. Liao and J. F. Hartwig, *Journal of the American Chemical Society*, 2007, **129**, 15434-15435.
26. Y. Hirano, S. Kojima and Y. Yamamoto, *The Journal of Organic Chemistry*, 2011, **76**, 2123-2131.
27. D. Gelman and S. L. Buchwald, *Angewandte Chemie International Edition*, 2003, **42**, 5993-5996.
28. M. C. O'Sullivan, J. K. Sprafke, D. V. Kondratuk, C. Rinfray, T. D. W. Claridge, A. Saywell, M. O. Blunt, J. N. O'Shea, P. H. Beton, M. Malfois and H. L. Anderson, *Nature*, 2011, **469**, 72-75.
29. A. A. Cant, R. Bhalla, S. L. Pimlott and A. Sutherland, *Chemical Communications*, 2012, **48**, 3993-3995.
30. M. O. Senge, N. N. Sergeeva and K. J. Hale, *Chemical Society Reviews*, 2021, **50**, 4730-4789.
31. S. Hiroto, Y. Miyake and H. Shinokubo, *Chemical Reviews*, 2017, **117**, 2910-3043.
32. M. Drobizhev, Y. Stepanenko, A. Rebane, C. J. Wilson, T. E. O. Screen and H. L. Anderson, *Journal of the American Chemical Society*, 2006, **128**, 12432-12433.
33. A. Osuka, N. Tanabe, S. Nakajima and K. Maruyama, *Journal of the Chemical Society, Perkin Transactions 2*, 1996, DOI: 10.1039/P29960000199, 199-203.
34. F. C. Grozema, C. Houarner-Rassin, P. Prins, L. D. A. Siebbeles and H. L. Anderson, *Journal of the American Chemical Society*, 2007, **129**, 13370-13371.
35. M. J. Plater, S. Aiken and G. Bourhill, *Tetrahedron*, 2002, **58**, 2405-2413.
36. P. Parkinson, C. E. I. Knappke, N. Kamonsutthipaijit, K. Sirithip, J. D. Matichak, H. L. Anderson and L. M. Herz, *Journal of the American Chemical Society*, 2014, **136**, 8217-8220.
37. A. Tsuda, T. Nakamura, S. Sakamoto, K. Yamaguchi and A. Osuka, *Angew Chem Int Ed Engl*, 2002, **41**, 2817-2821.
38. M. U. Winters, E. Dahlstedt, H. E. Blades, C. J. Wilson, M. J. Frampton, H. L. Anderson and B. Albinsson, *Journal of the American Chemical Society*, 2007, **129**, 4291-4297.
39. M. K. Kuimova, M. Hoffmann, M. U. Winters, M. Eng, M. Balaz, I. P. Clark, H. A. Collins, S. M. Tavender, C. J. Wilson, B. Albinsson, H. L. Anderson, A. W. Parker and D. Phillips, *Photochemical & Photobiological Sciences*, 2007, **6**, 675-682.
40. M. U. Winters, J. Kärnbratt, M. Eng, C. J. Wilson, H. L. Anderson and B. Albinsson, *The Journal of Physical Chemistry C*, 2007, **111**, 7192-7199.
41. M. Hoffmann, C. J. Wilson, B. Odell and H. L. Anderson, *Angewandte Chemie International Edition*, 2007, **46**, 3122-3125.
42. A. Bellamy-Carter, C. Roche, H. L. Anderson and A. Saywell, *Scientific Reports*, 2021, **11**, 20388.
43. C. J. Judd, A. S. Nizovtsev, R. Plougmann, D. V. Kondratuk, H. L. Anderson, E. Besley and A. Saywell, *Physical Review Letters*, 2020, **125**, 206803.
44. M. Hutin, J. K. Sprafke, B. Odell, H. L. Anderson and T. D. W. Claridge, *Journal of the American Chemical Society*, 2013, **135**, 12798-12807.

45. J. Kärnbratt, M. Gilbert, J. K. Sprafke, H. L. Anderson and B. Albinsson, *The Journal of Physical Chemistry C*, 2012, **116**, 19630-19635.
46. H. Gotfredsen, J. Hergenhahn, F. Duarte, T. D. W. Claridge and H. L. Anderson, *Journal of the American Chemical Society*, 2024, **146**, 25232-25244.
47. M. D. Peeks, T. D. W. Claridge and H. L. Anderson, *Nature*, 2017, **541**, 200-203.
48. S. M. Kopp, H. Gotfredsen, J.-R. Deng, T. D. W. Claridge and H. L. Anderson, *Journal of the American Chemical Society*, 2020, **142**, 19393-19401.
49. S. M. Kopp, H. Gotfredsen, J. Hergenhahn, A. Rodríguez-Rubio, J.-R. Deng, H. Zhu, W. Stawski and H. L. Anderson, *Chem*, 2024, **10**, 3410-3427.
50. M. Hoffmann, J. Kärnbratt, M. H. Chang, L. M. Herz, B. Albinsson and H. L. Anderson, *Angew Chem Int Ed Engl*, 2008, **47**, 4993-4996.
51. D. V. Kondratuk, J. K. Sprafke, M. C. O'Sullivan, L. M. A. Perdigao, A. Saywell, M. Malfois, J. N. O'Shea, P. H. Beton, A. L. Thompson and H. L. Anderson, *Chemistry – A European Journal*, 2014, **20**, 12826-12834.
52. D. V. Kondratuk, L. M. A. Perdigao, M. C. O'Sullivan, S. Svatek, G. Smith, J. N. O'Shea, P. H. Beton and H. L. Anderson, *Angewandte Chemie International Edition*, 2012, **51**, 6696-6699.
53. P. S. Bols, M. Rickhaus, L. Tejerina, H. Gotfredsen, K. Eriksen, M. Jirasek and H. L. Anderson, *Journal of the American Chemical Society*, 2020, **142**, 13219-13226.
54. L. Favereau, A. Cnossen, J. B. Kelber, J. Q. Gong, R. M. Oetterli, J. Cremers, L. M. Herz and H. L. Anderson, *Journal of the American Chemical Society*, 2015, **137**, 14256-14259.
55. I. Y. Lee, T. D. Gruber, A. Samuels, M. Yun, B. Nam, M. Kang, K. Crowley, B. Winterroth, H. I. Boshoff and C. E. Barry, 3rd, *Bioorg Med Chem*, 2013, **21**, 114-126.
56. H. L. Ozores, M. Amorín and J. R. Granja, *Journal of the American Chemical Society*, 2017, **139**, 776-784.
57. A. Mallinger, S. Crumpler, M. Pichowicz, D. Waalboer, M. Stubbs, O. Adeniji-Popoola, B. Wood, E. Smith, C. Thai, A. T. Henley, K. Georgi, W. Court, S. Hobbs, G. Box, M.-J. Ortiz-Ruiz, M. Valenti, A. De Haven Brandon, R. TePoele, B. Leuthner, P. Workman, W. Aherne, O. Poeschke, T. Dale, D. Wienke, C. Esdar, F. Rohdich, F. Raynaud, P. A. Clarke, S. A. Eccles, F. Stieber, K. Schiemann and J. Blagg, *Journal of Medicinal Chemistry*, 2015, **58**, 1717-1735.
58. A. Pelter, I. Jenkins and D. E. Jones, *Tetrahedron*, 1997, **53**, 10357-10400.
59. G. Li, X. Wang, J. Li, X. Zhao and F. Wang, *Tetrahedron*, 2006, **62**, 2576-2582.

2.9 Experimental

Contents

2.9.1 Known Compounds

As follows are the compound codes for the known molecules used in this thesis, along with citations for the procedures used to prepare them: **P3$_{OOct}$(C$_2$THS)$_2$,[50] P3$_{THS}$(C$_2$CPDIPS)$_2$,[54] 2.5,[55] 2.12,[56] 2.13,[57] 2.9,[26] 2.10,[26] 2.16,[58] 2.32,[59] T6,[50] 2.15.[5]**

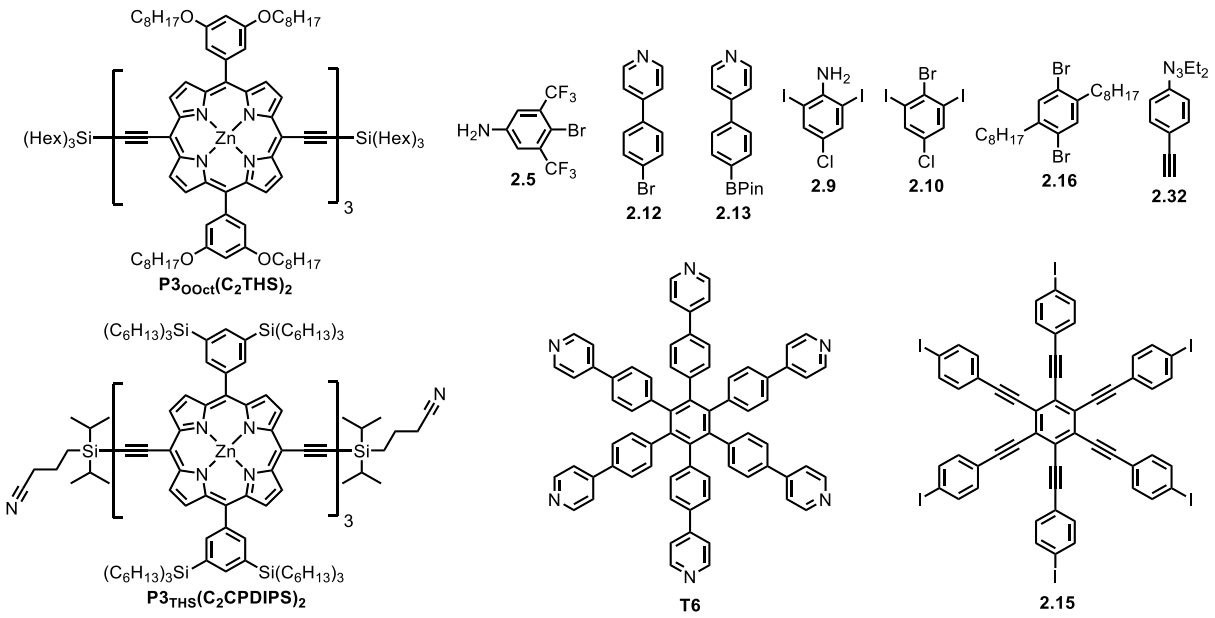

Figure 2.58: Chemical structures of known molecules used in this thesis.

2.9.2 Synthesis Towards T18$_A$ and T18$_B$

2.9.2.1 Synthesis of 2-Bromo-5-iodo-1,3-bis(trifluoromethyl)benzene (2.6)

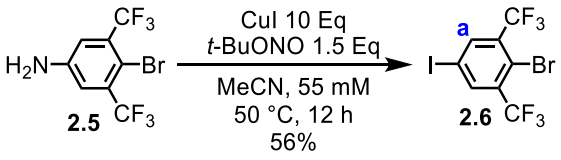

To a stirring solution of 3,5-bis(trifluoromethyl)-4-bromoaniline (**2.5**) (526 mg, 1 Eq, 1.71 mmol) in MeCN (31 mL) at 0 °C was added CuI (3.25 g, 10 Eq, 17.1 mmol). After 5 minutes of stirring, *t*-BuONO (305 µL, 1.5 Eq, 2.56 mmol) was added and the reaction vessel removed from the ice bath, then heated to 50 °C for 16 hours. After cooling to room temperature, EtOAc (100 mL) was added and the reaction mixture transferred to a separating funnel. The organic phase was then washed with saturated $Na_2S_2O_3 \cdot 5H_2O$ (3 × 100 mL), dried over Na_2SO_4,

concentrated and purified by flash column chromatography (SiO_2, PE) to afford compound **2.6** as a white crystalline solid (339 mg, 56%).

^{1}H NMR (400 MHz, $CDCl_3$) δ_H = 8.16 (s, 2H, **H_a**) ppm.

^{19}F NMR (377 MHz $CDCl_3$) δ_F = –62.32 ppm (referenced against C_6F_6 (δ_F –161.64) as an internal standard).

^{13}C NMR (101 MHz, $CDCl_3$) δ_C = 139.96 (q, J_{FC} = 5.9 Hz), 134.30 (q, J_{FC} = 31.5 Hz), 121.60 (q, J_{FC} = 275.7 Hz), 119.05, 91.55 ppm.

Unable to obtain mass by ESI or MALDI-ToF

2.9.2.2 Synthesis of 7-(4-Bromo-3,5-bis(trifluoromethyl)phenyl)-5,5-diisopropylhept-6-ynenitrile (2.7)

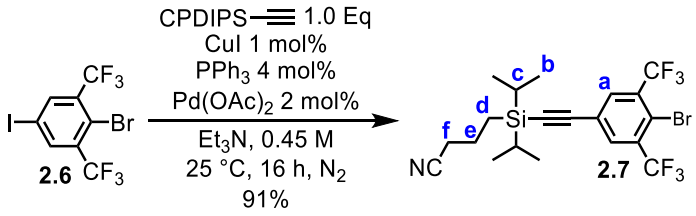

To an oven-dried Schlenk tube was added **2.6** (250 mg, 1 Eq, 597 µmol), CuI (1.14 mg, 0.01 Eq, 5.97 µmol), PPh_3 (6.26 mg, 0.04 Eq, 23.9 µmol) and $Pd(OAc)_2$ (2.49 mg, 0.02 Eq, 11.9 µmol). The tube was then stoppered and evacuated/refilled with N_2 (3×). Dry triethylamine (1.33 mL) was added and the reaction mixture freeze-pump-thaw degassed (3×). Under a positive pressure of N_2, CPDIPS-acetylene (124 mg, 138 µL, 1 Eq, 597 µmol) was then added and the reaction mixture stirred at room temperature for 16 hours. The resulting pale-yellow suspension was diluted with CH_2Cl_2 (20 mL), concentrated in vacuo onto a minimum of silica gel and loaded onto a silica gel column (SiO_2, 3.5 cm (*d*) × 14 cm (*h*), PE) for purification by flash column chromatography (0–20% CH_2Cl_2 in PE) to afford **2.7** as a pale-yellow oil (271 mg, 91%).

^{1}H NMR (400 MHz, $CDCl_3$) δ_H = 7.90 (s, 2H, **H_a**), 2.44 (t, J = 6.9 Hz, 2H, **H_f**), 1.89–1.81 (m, 2H, **H_e**), 1.13–1.08 (m, 14H, **H_b**, **H_c**), 0.91–0.82 (m, 2H, H_d) ppm.

^{19}F NMR (377 MHz $CDCl_3$) δ_F = –62.30 ppm (referenced against C_6F_6 (δ_F –161.64) as an internal standard)

^{13}C NMR (101 MHz, CDCl3) δ_C = 133.99 (q, J_{FC} = 5.8 Hz), 133.25 (q, J_{FC} = 31.4 Hz), 123.33, 122.25 (q, J_{FC} = 275.4 Hz), 119.65, 118.80, 103.65, 95.43, 21.24, 20.93, 18.23, 18.00, 11.64, 9.54 ppm.

Unable to obtain mass by ESI or MALDI-ToF

2.9.2.3 Synthesis of 5,5-Diisopropyl-7-(4-(pyridin-3-ylethynyl)-3,5-bis(trifluoromethyl) phenyl)hept-6-ynenitrile (2.8)

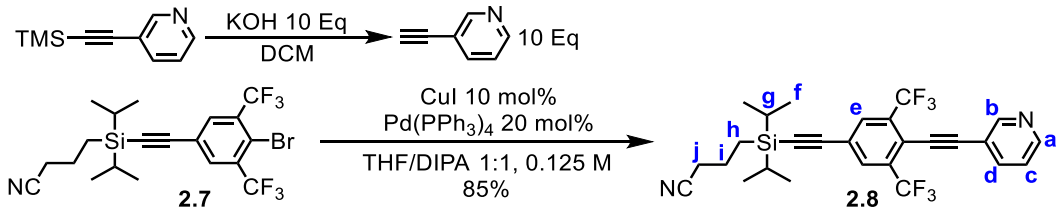

To a stirring solution of KOH (3.15 g, 10 Eq, 56.2 mmol) in CH_2Cl_2 (150 mL) and MeOH (25 mL) was added 3-((trimethylsilyl)ethynyl)pyridine (9.85 g, 10.7 mL, 10 Eq, 56.2 mmol). After 1 hour the reaction mixture was passed through a short plug of silica gel (CH_2Cl_2 + 2% MeOH) and concentrated in vacuo to afford 3-ethynylpyridine as a white crystalline solid, which was used in the next step with no further purification. In an oven dried Schlenk tube, 3-ethynylpyridine from the previous step and **2.7** (2.80 g, 1 Eq, 5.62 mmol) were dissolved in THF (22.5 mL) and DIPA (22.5 mL), then freeze-pump-thaw degassed (3×). After refreezing the solution and under a positive pressure of N_2, CuI (107 mg, 0.1 Eq, 562 µmol) and $Pd(PPh_3)_4$ (1.30 g, 0.2 Eq, 1.12 mmol) were added. The Schlenk tube was then evacuated/refilled with nitrogen (3×) and under a positive pressure of N_2, stirred at 80 °C for 16 hours. The crude

reaction mixture was cooled to 20 °C then diluted with CH_2Cl_2 (20 mL) and concentrated onto a minimum of silica gel. The desired compound **2.8** was obtained by flash column chromatography (SiO_2, 10% EtOAc in PE) as a viscous yellow oil (2.47 g, 85% yield).

^{1}H NMR (400 MHz, $CDCl_3$) δ_H = 8.78 (d, J = 2.2, 1H, **H_b**), 8.61 (dd, J = 4.9, 1.7 Hz, 1H, **H_a**), 7.92 (s, 2H, **H_e**), 7.83 (dt, J = 7.9, 1.9 Hz, 1H, **H_d**), 7.34–7.30 (m, 1H, **H_c**), 2.44 (t, J = 6.9 Hz, 2H, **H_j**), 1.90–1.79 (m, 2H, **H_i**), 1.14–1.07 (m, 14H, **H_g, H_f**), 0.92–0.82 (m, 2H, **H_h**) ppm.

^{19}F NMR (377 MHz $CDCl_3$) δ_F = –62.50 ppm (referenced against C_6F_6 (δ –161.64) as an internal standard)

^{13}C NMR (101 MHz, $CDCl_3$) δ_C = 152.43, 150.02, 138.78, 134.07 (q, J_{FC} = 31.1 Hz), 132.36 (q, J_{FC} = 5.2 Hz), 123.57, 123.28, 122.59 (q, J_{FC} = 275.7 Hz), 119.64, 119.22, 104.36, 100.09, 96.30, 84.0, 77.36, 21.26, 20.94, 18.25, 18.02, 11.66, 9.58 ppm.

HRMS (ESI$^+$) m/z: $[M+H]^+$ calcd. for $C_{27}H_{27}F_6N_2Si^+$ 521.1842; found 521.1835.

2.9.2.4 Synthesis of 2.11

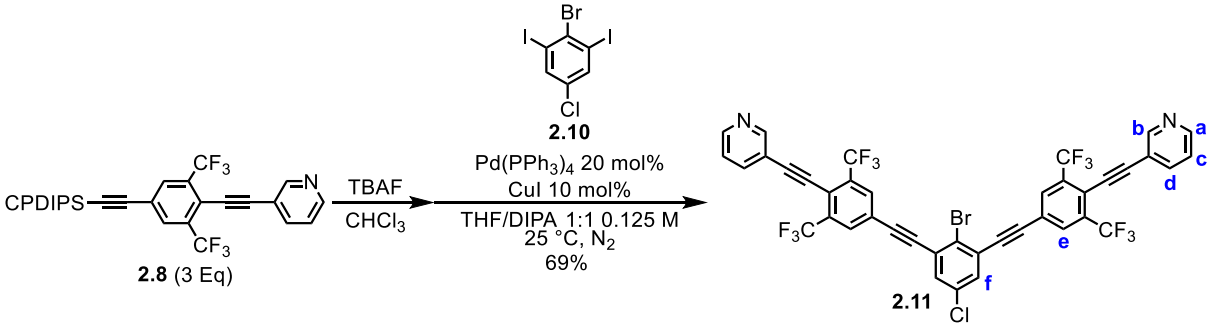

To a stirring solution of **2.8** (493 mg, 3 Eq, 948 µmol) in chloroform (10 mL) was added TBAF (1.10 mL, 1.0 M in THF, 3.5 Eq, 1.1 mmol). The solution was stirred for 5 minutes, after which TLC (30% EtOAc in PE) showed full deprotection of the CPDIPS group. The crude reaction mixture was then poured into a mixture of water (20 mL) and acetic acid (63 µL, 3.5 Eq, 1.1 mmol), extracted with chloroform, dried, and concentrated in vacuo.

In an oven dried Schlenk tube, deprotected **2.8** and 2-bromo-5-chloro-1,3-diiodobenzene **(2.10)** (140 mg, 1 Eq, 316 µmol) were dissolved in THF (6.32 mL) and DIPA (6.32 mL), then freeze-pump-thaw degassed (3×). After refreezing the solution and under a positive pressure of N_2, CuI (6.0 mg, 0.1 Eq, 31.6 µmol) and $Pd(PPh_3)_4$ (73 mg, 0.2 Eq, 63 µmol) were added. The Schlenk tube was then evacuated/refilled with nitrogen (3×) and under a positive pressure of N_2, stirred at 20 °C for 16 hours.

The crude reaction mixture was concentrated in vacuo, then CH_2Cl_2 (10 mL) was added and the mixture sonicated for 5 minutes. The resulting suspension was filtered to obtain **2.11** as a fine white powder (188 mg, 69% yield).

^{1}H NMR (400 MHz, $CDCl_3$) δ_H = 8.82 (s, 2H, **H_b**), 8.65 (d, *J* = 4.9 Hz, 2H, **H_a**), 8.07 (s, 4H, **H_e**), 7.90–7.85 (m, 2H, **H_d**), 7.59 (s, 2H, **H_f**), 7.36 (dd, *J* = 7.9, 4.9 Hz, 2H, **H_c**) ppm.

^{19}F NMR (377 MHz $CDCl_3$) δ_F = –62.52 ppm (referenced against C_6F_6 (δ_F –161.64) as an internal standard).

^{13}C NMR - Solubility too poor to record spectrum

HRMS (ESI^+) *m/z*: $[M+H]^+$ calcd. for $C_{40}H_{15}BrClF_{12}N_2^+$ 864.9910; found 864.9896.

2.9.2.5 Synthesis of $T3_A$

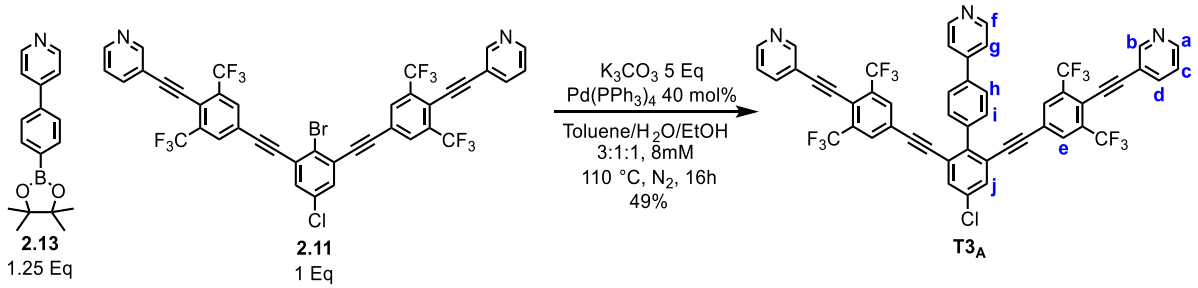

To an oven dried Schlenk tube was added **2.11** (300 mg, 1 Eq, 346 µmol), 4-(4-(4,4,5,5-tetramethyl-1,3,2-dioxaborolan-2-yl)phenyl)pyridine (**2.13**) (122 mg, 1.25 Eq, 433 µmol) and

potassium carbonate (239 mg, 5 Eq, 1.73 mmol). The Schlenk was stoppered, evacuated/refilled with N_2 (5×), then toluene (26.0 mL), water (8.7 mL) and ethanol (8.7 mL) were added and N_2 bubbled through the resulting solution for 10 minutes. Under a positive flow of N_2, $Pd(PPh_3)_4$ (80 mg, 0.2 Eq, 69 µmol) was added. The Schlenk was then stoppered, purged with N_2 for 10 minutes and vigorously stirred at 110 °C.

After 3 hours, the reaction was cooled to room temperature and under a positive flow of N_2, $Pd(PPh_3)_4$ (80 mg, 0.2 Eq, 69 µmol) was added. The Schlenk was then stoppered, purged with N_2 for 10 minutes then vigorously stirred at 110 °C for 16 hours.

After cooling to room temperature, the crude reaction mixture was poured into a separating funnel and extracted with chloroform (3 × 20 mL). The combined organic phase was concentrated in vacuo, then purified by flash column chromatography (SiO_2, chloroform to 5% MeOH in chloroform) to yield **T3$_A$** as a fine white powder (160 mg, 49% yield).

^{1}H NMR (600 MHz, $C_2D_2Cl_4$, 373 K) δ_H = 8.83–8.80 (m, 2H, **H$_b$**), 8.76 (d, *J* = 5.1 Hz, 2H, **H$_f$**), 8.66 (dd, *J* = 4.9, 1.7 Hz, 2H, **H$_a$**), 7.88 (d, *J* = 8.2 Hz, 2H, **H$_h$/H$_i$**), 7.87–7.84 (m, 2H, **H$_d$**), 7.78 (s, 2H, **H$_j$**), 7.74 (d, *J* = 8.2 Hz, 2H, **H$_h$/H$_i$**), 7.70 (s, 4H, **H$_e$**), 7.62–7.59 (m, 2H, **H$_g$**), 7.35 (dd, *J* = 8.0, 4.9 Hz, 2H, **H$_c$**) ppm.

^{19}F NMR (377 MHz, $CDCl_3$, 298 K) δ_F = –62.65 ppm (referenced against C_6F_6 (δ_F –161.64) as an internal standard).

^{13}C NMR (151 MHz, $C_2D_2Cl_4$, 373 K) δ_C = 152.10, 150.21, 149.76, 147.15, 145.11, 133.95, 133.94 (q, J_{FC} = 31.1 Hz), 133.61, 132.59, 131.37 (q, J_{FC} = 5.3 Hz), 130.69, 126.17, 123.61, 122.97, 122.87, 122.28 (q, J_{FC} = 274.9 Hz) 121.17, 119.01, 118.88, 100.43, 92.03, 91.63, 83.86, 74.04 ppm.

HRMS (ESI$^+$) *m*/*z*: $[M+H]^+$ calcd. for $C_{51}H_{23}ClF_{12}N_3^+$ 940.1383; found 940.1363.

2.9.2.6 Synthesis of 2.14

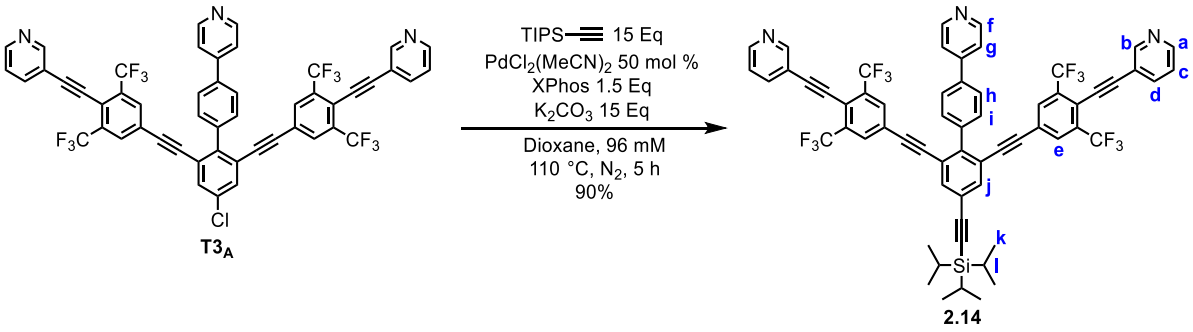

To an oven dried Schlenk tube was added **T3A** (96.0 mg, 1 Eq, 102 µmol), $PdCl_2(MeCN)_2$ (13.2 mg, 0.5 Eq, 51 µmol), potassium carbonate (212.0 mg, 15 Eq, 1.53 mmol) and XPhos (73.0 mg, 1.5 Eq, 153 µmol). The Schlenk was then evacuated and refilled with N_2 (5×) before dioxane (1.06 mL) was added and the resulting solution bubbled with N_2 for 10 minutes. (Triisopropylsilyl)acetylene (279 mg, 344 µL, 15 Eq, 1.53 mmol) was then added and the reaction stirred at 110 °C for 5 hours, after which ESI mass spectrometry showed no evidence of **T3A** remaining and a clear mass peak for **S10.** The reaction mixture was allowed to cool to 20 °C, concentrated, then purified by column chromatography (SiO_2, chloroform to chloroform + 1% MeOH) to yield **2.14** as a white solid (99.2 mg, 90%).

^{1}H NMR (400 MHz, $CDCl_3$) δ_H = 8.77 (dd, J = 2.1, 0.9 Hz, 2H, **H_b**), 8.76–8.73 (m, 2H, **H_f**), 8.63 (dd, J = 4.9, 1.7 Hz, 2H, **H_a**), 7.87–7.80 (m, 6H, **H_d**, **$H_{h/i}$**, **H_j**), 7.74 – 7.70 (m, 2H, **$H_{h/i}$**), 7.67 (s, 4H, **H_e**), 7.60–7.57 (m, 2H, **H_g**), 7.33 (ddd, J = 7.9, 4.9, 1.0 Hz, 2H, **H_c**), 1.19–1.16 (m, 21H, **H_k, H_l**) ppm.

^{19}F NMR (377 MHz $CDCl_3$) δ_F = –62.63 ppm (referenced against C_6F_6 (δ_F = –161.64) as an internal standard).

^{13}C NMR (101 MHz, $CDCl_3$) δ_F 152.45, 150.56, 150.08, 145.99, 138.82, 136.43, 134.12 (q, J_{FC} = 31.1 Hz), 131.61 (q, J_{FC} = 5.2 Hz), 131.15, 126.42, 124.03, 123.31, 122.55, 122.53 (q, J_{FC} = 275.7 Hz) 121.65, 119.20, 119.08, 104.29, 100.32, 94.88, 94.22, 92.70, 91.09, 84.07, 18.81, 18.57, 11.40, 11.14 ppm.

HRMS (ESI$^+$) *m*/*z*: $[M+H]^+$ calcd. for $C_{62}H_{44}F_{12}N_3Si^+$ 1086.3107; found 1086.3085.

2.9.2.7 Synthesis of 7-(4-Bromo-2,5-dioctylphenyl)-5,5-diisopropylhept-6-ynenitrile (2.31)

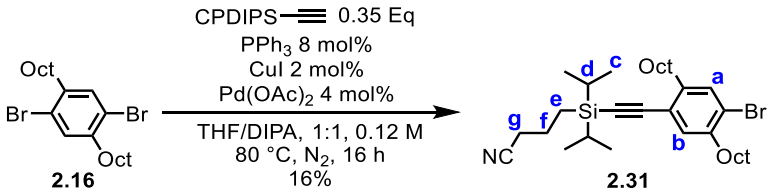

To an oven dried Schlenk tube was added **2.16** (1.95 g, 1 Eq, 4.24 mmol), $Pd(OAc)_2$ (38 mg, 0.04 Eq, 169 µmol), PPh_3 (89 mg, 0.08 Eq, 339 µmol) and CuI (16 mg, 0.02 Eq, 85 µmol). The tube was then stoppered and evacuated/refilled with N_2 (5×), before a freeze-pump-thaw degassed mixture of THF (17 mL) and DIPA (17 mL) was added via syringe. 4-(Ethynyldiisopropylsilyl)butanenitrile (307 mg, 341 uL, 0.35 Eq, 1.48 mmol) was then added via syringe and the mixture stirred at 80 °C for 16 hours. After cooling to room temperature, the crude reaction mixture was loaded onto a minimum of silica gel then purified by flash column chromatography (PE to 20% CH_2Cl_2 in PE) to yield the **2.31** as a yellow oil (405 mg, 16% yield).

^{1}H NMR (400 MHz, $CDCl_3$) δ_H = 7.35 (s, 1H, **H_a/H_b**), 7.26 (s, 1H, **H_a/H_b**), 2.72–2.61 (m, 4H, Ar-**CH_2**), 2.42 (t, *J* = 6.9 Hz, 2H, **H_g**), 1.91–1.82 (m, 2H, **H_f**), 1.64–1.55 (m, 4H, Ar-CH_2-**CH_2**), 1.38–1.22 (m, 30H, Ar-CH_2-**$(CH_2)_6$**-CH_3, N-CH_2-**CH_3**), 1.14–1.05 (m, 14H, **H_c/H_d**), 0.91–0.80 (m, 8H, Ar-$(CH_2)_7$-**CH_3**, **H_e**) ppm.

2.9.2.8 Synthesis of 7-(4-((4-(3,3-Diethyltriaz-1-en-1-yl)phenyl)ethynyl)-2,5-dioctylphenyl)-5,5-diisopropylhept-6-ynenitrile (2.33)

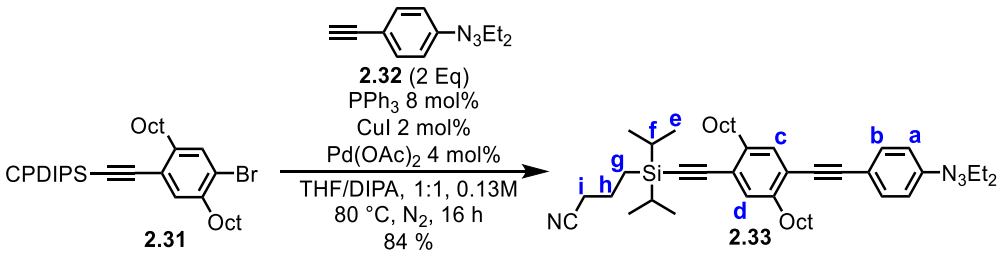

In an oven dried Schlenk tube, **2.31** (345 mg, 1 Eq, 588 µmol) and **2.32** (237 mg, 2 Eq, 1.18 mmol) were dissolved in THF (2.35 mL) and DIPA (2.35 mL), then freeze-pump-thaw degassed (3×). After refreezing the solution and under a positive pressure of N_2, $Pd(OAc)_2$ (5.28 mg, 0.04 Eq, 23.5 µmol), PPh_3 (12.3 mg, 0.08 Eq, 47.0 µmol) and CuI (2.24 mg, 0.02 Eq, 11.8 µmol) were added. The Schlenk was stoppered and evacuated/refilled with N_2 (5×) then stirred at 80 °C for 16 hours. After cooling to room temperature, the crude reaction mixture was concentrated onto a minimum of silica gel then purified by flash column chromatography (SiO_2, PE to 5% EtOAc in PE) to yield **2.33** as a yellow oil (350 mg, 84%).

^{1}H NMR (400 MHz, $CDCl_3$) δ_H = 7.50–7.45 (m, 2H, **H_a/H_b**), 7.43–7.38 (m, 2H, **H_a/H_b**), 7.31 (s, 1H, **H_c/H_d**), 7.28 (s, 1H, **H_c/H_d**), 3.79 (q, *J* = 7.2 Hz, 4H, N-**CH_2**), 2.75 (m, 4H, Ar-**CH_2**), 2.43 (t, *J* = 6.9 Hz, 2H, **H_i**), 1.94 – 1.82 (m, 2H, **H_h**), 1.74–1.57 (m, 2H, Ar-CH_2-**CH_2**), 1.43–1.22 (m, 30H, Ar-CH_2-**$(CH_2)_6$**-CH_3, N-CH_2-**CH_3**), 1.16–1.06 (m, 14H, **H_e/H_f**), 0.91–0.80 (m, 8H, Ar-$(CH_2)_7$-**CH_3**, **H_g**) ppm.

^{13}C NMR (101 MHz, $CDCl_3$) δ_C = 151.22, 142.66, 142.21, 133.00, 132.28, 132.24, 123.48, 121.92, 120.55, 119.80, 119.63, 106.84, 94.98, 93.76, 88.19, 53.54, 34.49, 34.33, 32.03, 30.95, 30.91, 29.80, 29.71, 29.63, 29.44, 22.79, 21.47, 20.94, 18.36, 18.13, 14.23, 11.93, 9.86, 1.14 ppm.

HRMS (ESI^+) *m/z*: $[M+H]^+$ calcd. for $C_{46}H_{71}N_4Si^+$ 707.5443; found 707.5430.

2.9.2.9 Synthesis of Extended Core (2.35)

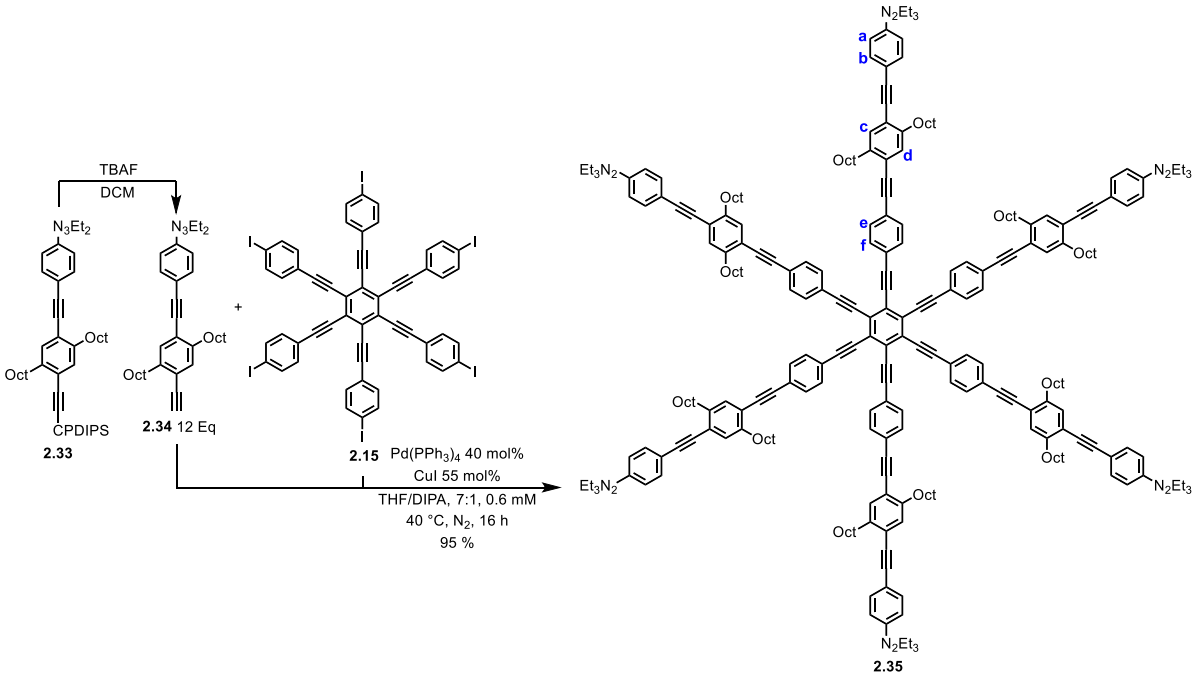

To a stirring solution of **2.33** (284 mg, 12 Eq, 402 µmol) in CH_2Cl_2 (2 mL) was added TBAF (803 µL, 1.00 M in THF, 24 Eq, 803 µmol). The solution was stirred for 15 minutes then CH_2Cl_2 (10 mL), water (25 mL) and acetic acid (100 µL) were added. The mixture was then poured into a separating funnel and extracted with chloroform (3 × 10 mL). The organic phase was dried with $MgSO_4$, then concentrated in vacuo and used in the next step without further purification.

In an oven dried Schlenk tube, deprotected **2.33** from the first step and **2.15** (48 mg, 1 Eq, 33.5 µmol) were dissolved in THF (48.8 mL) and DIPA (6.97 mL), then freeze-pump-thaw degassed (3×). After refreezing the solution and under a positive pressure of N_2, CuI (3.51 mg, 0.55 Eq, 18.4 µmol) and $Pd(PPh_3)_4$ (15.5 mg, 0.4 Eq, 13.4 µmol) were added. The Schlenk tube was stoppered, evacuated/refilled with N_2 (5×), then stirred at 40 °C for 16 hours.

After cooling to room temperature, the crude reaction mixture was concentrated in vacuo then purified by flash column chromatography (SiO_2, 5% EtOAc in PE to elute unreacted starting

material and Glaser coupling products, then 100% EtOAc to elute the desired product). The purified material was then passed through a size exclusion column (SX3 biobeads, $CHCl_3$) and concentrated to yield **2.35** as a yellow film (121.9 mg, 95% yield).

^{1}H NMR (500 MHz, $CDCl_3$) δ_H = 7.65 (d, *J* = 8.3 Hz, 12H, **H_a/H_b/H_e/H_f**), 7.57 (d, *J* = 8.3 Hz, 12H, **H_a/H_b/H_e/H_f**), 7.51 (d, *J* = 8.5 Hz, 12H, **H_a/H_b/H_e/H_f**), 7.43 (d, *J* = 8.5 Hz, 12H, **H_a/H_b/H_e/H_f**), 7.40 (s, 6H, **H_c/H_d**), 7.39 (s, 6H, **H_c/H_d**), 3.80 (q, *J* = 7.2 Hz, 24H, N-**CH_2**-CH_3), 2.88–2.80 (m, 24H, Ar-**CH_2**), 1.79–1.68 (m, 24H, Ar-CH_2-**CH_2**), 1.48–1.21 (m, 156H, Ar-CH_2-CH_2-**$(CH_2)_5$**-CH_3, N-CH_2-**CH_3**), 0.91–0.83 (m, 36H, Ar-$(CH_2)_2$-**CH_3**) ppm.

^{13}C NMR (126 MHz, $CDCl_3$) δ_C = 151.23, 142.44, 142.31, 132.52, 132.36, 131.93, 131.74, 127.63, 124.55, 123.49, 122.74, 121.95, 120.59, 119.77, 99.71, 95.11, 93.57, 91.45, 89.17, 88.37, 34.36, 34.28, 32.07, 30.83, 30.80, 29.79, 29.69, 29.67, 29.48, 29.42, 22.83, 22.81, 14.27 ppm.

2.9.2.10 Synthesis of Iodinated Extended Core (2.36)

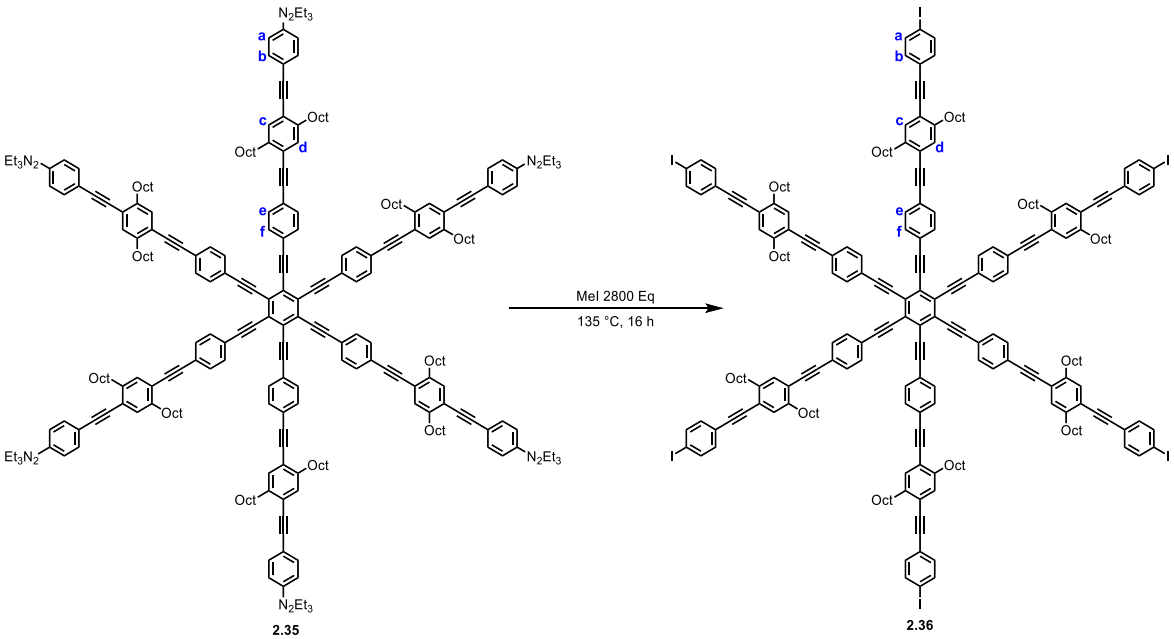

To an oven dried pressure tube was added **2.35** (109 mg, 1 Eq, 28.9 µmol) and MeI (5.0 mL, 2800 Eq, 80 mmol). The pressure tube was sealed, then stirred at 135 °C for 16 hours. After

cooling to room temperature, the MeI was removed by a stream of nitrogen, then the crude reaction mixture was purified on a size exclusion column (SX3 biobeads, $CHCl_3$) and concentrated in vacuo to yield **2.36** as a yellow solid (75 mg, 66%).

^{1}H NMR (500 MHz, $CDCl_3$) δ_H = 7.70 (d, *J* = 8.4 Hz, 12H, **H_b/H_e/H_f**), 7.63 (d, *J* = 8.4 Hz, 12H, **H_b/H_e/H_f**), 7.55 (d, J = 8.4 Hz, 12H, **H_b/H_e/H_f**), 7.38 (s, 6H, **H_c/H_d**), 7.36 (s, 6H, **H_c/H_d**), 7.24 (d, *J* = 8.4 Hz, 12H, **H_a**), 2.84–2.77 (m, 24H, Ar-**CH_2**), 1.74–1.64 (m, 24H, Ar-CH_2-**CH_2**), 1.44–1.20 (m, 120H, Ar-CH_2-CH_2-**$(CH_2)_5$**-CH_3), 0.85 (m, 36H, Ar-$(CH_2)_2$-**CH_3**) ppm.

^{13}C NMR (126 MHz, CDCl3) δ_C = 142.36, 142.34, 137.60, 132.94, 132.40, 132.29, 131.77, 131.55, 127.48, 124.20, 122.98, 122.82, 122.53, 122.49, 99.48, 94.13, 93.77, 93.19, 91.12, 89.92, 89.32, 34.20, 34.14, 31.96, 31.94, 30.72, 30.62, 29.68, 29.60, 29.56, 29.37, 29.33, 22.72, 22.70, 14.18, 14.16 ppm.

2.9.2.11 Synthesis of template T18$_A$

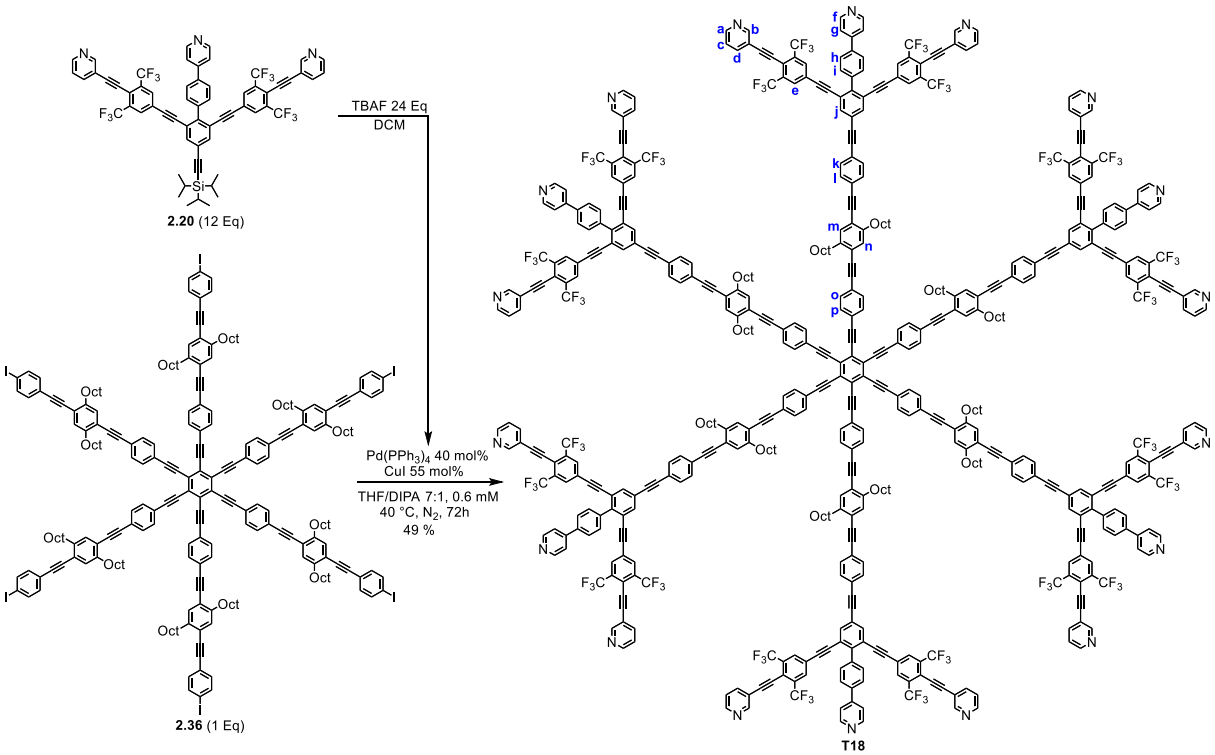

To a stirring solution of **2.20** (62.1 mg, 12 Eq, 57.3 µmol) in CH_2Cl_2 (2 mL) was added TBAF (115 µL, 1.0 M in THF, 24 Eq, 115 µmol). The solution was stirred for 15 minutes then CH_2Cl_2

(2mL), water (5 mL) and acetic acid (20 µL) were added. The mixture was then poured into a separating funnel and extracted with chloroform (3 × 10 mL). The organic phase wasdried with $MgSO_4$, then concentrated in vacuo and used in the next step without further purification.

In an oven dried Schlenk tube, deprotected **2.20** and **2.36** (19.0 mg, 1 Eq, 4.77 µmol) were dissolved in THF (6.96 mL) and DIPA (994 µL), then freeze-pump-thaw degassed (5×). After refreezing the solution and under a positive pressure of N_2, CuI (0.50 mg, 0.55 Eq, 2.62 µmol) and $Pd(PPh_3)_4$ (2.21 mg, 0.4 Eq, 1.91 µmol) were added. The Schlenk tube was stoppered, evacuated/refilled with N_2 (5×), then stirred at 40 °C for 72 hours. The crude reaction mixture was allowed to cool, then transferred into a vial and centrifuged. The brown supernatant solution was pipetted off, reduced to half its volume and centrifuged again. The bright yellow precipitate collected from both centrifugations was combined then suspended in MeOH (10 mL), sonicated and centrifuged. This process was repeated three times before the yellow solid was dried under a high vacuum to yield exceptionally clean **T18$_A$** (9.33 mg, 22% yield). The remaining brown supernatant was concentrated in vacuo then purified by flash column chromatography (SiO_2, 10% MeOH in $CHCl_3$ to 15% MeOH + 1% *t*-$BuNH_2$ in $CHCl_3$) to yield additional **T18$_A$** (11.18 mg, 27% yield). Total yield of **T18$_A$** (20.51 mg, 49% yield).

* Both the precipitated and columned **T18$_A$** show no evidence of incomplete coupling, however the VT NMR of the precipitated material is sharper and TLC (10% MeOH, 0.5% $^tBuNH_2$ in $CHCl_3$) cleaner than the columned material *

^{1}H NMR (600 MHz, $C_2D_2Cl_4$, 393 K) δ_H = 8.20–8.16 (m, 12H, **H$_b$**), 8.15–8.12 (m, 12H, **H$_f$**), 8.04–8.00 (m, 12H, **H$_a$**), 7.32 (s, 12H, **H$_j$**), 7.27–7.23 (m, 12H, **H$_h$**), 7.22–7.19 (m, 12H, **H$_d$**), 7.14 (d, *J* = 8.4 Hz, 12H, **H$_i$**), 7.10 – 7.06 (m, 36H, **H$_e$**, **H$_{k/l/o/p}$**), 7.02–6.96 (m, 48H, **H$_g$**, **H$_{k/l/o/p}$**), 6.85–6.81 (m, 12H, **H$_m$**, **H$_n$**), 6.72–6.69 (m, 12H, **H$_c$**), 2.33–2.26 (m, 24H, Ar-**C**$\mathbf{H_2}$), 1.23–1.17 (m, 24H, Ar-CH_2-**C**$\mathbf{H_2}$), 0.94–0.69 (m, 120H Ar-$(CH_2)_2$-$\mathbf{(CH_2)_5}$-CH_3), 0.32 (dt, *J* = 14.1, 6.8 Hz, 36H, Ar-$(CH_2)_7$-**C**$\mathbf{H_3}$) ppm.

^{19}F NMR (470 MHz, $CDCl_3$, 298 K) δ_F = –65.64 ppm (referenced against C_6F_6 (δ_F = –161.64) as an internal standard).

^{13}C NMR – (151 MHz, $C_2D_2Cl_4$, 393 K) δ_C = 152.09, 149.94, 149.72, 146.09, 142.29, 138.73, 138.57, 138.12, 135.60, 134.00 (q, J_{FC} = 30.2 Hz), 132.34, 131.58, 131.34, 131.32 (Expected to be CF_3), 130.66, 127.58, 126.11, 124.39, 124.19, 123.61, 122.78, 122.33 (q, J_{FC} = 274.8 Hz), 122.65, 122.16, 121.18, 120.23, 118.90,100.42, 99.72, 93.79, 93.69, 92.62, 91.63, 91.28, 91.18, 91.10, 89.12, 88.72, 83.88, 33.95, 31.58, 30.29, 30.25, 29.33, 29.28, 29.19, 28.93, 28.90, 27.75, 22.28, 13.62.

MALDI-ToF *m/z* 8799.827 (calculated for ($[C_{564}H_{396}F_{72}N_{18}]^{\bullet+}$) = **(M)$^{\bullet+}$**: 8788.046).

2.9.2.12 Synthesis of template T18$_B$

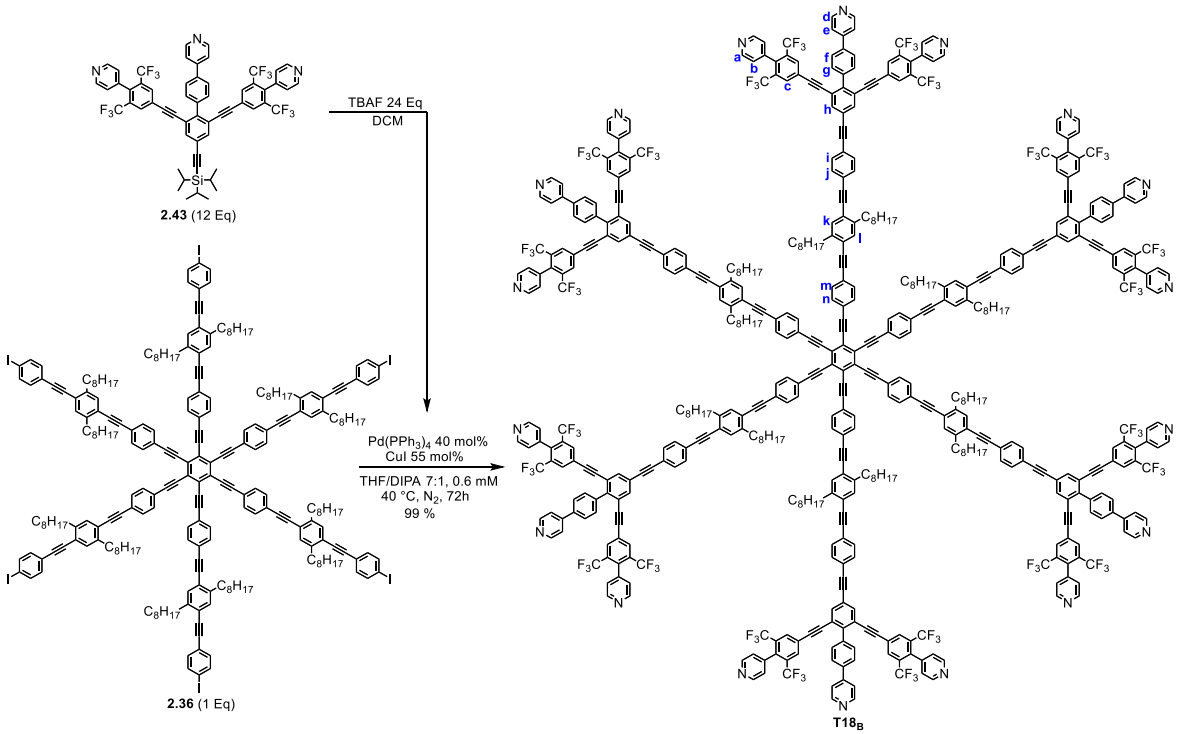

To a stirring solution of **2.43** (29.1 mg, 12 Eq, 28.0 µmol) in CH_2Cl_2 (5 mL) was added TBAF (84 µL, 1.0 M in THF, 24 Eq, 84 µmol). The solution was stirred for 15 minutes then CH_2Cl_2 (2 mL), water (5 mL) and acetic acid (10 µL) were added. The mixture was then poured into a

separating funnel and extracted with chloroform (3 × 10 mL). The organic phase was dried with $MgSO_4$, then concentrated in vacuo and used in the next step without further purification.

In an oven dried Schlenk tube, deprotected **2.43** and **2.36** (9.3 mg, 1 Eq, 2.3 μmol) were dissolved in THF (3.41 mL) and DIPA (487 μL), then freeze-pump-thaw degassed (5×). After refreezing the solution and under a positive pressure of N_2, CuI (0.25 mg, 0.55 Eq, 1.28 μmol) and $Pd(PPh_3)_4$ (1.08 mg, 0.4 Eq, 0.934 μmol) were added. The Schlenk tube was stoppered, evacuated/refilled with N_2 (5×), then stirred at 40 °C for 72 hours.

The crude reaction mixture was concentrated and redissolved in a minimum of chloroform + 3% methanol, then purified by flash column chromatography (SiO_2, chloroform + 3% MeOH, then chloroform + 3% MeOH + 1% $^tBuNH_2$) to yield **T18$_B$** as a yellow film (19.7 mg, 99%).

^{1}H NMR (600 MHz, $CDCl_3$) δ_H = 8.72 – 8.69 (m, 12H, **H$_d$**), 8.67 – 8.64 (m, 24H, **H$_a$**), 7.91 (s, 12H, **H$_h$**), 7.85 (d, *J* = 7.9 Hz, 12H, **H$_f$**), 7.80 – 7.76 (m, 36H, **H$_g$**, **H$_c$**), 7.65 (d, *J* = 7.3 Hz, 12H, **H$_n$**), 7.59 – 7.52 (m, 48H, **H$_e$**, **H$_i$**, **H$_j$**, **H$_m$**), 7.41 (m, 12H, **H$_k$**, **H$_l$**), 7.14 (d, *J* = 5.0 Hz, 24H, **H$_b$**), 2.89 – 2.72 (m, 24H, Ar-**CH$_2$**), 1.78 – 1.66 (m, 24H, Ar-CH$_2$-**CH$_2$**), 1.47 – 1.19 (m, 120H, **-CH$_2$-**), 0.92 – 0.80 (m, 36H, **CH$_3$**).

^{19}F NMR (470 MHz, $CDCl_3$) δ_F = –57.61 ppm (Referenced against C_6F_6 (δ_F = –161.64) as an internal standard).

^{13}C NMR – (151 MHz, $CDCl_3$) δ_C = 150.61, 148.93, 147.48, 146.08, 142.60, 141.94, 138.78, 136.70, 136.04, 132.63, 131.92, 131.81, 131.71, 131.57, 131.37, 131.18, 127.66, 126.44, 124.76, 124.50, 124.27, 123.68, 123.48, 122.78, 122.32, 121.65, 121.53, 119.83, 99.75, 93.84, 91.67, 91.50, 91.03, 90.72, 89.18, 88.89, 34.33, 34.29, 32.06, 30.86, 30.80, 29.75, 29.68, 29.46, 29.43, 28.42, 22.83, 14.28.

MALDI-ToF *m/z* 8506.068 (calculated for ($[C_{540}H_{396}F_{72}N_{18}]^{\bullet+}$) = **(M)$^{\bullet+}$**: 8500.046).

2.9.3 Synthesis of Porphyrin Oligomers and Nanorings

2.9.3.1 Synthesis of $P9_{OOct}(C_2THS)_2$

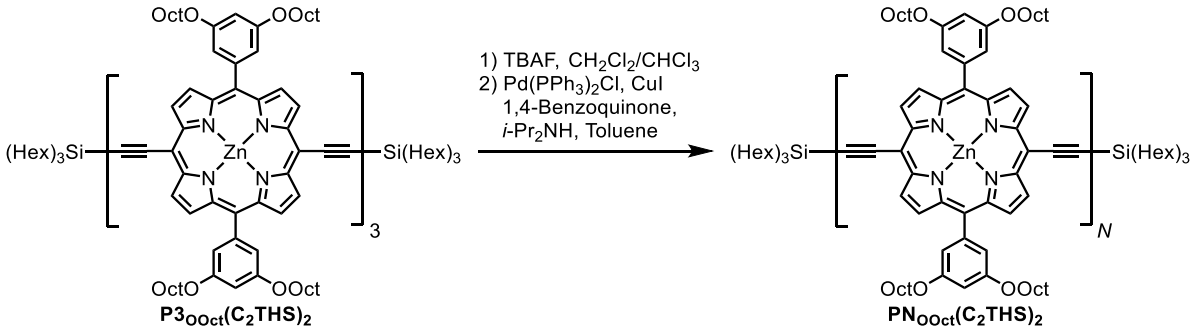

$P3_{OOct}(C_2THS)_2$ (172 mg, 31%), **$P6_{OOct}(C_2THS)_2$** (112 mg, 20%), **$P9_{OOct}(C_2THS)_2$** (75 mg, 13%), **$P12_{OOct}(C_2THS)_2$** (42 mg, 7.6%), **$P15_{OOct}(C_2THS)_2$** (25 mg, 4.5%)

A solution of TBAF (1.0 M in THF, 145 µL, 0.145 mmol) was added to a solution of **$P3_{OOct}(C_2THS)_2$** (553 mg, 0.145 mmol) in $CHCl_3$ (25 mL), CH_2Cl_2 (25 mL), and pyridine (1 mL). The deprotection was monitored by TLC (PE : EtOAc : pyridine = 10 : 1 : 1). Once a desired ratio of bis-deprotected, mono-deprotected, and starting material had been formed, AcOH (20 µL) was added, and the reaction mixture was immediately filtered through a short plug (SiO_2, $CHCl_3$ + 1% pyridine). The filtered mixture was concentrated under reduced pressure and redissolved in toluene (65 mL). A freshly prepared catalyst solution of $Pd(PPh_3)_2Cl_2$ (66 mg, 0.094 mmol), CuI (163 mg, 0.854 mmol), and 1,4-benzoquinone (156 mg, 1.45 mmol) in diisopropylamine (12 mL) and toluene (45 mL) was added to the porphyrin solution, and the reaction mixture was stirred vigorously in an open flask. After one hour, the reaction mixture was filtered through a plug (SiO_2, $CHCl_3$ + 1% pyridine) and concentrated under reduced pressure. The crude oligomer mixture was redissolved in toluene + 1% pyridine (10 mL), passed through a size-exclusion column (Bio-Beads, S-X1, toluene + 1% pyridine) and separated by recycling GPC (toluene + 1% pyridine). Each fraction of separated oligomer was concentrated under reduced pressure and precipitated from MeOH/$CHCl_3$ (ca. 9:1) by layered addition of MeOH onto a solution of oligomer in $CHCl_3$, which yielded each porphyrin oligomer as a solid brown powder.

Isolated yields: **P3$_{OOct}$(C$_2$THS)$_2$** (172 mg, 31%), **P6$_{OOct}$(C$_2$THS)$_2$** (112 mg, 20%), **P9$_{OOct}$(C$_2$THS)$_2$** (75 mg, 13%), **P12$_{OOct}$(C$_2$THS)$_2$** (42 mg, 7.6%), **P15$_{OOct}$(C$_2$THS)$_2$** (25 mg, 4.5%).

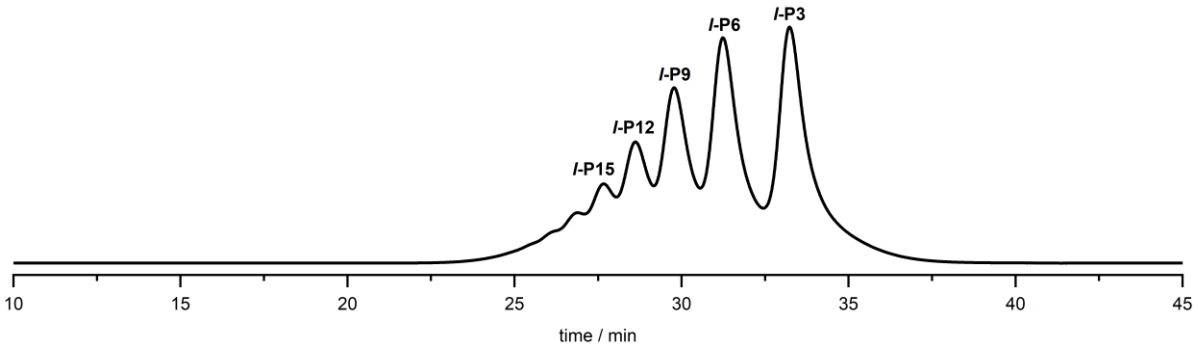

Figure 2.59. Analytical GPC trace of the crude reaction mixture from alkyne homo-coupling of a partially deprotected mixture of **P9$_{OOct}$(C$_2$THS)$_2$** (THF + 1% pyridine, λ = 500 nm).

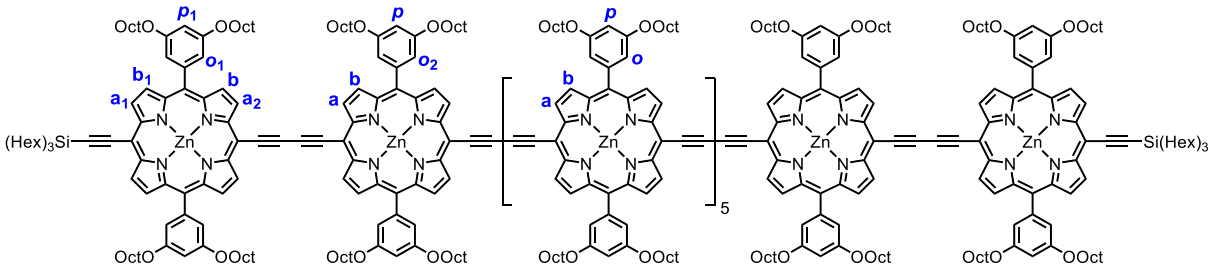

^{1}H NMR (600 MHz, $CDCl_3$, 298 K) δ_H = 9.91–9.87 (m, 28H, a), 9.87 (d, J = 5.1 Hz, 4H, a_2), 9.63 (d, J = 4.5 Hz, 4H, a_1), 9.12–9.04 (m, 32H, b), 8.95 (d, J = 4.5 Hz, 4H, b_1), 7.43–7.42 (m, 20H, *o*), 7.41 (d, J = 2.1 Hz, 8H, o_2), 7.37 (d, J = 2.0 Hz, 8H, o_1), 6.95–6.92 (m, 14H, *p*), 6.91 (t, J = 2.0 Hz, 4H, p_1), 4.31–4.06 (m, 72H, -OCH_2-), 1.96–1.24 (m, 492H, -CH_2-), 1.06–0.82 (m, 126H, -CH_3) ppm.

MALDI-ToF *m/z* 10331 (calculated for $[C_{648}H_{816}N_{36}O_{36}Si_2Zn_9]^{\bullet+}$ = **(M)**$^{\bullet+}$: 10330).

UV-vis-NIR ($CDCl_3$ +1% pyridine, 298 K) λ_{max} (ε / 10^6 M^{-1} cm^{-1}): 469 (1.13), 592 (0.09), 808 (0.63) nm.

2.9.3.2 Oligomerization of Partially Deprotected $P3_{THS}(C_2CPDIPS)_2$

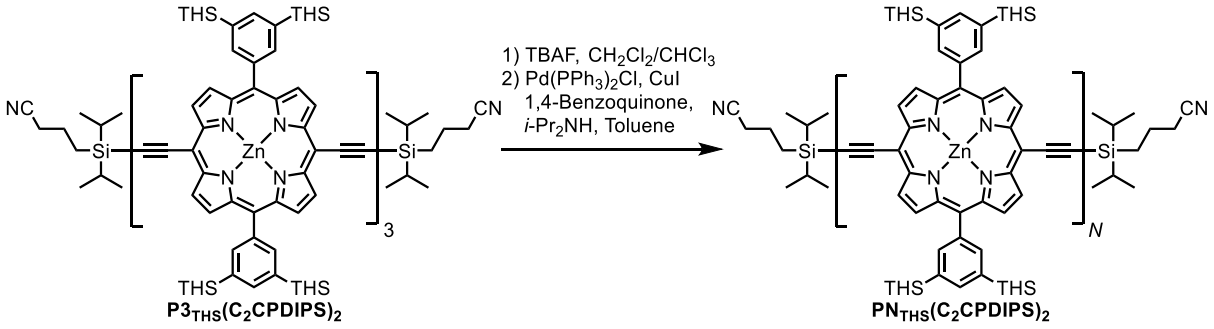

$P3_{THS}(C_2CPDIPS)_2$

$PN_{THS}(C_2CPDIPS)_2$

$P3_{THS}(C_2CPDIPS)_2$ (64 mg, 18%), **$P6_{THS}(C_2CPDIPS)_2$** (58 mg, 16%), **$P9_{THS}(C_2CPDIPS)_2$** (54 mg, 15%), **$P12_{THS}(C_2CPDIPS)_2$** (34 mg, 9.6%), **$P15_{THS}(C_2CPDIPS)_2$** (23 mg, 6.5%)

A solution of TBAF (1.0 M in THF, 65 µL, 65 µmol) was added to a solution of **$P3_{THS}(C_2CPDIPS)_2$** (356 mg, 65 µmol) in $CHCl_3$ (12 mL), CH_2Cl_2 (12 mL), and pyridine (1 mL). The deprotection was monitored by TLC (CH_2Cl_2 : PE = 1 : 4 + 1% pyridine). Once a desired ratio of bis-deprotected, mono-deprotected, and starting material had been formed, AcOH (10 µL) was added, and the reaction mixture was immediately filtered through a short plug (SiO_2, $CHCl_3$ + 1% pyridine). The filtered mixture was concentrated under reduced pressure and redissolved in toluene (20 mL). A freshly prepared catalyst solution of $Pd(PPh_3)_2Cl_2$ (9.1 mg, 13 µmol), CuI (25 mg, 131 µmol), and 1,4-benzoquinone (53 mg, 521 µmol) in diisopropylamine (9 mL) and toluene (20 mL) was added to the porphyrin solution, and the reaction mixture was stirred vigorously in an open flask. After 1.5 h, the reaction mixture was filtered through a plug (SiO_2, $CHCl_3$ + 1% pyridine) and concentrated under reduced pressure. The crude oligomer mixture was redissolved in toluene + 1% pyridine (5 mL), passed through a size-exclusion column (Bio-Beads, S-X1, toluene + 1% pyridine) and separated by recycling GPC (toluene + 1% pyridine). Each fraction of separated oligomer was concentrated under reduced pressure and precipitated from MeOH/$CHCl_3$ (ca. 9:1) by layered addition of MeOH onto a solution of oligomer in $CHCl_3$, which yielded each porphyrin oligomer as a solid brown powder.

Isolated yields: **P3$_{THS}$(C$_2$CPDIPS)$_2$** (64 mg, 18%), **P6$_{THS}$(C$_2$CPDIPS)$_2$** (58 mg, 16%), **P9$_{THS}$(C$_2$CPDIPS)$_2$** (54 mg, 15%), **P12$_{THS}$(C$_2$CPDIPS)$_2$** (34 mg, 9.6%), **P15$_{THS}$(C$_2$CPDIPS)$_2$** (23 mg, 6.5%).

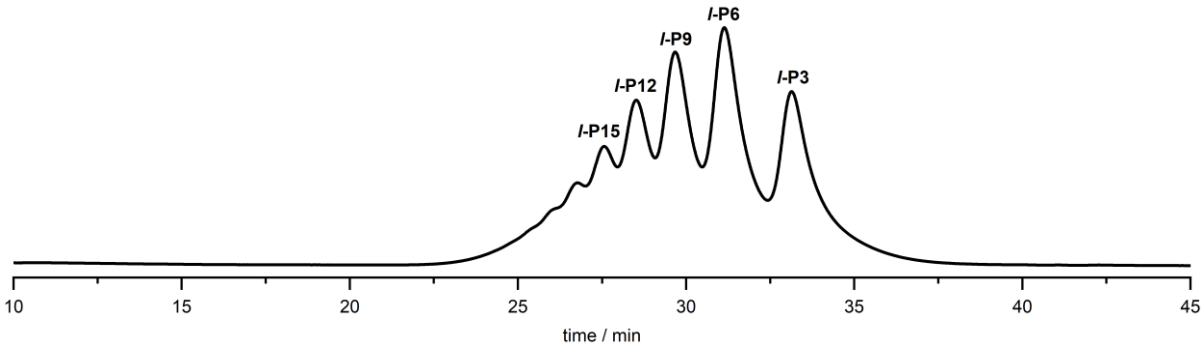

Figure 2.60. Analytical GPC trace of the crude reaction mixture from alkyne homo-coupling of a partially deprotected mixture of **P9$_{THS}$(C$_2$CPDIPS)$_2$** (THF + 1% pyridine, λ = 500 nm).

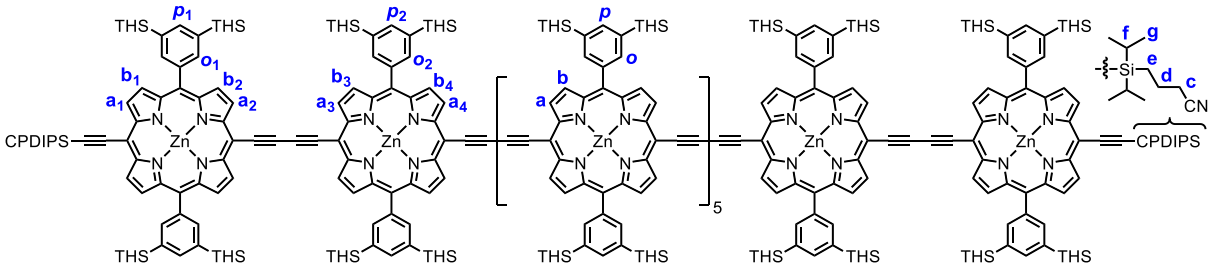

^{1}H NMR (600 MHz, $CDCl_3$, 298 K) δ_H = 9.90–9.86 (m, 28H, a_3 + a_4 + a), 9.86 (d, J = 4.4 Hz, 4H, a_2), 9.62 (d, J = 4.4 Hz, 4H, a_1), 8.96–8.91 (m, 28H, b_3 + b_4 + b), 8.91 (d, J = 4.4 Hz, 4H, b_2), 8.84 (d, J = 4.4 Hz, 4H, b_1), 8.33–8.30 (m, 20H, *o*), 8.30 (s, 8H, o_2), 8.25 (s, 8H, o_1), 8.03–8.01 (m, 10H, *p*), 8.01 (s, 4H, p_2), 7.99 (s, 4H, p_1), 2.54 (t, J = 6.9 Hz, 4H, c), 2.24–2.17 (m, 4H, d), 1.58–1.46 (m, 216H, -CH_2-), 1.46–1.36 (m, 244H, -CH_2- + f + g), 1.36–1.27 (m, 432H, -CH_2-), 1.18–1.15 (m, 4H, e), 0.99 – 0.92 (m, 216H, -CH_2-), 0.91–0.85 (m, 324H, -CH_3) ppm.

MALDI-ToF *m*/*z* 15687 (calculated for $[C_{992}H_{1569}N_{38}Si_{38}Zn_9]^{\bullet+}$ = **(M)**$^{\bullet+}$: 15684).

UV-vis-NIR ($CDCl_3$ +1% pyridine, 298 K) λ_{max} (ε / 10^6 M^{-1} cm^{-1}): 467 (1.21), 592 (0.09), 818 (0.67) nm.

2.9.3.3 Synthesis of *c*-P18$_{OOct}$ from P9$_{OOct}$(C$_2$THS)$_2$ and T6

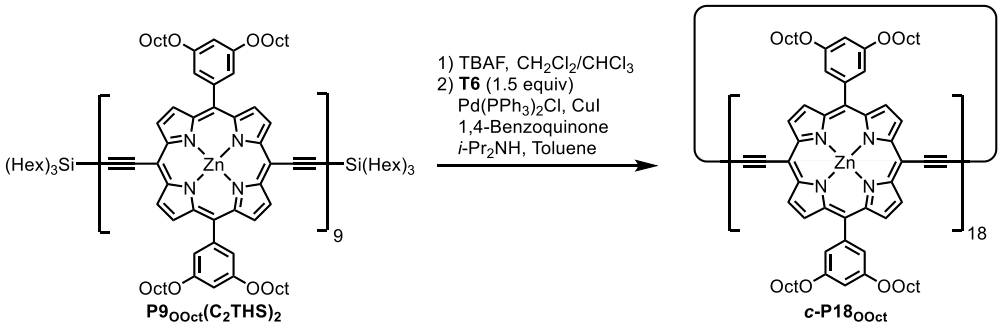

A solution of TBAF (1.0 M in THF, 30 µL, 30 µmol) was added to a solution of **P9$_{OOct}$(C$_2$THS)$_2$** (10.0 mg, 0.968 µmol) in CH_2Cl_2 (5.5 mL) and pyridine (55 µL). After one hour, MeOH (0.2 mL) was added and the reaction volume was reduced to 1/5th its original volume using a stream nitrogen. Additional MeOH (10 mL) was added to induce precipitation. The supernatant was removed after centrifugation and the porphyrin oligomer was washed using MeOH (2 × 10 mL) and dried under reduced pressure to give **P9$_{OOct}$(C$_2$)$_2$** (9.40 mg, 0.960 µmol) as confirmed by MALDI. A solution of **T6** template (1.44 mg, 1.44 µmol, 1.5 equivalents) dissolved in $CDCl_3$ (2.7 mL) and MeOH (0.3 mL) was added to a solution of **P9$_{OOct}$(C$_2$)$_2$** in $CDCl_3$ (9.3 mL) and pyridine (93 µL), and the resulting mixture was sonicated for 10 minutes and concentrated under reduced pressure. The dry mixture was redissolved in $CDCl_3$ (9.3 mL) and sonicated for 10 minutes. A catalyst stock solution was prepared of $Pd(PPh_3)_2Cl_2$ (5.3 mg, 7.6 µmol), CuI (8.0 mg, 42 µmol), and 1,4-benzoquinone (18.6 mg, 172 µmol) in diisopropylamine (0.14 mL) and $CDCl_3$ (2.0 mL). Fresh catalyst stock solution (660 µL) was added to the solution of **P9$_{OOct}$(C$_2$)$_2$** and **T6**, and the reaction mixture was stirred vigorously in an open flask. After 12 h, freshly prepared catalyst stock solution is added for a second time (660 µL) and the reaction mixture was stirred for 5 hours, passed through a short plug (SiO_2, $CHCl_3$ + 1% pyridine), and concentrated under reduced pressure. The crude mixture was redissolved in toluene + 1% pyridine (5 mL), passed through a size-exclusion column (Bio-Beads, S-X1, toluene + 1% pyridine) and separated by recycling GPC (toluene + 1% pyridine).

Each isolated oligomer was concentrated under reduced pressure and precipitated from MeOH/$CHCl_3$ (ca. 9:1) by layered addition of MeOH onto a solution of oligomer in $CHCl_3$, which yielded ***c*-P18$_{OOct}$** (4.28 mg, 46%), and ***c*-P9$_{OOct}$** (0.45 mg, 5%) as solid brown powders.

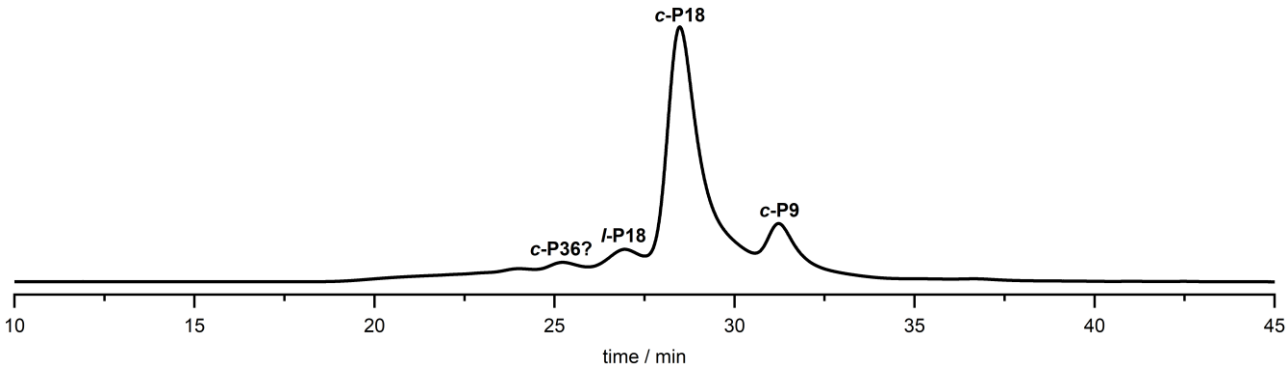

Figure 2.61. Analytical GPC trace of the crude reaction mixture from Vernier-templated alkyne homo-coupling of **P9$_{OOct}$(C$_2$)$_2$** with **T6** (THF + 1% pyridine, λ = 500 nm).

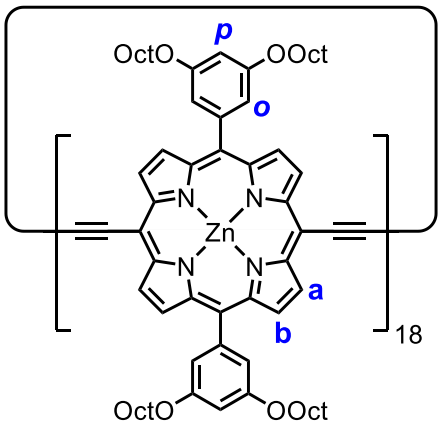

^{1}H NMR (500 MHz, $CDCl_3$, 298 K) δ_H = 9.87 (d, *J* = 4.6 Hz, 72H, **H$_a$**), 9.07 (d, *J* = 4.6 Hz, 72H, **H$_b$**), 7.41 (d, *J* = 1.9 Hz, 72H, **H$_o$**), 6.93 (t, *J* = 1.9 Hz, 36H, **H$_p$**), 4.32–4.05 (m, 144H, **-OCH$_2$-**), 1.97–1.85 (m, 144H, **-CH$_2$-**), 1.61–1.22 (m, 720H, **-CH$_2$-**), 0.91–0.81 (m, 216H, **-CH$_3$**) ppm.

MALDI-ToF *m*/*z* 19449.921 (calculated for $[C_{1224}H_{1476}N_{72}O_{72}Zn_{18}]^{\bullet+}$ = **(M)**$^{\bullet+}$: 19526.142).

UV-vis-NIR ($CDCl_3$ +1% pyridine, 298 K) λ_{max} (ε / 10^5 M^{-1} cm^{-1}): 472 (2.322), 812 (1.563) nm.

2.9.3.4 Synthesis of *c*-P18$_{THS}$ from P9$_{THS}$(C$_2$CPDIPS)$_2$ and T18$_A$

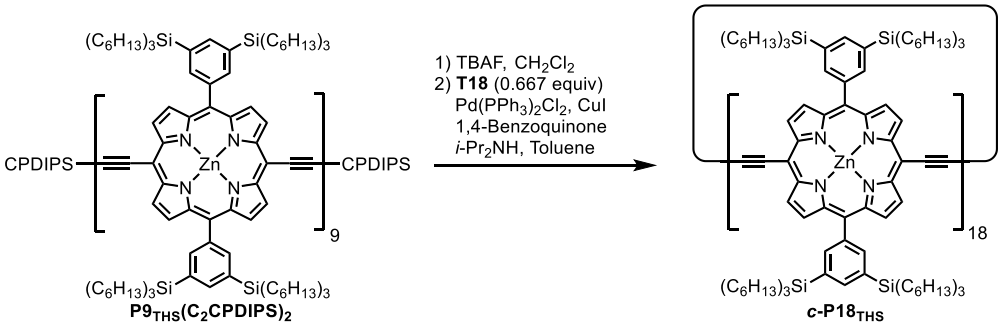

A solution of TBAF (1.0 M in THF, 32 µL, 32 µmol) was added to a solution of **P9$_{THS}$(C$_2$CPDIPS)$_2$** (16.5 mg, 1.05 µmol) in CH_2Cl_2 (6.1 mL) and pyridine (61 µL). After one hour, MeOH (0.3 mL) was added and the reaction volume was reduced to 1/5th its original volume using a stream nitrogen. Additional MeOH (10 mL) was added to induce precipitation. The supernatant was removed after centrifugation and the porphyrin oligomer was washed using MeOH (2 × 10 mL) and dried under reduced pressure to give fully deprotected **P9$_{THS}$(C$_2$)$_2$** (16 mg, 1.0 µmol) as confirmed by MALDI.

A solution of **T18$_A$** template (6.12 mg, 0.696 µmol, 0.667 equivalents) dissolved in $CDCl_3$ (3.93 mL) was added to a solution of **P9$_{THS}$(C$_2$)$_2$** (16.0 mg, 1.04 µmol, 1 equivalent) in $CDCl_3$ (9.91 mL) and the resulting mixture was sonicated for 10 minutes. A catalyst stock solution was prepared of $Pd(PPh_3)_2Cl_2$ (5.3 mg, 7.6 µmol), CuI (8.0 mg, 42 µmol), and 1,4-benzoquinone (18.6 mg, 172 µmol) in diisopropylamine (0.14 mL) and $CDCl_3$ (2.0 mL). Fresh catalyst stock solution (560 µL) was added to the solution of **P9$_{THS}$(C$_2$)$_2$** and **T18$_A$**, and the reaction mixture was stirred vigorously in an open flask. After 12 h, freshly prepared catalyst stock solution was added for a second time (560 µL) and the reaction mixture was stirred for 5 h, passed through a short plug (SiO_2, $CHCl_3$ + 5% pyridine), and concentrated under reduced pressure. The silica plug was then flushed with a mixture of $CHCl_3$:MeOH:*t*-BuNH (84:15:1, 200 mL), and the collected eluent concentrated and subjected to the same purification procedure as described for

T18$_A$, to recover **T18$_A$** (4.88 mg, 80%). The crude reaction mixture was redissolved in toluene + 1% pyridine (5 mL), passed through a size-exclusion column (Bio-Beads, S-X1, toluene + 1% pyridine) and separated by recycling GPC (toluene + 1% pyridine). Each isolated oligomer was concentrated under reduced pressure and precipitated from MeOH/$CHCl_3$ (ca. 9:1) by layered addition of MeOH onto a solution of oligomer in $CHCl_3$, which yielded ***c*-P18$_{THS}$** (4.04 mg, 25%) as a solid brown powder.

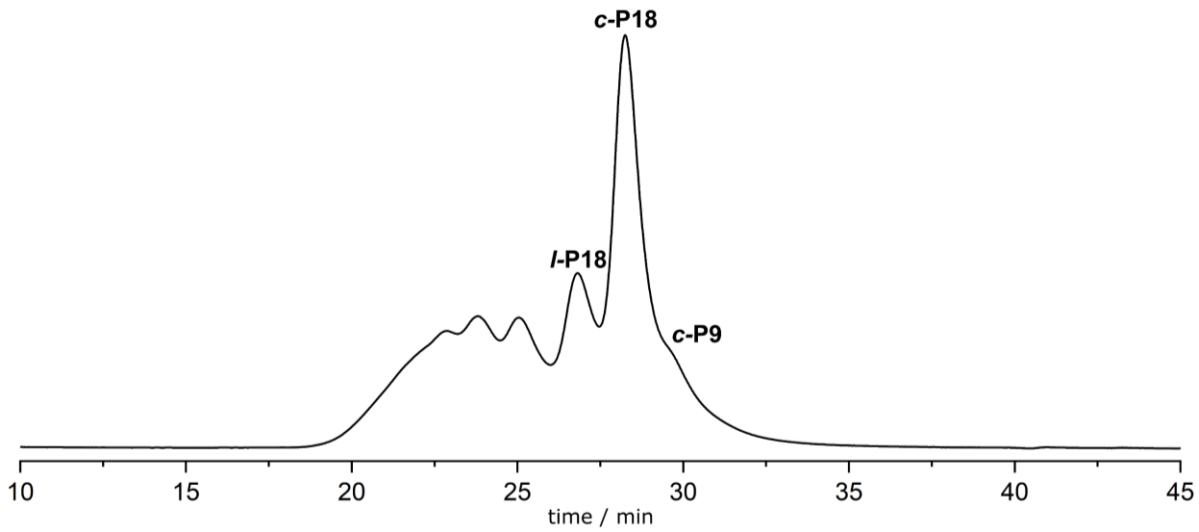

Figure 2.62. Analytical GPC trace of the crude reaction mixture from Vernier-templated alkyne homo-coupling of **P9$_{THS}$(C$_2$)$_2$** with **T18$_A$** (THF + 1% pyridine, λ = 500 nm).

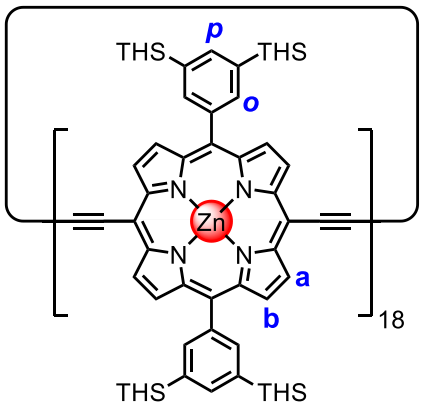

^{1}H NMR (600 MHz, $CDCl_3$) δ 9.86 (d, *J* = 4.6 Hz, 72H, **H$_a$**), 8.93 (d, *J* = 4.5 Hz, 72H, **H$_b$**), 8.30 (s, 72H, **H$_o$**), 8.02 (s, 36H, **H$_p$**), 1.57 – 1.48 (m, 216H, Ar-**CH$_2$**), 1.40 (t, *J* = 7.3 Hz, 216H,

-CH$_2$-), 1.36 – 1.28 (m, 432H, **-CH$_2$-**), 1.00 – 0.94 (m, 216H, **-CH$_2$-**), 0.92 – 0.86 (m, 324H, **-CH$_3$**).

MALDI-ToF *m/z* 30767.8 (calculated for $[C_{1944}H_{3060}N_{72}Si_{72}Zn_{18}]^{\bullet+}$ = **(M)**$^{\bullet+}$: 30639.26).

UV-vis-NIR ($CDCl_3$ +1% pyridine, 298 K) λ_{max} (ε / 10^6 M^{-1} cm^{-1}): 467 (1.645), 486 (1.495), 777 (0.978) nm.

2.9.4 Formation of Nanoring Complexes

2.9.4.1 Formation of *c*-P18$_{OOct}$·T18$_A$

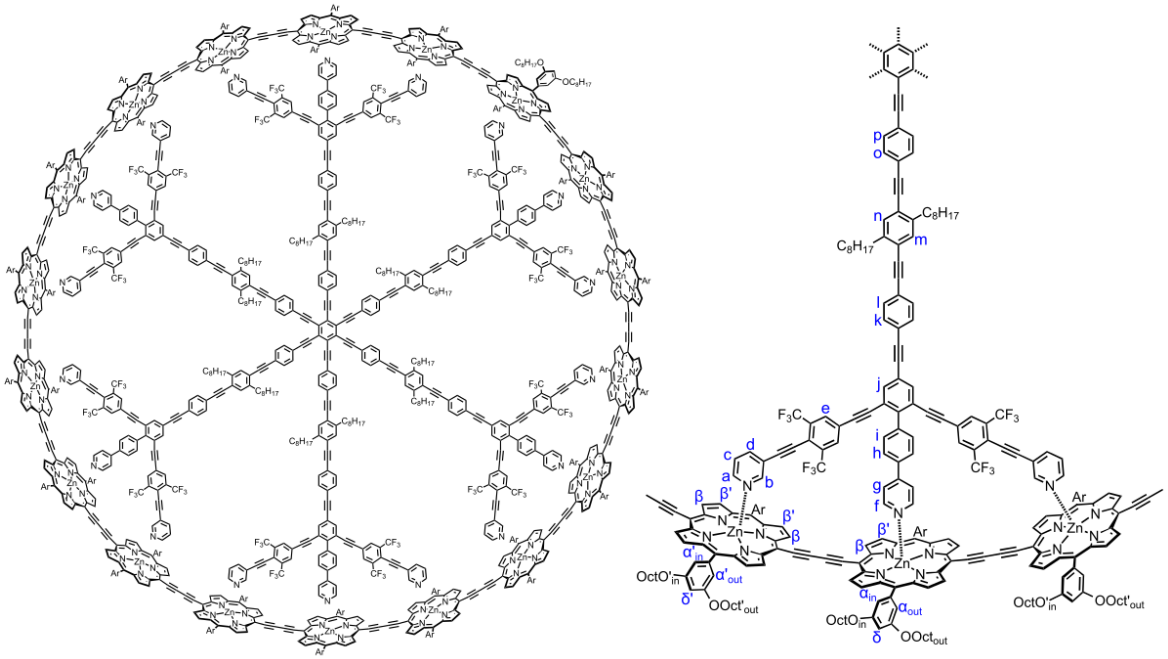

To a dried sample of ***c*-P18$_{OOct}$** (0.60 mg, 1 Eq, 31 nmol) in an NMR tube, was added $CDCl_3$ (450 µL) that had been freshly filtered over Al_2O_3. ^1H and ^{19}F NMR spectra were recorded for this sample after each addition of **T18$_A$** (0.54 mg, 2 Eq, 62 nmol, 3.07×10^{-4} M in $CDCl_3$). The titration was stopped as soon as the free **T18$_A$** fluorine signal was observed ($\delta_F \approx -62.70$ ppm). The NMR sample was dried under a stream of nitrogen then dissolved in 1:1 $CHCl_3$:pentane and passed over a short plug of silica (SiO_2, 1:1 $CHCl_3$:pentane), to remove excess **T18**.

Concentrating this fraction yielded the ***c*-P18$_{OOct}$·T18$_A$** 1:1 complex as a green film (0.66 mg, 76% yield).

T18$_A$ retained on the silica plug was recovered by eluting with $CHCl_3$:MeOH:*t*-$BuNH_2$ 84:15:1.

Characterization of ***c*-P18$_{OOct}$·T18$_A$**:

^{1}H NMR (600 MHz, CD_2Cl_2) δ_H = 9.96–9.86 (m, 72H, **H$_\beta$**), 9.15–9.05 (m, 72, **H$_{\beta'}$**), 7.65 (s, 12H, **H$_j$**), 7.65–7.60 (m, 18H, **H$_p$, H$_{\alpha in}$**), 7.56–7.52 (m, 12H, **H$_o$**), 7.47–7.43 (m, 24H, **H$_k$**, **H$_l$**), 7.43–7.40 (m, 24H, **H$_{\alpha'in}$ + H$_{\alpha'out}$**), 7.40 (s, 24H, **H$_e$**), 7.35–7.32 (m, 12H, **H$_m$**, **H$_n$**), 7.32–7.27 (m, 18H, **H$_i$ + H$_{\alpha out}$**), 6.95 (s, 6H, **H$_\delta$**), 6.93 (s, 12H, **H$_{\delta'}$**), 6.87–6.83 (m, 12H, **H$_h$**), 6.57 (d, *J* = 7.7 Hz, 12H, **H$_d$**), 5.97–5.92 (m, 12H, **H$_g$**), 5.77–5.72 (m, 12H, **H$_c$**), 4.33–4.24 (m, 24H, **(OCH$_2$)$_{in}$**), 4.24–4.07 (m, 120H, **(OCH$_2$)$_{out}$** + **(O'CH$_2$)**), 2.87–2.82 (m, 12H, **H$_f$**), 2.81–2.69 (m, 24H, **Ar-CH$_2$**), 2.81–2.76 (m, 12H, **H$_b$**), 2.76–2.69 (s, 12H, **H$_a$**), 2.00–1.80 (m, 144H, OCH_2-**CH$_2$-**), 1.70 – 1.14 (m, 888H, **-CH$_2$-**), 0.96 – 0.74 (m, 252H, **-CH$_3$**) ppm.

^{19}F NMR (470 MHz, CD_2Cl_2, 298K) δ_F = –63.19 ppm (Referenced against C_6F_6 (δ_F = –162.61) as an internal standard).

MALDI-ToF *m*/*z* 28244.3 (calculated for $[C_{1788}H_{1872}F_{72}N_{90}O_{72}Zn_{18}]^{\bullet+}$ = **(M)$^{\bullet+}$**: 28319.20).

UV-vis-NIR ($CDCl_3$, 298 K) λ_{max} (ε / 10^6 M^{-1} cm^{-1}): 489 (2.396), 812 (2.029) nm.

2.9.4.2 Formation of *c*-P18$_{THS}$·T18$_{A}$

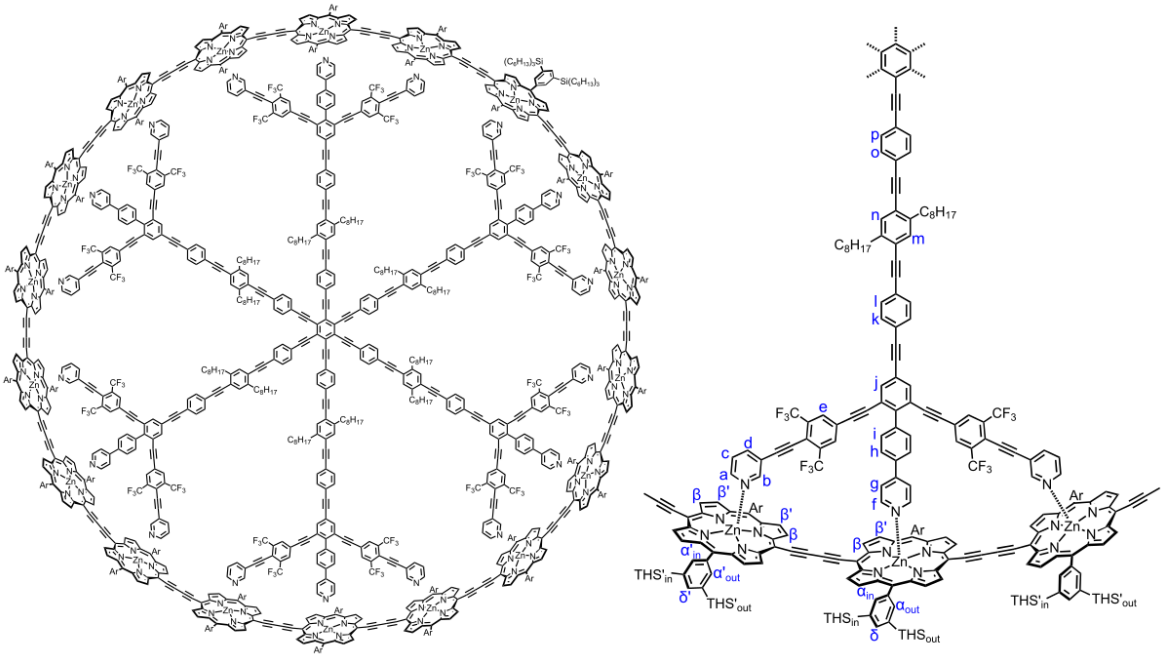

To a dried sample of ***c*-P18$_{THS}$** (4.04 mg, 1 Eq, 132 nmol) in an NMR tube, was added $CDCl_3$ (450 µL) that had been freshly filtered over Al_2O_3. ^{1}H and ^{19}F NMR spectra were recorded for this sample, and after each addition of **T18$_{A}$** (1.74 mg, 1.5 Eq, 198 nmol, 6.59×10^{-4} M in $CDCl_3$). The titration was stopped as soon as a the free **T18$_{A}$** fluorine signal was observed (δ_F = –62.7 ppm). The NMR sample was dried under a stream of nitrogen, then dissolved in 1:1 $CHCl_3$:pentane, and passed over a short plug of silica (SiO_2, 1:1 $CHCl_3$:pentane) to remove excess **T18$_{A}$**. Concentration of this fraction yielded the ***c*-P18$_{THS}$·T18$_{A}$** 1:1 complex as a green film (3.69 mg, 71% yield).

T18$_{A}$ retained on the silica plug was recovered by eluting with $CHCl_3$:MeOH:*t*-$BuNH_2$ 84:15:1.

Characterization of ***c*-P18$_{THS}$·T18$_{A}$**:

^{1}H NMR (600 MHz, CD_2Cl_2) δ 9.99 – 9.82 (m, 72H, **H$_{β}$**), 9.08 – 8.92 (m, 72H, **H$_{β'}$**), 8.59 – 8.53 (m, 12H, **H$_{αin}$**), 8.38 – 8.28 (m, 48H, **H$_{α'}$**), 8.28 – 8.20 (m, 12H, **H$_{αout}$**), 8.09 (s, 12H, **H$_{δ}$**), 8.05 (s, 24H, **H$_{δ'}$**), 7.69 – 7.61 (m, 24H, **H$_{j}$**, **H$_{p}$**), 7.57 – 7.52 (m, 12H, **H$_{o}$**), 7.48 – 7.42 (m, 24H, **H$_{k}$**, **H$_{l}$**), 7.37 – 7.31 (m, 36H, **H$_{e}$**, **H$_{m}$**, **H$_{n}$**), 7.29 – 7.25 (m, 12H, **H$_{i}$**), 6.84 – 6.80 (m, 12H, **H$_{h}$**),

6.58 – 6.53 (m, 12H, **H$_d$**), 5.96 – 5.89 (m, 12H, **H$_g$**), 5.74 – 5.68 (m, 12H, **H$_c$**), 2.92 – 2.87 (m, 12H, **H$_f$**), 2.87 – 2.83 (m, 12H, **H$_b$**), 2.82 – 2.68 (m, 36H, **H$_a$**, **Ar-CH$_2$**), 1.68 – 0.73 (m, 2988H, **THS+Octyl**).

^{19}F NMR (470 MHz, CD_2Cl_2, 298K) δ_F = –63.21 ppm (referenced against C_6F_6 (δ_F = –162.61) as an internal standard).

MALDI-ToF *m/z* 39468.6 (calculated for $[C_{2508}H_{3456}F_{72}N_{90}Si_{72}Zn_{18}]^{\bullet+}$ = **(M)**$^{\bullet+}$: 39395).

UV-vis-NIR ($CDCl_3$, 298 K) λ_{max} (ε / 10^6 M^{-1} cm^{-1}): 471 (3.222), 488 (3.299), 818 (2.432) nm.

2.9.4.3 Formation of *c*-P18$_{THS}$·T18$_B$

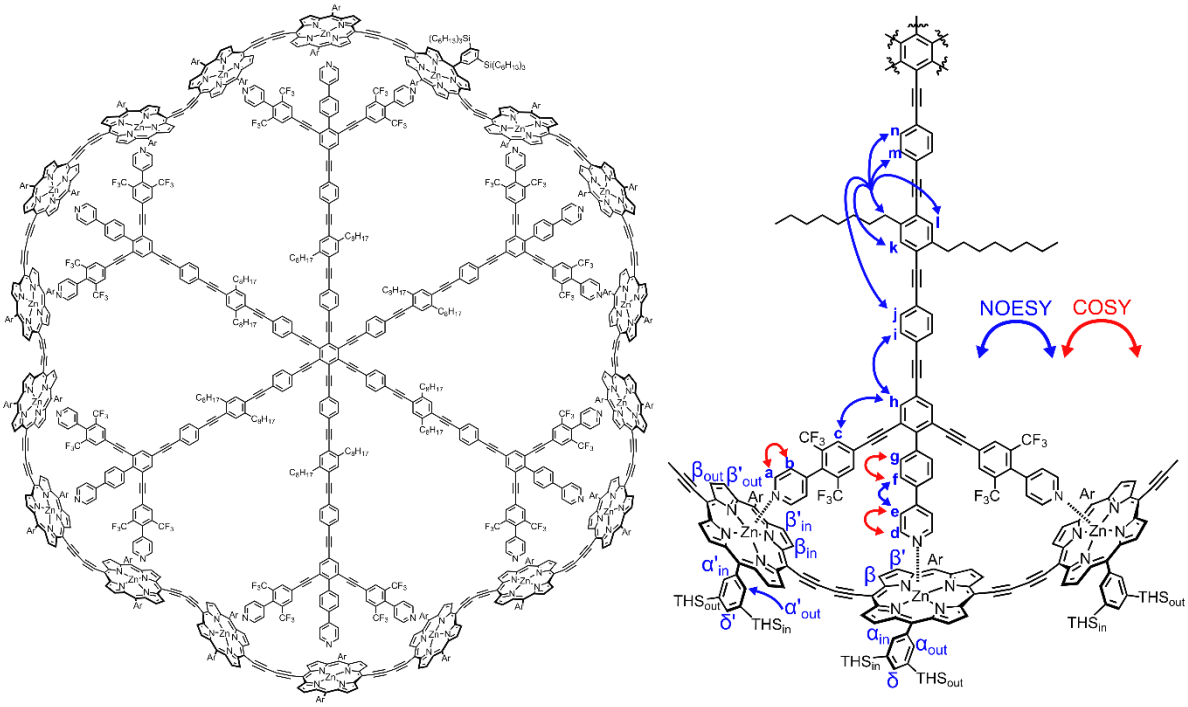

To a dried sample of ***c*-P18$_{THS}$** (0.795 mg, 1 Eq, 26 nmol) in an NMR tube, was added $CDCl_3$ (450 µL) that had been freshly filtered over Al_2O_3. ^{1}H and ^{19}F NMR spectra were recorded for this sample, and after each addition of **T18$_B$** (1.10 mg, 1.1 Eq, 29 nmol, 1.77×10^{-4} M in $CDCl_3$). The titration was stopped as soon as a the free **T18$_B$** fluorine signal was observed. The NMR

sample was dried under a stream of nitrogen, then dissolved in 1:1 $CHCl_3$:pentane, and passed over a short plug of silica (SiO_2, 1:1 $CHCl_3$:pentane) to remove excess **T18$_B$**. Concentration of this fraction yielded the ***c*-P18$_{THS}$·T18$_B$** 1:1 complex as a green film (0.77 mg, 76% yield).

T18$_B$ retained on the silica plug was recovered by eluting with $CHCl_3$:MeOH:*t*-$BuNH_2$ 84:15:1.

Characterization of ***c*-P18$_{THS}$·T18$_B$**:

^{1}H NMR (600 MHz, CD_2Cl_2) δ 9.96 (s, 4H, **H$_{βout}$**), 9.86 (s, 4H, **H$_β$**), 9.74 (s, 4H, **H$_{βin}$**), 9.03 (s, 4H, **H$_{β'out}$**), 8.95 (s, 4H, **H$_{β'}$**), 8.92 (s, 4H, **H$_{β'in}$**), 8.55 (s, 2H, **H$_{αin}$**), 8.40 (s, 8H, **H$_{α'}$**), 8.21 (s, 2H, **H$_{αout}$**), 8.11 (s, 6H, **H$_δ$**, **H$_{δ'}$**), 7.61 – 7.55 (m, 2H, **H$_{i/j/m/n}$**), 7.53 (s, 2H, **H$_h$**), 7.48 (d, J = 8.9 Hz, 2H, **H$_{i/j/m/n}$**), 7.39 – 7.31 (m, 4H, **H$_{i/j/m/n}$**), 7.28 (s, 1H, **H$_{k/l}$**), 7.25 (s, 1H, **H$_{k/l}$**), 7.19 – 7.14 (m, 2H, **H$_f$**), 7.12 (s, 4H, **H$_c$**), 6.74 – 6.64 (m, 2H, **H$_g$**), 5.81 – 5.73 (m, 2H, **H$_e$**), 5.45 – 5.38 (m, 4H, **H$_b$**), 2.92 – 2.86 (m, 2H, **H$_d$**), 2.87 – 2.79 (m, 4H, **H$_a$**), 2.75 – 2.62 (m, 4H, **Ar-CH$_2$**), 1.65 – 0.79 (m, 2988H, **THS+Octyl**).

^{19}F NMR (470 MHz, $CDCl_3$, 298K) δ_F = –58.67 ppm (referenced against C_6F_6 (δ_F = –161.64) as an internal standard).

MALDI-ToF *m*/*z* 39279.252 (calculated for $[C_{2484}H_{3456}F_{72}N_{90}Si_{72}Zn_{18}]^{\bullet+}$ = $(M)^{\bullet+}$: 39146.025).

UV-vis-NIR ($CDCl_3$, 298 K) λ_{max} (ε / 10^6 M^{-1} cm^{-1}): 496 (1.216), 870 (1.622) nm.

3

Properties of *c*-P18·T18$_{A/B}$

Contents

Chapter 3 - Properties of *c*-P18·T18$_{A/B}$

3.1 Molecular Dynamics Simulations of P3·T3$_{A/B}$ and *c*-P18·T18$_{A/B}$

3.1.1 A Brief Introduction to Molecular Dynamics

To supplement the molecular modelling completed in Section 2.2, molecular dynamics (MD) simulations were completed on all trimeric and cyclic complexes present in this project. These calculations were completed by Janko Hergenhahn and specifically undertaken to investigate the expected differences between the A and B versions of the templates, prior to the synthesis of **T18$_B$**.

Molecular dynamics simulations aim to model the behavior of a molecular system over time as they move in a simulated solution.[1] Due to the large number of atoms (molecule of interest + solvent) and time scale (2 fs step size for 200 ns (**P3**) and 50 ns (***c*-P18**) in this work) over which these simulations run, molecular mechanics methods are typically used as they are less computationally expensive than higher level methods such as DFT. In this work we used the General AMBER Force Field,[2] with parameters added to specifically improve the modelling of porphyrin units, which were derived from experimental data[3, 4] (Full methodology in section 3.8).

MD simulations contrast the calculations in Section 2.2, which focused on the lowest energy conformation of the complexes studied. In this regard, MD can provide useful insights into the stability of supramolecular complexes, by the exploration of geometries that lie close to the energetic global minimum. For a rigid, tightly bound complex, it is expected that MD simulations would show little variance in geometry to that of the global minimum. Conversely, MD simulations of a more flexible or weakly bound complexes, would explore a wider range of geometries around the global minimum, because of the lower energy barrier required to reach these geometries.[1] In the context of this project, we hoped MD simulations would predict some differences in the rigidity of the various complexes and inform us on the relative degrees of π-

conjugation between the A and B complexes. This information would support our rationalizations of the photophysical properties of these complexes, which are discussed later in this chapter.

3.1.2 Simulations and UV-Vis Spectroscopy of P3·T3 Complexes

MD simulations were first conducted on a butadiyne-linked porphyrin trimer **P3** with either: no template, **T3A** bound, **T3B** bound, or the previously reported **T3*** bound (Figure 3.1). The results of these simulations have been summarized into Figure 3.2 which displays 2D histograms of the two dihedral angles between the central and peripheral porphyrin groups in each complex.

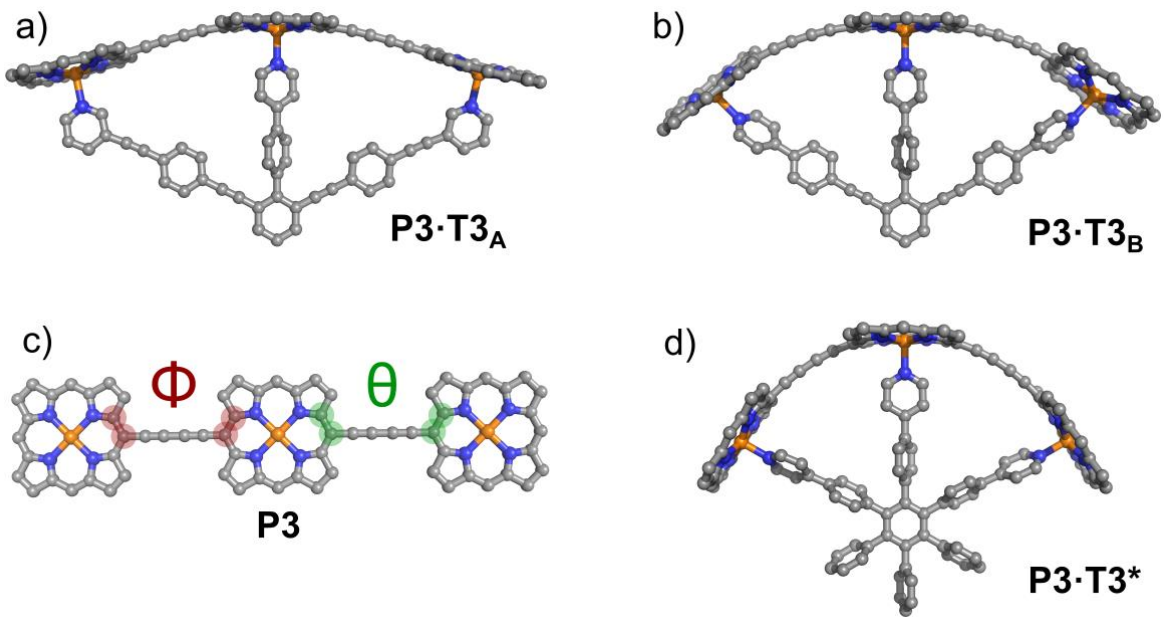

Figure 3.1 Models of (a) **P3·T3A**, (b) **P3·T3B**, (c) **P3** and (d) **P3·T3***.

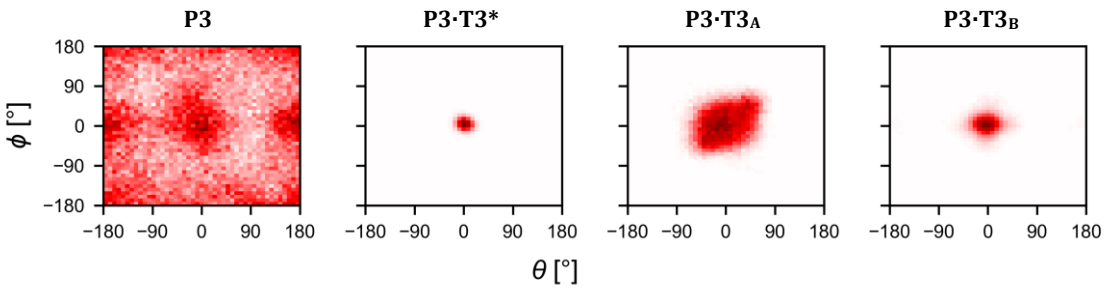

Figure 3.2 2D histograms of the dihedral angles between porphyrins in **P3**, **P3·T3***, **P3·T3A** and **P3·T3B**.

In the free trimer (**P3**), we see the expected broad distribution of dihedral angles, due to the lack of any constraint on the oligomer. A noticeable bias toward 0° and 180° is however observed, which we attribute to the energetic stabilization afforded through the increased π-conjugation in these geometries. This rationale also explains the 4 nodes seen when each dihedral is at ±90°, as these are the positions of least π-conjugation. **T3*** appears to form an exceptionally rigid complex with **P3**, locking both dihedral angles at 0°. This computational result is supported by the experimental UV-Vis spectrum of **P3·T3***, which shows a dramatic red shift in the Q-band (+61 nm) of **P3** upon binding **T3***, due to the increased π-conjugation of the complex (Figure 3.3).[5]

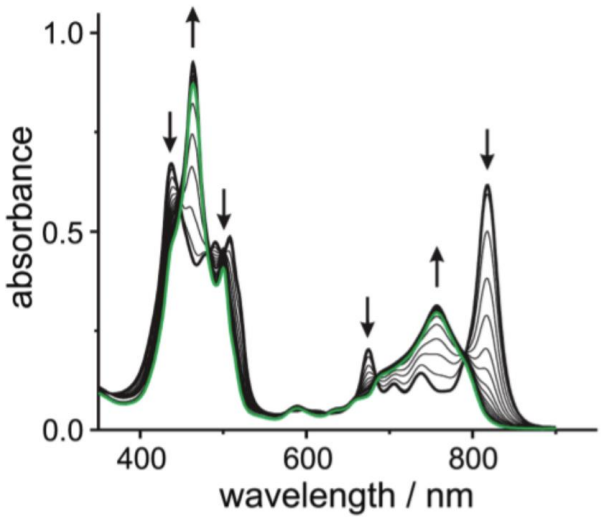

Figure 3.3 Titration of pyridine into **P3·T3*** monitored by UV-Vis spectroscopy ($CHCl_3$ at 298 K). Black trace is **P3·T3***. Green trace is **P3·Py3.** Figure reproduced from reference.[5]

The **P3·T3$_B$** complex has a remarkably similar MD plot to **P3·T3***, whereas **P3·T3$_A$** shows significant conformation flexibility, by the almost uniform exploration of all dihedral angles from +45° to - 45°. We propose that the primary factor causing this difference is the meta vs para link to the peripheral pyridyl groups in **T3$_A$** and **T3$_B$**. As discussed in Section 2.2, the meta linkage in **T3$_A$** creates an internal rotation which alters the direction of the nitrogen lone pair. Opposing rotations of this group at each side of **T3$_A$,** combined with a rotation about the C2 axis of the complex, results in a deviation of both measured dihedral angles from 0° (Figure 3.4). The conformations formed through this rotation must lie close in energy to the planar

global minimum, as they are relatively evenly explored in the time scale of the MD simulation (200 ns). Furthermore, the limit of this rotation appears to be +45°, as a dramatic reduction in the histogram intensities are observed past this point. We therefore expect that passing this threshold requires breaking the N-Zn interaction, which is energetically expensive, and therefore not accessible under the conditions of the MD simulation (300 K, 1 bar, explicit chloroform).

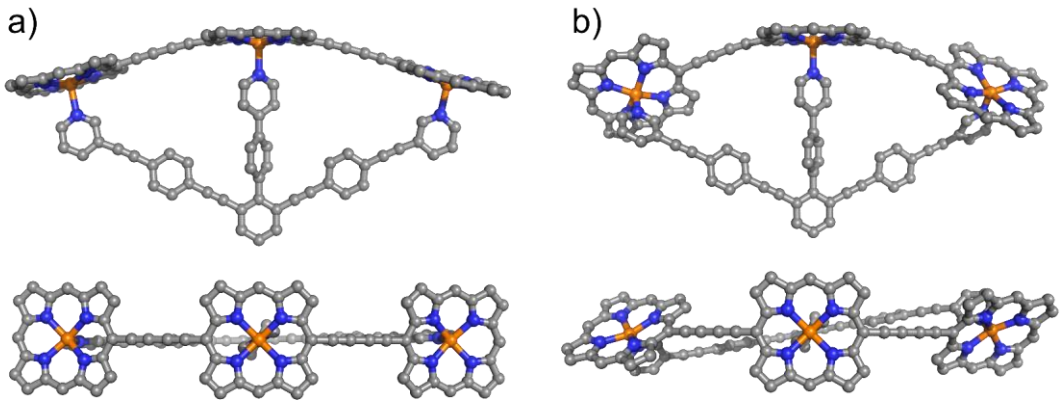

Figure 3.4 (a) DFT (B3LYP/6-31g(d)) optimized model of **P3·T3$_A$**. Structure from (a) twisted to demonstrate the dihedral angle variance seen in the MD simulations.

The rotation described for **T3$_A$** is not possible with **T3$_B$** or **T3***, as rotation of the para-pyridyl group does not affect the direction of the pyridyl nitrogen lone pair. This explains the reduced distribution of the dihedral angles in these complexes. However, **P3·T3$_B$** still displays a noticeably larger distribution than **P3·T3***. This can possibly be attributed to the poorer alignment of the pyridyl nitrogen's lone pair with the zinc dz^2 orbital in **P3·T3$_B$** allowing for slightly more rotation (Figure 3.1).

After the synthesis of **T3$_A$**, **T3$_B$** and **P3$_{THS}$(C$_2$CPDIPS)$_2$,** the complexes **P3$_{THS}$(C$_2$CPDIPS)$_2$·T3$_A$** and **P3$_{THS}$(C$_2$CPDIPS)$_2$·T3$_B$** were formed and their UV-Vis spectra measured. These data are shown in Figure 3.5 and match our expectations from the MD simulations. Free **P3$_{THS}$(C$_2$CPDIPS)$_2$** has the most blue shifted and broadest Q-band, which red shifts and sharpens when **T3$_A$** is added. Binding **T3$_B$** produces the most red shifted and

sharpest Q-band, as a result of the increased π-conjugation and conformational rigidity previously discussed in this chapter.

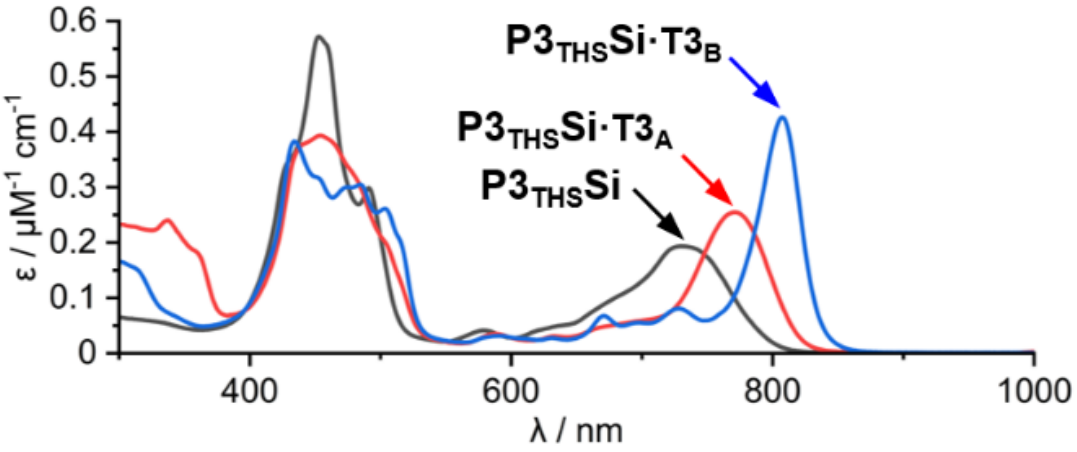

Figure 3.5 UV-Vis spectrum of **P3$_{THS}$(C$_2$CPDIPS)$_2$**, **P3$_{THS}$(C$_2$CPDIPS)$_2$·T3$_A$** & **P3$_{THS}$(C$_2$CPDIPS)$_2$·T3$_B$** ($CHCl_3$ at 298 K).

3.1.3 Simulations and UV-Vis Spectroscopy of *c*-P18·T18 Complexes

The higher conformational rigidity and increased π-conjugation promoted by the **T3$_B$** ligand encouraged us that it may perform as a better component of a **T18** template than **T3$_A$**. As we expect global ring currents to be formed and sustained more readily in macrocycles with greater π-conjugation. This is despite the warped geometry observed in the energy minimized structure of ***c*-P18·T18$_B$**, which we confirmed by ^{1}H NMR of the ***c*-P18$_{THS}$·T18$_B$** complex (Section 2.5.3). To further assess these templates, we next performed MD simulations on ***c*-P18**, ***c*-P18·T18$_A$** and ***c*-P18·T18$_B$** (Figure 3.6).

From the MD simulations, we first note that ***c*-P18** in the absence of any template shows an average of between 2-3 porphyrins aligned (porphyrin-porphyrin dihedral < 45°) at any given point in the simulation. From this baseline, we observe that the addition of **T18$_A$** pushes this distribution to a higher average number of aligned porphyrin units, but that this distribution is broad; ranging from 2-13 aligned units, centered about 6. In comparison, the addition of **T18$_B$** shifts the distribution sharply to an almost perfectly aligned geometry, with predominantly 18 porphyrin units aligned at any given time.

As with the **P3·T3** series, after the synthesis of **T18$_A$**, **T18$_B$** and ***c*-P18$_{THS}$**, the complexes ***c*-P18$_{THS}$·T18$_A$** and ***c*-P18$_{THS}$·T18$_B$** were formed and their UV-Vis spectrum measured, along with that of ***c*-P18$_{THS}$**. These data are shown in Figure 3.7, which again match our expectations from the MD simulations. ***c*-P18$_{THS}$** has the most blue shifted and broadest Q-band, which sharpens and red shifts with the addition of **T18$_A$**, and even more so with **T18$_B$**. This trend is a direct reflection of the increasing π-conjugation generated by the complexation of each template, as predicted by the MD simulations.

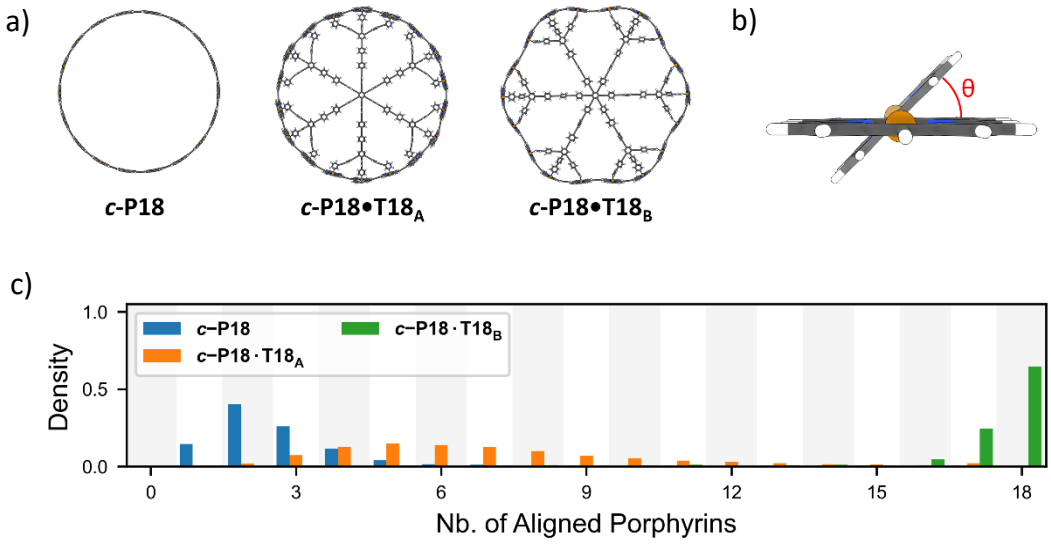

Figure 3.6 (a) Structures of ***c*-P18**, ***c*-P18·T18$_A$** and ***c*-P18·T18$_B$** (b) Dihedral angle measured in the MD simulation, shown here at a 45° angle, which was used a cut off for alignment. (c) Plot from the MD simulation data showing the distribution of aligned porphyrin units in each structure.

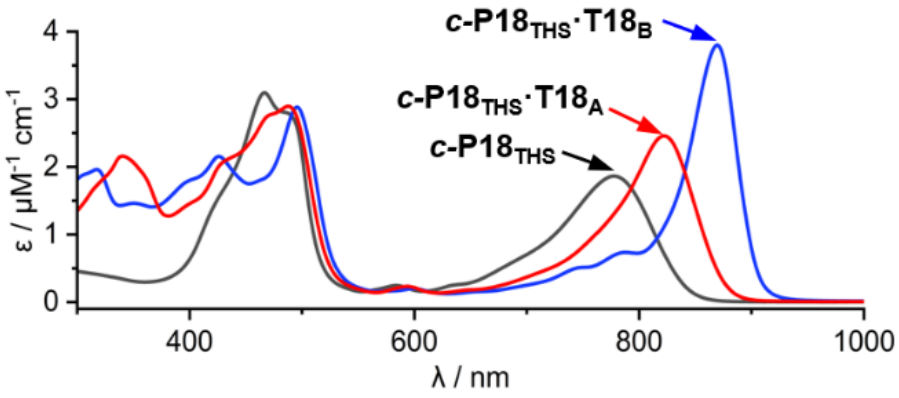

Figure 3.7 UV-Vis spectrum of ***c*-P18$_{THS}$**, ***c*-P18$_{THS}$·T3$_A$** and ***c*-P18$_{THS}$·T3$_B$** ($CHCl_3$ at 298 K)

These results are particularly important in the context of the oxidative NMR titrations, as we expect disruptions in the π-circuit of π-conjugated macrocycles will hinder the formation of global ring currents, therefore eliminating global aromaticity in these macrocycles. The results of these MD simulations and UV-Vis data indicate that the **T18$_B$** template is a more appropriate template for the study of global aromaticity in ***c*-P18.**

Finally, we found it interesting to compare the ***c*-P18** results with those of the previously studied ***c*-P12$_{THS}$·(T6$_e$)$_2$** complex, which is confirmed to be globally aromatic in the +6 state.[6] Figure 3.8 shows the MD results obtained for this complex and in Figure 3.9 the UV-Vis spectrum of ***c*-P12$_{THS}$·Py$_{12}$** and ***c*-P12$_{THS}$·(T6$_e$)$_2$.** Both sets of data indicate that ***c*-P18$_{THS}$·T18$_B$** is more comparable to ***c*-P12$_{THS}$·(T6$_e$)$_2$** as they have a more similar percentage of porphyrin units aligned and show similarly sharp and red shifted UV-Vis spectra.

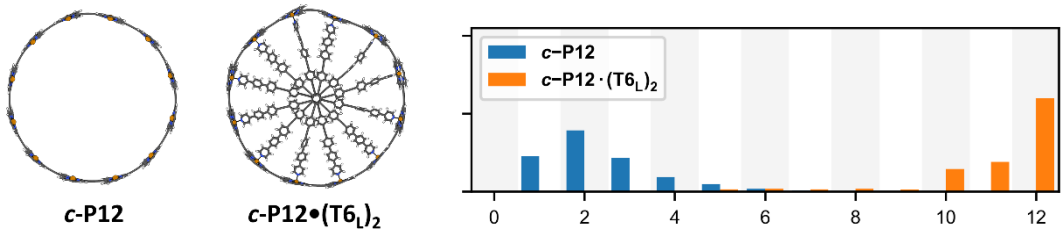

Figure 3.8 (a) Structures of ***c*-P12** and ***c*-P12·(T6$_e$)$_2$** (b) Plot from the MD simulation of ***c*-P12·(T6$_e$)$_2$** showing the distribution of aligned porphyrin units in each structure.

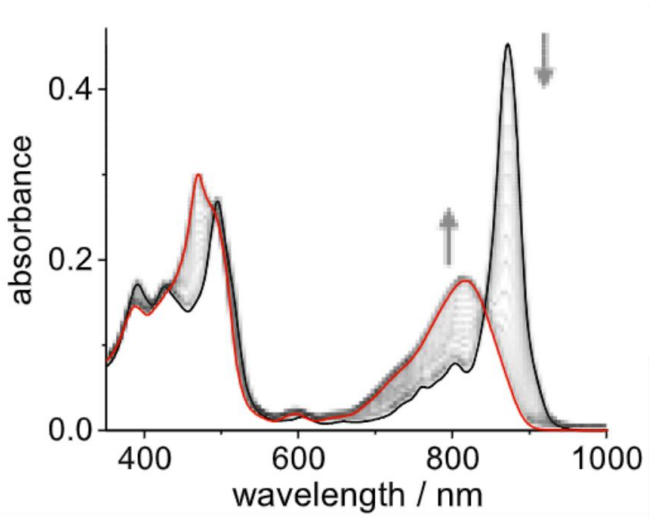

Figure 3.9 Titration of pyridine into ***c*-P12$_{THS}$·(T6$_e$)$_2$** monitored by UV-Vis spectroscopy ($CHCl_3$ at 298 K)**.** Black trace is ***c*-P12$_{THS}$·(T6$_e$)$_2$.** Red trace is ***c*-P12$_{THS}$·Py$_{12}$.** Reproduced from reference.[7]

3.2 UV-Vis-IR and Fluorescence Binding Studies of $P_3THS{\cdot}T3_{A/B}$ and *c*-$P18_{THS}{\cdot}T18_{A/B}$

3.2.1 $P3_{THS}(C_2CPDIPS)_2{\cdot}T3_{A/B}$: Formation, Denaturation and Competition Titrations

We next performed binding titrations on the **$P3_{THS}(C_2CPDIPS)_2{\cdot}T3_{A/B}$** complexes, which were monitored by UV-Vis spectroscopy (Figure 3.10 and Figure 3.11). In these experiments either **$T3_A$** or **$T3_B$** was titrated into a solution of **$P3_{THS}(C_2CPDIPS)_2$**. To analyze the binding the change in Q-band absorbance of both data sets were fit to the 1:1 binding model[8] (Eq 3.1) with the following parameters: K_f (formation constant), $[H]_0$ (Porphyrin concentration) and $[L]_0$ (Ligand concentration). $(A-A_0)/(A_f-A_0)$ can be simplified as the difference in absorption between two wavelengths throughout the titration, which in these experiments was the difference between the bound and unbound Q-band λ_{max}. These titrations show strong binding for both **T3** units, with magnitudes of K_f greater than $1x10^7$ M^{-1} (**$P3_{THS}{\cdot}T3_A$ K_f** = 1.86 x 10^9 M^{-1}, **$P3_{THS}{\cdot}T3_B$ K_f** = 5.92 x 10^7 M^{-1}). The 1:1 binding isotherm is not reliable for determining formation constants this large, as it fits binding data similarly well for all K_f values with magnitude greater than $1x10^6$ M^{-1}.[7]

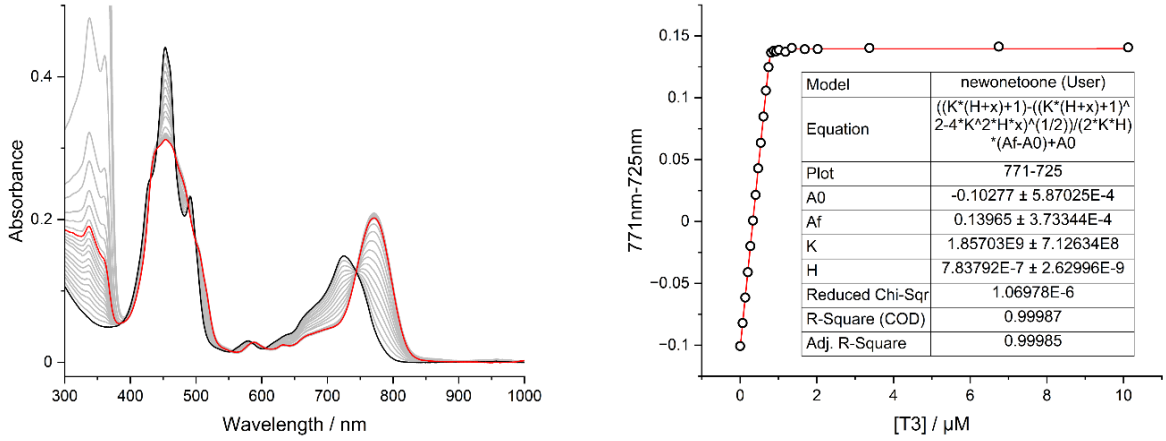

Figure 3.10 (left) Raw data from the titration of **$T3_A$** into **$P3_{THS}(C_2THS)_2$**. (right) Difference in Q-band absorbance fit to the 1:1 binding model (Eq. 3.1)(298 K, $CDCl_3$ filtered over Al_2O_3, rt)

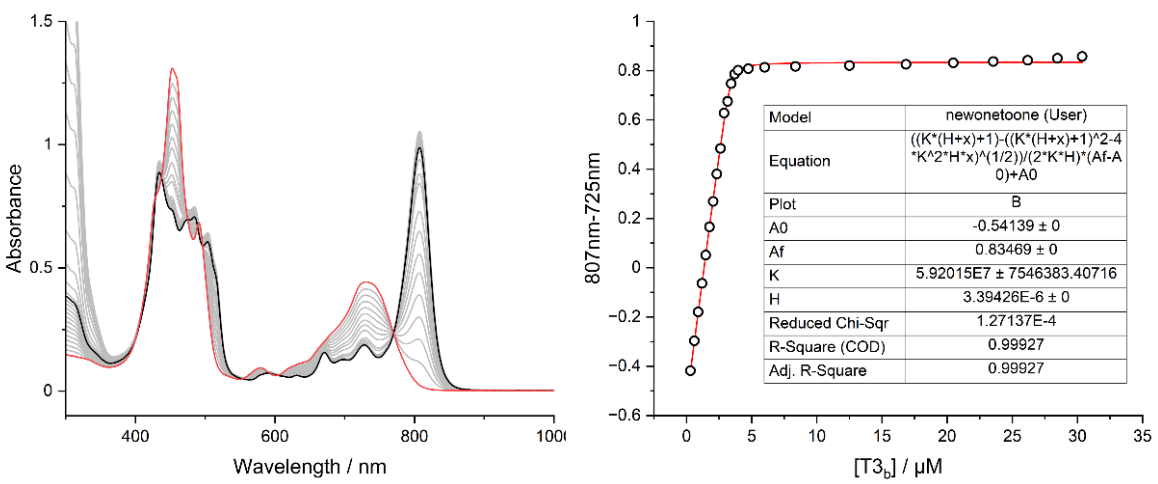

Figure 3.11 (left) Raw data from the titration of **T3B** into **P3THS(C2THS)2**. (right) Difference in Q-band absorbance fit to the 1:1 binding model (Eq. 3.1) (298 K, $CDCl_3$ filtered over Al_2O_3, rt)

$$\frac{A-A_0}{A_f-A_0} = \frac{(K_f([\mathrm{H}]_0+[\mathrm{L}]_0)+1)-\sqrt{(K_f([\mathrm{H}]_0+[\mathrm{L}]_0)+1)^2-4K_f^2[\mathrm{H}]_0[\mathrm{L}]_0}}{2K_f[\mathrm{H}]_0} \qquad \text{Eq 3.1}$$

To more accurately determine the formation constants, titrations were conducted in which pyridine was titrated into the **P3THS(C2CPDIPS)2·T3A/B** complexes and the denaturation to **P3THS(C2CPDIPS)2·Py3** monitored by UV-Vis spectroscopy. The data from these titrations (Figure 3.12 and 3.13) were fit to the knockout model[8] (Eq 3.2) with the following parameters: K_{dn} (denaturation constant), $[H]_0$ (concentration of porphyrin species), $[Py]_0$ (concentration of pyridine) and n (number of sites = 3). Fitting these data to the model outputs K_{dn} for each complex as the following: **P3THS·T3A** K_{dn} = 120±10 M^{-2}, **P3THS·T3B** K_{dn} = (1.57±0.09) x 10^4 M^{-2}. Considering the scheme shown in Figure 3.14, the formation constant of each complex can be calculated from K_{dn} and the binding constant of pyridine to a porphyrin monomer (K_f = (1.47 ± 0.05) x 10^4 M^{-1}, see experimental), which was obtained by fitting the 1:1 binding isotherm in Eq 3.1 to formation titrations of the **P1THS(C2CPDIPS)2·Py** complex. Note that due to the weak binding of pyridine to **P1THS(C2CPDIPS)2** (K_f = 1.47 ± 0.05) x 10^4 M^{-1}) the 1:1 binding model is an appropriate method for calculating Kf.

$$\frac{A-A_0}{A_f-A_0} = \frac{-K_{dn}[\mathrm{Py}]_0^n + \sqrt{K_{dn}^2[\mathrm{Py}]_0^{2n} + 4K_{dn}[\mathrm{Py}]_0^n[H]_0}}{2[H]_0} \qquad \text{Eq 3.2}$$

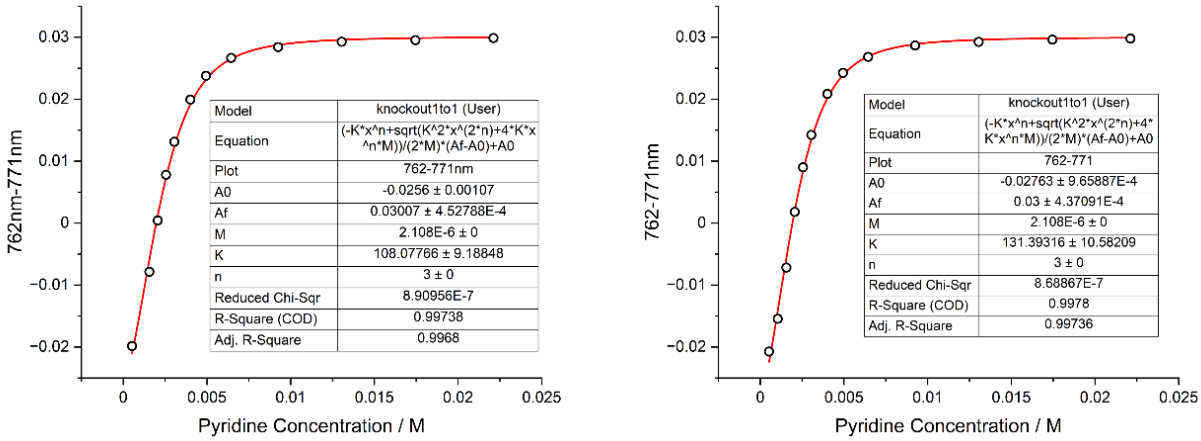

Figure 3.12. Change in Q-band absorbance during titration of pyridine into **P3$_{THS}$(C$_2$CPDIPS)$_2$·T3$_A$** ($CDCl_3$ filtered over Al_2O_3, rt).

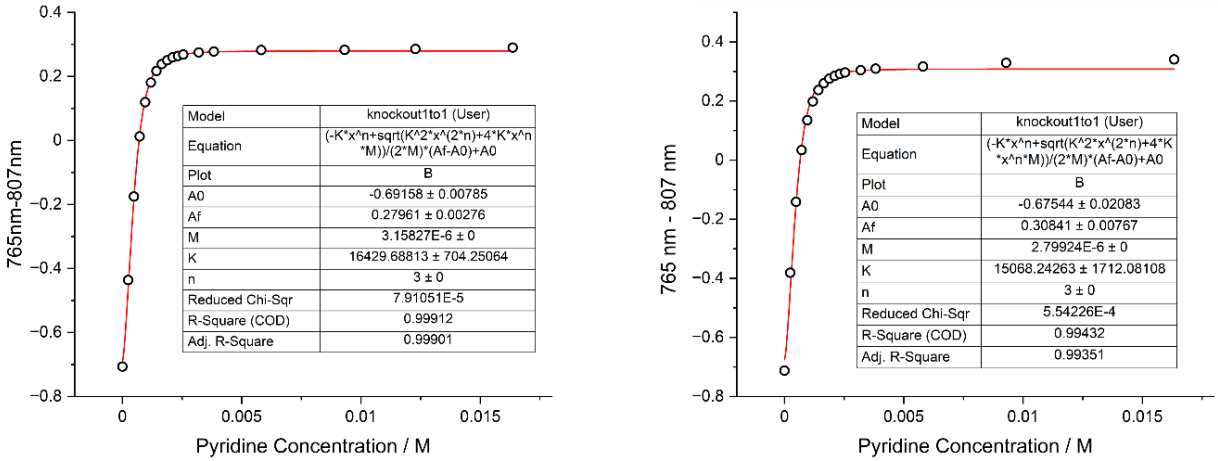

Figure 3.13. Change in Q-band absorbance during titration of pyridine into **P3$_{THS}$(C$_2$CPDIPS)$_2$·T3$_B$** ($CDCl_3$ filtered over Al_2O_3, rt).

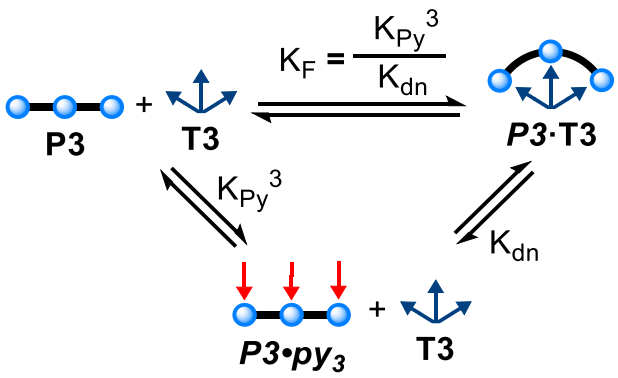

Figure 3.14. Scheme depicting the formation and denaturation of a **P3·T3** complex.

From these calculations we concluded that **T3A** (K_f = (2.65 ± 1.10) x 10^{10} M^{-1}) binds more strongly to **P3THS(C2CPDIPS)2** than **T3B** (K_f = (2.02 ± 0.84) x 10^8 M^{-1}). The binding strength of **T3A** is comparable to that of **T3*** binding to **P3tBu(C2THS)2** (1x10^{10} M^{-1}).[5] We propose that the weaker binding of **T3B** is a result of the large distortion it applies to the **P3** unit, in combination with the pyridyl nitrogen lone pair of this ligand not being well aligned with the porphyrin zinc center (Figure 3.1).

We also carried out competition titrations in which the solution in a cuvette is titrated from 1 eq **P3THS(C2CPDIPS)2·T3A** complex + 1 eq **T3A**, to 1 eq **P3THS(C2CPDIPS)2·T3B** complex + 1 eq **T3B**. This experimental set up allows us to analyze how the ligands compete for **P3THS(C2CPDIPS)2** by measuring data at multiple ratios of the components of interest. Figure 3.15 shows the raw titration data along with the processed data fit to a model we derived to describe the competition binding (See experimental for details of derivation and fitting). This analysis concludes that K_B/K_A has a value of 0.16, which corresponds to a 1:1:1 mix of all components containing 71% A complex and 29% B complex (See experimental). These data qualitatively agree with the pyridine denaturation experiments previously discussed but has a noticeably smaller bias towards the A template.

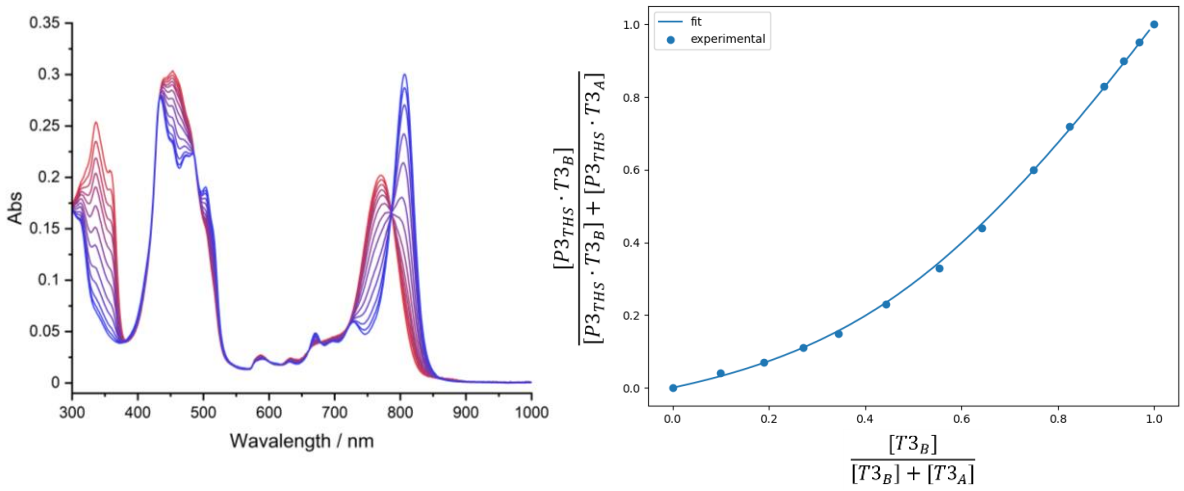

Figure 3.15 (left) Raw competition titration between **T3A** and **T3B** for **P3THS(C2CPDIPS)2** (Red trace is pure **P3THS·T3A**, Blue trace is pure **P3THS·T3B**)(298 K, $CDCl_3$ filtered over Al_2O_3). (right) Processed raw data and fit to the competition binding model used to determine K_B/K_A (x-axis is the mole fraction of **T3B**, y-axis is the mole fraction of **P3THS(C2CPDIPS)2·T3B**).

3.2.2 *c*-P18THS·T18A/B: Formation, Denaturation and Competition Titrations

We conducted similar UV-Vis formation titrations on the ***c*-P18THS** complexes using **T18A** and **T18B**, which also had too large K_f values ($>10^7\ M^{-1}$) to be reliably determined by these titrations. We therefore performed denaturation titrations with pyridine to assess the binding. Due to the strong fluorescence of both **T18A** and **T18B**, which is quenched when bound to ***c*-P18THS**, fluorescence could be used instead of UV-Vis to monitor this process (Figure 3.16 and 3.17). This is particularly advantageous for investigating the ***c*-P18THS·T18A** complex, as ***c*-P18THS·T18A** and ***c*-P18THS·Py18** have rather similar UV-Vis spectrum, so only a small change is observed by UV-Vis during the denaturation titration. The fluorescence on the other hand shows a drastic change once **T18A** is displaced.

From these denaturation titrations we calculate the K_{dn} for each complex using the knockout model in Eq 3.2, then based on the binding/denaturation scheme in Figure 3.18, calculate K_f for ***c*-P18THS·T18A** as $(1.27 \pm 0.19) \times 10^{75}\ M^{-1}$ and for ***c*-P18THS·T18B** as $(1.07 \pm 0.17) \times 10^{74}\ M^{-1}$. These values are incredibly close and dominated by the contribution from K_{py}. Additionally, the fitting of Eq 3.2 to our experimental data in Figures 3.16 and 3.17 is best when N = 6. This is slightly unexpected as we anticipated that each pyridyl group on **T18** would independently

contribute to the binding leading to N = 18 giving the best fit. However, this result seems to indicate that each **T3** unit in **T18** behaves as an independent binding unit, which gives N = 6 in the fitting. We are skeptical of these results but decided to include these experiments here to give the full picture of our binding study.

To directly compare the templates, we again performed competition binding titrations as described in 3.2.1. Figure 3.19 shows the raw and processed data fit to our model (See experimental section) which concludes that K_B/K_A = 1.69, suggesting that a 1:1:1 mixture of the components is composed of 43% ***c*-P18$_{THS}$·T18$_A$** and 57% ***c*-P18$_{THS}$·T18$_B$**.

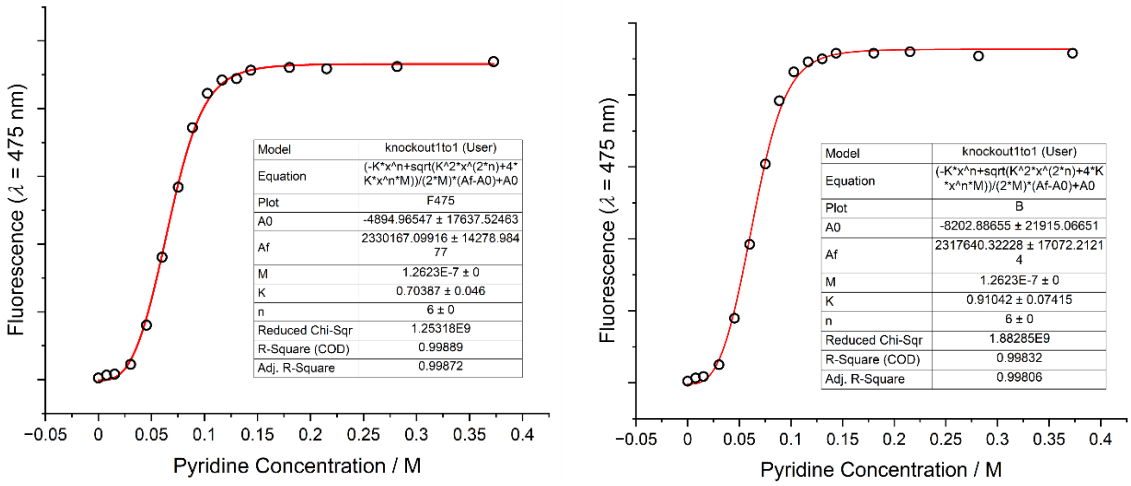

Figure 3.16. Fluorescence at 475 nm as pyridine is added to **c-P18$_{THS}$·T18$_A$**, fit to the knockout model in Eq 3.2 ($CDCl_3$ filtered over Al_2O_3, rt, excitation at 347 nm).

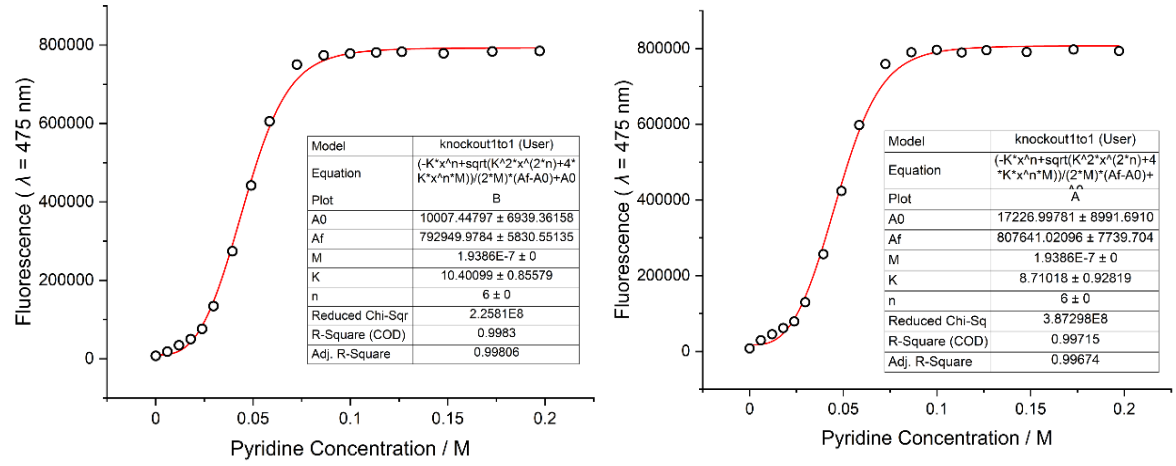

Figure 3.17. Fluorescence at 475 nm as pyridine is added to **c-P18$_{THS}$·T18$_B$**, fit to the knockout model in Eq 3.2 ($CDCl_3$ filtered over Al_2O_3, rt, excitation at 347 nm).

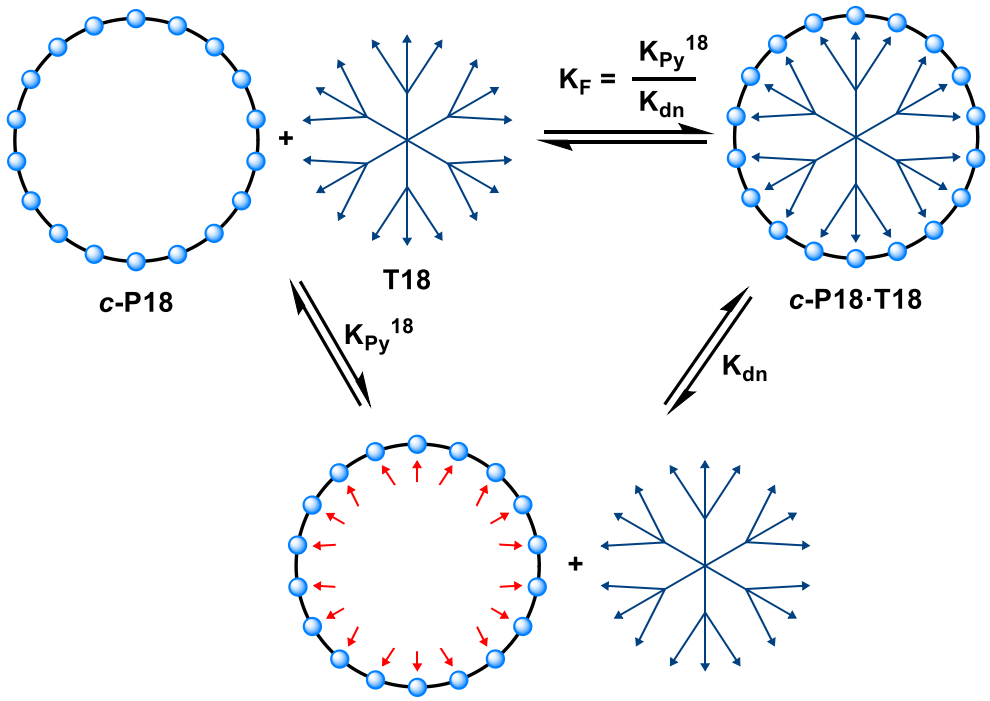

Figure 3.18. Scheme depicting the formation and denaturation of a ***c*-P18$_{THS}$·T18** complex.

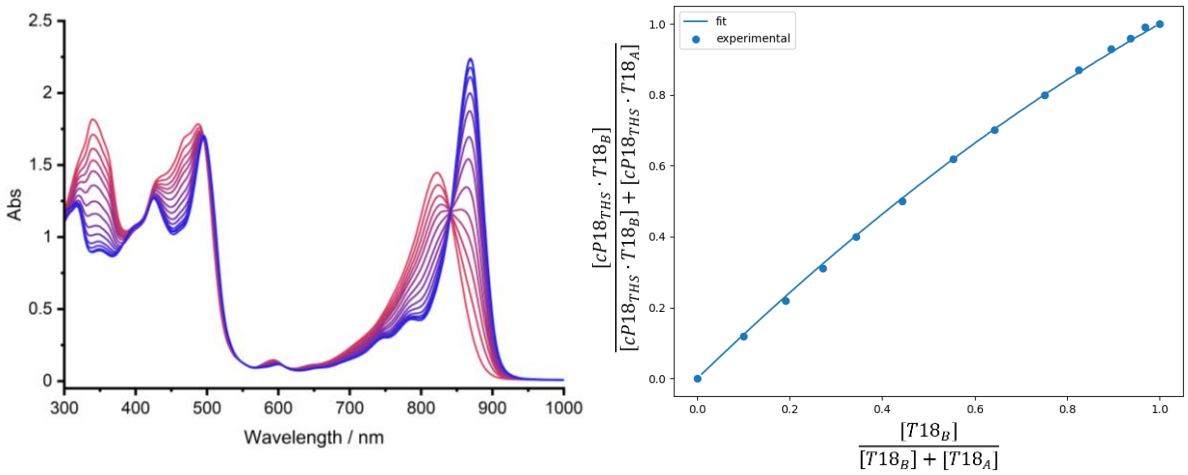

Figure 3.19. (left) Raw competition titration between **T18$_A$** and **T18$_B$** for ***c*-P18$_{THS}$** (Red trace is pure ***c*-P18$_{THS}$·T18$_A$**, Blue trace is pure ***c*-P18$_{THS}$·T18$_B$**). (right) Processed raw data and fit to our competition binding model used to determine K_B/K_A (x-axis is the mole fraction of **T18$_B$**, y-axis is the mole fraction of ***c*-P18$_{THS}$·T18$_B$**).

With these particular components and at such high binding constants, we have found the determination of the value of K_f to be quite challenging. However, the purpose of these **T18** templates is to hold the ***c*-P18** nanoring in a defined, stable and highly π-conjugated geometry for the oxidative NMR titrations. The large red shift of the ***c*-P18** Q-band upon binding either **T18$_A$** or **T18$_B$** confirms that the templates induce better π-conjugation in the nanoring.

Additionally, the sharpness of these red shifted Q-bands indicates that the geometry is well defined and the high pyridine concentrations required to remove the template confirms that the complex is quite stable to competing ligands. Therefore, while we cannot precisely quantify the binding of these **T18** templates to ***c*-P18**, we can confirm that they are able to complete the function they were designed for.

We can only speculate on why the competition binding shows a slight preference for **T18$_B$**, and suggest it is due to the following factors: (1) **T18$_B$** binds **c-P18** in a more π-conjugated conformation. This is energetically favorable. (2) **T18$_B$** distorts **c-P18** more than **T18$_A$**. However, as **c-P18** is already cyclic some of this strain is already built into the nanoring. Binding **T18$_B$** therefore incurs less of an energetic strain penalty than in the analogous case when **T3$_B$** binds linear **P3.** We propose that the residual strain incurred by binding **T18$_B$** is greatly compensated for by the increased π-conjugation, leading to a slight preference for this template. This contrasts with the **T3** study, in which **T3$_A$** binds more strongly. We suggest that in this case the distortion **T3$_B$** places on **P3** upon binding outweighs the increased π-conjugation, this distortion is more significant here because **P3** is perfectly linear prior to binding.

3.3 Nucleus Independent Chemical Shift Calculations on *c*-P18

3.3.1 NICS Results

Nucleus Independent Chemical Shift (NICS) calculations[9] can be used to predict aromaticity in π-conjugated macrocycles.[6, 10] In these calculations, the geometry of the species of interest is first optimized using an appropriate DFT functional and basis set. Here this required optimizing the geometry of **c-P18** in all of the even positively charged states from 0 to +18 (B3LYP/6-31g(d)). To minimize the computational cost of these calculations, all aryl solubilizing groups were omitted from the **c-P18** model. Next, spectator atoms are positioned at regions of interest and an NMR calculation is completed to obtain their shielding tensors. In our case, an evenly

spaced grid of spectator atoms was positioned through the XY plane of the zinc atoms (Figure 3.20). NICS plots are then constructed by plotting the zz component of the shielding tensor for each spectator atom (multiplied by -1), at each atoms x, y, z position. We also interpolate these points and plot the data as a gradient map for better visualization of the regions of shielding/deshielding. NICS results for ***c*-P18** are summarized in Figures 3.21 and 3.22 which use the BLYP35 and LC-ωhPBE (ω = 0.1) functionals respectively for the NMR calculations.

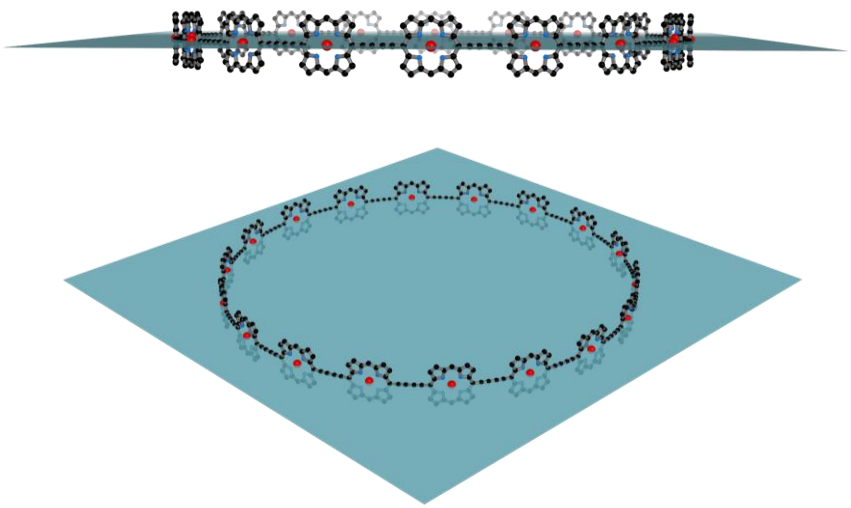

Figure 3.20. Spectator atom (Bz in Gaussian16) grid overlayed on ***c*-P18**.

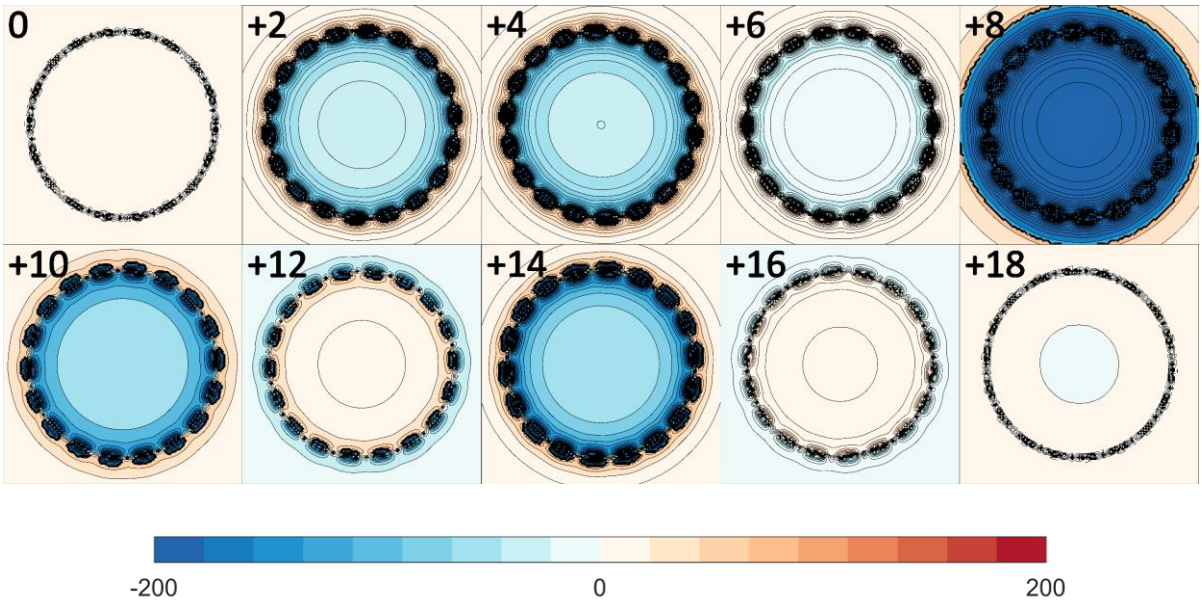

Figure 3.21. NICS(0)$_{zz}$ plots of **c-P18** in all even oxidation states from 0 to +18. Nanoring geometries optimized using B3LYP/6-31g(d) and NMR calculations with **BLYP35** (6-31g(d)). Blue denotes regions where the magnetic field generated by the ring current opposes the external field, red denotes regions where it is aligned with the external field.

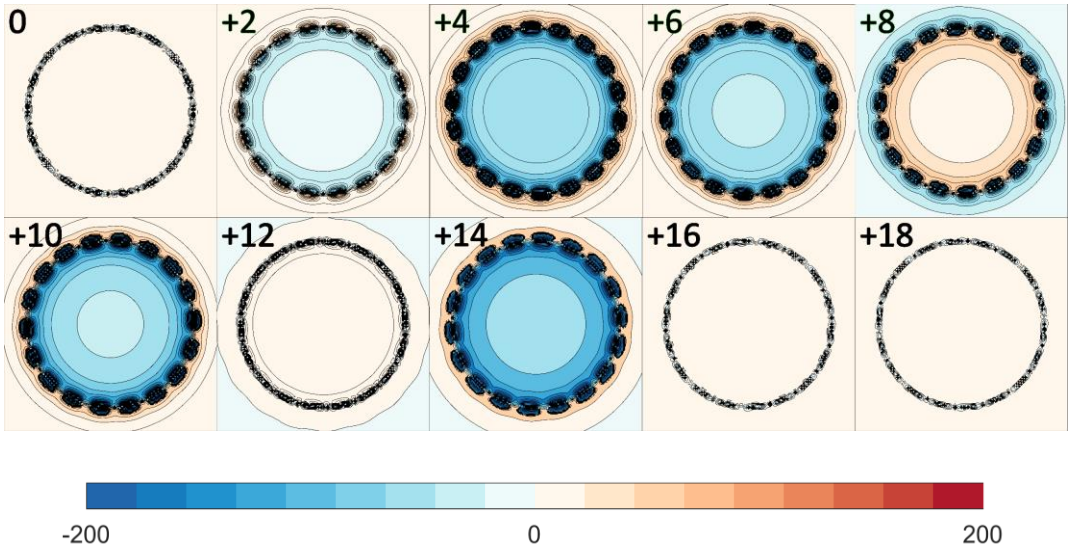

Figure 3.22. NICS(0)$_{zz}$ plots of ***c*-P18** in all even oxidation states from 0 to +18. Nanoring geometries optimized using B3LYP/6-31g(d) and NMR calculations with **LC-*ω*hPBE** (ω = 0.1). Blue denotes regions where the magnetic field generated by the ring current opposes the external field, red denotes regions where it is aligned with the external field.

The choice of these functionals was informed by an in-depth correspondence between Matito[11, 12] and Anderson[10] which investigated the use of different functionals for predicting global anti/aromaticity in porphyrin nanorings. In these publications, it is established that NMR calculations using B3LYP exaggerate electron delocalization, leading to an overestimation in the strength of anti/aromatic states, which poorly match experimental data. However, either increasing the amount of exact Hartree-Fock exchange in the functional by instead using BLYP35 (B3LYP has 20% exact HF exchange,[13] BLYP35 has 35%[14]), or by using a functional such as LC-ωhPBE (ω = 0.1),[15] which includes a range correction to the electron exchange, leads to significantly better agreement with experimental NMR values. The study by Anderson[10] notes, however, that though both BLYP35 and LC-ωhPBE (ω = 0.1) match the experimental ^{1}H NMR data well, LC-ωhPBE (ω = 0.1) often underestimates the strength of antiaromatic ring currents.

In the case of ***c*-P18,** both functionals predict no global aromaticity in the 0 and +18 states. This was expected, as butadiyne linked nanorings in the 0 and +N states (where N is the number of porphyrin units in the nanoring) are typically not globally anti/aromatic, as local porphyrin ring currents dominate instead.[6, 10] These local ring currents act in the xy plane, so are not observed

in a NICS(0)zz plot. From previous studies, we understand that oxidizing the butadiyne-linked nanorings can generate global ring currents.[16] However, this effect is typically weak for charged states lower than +N/2.[6] A key example of this is that global aromaticity is observed for ***c*-P12$_{THS}$·(T6$_e$)$_2$** in the +6 state, but there is no evidence of global antiaromaticity in the +4 state.[6] For ***c*-P18** we therefore did not expect to observe global ring current effects from 0 to +8, but calculated the NICS plots for completeness of the series.

Our main focus in these calculations was the +10 to +16 states, as these were more likely to be observable in our oxidative NMR experiments. Hückel's rule predicts that the +12 and +16 states should be antiaromatic, and that the +10 and +14 states should be aromatic. Both functionals handle the aromatic states as expected, producing almost identical NICS plots for both. The antiaromatic states, however, show significantly more variance between the functionals, with BLYP35 predicting significantly stronger global ring currents than LC-ωhPBE (ω = 0.1), in agreement with the previously discussed publication from Anderson.[10]

The magnitudes of the calculated NICS values presented here are larger than the shifts observed in the oxidative ^{1}H and ^{19}F NMR titrations of previous porphyrin nanorings. Therefore, we cannot use these calculations to predict the exact shifts expected in the NMR titration. Instead, these calculations serve as a reference to qualitatively compare the oxidative titration data to.

3.4 Oxidative NMR Titrations to Probe Global Aromaticity of *c*-P18$_{THS}$·T18$_{A/B}$

3.4.1 Experimental Set Up

In order to probe the presence of global ring currents in **c-P18**, oxidative NMR titrations were performed on samples of both ***c*-P18$_{THS}$·T18$_A$** and ***c*-P18$_{THS}$·T18$_B$**. In these titrations, an oxidant solution (Here ThnBArF in $CDCl_3$, Figure 3.23) is titrated into an NMR sample of the nanoring

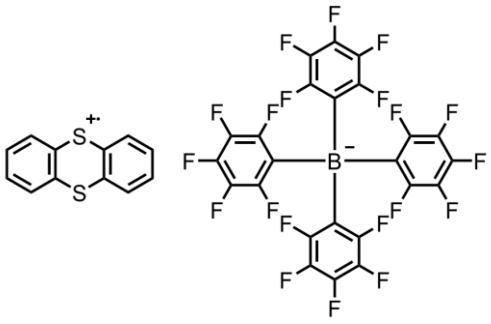

Figure 3.23. Chemical structure of ThnBArF

complex (in $CDCl_3$), with ^1H and ^{19}F NMR spectrum measured after each addition.This process collects NMR data of the complex as it is oxidized from 0 to the +18 state and therefore observes multiple transitions from the complex having 4n + 2 (Hückel Aromatic) and 4n (Hückel antiaromatic) π-electrons in its global π-circuit. In previous nanoring complexes, such as ***c*-P12$_{THS}$·(T6$_e$)$_2$**, evidence of global aromaticity has been obtained from these titrations by observing the shielding and deshielding of probe nuclei in the complex, such as fluorine atoms positioned on the template (Figure 3.24).[6]

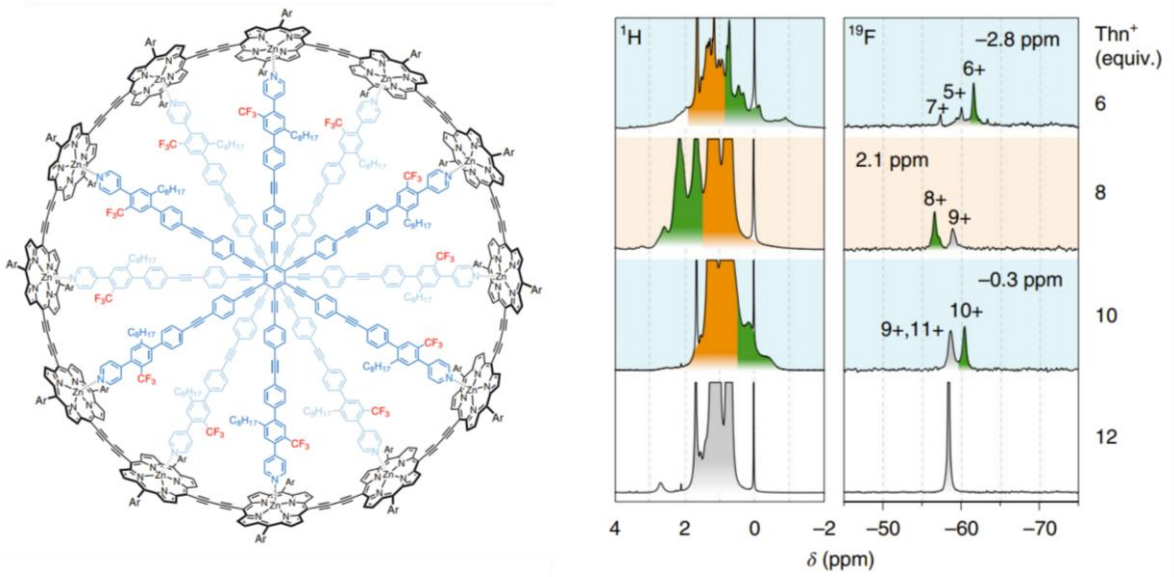

Figure 3.24 (left) chemical structure of **c-P12$_{THS}$·(T6e)$_2$**. (right) Oxidative NMR titration data from ***c*-P12$_{THS}$·(T6$_e$)$_2$** demonstrating shielding and deshielding of CF_3 groups in aromatic (+6 and +10) and antiaromatic (+8) states. Figures reproduced from reference.[6]

To minimize exposure to oxygen and moisture, the oxidative titrations presented in this thesis were all conducted in NMR tubes fitted with J Young caps and sealed under an argon atmosphere. All additions of ThnBArF were completed under a positive pressure of argon and in the case of the -40 °C titrations, the NMR tube was kept in a dry ice/acetone bath at -40 °C whilst out of the spectrometer for oxidant additions. Hexafluorobenzene was also added as a ^{19}F internal standard in all titrations.

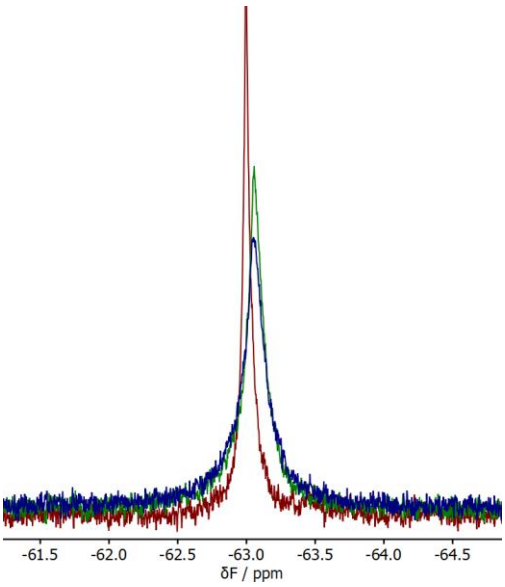

Figure 3.25 ^{19}F NMR spectrum of ***c*-P18$_{THS}$·T18$_{A}$** at varying temperature. (red) 25 ℃. (green) -40 ℃. (blue) -60 ℃.

In the following sections of this thesis, I will present the titration data from ***c*-P18$_{THS}$·T18$_{A}$** and of ***c*-P18$_{THS}$·T18$_{B}$** at both room temperature and -40 ℃. At lower temperature the ^{19}F signal becomes slightly broader, however, we expected that the π-conjugation across the nanoring would increase at lower temperatures, as a result of the reduced vibrations and internal rotations. The lower temperature of -40 ℃ was selected by measuring ^{19}F NMR spectra of ***c*-P18$_{THS}$·T18$_{A}$** from 25 ℃ to -60 ℃ and analyzing the signal broadening with decreasing temperature (Figure 3.25).

3.4.2 Room Temperature Titrations of *c*-P18$_{THS}$·T18$_{A/B}$

3.4.2.1 Raw Experimental Results

Figure 3.26 and 3.27 present the raw ^{1}H and ^{19}F NMR spectra from the room temperature oxidative titrations of ***c*-P18$_{THS}$·T18$_{A}$** and ***c*-P18$_{THS}$·T18$_{B}$**. The oxidation state of the sample at any given point in the titration was determined by the broadening of the thianthrene signals and the amount of ThnBArF added up to that point. As soon as excess oxidant is added to the +18 state nanoring, the thianthrene ^{1}H signal at around 7.5 ppm broaden due to exchange between itself and the newly added thianthrenium (which can no longer oxidise the nanoring). Appearance of this broadening signals the end point of the titration and confirms our assignment of the oxidation states at each point in the titration.

The room temperature titration data for both of the nanoring complexes show no evidence for the formation of global ring currents. Instead of clearly defined shifts for each oxidation state, we instead see only broad sweeping trends towards more positive ppm values. We attribute this to the gradual increase in positive charge accumulating on the **c-P18** nanoring, which draws electron density from both **T18** templates, therefore deshielding the ^{19}F probes.

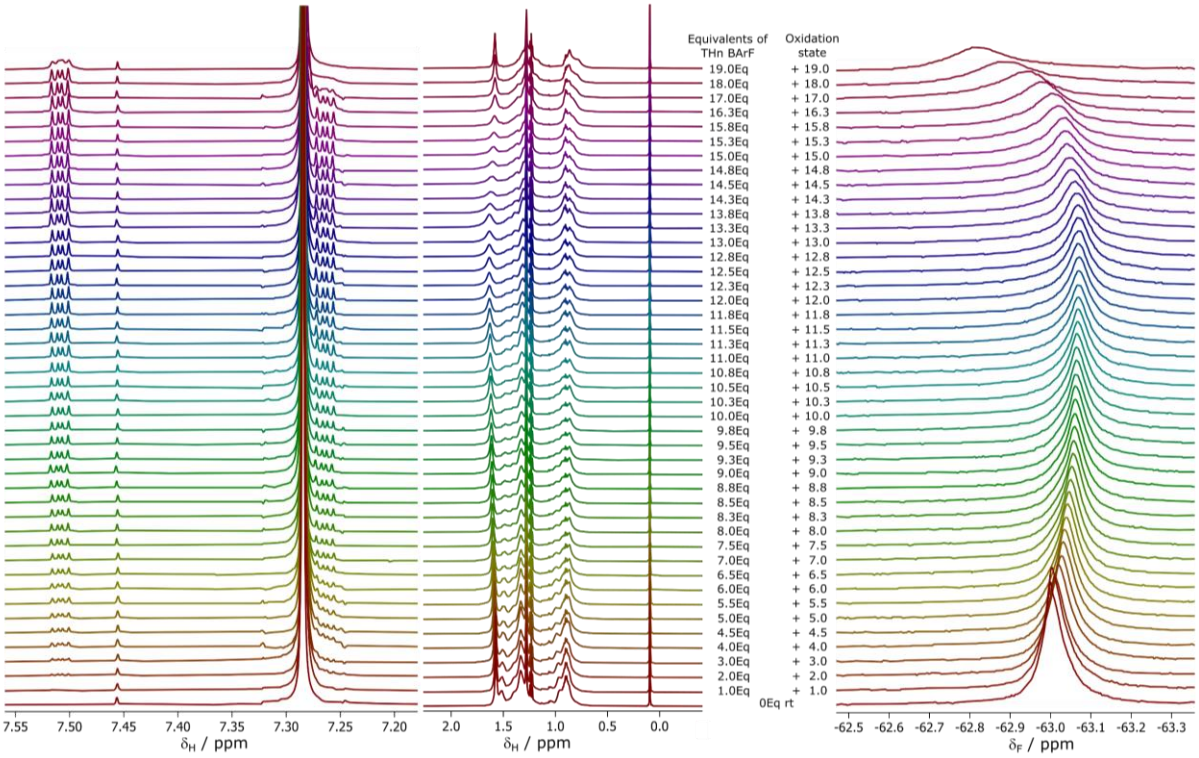

Figure 3.26 ^{1}H and ^{19}F NMR NMR spectra of ***c*-P18$_{THS}$·T18$_{A}$** at 298 K with increasing equivalents of ThnBArF ($CDCl_3$, ^{1}H 600MHz/ ^{19}F 565 MHz).

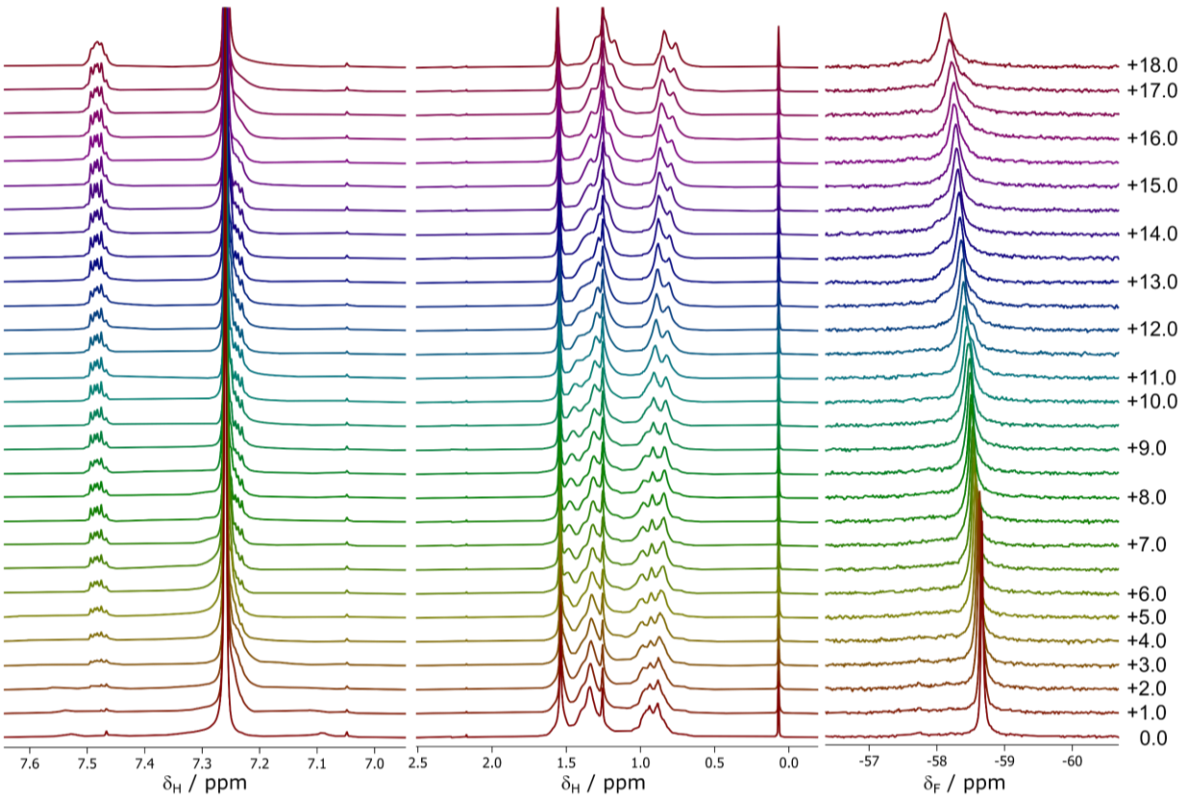

Figure 3.27. ^{1}H and ^{19}F NMR NMR spectra of ***c*-P18$_{THS}$·T18$_{B}$** at 298 K with increasing equivalents of ThnBArF ($CDCl_3$, ^{1}H 500MHz/ ^{19}F 470 MHz).

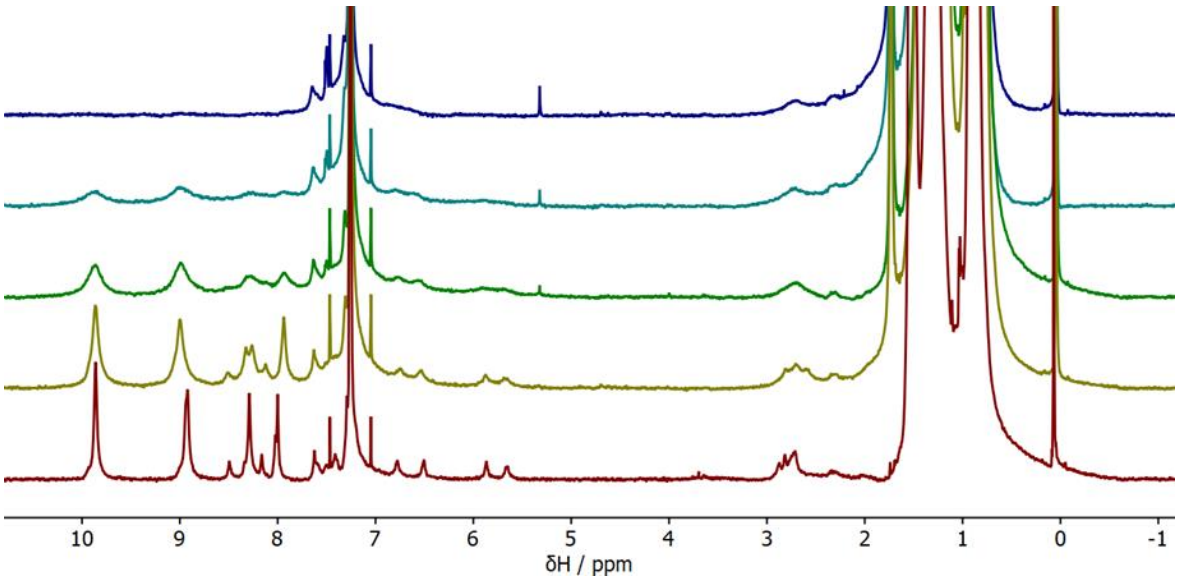

Figure 3.28. ^{1}H NMR spectra of **c-P18$_{THS}$·T18$_{A}$** with increasing equivalents of ThnBArF. Bottom to top: 0 Eq, 0.5 Eq, 1.0 Eq, 1.5 Eq and 2 Eq ThnBArF.

Another important point to note is the complete disappearance of most of the ^{1}H peaks of both complexes after the addition of only a few equivalents of oxidant. This is not observed in smaller nanoring complexes (e.g. ***c*-P6·T6**) however was observed in titrations of ***c*-P12$_{THS}$·(T6e)$_2$** (Figure 3.24).[6] The loss of ^{1}H peaks in ***c*-P18$_{THS}$·T18$_{A}$** is highlighted in Figure 3.28 to stress the importance of including the CF_3 groups as a probe for global aromaticity as the ^{19}F peak from this group remains during the titration.

3.4.3 Low Temperature Titrations of *c*-P18$_{THS}$·T18$_{A/B}$

3.4.3.1 Raw Experimental Results

Oxidative NMR titrations of the nanoring complexes were conducted at –40 °C, to minimize internal rotations which may disrupt the global π-system and to reduce the rate of chemical exchange between nanoring complexes in different oxidation states. Fast exchange between the oxidation states on the NMR time scale would lead to the observed ^{19}F peaks being an average of these oxidation states, which makes the observation of global ring currents challenging. The raw results of these titrations are presented in Figures 3.29 and 3.30. In contrast to the room temperature experiments, the titrations at -40 °C show the growth and decay of additional peaks either side of the main ^{19}F signal. While these broad shoulders are not as definitive as the

resolved peaks in the titration of ***c*-P12$_{THS}$·(T6$_e$)$_2$**, they may still be attributable to globally anti/aromatic oxidation states.

In the case of ***c*-P18$_{THS}$·T18$_A$** the main signal initially broadens to more negative ppm when the average oxidation state of the sample is +10.3 (Figure 3.29). Hückel's rule and the NICS calculations predict that this state should be aromatic with shielded CF_3 probes. For this oxidation state the experimental data, though poorly resolved, supports the assertion that a global ring current is present. As another example, the +12.0 state has significant broadening to more positive ppm. Again, Hückel's rule and the NICS calculations predict this state to be antiaromatic, so the CF_3 probes should be deshielded if a globally antiaromatic ring current is present. These experimental results therefore support the conclusion that **c-P18$_{THS}$** can sustain global ring currents.

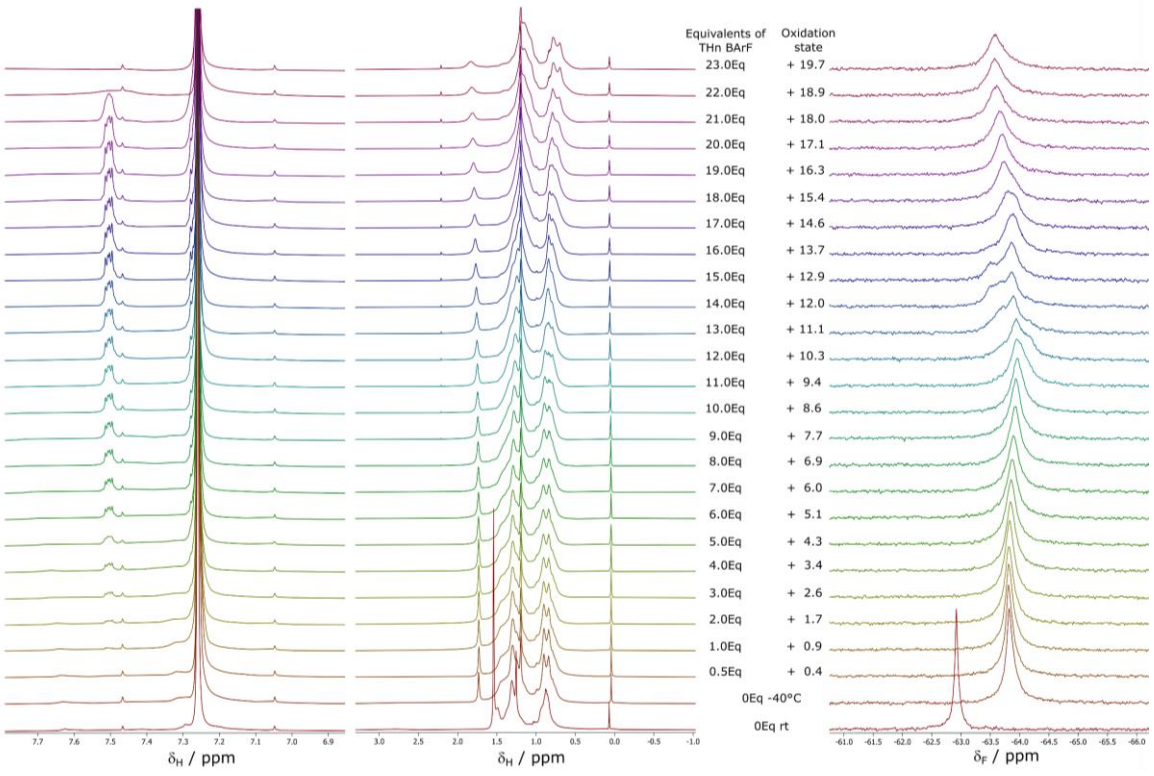

Figure 3.29. ^{1}H and ^{19}F NMR spectra of ***c*-P18$_{THS}$·T18$_A$** at 233 K with increasing equivalents of ThnBArF ($CDCl_3$, ^{1}H 500MHz/ ^{19}F 470 MHz).

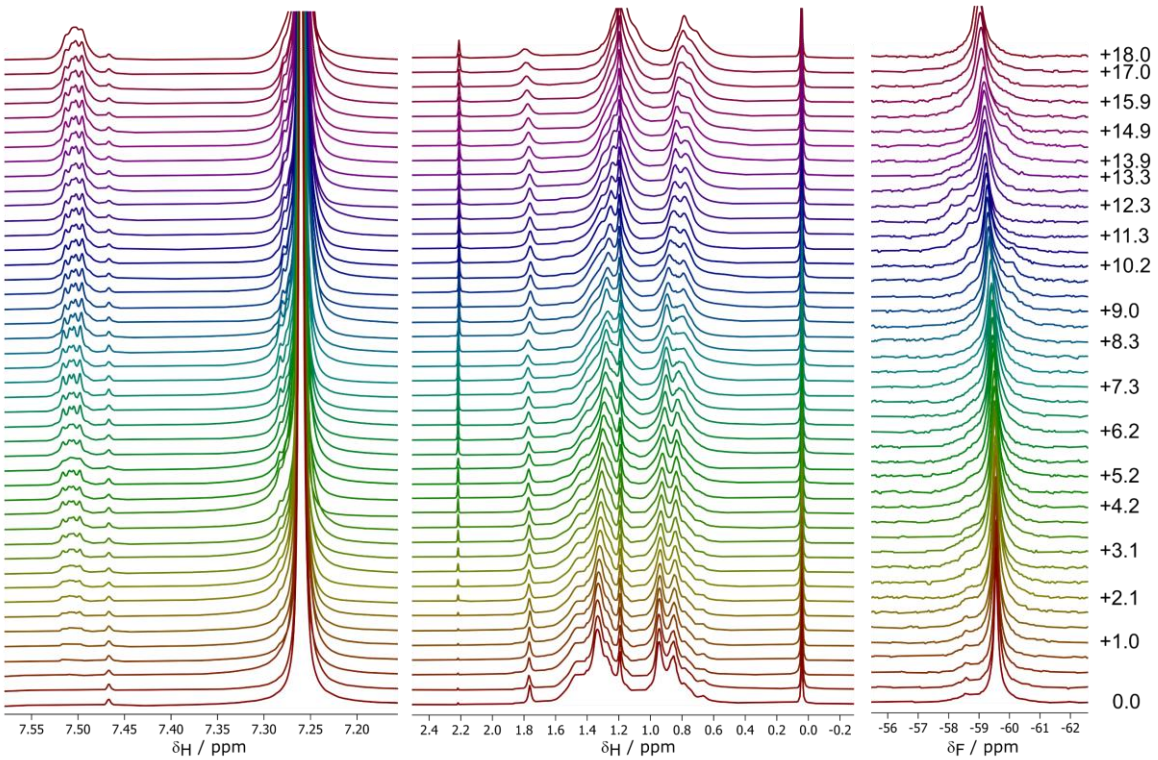

Figure 3.30. ^{1}H and ^{19}F NMR spectra of ***c*-P18$_{THS}$·T18$_{B}$** at 233 K with increasing equivalents of ThnBArF ($CDCl_3$, ^{1}H 500MHz/ ^{19}F 470 MHz).

Similar arguments can also be made for the ***c*-P18$_{THS}$·T18$_{B}$** complex. The broadening in this case is far less intense, however, sharp peaks can be observed either side of the main signal which are reminiscent of those observed in the ***c*-P12$_{THS}$·(T6$_{e}$)$_2$** data.

We attempted a few different approaches to quantitatively examine these low temperature NMR data, which will be discussed in the following sections.

3.4.3.2 Median PPM Analysis

The first approach we attempted was to calculate the median ppm value of each ^{19}F signal, and plot this as a function of the average oxidation state of the NMR sample. To obtain the median ppm value of each spectrum, we first defined a spectral window for all ^{19}F spectra in a series, which was a range of 2 ppm centered about the neutral ^{19}F spectrum. Once cut, every spectrum was integrated, normalized to a total area of 1, and then the ppm value corresponding to an area of 0.5 was taken as the median. This approach identifies the ppm value at which the ^{19}F

spectrum to the right and left have equal area. This process was completed for the ***c*-P18$_{THS}$·T18$_{A}$** data at 25 ℃ and -40 ℃, and for the ***c*-P18$_{THS}$·T18$_{B}$** data at -40 ℃ (Figure 3.31).

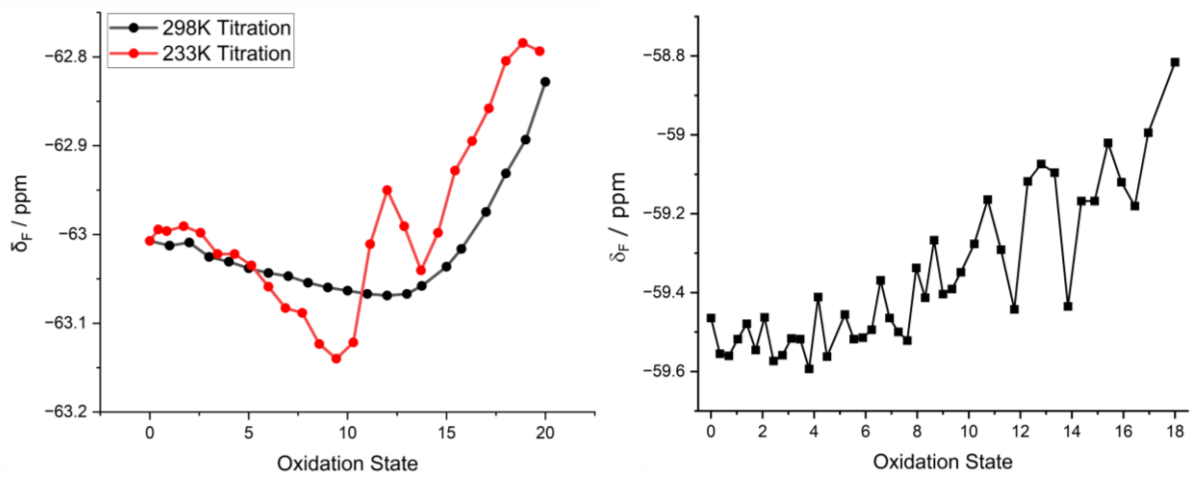

Figure 3.31 Median ppm analysis of (a) ***c*-P18$_{THS}$·T18$_{A}$** at 25 ℃ (298 K, black) and -40 ℃ (233 K, red). -40 ℃ data adjusted to start at the same ppm value as the 25 ℃ data for better comparison. (b) ***c*-P18$_{THS}$·T18$_{B}$** at -40 ℃.

Analysis of the ***c*-P18$_{THS}$·T18$_{B}$** data by the median ppm method shows a gradual shift to more positive ppm values. This is probably because the broadening to the left and right in this dataset is very small in proportion to the main ^{19}F signal, which gets lost in the poor signal to noise and general broadening of the data. At 25 ℃, ***c*-P18$_{THS}$·T18$_{A}$** also shows this same shift to more positive ppm values, however at -40 ℃ a clear oscillation is observed at around the +10 to +16 oxidation states. These shifts are in line with the aromaticity predicted by Hückel's rule and the NICS calculations; with +10 being aromatic (shielded CF_3), +12 as antiaromatic (deshielded CF_3), +14 as aromatic (shielded CF_3), and +16 as antiaromatic (deshielded CF_3).

To quantitatively compare this trend to the NICS plots, the NICS data (LC-ωhPBE (ω = 0.1)) were processed in the following manner. First, the spectator atom from the NICS grid that best represents the average position of the CF_3 probe nuclei was selected. The NICS value of this spectator atom was then extracted from the calculations at every oxidation state, then scaled by x 0.002 and shifted by -63.009 ppm to align it with the experimental data. The results of this analysis are shown in Figure 3.32.

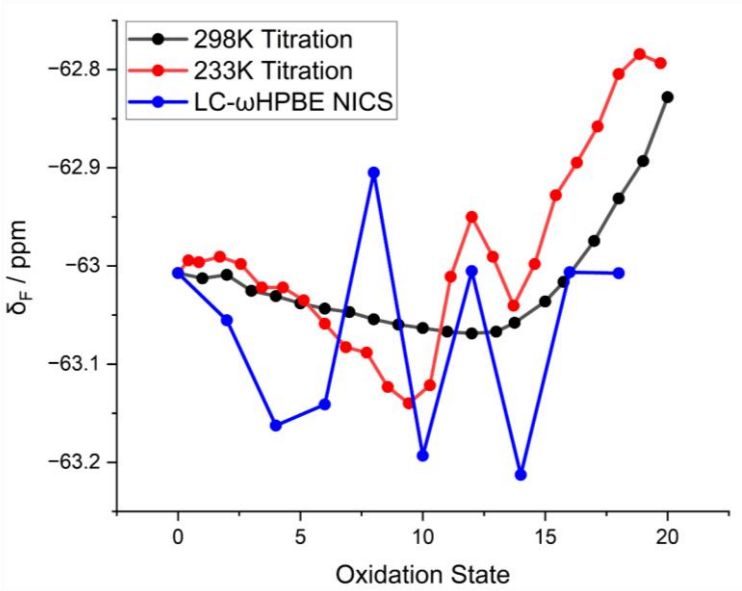

Figure 3.32 Scaled NICS data overlayed on the average ppm analysis of the 298 K and 233 K oxidative titrations of ***c*-P18$_{THS}$·T18$_{A}$**.

Despite the need to scale the NICS data considerably to be able to compare them to the experimental data, we can see that the relative strength of the +10 and +12 states agrees with the experimentally observed shifts. The agreement between NICS and the experimental data is poorer for the +14 state, with NICS predicting there should be significantly more shielding than is experimentally observed. Finally, a clear discrepancy is noted for the +8 state. However, NICS results of this state were dramatically different with the two functional tested and we did not expect to observe any global ring currents in this state as it lies below +N/2 (Where N is the number of porphyrin units in the nanoring.

3.4.3.3 Manual Deconvolution *c*-P18$_{THS}$·T18$_{A}$

To further investigate the presence of global ring currents in ***c*-P18$_{THS}$·T18$_{A/B}$** a manual deconvolution of both low temperature datasets was conducted. The goal of this process was to determine if the broad spectrum obtained from the titrations could rationally be deconvoluted into contributions from the various oxidation states present at a given point in the titration. From studies on previous nanorings[6, 17] there are a few key qualitative trends that are observable in the titration data; (1) Oxidation states grow in and decay away in sequence, i.e. +1 then +2 then

+3. (2) The ^{19}F peak for a nanoring in a given oxidation state is consistent regardless of the average oxidation state of the sample. For example, the ^{19}F peak assigned to the aromatic +6 state in ***c*-P12$_{THS}$·(T6$_e$)$_2$** remains at -60.5 ppm even as the average oxidation state of the NMR sample moves from +5.4 to +6.9 (5 titration points).[17] (3) At any given point in the titration a distribution of nanoring oxidation states is populated about the average oxidation state of the sample. ^{19}F peaks from nanorings in multiple different oxidation states can therefore be observed at any given point in the titration (e.g. +4, +5 and +6 all present in one spectrum[17]). Given these qualitative observations, if a nanoring showed global anti/aromaticity, we would expect to be able to fit the experimental data to a model that: (1) allows for multiple oxidation states to be present in a given spectrum. (2) the ppm values of these oxidation states are consistent across the titration. (3) the speciation of each oxidation state follows a curved shape (i.e. rises to a single maximum then decays) (4) the speciation curves are in order (+10 before +11 before +12).

Figure 3.33 presents the manual deconvolution of the -40 °C ***c*-P18$_{THS}$·T18$_A$** dataset, which fits multiple Lorentzian peaks to each experimental ^{19}F spectrum. This manual deconvolution was started from the +12.0 average oxidation state spectrum, as it showed a strong indication of two additional peaks on the more positive ppm side of the main ^{19}F peak. These peaks were initially assigned to +11 and +12, with a third broad peak on the more negative side of the spectrum assigned to the +10 state. Moving forward to the +12.9 spectrum, the manual deconvolution shows a decrease in the contributions from the +10 and +11 states, whilst +12 remains consistent. Moving backwards to the +11.1 spectrum we see a decreased contribution from the +12 state and larger contributions from +10 and +11. These manually deconvoluted peaks also show consistent ppm values across the spectra (Figure 3.34) and match the expected anti/aromaticity of the even oxidation states predicted by Hückel's rule and by NICS calculations.

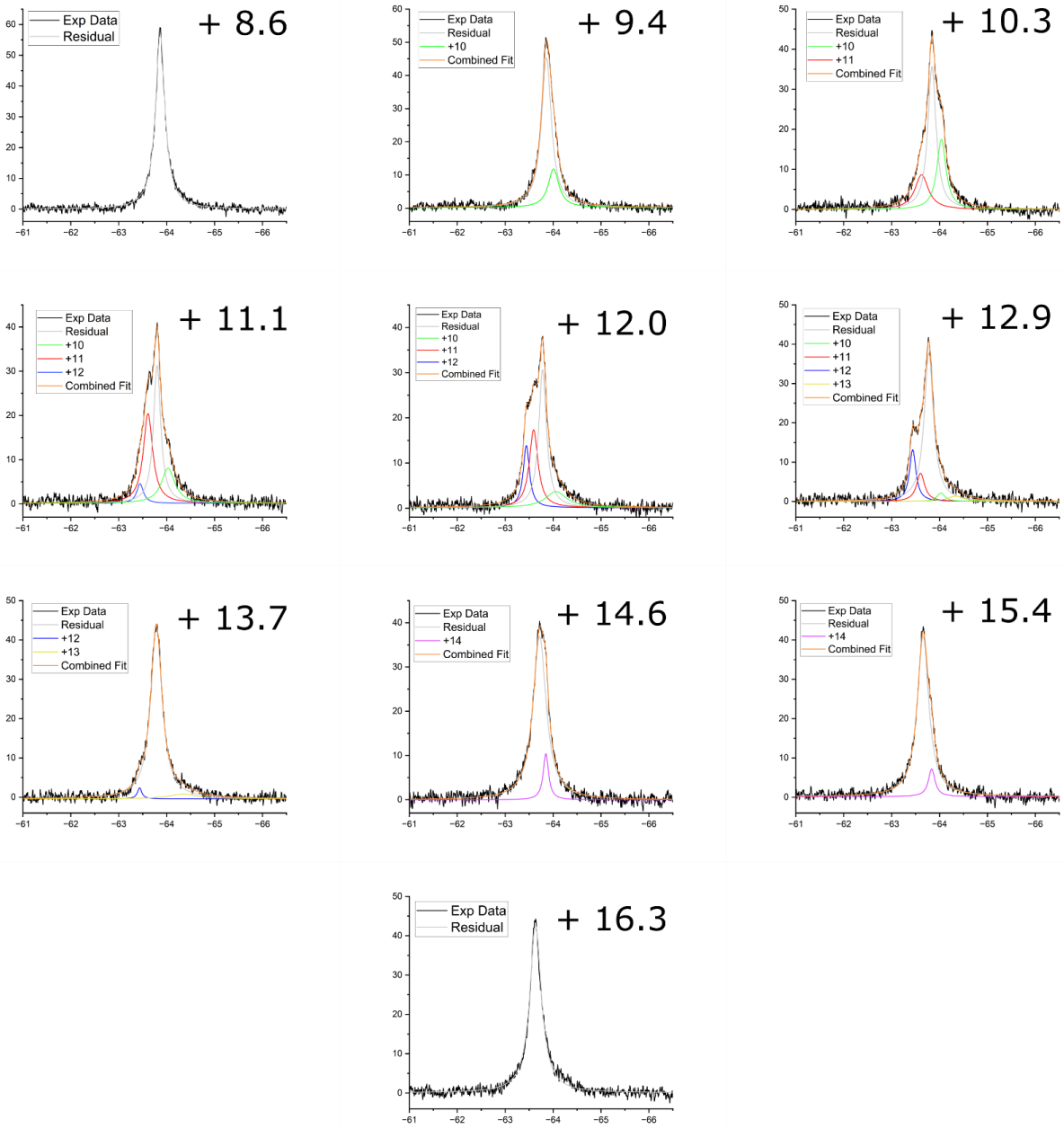

Figure 3.33 Manual deconvolution of the -40 °C ***c*-P18$_{THS}$·T18$_{A}$** dataset.

This manual deconvolution was continued to cover the full range of spectra from +8.6 to +16.3, however, the lack of any other discernable peaks made the assignment of additional oxidation states significantly more challenging. Furthermore, every deconvolution in this series requires a contribution from a peak we assigned as "residual" in order to fit the experimental data. In most cases this "residual" peak accounts for >50% of the total spectrum and only drops below this threshold in the +11.1 and +12.0 spectra, where the contributions from globally aromatic states are more pronounced. Despite this, from our manual deconvolution we observe all of the

expected trends that were outlined at the start of the section, which is best presented by the plots in Figure 3.34.

We cannot be certain why the residual peak is present but speculate that it represents ***c*-P18$_{THS}$·T18$_{A}$** nanoring complexes in geometries that prohibit the formation of global ring currents. This could be through aggregation of the nanoring complexes which introduces distortions to the nanoring geometry that break the conjugation of the global π-circuit.

Aggregation is more likely at lower temperature, and we see broadening of the neutral complexes ^{19}F NMR upon cooling (Figure 3.25), so this may be a factor. However, the gradual deshielding of the residual peak across the titration, as seen in Figure 3.34a, is reminiscent of the gradual deshielding observed in the room temperature titration of ***c*-P18$_{THS}$·T18$_{A}$** (Figure 3.26). In the room temperature titration, we attributed this gradual deshielding to accumulating positive charge on ***c*-P18$_{THS}$** withdrawing electron density from **T18$_{A}$** and therefore deshielding the fluorine nuclei. The lack of any global anti/aromatic states in this higher temperature titration was attributed to the poor global π-conjugation of the nanoring as a result of the internal rotations discussed in the molecular dynamics section of this chapter. We propose that at the lower temperature of -40 °C these internal rotations are slowed enough that some portion of the ***c*-P18$_{THS}$·T18$_{A}$** sample sit in geometries that allow global ring currents to form. Using this rationale, in a given NMR scan the nanorings in the correct geometries generate global ring currents dependent on their individual oxidation states (e.g. +10, +11 and +12). Many of the nanorings will not be in the correct geometry, with any number of porphyrn-porphyrin dihedrals > 45°, so therefore contribute a ^{19}F signal that is devoid of the effects of aromaticity and only represents the deshielding the fluorine nuclei experience from the accumulation of charge on ***c*-P18$_{THS}$**. The absence of global anti/aromatic states below +10 and above +14 may be due to these states being particularly weak and therefore hidden below the main residual peak.

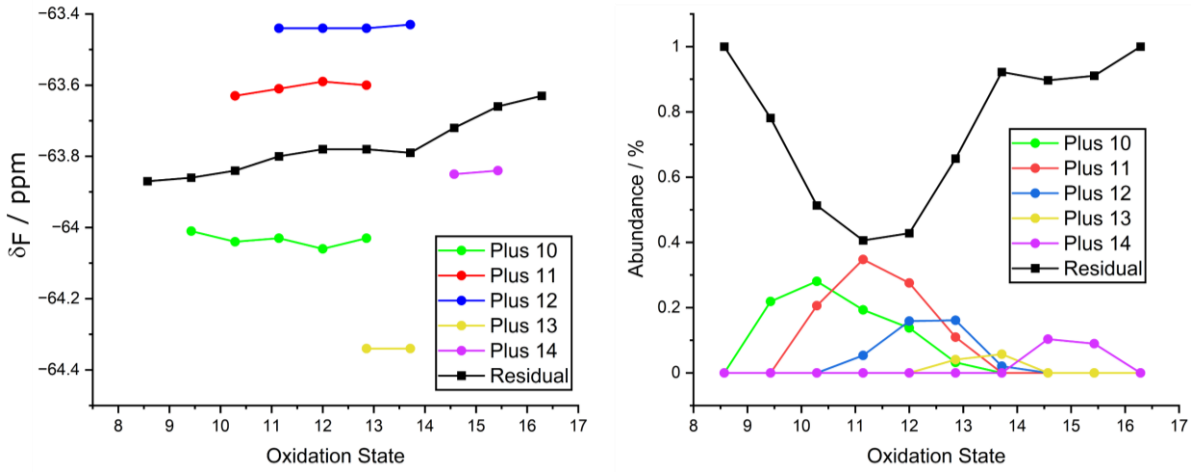

Figure 3.34. Processed deconvolution data from the 40 °C ***c*-P18$_{THS}$·T18$_{B}$** dataset. (a) ppm values of the deconvoluted peaks assigned to each oxidation state (coloured lines) at each point in the titration, as indicated by the average oxidation state of the sample on the x-axis. (b) speciation curves of each oxidation state at each point in the titration.

3.4.3.4 Manual Deconvolution *c*-P18$_{THS}$·T18$_{B}$

The manual deconvolution was also applied to ***c*-P18$_{THS}$·T18$_{B}$** (Figure 3.35). As with ***c*-P18$_{THS}$·T18$_{A}$**, there is a significant contribution from the residual peak, however, due to the presence of more defined peaks either side of this residual, we can be more confident in our assignment of the global anti/aromatic states. As before, this manual deconvolution was started from the +11.8 state, as it showed two clear peaks at more positive ppm, which were assigned as the +11 and +12 states. Working forward and backwards, oxidation states from +5 to +14 were assigned, however the +8 to +14 states are the most clearly identifiable so will be the focus of the following discussion.

Figure 3.36 presents the ppm values of each deconvoluted peak, grouped by nanoring oxidation state, and the speciation curves of these oxidation states across the titration. As before, the ppm values of all oxidation states are quite consistent across the titration and the speciation curves rise to a single maximum and decay in order.

The rationale for the presence of the residual peak given for ***c*-P18$_{THS}$·T18$_{A}$** can equally be applied to the data from ***c*-P18$_{THS}$·T18$_{B}$**. However, we propose that the higher conformational stability and increased π-conjugation of ***c*-P18$_{THS}$·T18$_{B}$**, as discussed in the molecular dynamics section of this chapter, leads to more nanorings being in global anti/aromatic

conformations in a given NMR scan, which explains why the residual peak is less dominant in the ***c*-P18$_{THS}$·T18$_{B}$** data. Furthermore, as is seen in the geometry optimized models of **P3·T3$_{A}$** and **P3·T3$_{B}$** (Figure 3.37), the CF_3 probe in the B templates is closer to the porphyrin units than in the A templates. It is therefore expected that the CF_3 probes in ***c*-P18$_{THS}$·T18$_{B}$** would experience stronger de/shielding as a result of global ring currents.

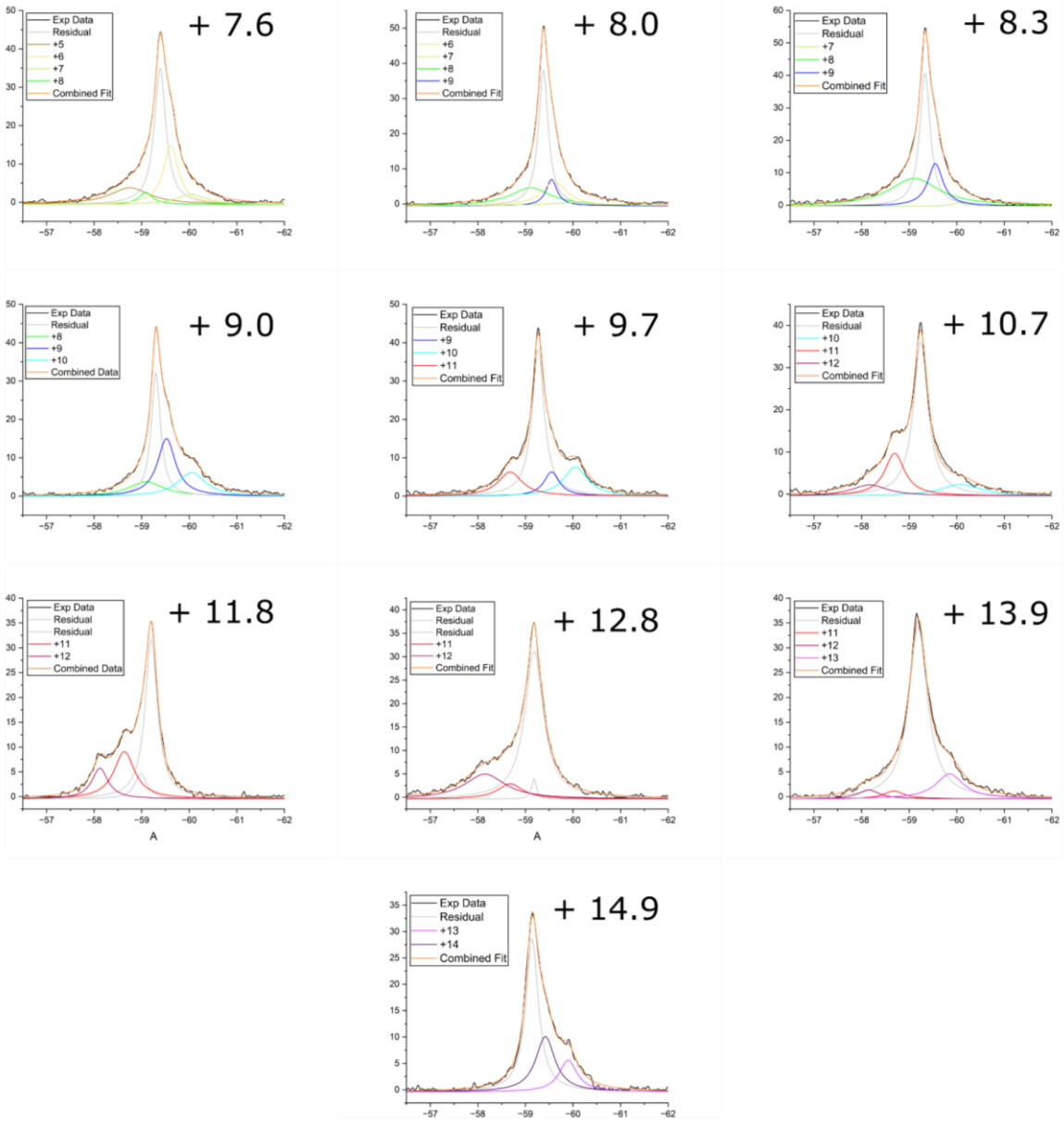

Figure 3.35 Manual deconvolution of the -40 °C ***c*-P18$_{THS}$·T18$_{B}$** dataset.

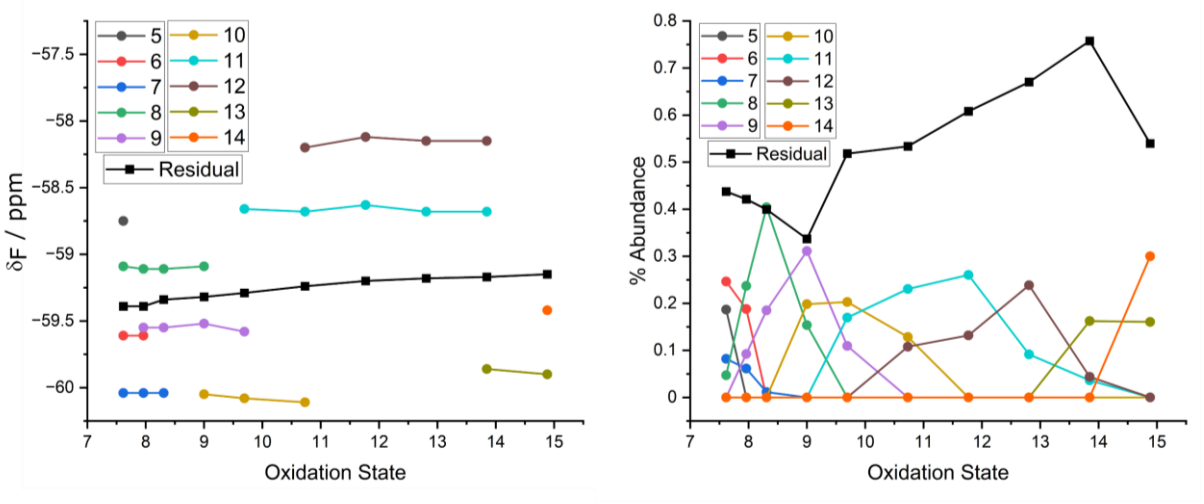

Figure 3.36. Processed deconvolution data from the 40 °C ***c*-P18$_{THS}$·T18$_{B}$** dataset. (a) ppm values of the deconvoluted peaks assigned to each oxidation state (coloured lines) at each point in the titration, as indicated by the average oxidation state of the sample on the x-axis. (b) speciation curves of each oxidation state at each point in the titration.

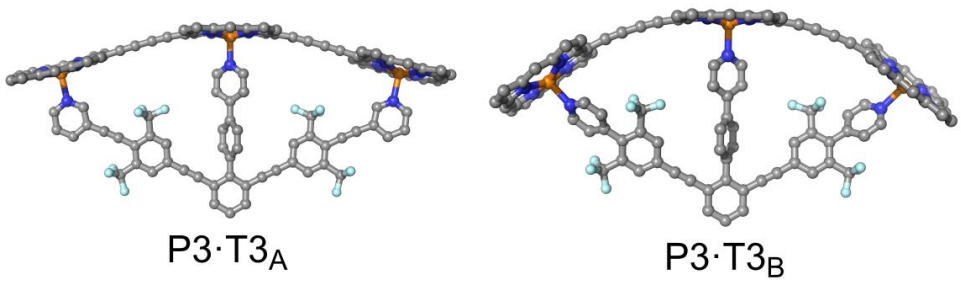

Figure 3.3712. Models of **P3·T3$_{A/B}$** complexes with CF_3 groups added.

To compare the de/shielding of each oxidation state the following processing was applied to the titration data for both ***c*-P18$_{THS}$·T18$_{A}$** and ***c*-P18$_{THS}$·T18$_{B}$**: (1) An oxidation state was selected (e.g. ***c*-P18$_{THS}$·T18$_{B}^{+12}$**, Figure 3.36a). (2) The ppm values of all deconvoluted peaks for this species was averaged (for ***c*-P18$_{THS}$·T18$_{B}^{+12}$** this is 4 values from spectra +10.7 to +13.9). (3) The ppm values of the residual peak in these spectra were also averaged. (4) The difference between (2) and (3) was calculated and plotted as a function of oxidation state. This method of data processing aims to measure how de/shielded each oxidation state is relative to the residual peak and is presented for both ***c*-P18$_{THS}$·T18$_{A}$** and ***c*-P18$_{THS}$·T18$_{B}$** in Figure 3.38. As expected, ***c*-P18$_{THS}$·T18$_{B}$** shows significantly more de/shielding than ***c*-P18$_{THS}$·T18$_{A}$**, which rationalizes why more oxidation states are identifiable in this complex, as they are shifted further from the main residual peak.

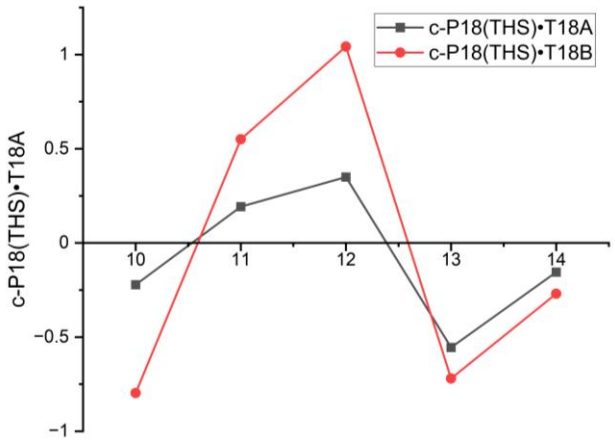

Figure 3.38. Difference in PPM value between the observed oxidation state and the residual value in the deconvoluted spectra of ***c*-P18$_{THS}$·T18$_{A}$** (Black) and ***c*-P18$_{THS}$·T18$_{B}$** (Red).

3.4.3.5 Automated Deconvolution

Though successful, the manual deconvolution, being a manual method, is vulnerable to human biases. In an attempt to eliminate all biases from our analysis, we wrote a short piece of code (See experimental section) that automatically deconvolutes a given titration series, using Bayesian Information Criterion (BIC)[18] to determine how many Lorentzian peaks to fit to each spectrum (See experimental section). This inclusion of the BIC was the primary motivation for the automated deconvolution, as it provides a statistical rationale for why a given number of peaks should be fit to a given spectrum. As opposed to the manual deconvolution which used trial and error combined with a qualitative assessment of the goodness of fit. Briefly, the automated deconvolution follows this sequence of processes: (1) For a given spectrum, the code uses non-linear least squares by modification of the Levenberg-Marquardt algorithm[19] to establish the optimal fits of 1-6 Lorentzian peaks to the experimental data. (2) From this, the code uses the BIC to select which number of Lorentzian peaks best represents the data. The BIC has a penalty for each added Lorentzian peak to minimize overfitting of the data. (3) The deconvoluted peaks for each spectrum are plotted alongside the raw data.

Figure 3.39 presents the fully automated deconvolution of the -40 ℃ ***c*-P18$_{THS}$·T18$_{B}$** dataset along with the oxidation state ppm tracker in Figure 3.40. We conclude from this approach that the code generally overfits the experimental data despite the harsh penalty imposed by the BIC

to overfitting. This is clearly apparent in the ppm tracker which has significantly more points in comparison to the analogous manually deconvoluted Figure 3.36. Despite this overfitting, some oxidation states are still identifiable (+10, +11, +12 and +13, Figure 3.40) which supports our discussion of global aromaticity in this complex in the previous section of this thesis.

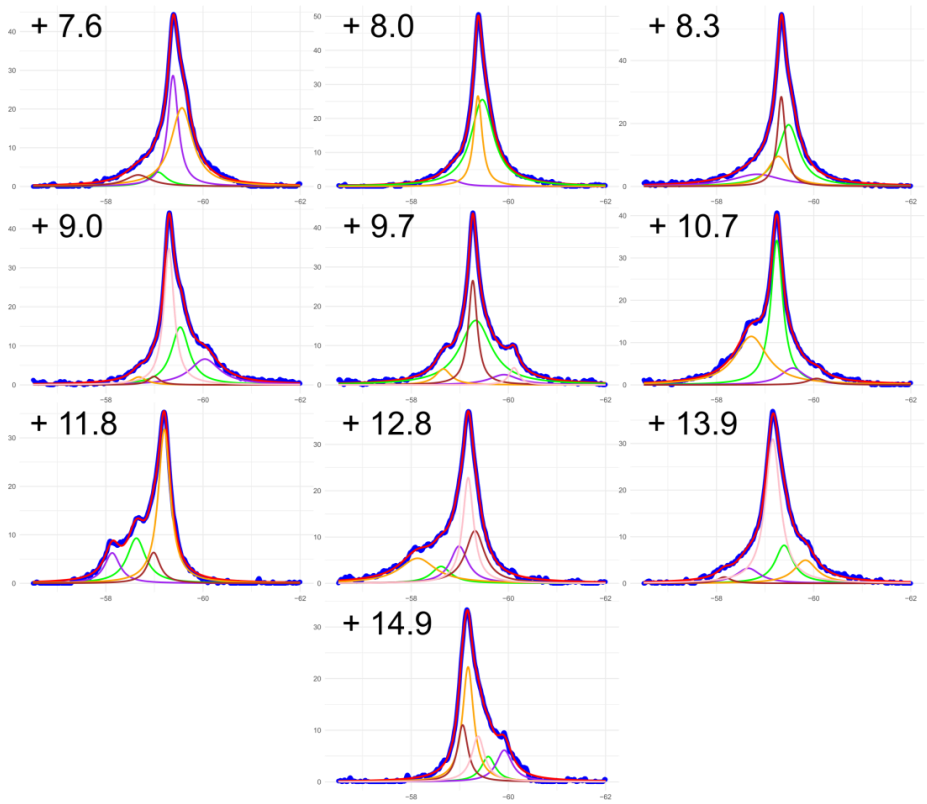

Figure 3.3913 Automatically deconvoluted ^{19}F NMR data from the 233 K oxidative titration of ***c*-P18$_{THS}$·T18$_{B}$.**

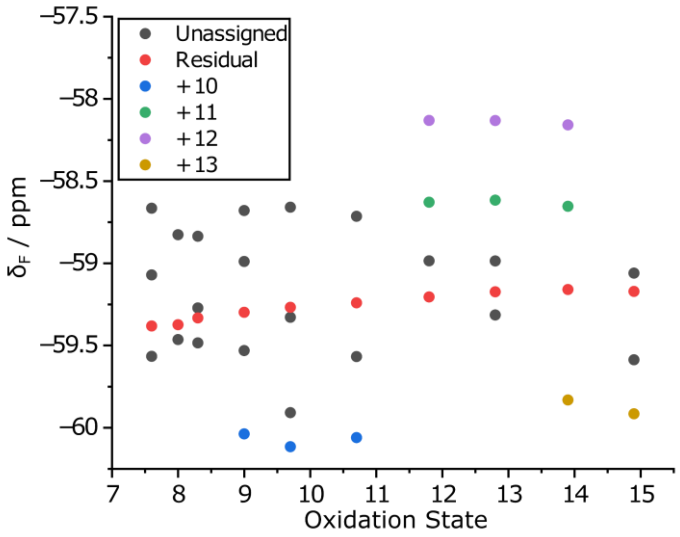

Figure 3.4014 ppm values of the deconvoluted Lorentzian peaks at each point in the titration. With oxidation states assigned by comparison to Figure 3.36.

3.4.4 Reference Titration on $P18_{THS}(C_2CPDIPS)_2 \cdot T18_B$

To test our interpretation of the low temperature oxidative NMR data for ***c*-$P18_{THS} \cdot T18_{A/B}$** we performed a titration on a 1:1 complex of **$P18_{THS}(C_2CPDIPS)_2 \cdot T18_B$** at -40 °C, which we anticipated should show none of the additional peaks growing and decaying as this system is not able to sustain global ring currents due to the break in the π-system. Figure 3.41 presents the chemical structure of **$P18_{THS}(C_2CPDIPS)_2 \cdot T18_B$** along with a titration of **$T18_B$** into **$P18_{THS}(C_2CPDIPS)_2$** which was monitored by UV-Visible spectroscopy.

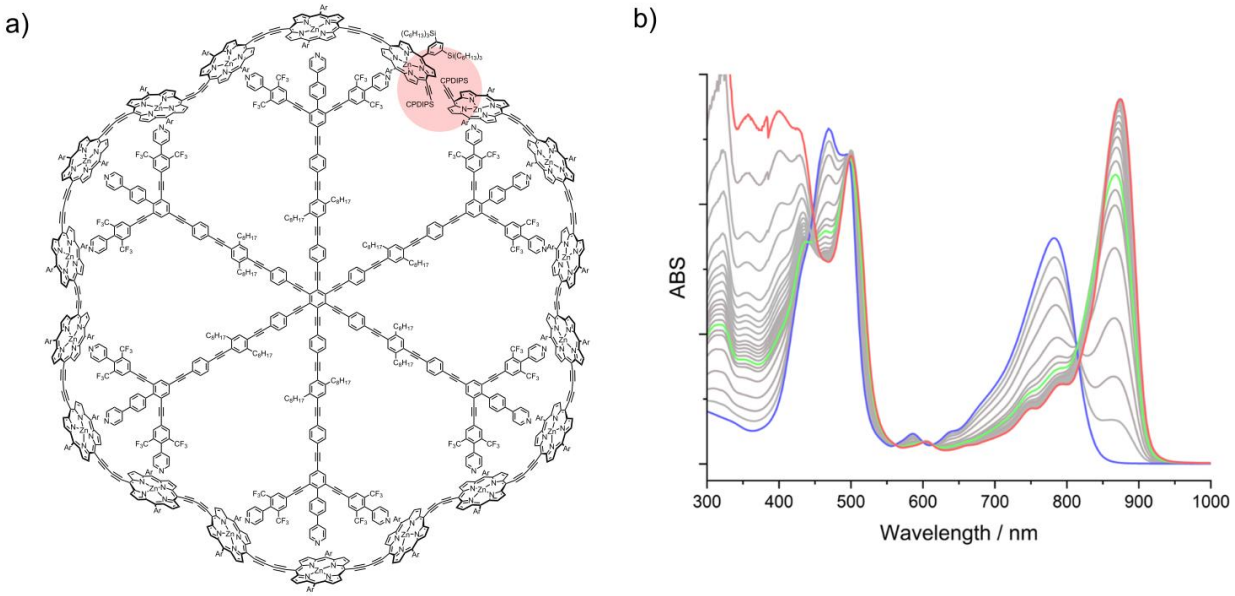

Figure 3.41. (a) Chemical structure of **$P18_{THS}(C_2CPDIPS)_2 \cdot T18_B$**. (b)Titration of **$T18_B$** into **$P18_{THS}(C_2CPDIPS)_2$** monitored by UV-Vis spectroscopy. (Room temperature in $CDCl_3$ which was filtered over Al_2O_3 prior to use). Blue is **$P18_{THS}(C_2CPDIPS)_2$**, Green is 1:1 stoichiometry and Red is 1:2 stoichiometry.

In this titration we observe a rapid decay of the **$P18_{THS}(C_2CPDIPS)_2$** Q-band at 782 nm as soon as **$T18_B$** is added and the growth of a new band at 873 nm. This change is accompanied by a sharp isosbestic point at 814 nm. Past the 1:1 stoichiometry we see a continual growth of the intensity of the new Q-band, which is accompanied by a change in intensity at the first isosbestic point and the appearance of a new isosbestic point at 861 nm. Past the 1:2 stoichiometry of **$P18_{THS}(C_2CPDIPS)_2$: $T18_B$** there are no further changes in the spectrum aside from growth of excess **$T18_B$** at 300 – 450 nm. From this experiment we conclude that the 1:1 complex forms up to the 1:1 stoichiometry but is converted into a 1:2 complex as more **$T18_B$** is added.

^{19}F NMR spectra were recorded of samples containing 1:1, 1:2 and 1:5 stoichiometries of **P18$_{THS}$(C$_2$CPDIPS)$_2$: T18$_B$**, which clearly show that only at the 1:1 stoichiometry are all of the pyridyl binding sites of **T18$_B$** bound, as evidenced by the free **T18$_B$** signal observed at the 1:2 and 1:5 stoichiometries (Figure 3.42). We anticipate that the ^{19}F signal termed "Free **T18$_B$**" can arise from either truly free **T18$_B$** or from any CF_3 group that is not positioned below a porphyrin (for example a CF_3 group in the 1:2 complex on an uncoordinated $T3_B$ unit).

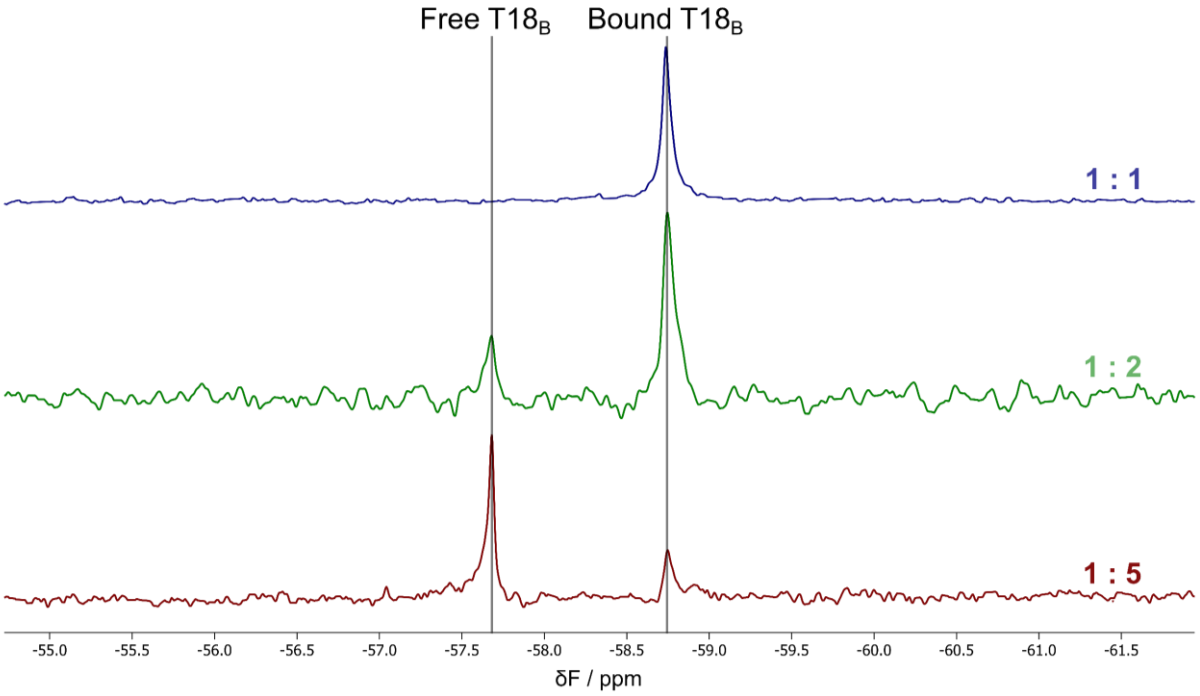

Figure 3.42. ^{19}F NMR of 1:1, 1:2 and 1:5 stoichiometries of **P18$_{THS}$(C$_2$CPDIPS)$_2$: T18$_B$** in $CDCl_3$ at 298K. Referenced against C_6F_6 δ_F = –161.64.

The oxidative NMR experiment was performed on a 1:1 stoichiometry of **P18$_{THS}$(C$_2$CPDIPS)$_2$:T18$_B$** at –40 °C using the experimental set up previously described. Figure 3.43 presents the raw ^{1}H and ^{19}F NMR data from this experiment, with the average oxidation state of **P18$_{THS}$(C$_2$CPDIPS)$_2$** stated alongside each spectrum, as calculated from the point at which the thianthrene signal first broadens in comparison to the amount of oxidant added. From these data we observe no additional peaks growing in and decaying. Instead, only a broadening of the ^{19}F signal is observed along with a gradual shift to more positive ppm values over the course of the titration. Due to the featureless spectrum at all points in the titration, each

^{19}F signal can be well described by a single Lorentzian peak. This reference experiment therefore supports our conclusion that the additional peaks that grow in and decay in the titrations of ***c*-P18$_{THS}$·T18$_{A/B}$** can be assigned to globally aromatic states.

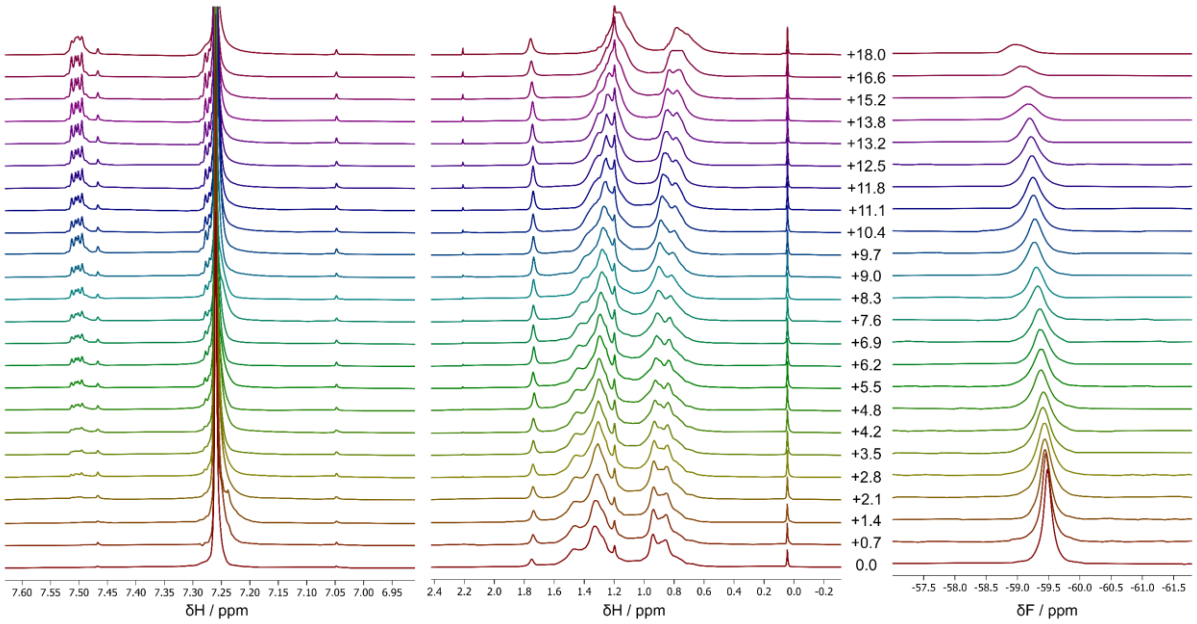

Figure 3.43. ^{1}H and ^{19}F NMR spectra from the oxidative titration of **P18$_{THS}$(C$_2$CPDIPS)$_2$·T18$_B$** at 233K in $CDCl_3$. ^{19}F spectra referenced against C_6F_6 δ_F = –161.64.

3.4.5 Conclusions from the Oxidative NMR Titrations

In conclusion, the oxidative NMR titrations of ***c*-P18$_{THS}$·T18$_{A/B}$** at room temperature showed no evidence of global anti/aromaticity. We tentatively attribute this to rapid internal rotations in the ***c*-P18$_{THS}$** nanoring breaking global π-conjugation on the NMR time scale and therefore preventing the formation of global ring currents. Upon cooling both samples, evidence of global anti/aromaticity is observed, by the growth and decay of additional ^{19}F peaks either side of the main ^{19}F signal. Manual deconvolution of both titration series can be used to extract the ppm values of each oxidation state and therefore assign them as aromatic or antiaromatic. Both of the manually deconvoluted series follow the expected trends previously established from oxidative titrations of smaller porphyrin nanorings. Namely; (1) assigned oxidation states have consistent ppm values across the titration. (2) The absolute abundance of each species grows to a single maximum then decays. (3) Each oxidation state is observed in sequence (i.e. +10 before

+11 before +12). Comparing ***c*-P18$_{THS}$·T18$_{A}$** and ***c*-P18$_{THS}$·T18$_{B}$** we observe that all identifiable oxidation states occur at the same points in both titrations, with relatively similar amounts of de/shielding between the series, though the absolute shifts are larger for the ***c*-P18$_{THS}$·T18$_{B}$** complex, which is likely due to the closer proximity of the CF_3 probes in this template to the porphyrin nanoring.

Our reference low temperature oxidative titration on **P18$_{THS}$(C$_2$CPDIPS)$_2$·T18$_{B}$** further supports our conclusion that both ***c*-P18$_{THS}$·T18$_{A}$** and ***c*-P18$_{THS}$·T18$_{B}$** are globally aromatic, as this complex does not show the growth and decay of any additional features. Instead, we observe a gradual broadening of the ^{19}F signal and a shift to a more positive ppm value over the titration. We attribute this featureless titration to the inability of **P18$_{THS}$(C$_2$CPDIPS)$_2$·T18$_{B}$** to sustain global ring currents, as the break in the chain means it does not have a cyclic π-conjugated circuit. Figure 3.44 directly compares the oxidative NMR titration data for the ***c*-P18$_{THS}$·T18$_{B}$** and **P18$_{THS}$(C$_2$CPDIPS)$_2$·T18$_{B}$** complexes.

The shifts observed in the ^{19}F spectra of both nanoring complexes, during the low temperature oxidative titrations, are limited to a range of about ±1 ppm from the starting point of the neutral complexes. These shifts are significantly weaker than those observed in the smaller 12-porphyrin nanoring complex (***c*-P12$_{THS}$·(T6e)$_2$**) which demonstrates shifts over a range of +2 to -3 ppm. From these results we can conclude that the global ring currents in ***c*-P18** are weaker than those in ***c*-P12**. These weaker currents made the identification of the anti/aromatic states of ***c*-P18** challenging. We anticipate that even larger rings will produce yet weaker ring currents, which are unlikely to be observable by NMR. Therefore, to further study the size limit of global aromaticity, we may need to explore alternative techniques for the identification of global anti/aromatic states.

Finally, the observation of global ring currents only at low temperatures for ***c*-P18$_{THS}$·T18$_{A/B}$** is an intriguing observation, as it mirrors the behavior of the superconducting metal rings

introduced in Section 2.1.2, which only exhibit their superconducting behaviors below a critical temperature (T_c).

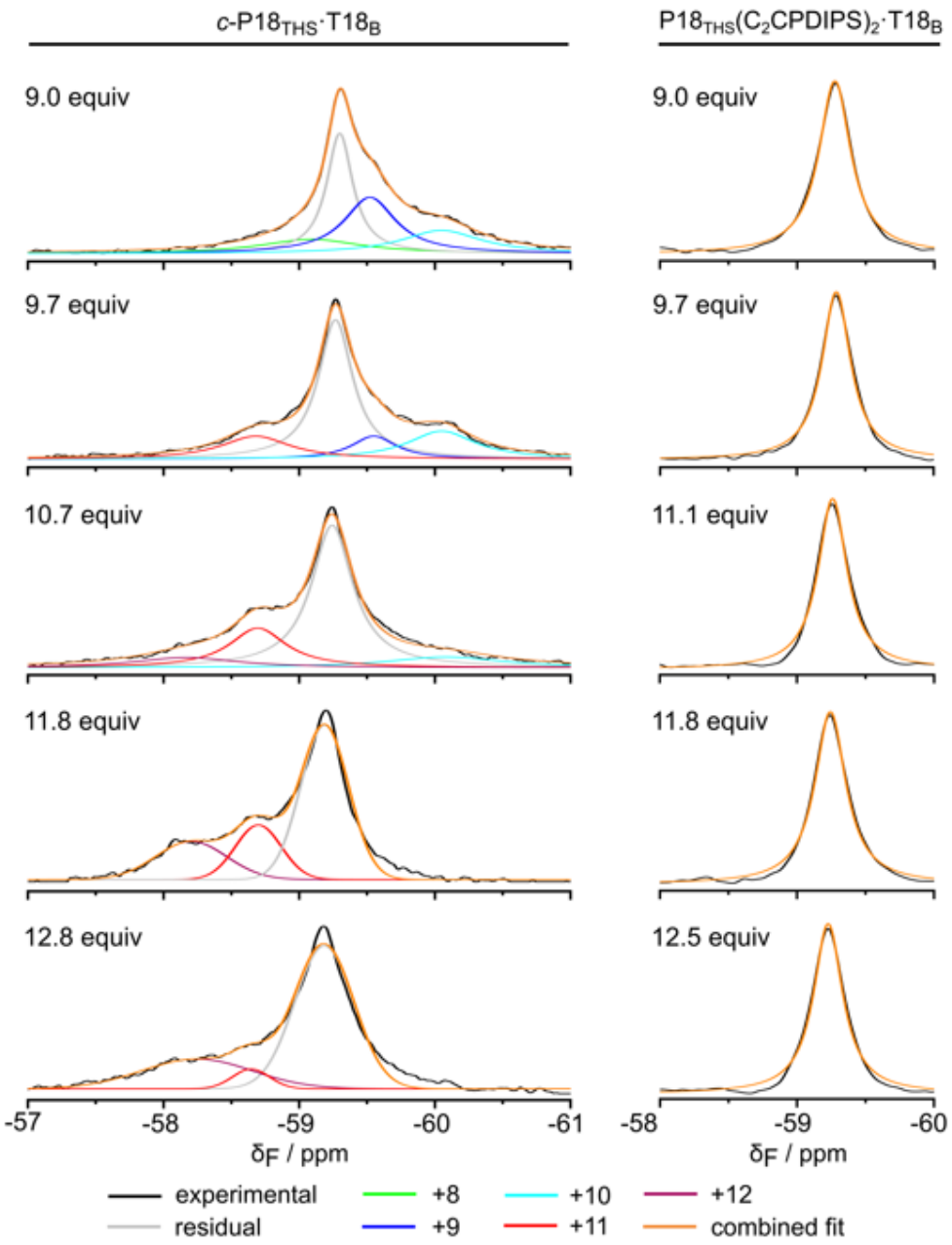

Figure 3.44. Comparison of the ^{19}F oxidative NMR titration data for ***c*-P18$_{THS}$·T18$_B$** and **P18$_{THS}$(C$_2$CPDIPS)$_2$·T18$_B$**. Equiv dennotes the equivalents of ThnBArF added. (233 K, $CDCl_3$).

3.5 Summary and Outlook

To summarize this chapter, we have first established that both **T18$_A$** and **T18$_B$** bind strongly to ***c*-P18$_{THS}$** and remain in place even at high concentrations of competing ligands. To directly

compare the two templates, we performed competition binding experiments which concluded that **T18$_B$** binds marginally more strongly than **T18$_A$** with $K_B/K_A = 1.69$.

Molecular dynamics simulations on the complexes **P3$_{THS}$·T3$_{A/B}$** and ***c*-P18$_{THS}$·T18$_{A/B}$** predicted that the A template complexes are less π-conjugated than the B template complexes, due to the meta-pyridyl link in the A templates allowing for internal rotations that break the π-conjugation of the porphyrin species. Confirmation of this behavior was found in the UV-Vis spectrum of the complexes, by analysis of the porphyrin Q-band, which showed in all cases an increase in π-conjugation (Red shift of the Q-band) across the series: free porphyrin < A complex < B complex.

The combination of the binding study, computational modelling, MD simulations, UV-Vis data and NMR data confirm that both nanoring complexes are planar, relatively rigid, well defined supramolecular structures with high formation constants and which possess a conjugated π-system that is delocalized over the whole macrocycle. All of which are essential characteristics for the study of global aromaticity in macrocyclic molecules.

To probe the global aromaticity of these complexes, oxidative NMR titrations were performed which at room temperature show no evidence of global ring currents. Conversely, at low temperature (-40 °C) evidence of global ring currents in both complexes is observed, by the growth and decay of ^{19}F peaks either side of the main ^{19}F signal. These additional signals were manually deconvoluted and shown to match the predictions of global aromaticity from Hückels rule and NICS calculations on ***c*-P18**. Comparing the two templates we observed that ***c*-P18$_{THS}$·T18$_B$** shows a larger anti/aromatic shift and a lower abundance of unassigned ^{19}F peaks, which we attribute to the closer proximity of the CF_3 probe to ***c*-P18** in this complex and to the higher conformational stability of ***c*-P18$_{THS}$·T18$_B$** relative to ***c*-P18$_{THS}$·T18$_A$**. Our reference titration on the complex **P18$_{THS}$(C$_2$CPDIPS)$_2$·T18$_B$** further supports our conclusion that ***c*-P18$_{THS}$·T18$_A$** and ***c*-P18$_{THS}$·T18$_B$** are globally aromatic, as this complex shows no growth and decay of additional peaks, which we attribute to its inability to sustain global ring currents.

The ^{19}F shifts observed in the anti/aromatic states of ***c*-P18$_{THS}$·T18$_{A/B}$** are significantly weaker than those observed for ***c*-P12$_{THS}$·(T6$_e$)$_2$** and are additionally challenging to identify due to the broadness of the signals and poor signal to noise. It could therefore be concluded from this study that we have reached the size limit of molecular aromaticity, as it is unlikely that anti/aromatic ring currents will be observed in larger nanorings using this methodology, as these effects are barely identifiable in the ***c*-P18$_{THS}$·T18$_{A/B}$** system. However, a conclusion like this assumes that size is the only factor allowing/disallowing global aromaticity in π-conjugated macrocycles. As seen in this study, temperature is one crucial factor which has been shown to improve the identification of global ring currents. Solubility limits the minimum temperature that oxidative NMR titrations can be performed at, however, if alternative methodologies to probe global aromaticity were identified which could go to lower temperatures, perhaps global ring currents in larger nanorings could be observed. Furthermore, the butadiyne link is one of the weaker interporphyrin links for maintaining π-conjugation in porphyrin oligomers. The strongest link would be to directly fuse adjacent porphyrin units, to form nanobelts. These structures are predicted to have exceptional π-conjugation across the macrocycle which is expected to lead to global aromaticity in the neutral state;[20] a phenomenon that has never been observed in porphyrin-based nanorings. Porphyrin nanobelts are additionally far more rigid than butadiyne-linked nanorings, so, would not suffer from the internal rotations described in this thesis which break global π-conjugation. Macrocycles like pophryin nanobelts may therefore be expected to exhibit global aromaticity at the size regime of ***c*-P18$_{THS}$·T18$_{A/B}$** and even larger, as a result of their increased π-conjugation and conformational stability.

3.6 References

1. S. A. Hollingsworth and R. O. Dror, *Neuron*, 2018, **99**, 1129-1143.
2. J. Wang, R. M. Wolf, J. W. Caldwell, P. A. Kollman and D. A. Case, *Journal of Computational Chemistry*, 2004, **25**, 1157-1174.
3. H. Gotfredsen, J.-R. Deng, J. M. Van Raden, M. Righetto, J. Hergenhahn, M. Clarke, A. Bellamy-Carter, J. Hart, J. O'Shea, T. D. W. Claridge, F. Duarte, A. Saywell, L. M. Herz and H. L. Anderson, *Nature Chemistry*, 2022, **14**, 1436-1442.
4. H. Gotfredsen, J. Hergenhahn, F. Duarte, T. D. W. Claridge and H. L. Anderson, *Journal of the American Chemical Society*, 2024, **146**, 25232-25244.
5. H. J. Hogben, J. K. Sprafke, M. Hoffmann, M. Pawlicki and H. L. Anderson, *Journal of the American Chemical Society*, 2011, **133**, 20962-20969.
6. M. Rickhaus, M. Jirasek, L. Tejerina, H. Gotfredsen, M. D. Peeks, R. Haver, H.-W. Jiang, T. D. W. Claridge and H. L. Anderson, *Nature Chemistry*, 2020, **12**, 236-241.
7. P. S. Bols, M. Rickhaus, L. Tejerina, H. Gotfredsen, K. Eriksen, M. Jirasek and H. L. Anderson, *Journal of the American Chemical Society*, 2020, **142**, 13219-13226.
8. N. Kamonsutthipaijit, University of Oxford, 2016.
9. P. V. R. Schleyer, C. Maerker, A. Dransfeld, H. Jiao and N. J. R. van Eikema Hommes, *J Am Chem Soc*, 1996, **118**, 6317-6318.
10. J.-R. Deng, D. Bradley, M. Jirásek, H. L. Anderson and M. D. Peeks, *Angewandte Chemie International Edition*, 2022, **61**.
11. I. Casademont-Reig, R. Guerrero-Avilés, E. Ramos-Cordoba, M. Torrent-Sucarrat and E. Matito, *Angewandte Chemie International Edition*, 2021, **60**, 24080-24088.
12. I. Casademont-Reig, L. Soriano-Agueda, E. Ramos-Cordoba, M. Torrent-Sucarrat and E. Matito, *Angewandte Chemie International Edition*, 2022, **61.**
13. A. D. Becke, *The Journal of Chemical Physics*, 1993, **98**, 5648-5652.
14. M. Renz, M. Kess, M. Diedenhofen, A. Klamt and M. Kaupp, *J Chem Theory Comput*, 2012, **8**, 4189-4203.
15. T. M. Henderson, A. F. Izmaylov, G. Scalmani and G. E. Scuseria, *The Journal of Chemical Physics*, 2009, **131**.
16. M. Jirásek, H. L. Anderson and M. D. Peeks, *Accounts of Chemical Research*, 2021, **54**, 3241-3251.
17. S. M. Kopp, H. Gotfredsen, J. Hergenhahn, A. Rodríguez-Rubio, J.-R. Deng, H. Zhu, W. Stawski and H. L. Anderson, *Chem*, 2024, **10**, 3410-3427.
18. G. Schwarz, *The Annals of Statistics*, 1978, **6**, 461-464, 464.
19. H. P. Gavin, 2019.
20. M. Vitek, J.-R. Deng, H. L. Anderson and I. Rončević, *ACS Nano*, 2025, **19**, 1405-1411.
21. M. J. Abraham, T. Murtola, R. Schulz, S. Páll, J. C. Smith, B. Hess and E. Lindahl, *SoftwareX*, 2015, **1-2**, 19-25.
22. G. Bussi, D. Donadio and M. Parrinello, *The Journal of Chemical Physics*, 2007, **126**.
23. M. Parrinello and A. Rahman, *Journal of Applied Physics*, 1981, **52**, 7182-7190.
24. P. Cieplak, J. Caldwell and P. Kollman, *Journal of Computational Chemistry*, 2001, **22**, 1048-1057.
25. U. Essmann, L. Perera, M. L. Berkowitz, T. Darden, H. Lee and L. G. Pedersen, *The Journal of Chemical Physics*, 1995, **103**, 8577-8593.
26. B. Hess, H. Bekker, H. J. C. Berendsen and J. G. E. M. Fraaije, *Journal of Computational Chemistry*, 1997, **18**, 1463-1472.
27. OpenAI, *ChatGPT*, 2024.

3.7 Experimental

Contents

3.7.1 Molecular Dynamics

All molecular dynamics simulations were performed in an isothermal-isobaric (NPT) ensemble at 1 bar and 300 K at a time step of 2 fs using GROMACS (version 2019.2)[21]. The General AMBER force field[2] was used for all simulations, with modifications to the parameters used to describe zinc ions and porphyrin connections.[3, 4] To reduce the computational cost, all aryl solubilizing groups on the porphyrin species were replaced with hydrogen atoms. Molecular systems were minimized with the steepest descent algorithm for 5000 steps, or until the maximum force on any atom was below 1000 kJ $mol^{-1}nm^{-1}$, then equilibrated using a velocity-rescaling thermostat[22] and Parinello-Rahman barostat.[23] Explicit chloroform[24] was used for all simulations with three-dimensional boundary conditions. Box sizes were selected by leaving a distance of 1 nm between the solute and box boundary. Long-range electrostatic interactions were calculated using the particle mesh Ewald method.[25] Bond lengths involving hydrogen atoms were constrained using the LINCS algorithm.[26] All simulations were repeated three times with different random starting seeds. Simulations on P3 species were run for 200 ns and cP18 species for 50 ns.

3.7.2 Binding Study

3.7.2.1 Pyridine Binding to P1$_{THS}$(C$_2$CPDIPS)$_2$

To determine the binding constant of pyridine to **P1$_{THS}$(C$_2$CPDIPS)$_2$** (Figure 3.45) we completed formation titrations in which pyridine is titrated into a solution of **P1$_{THS}$(C$_2$CPDIPS)$_2$** in $CDCl_3$. The raw experimental data from these titrations is presented in Figures 3.46 and 3.47, along with the change in Q-band absorbance fit to Eq 3.1, which outputs a formation constant of $K_{py} = (1.47 \pm 0.05) \times 10^4\ M^{-1}$.

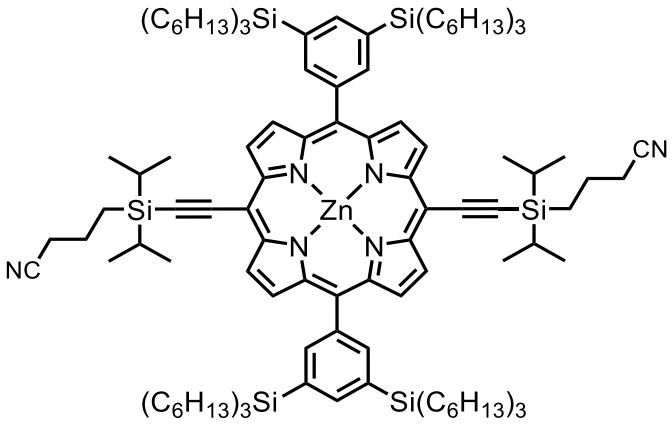

Figure 3.45. Chemical structure of **P1$_{THS}$(C$_2$CPDIPS)$_2$.**

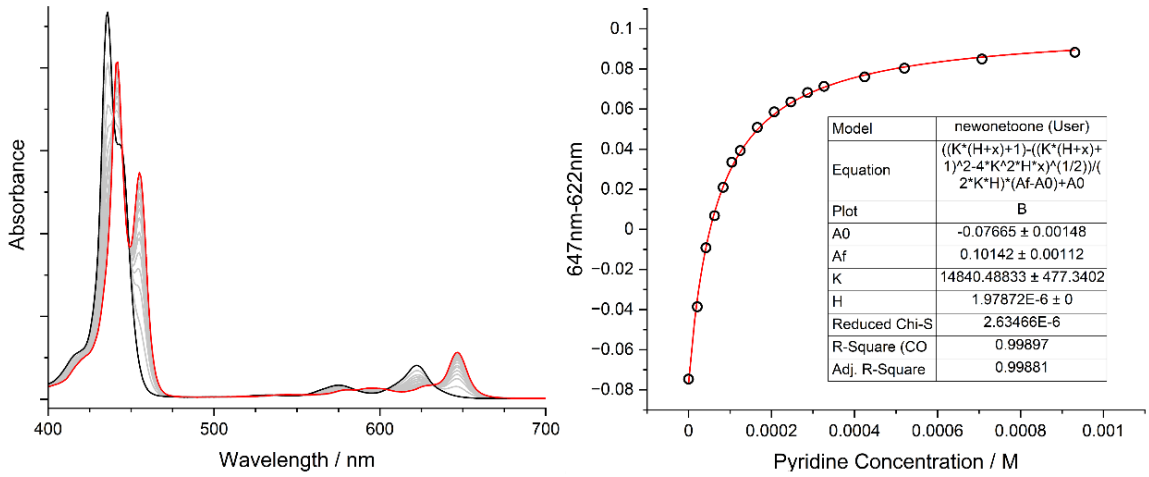

Figure 3.46. (left) First UV-vis titration of pyridine into **P1$_{THS}$(C$_2$CPDIPS)$_2$** ($CDCl_3$, 298 K). (right) Change in Q-band absorbance and fit to a one-to-one binding model using Eq. 3.1.

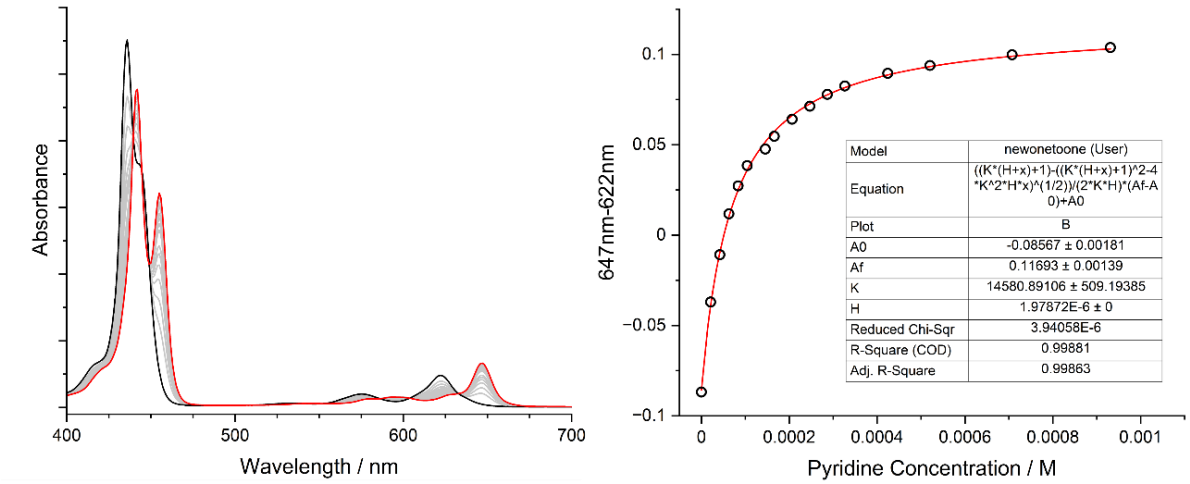

Figure 3.47. (left) Second UV-vis titration of pyridine into **P1$_{THS}$(C$_2$CPDIPS)$_2$** ($CDCl_3$, 298 K). (right) Change in Q-band absorbance and fit to a one-to-one binding model using Eq. 3.1.

3.7.2.2 Derivation of Competition Binding Model and Experimental Fit

Figure 3.48 presents the raw experimental data and fit data from the competition titration between **T3$_A$** and **T3$_B$** for **P3$_{THS}$(C$_2$CPDIPS)$_2$**, which we will use as an example of how the data was fit to obtain K_B/K_A. The same process was used for the **T18** competition data.

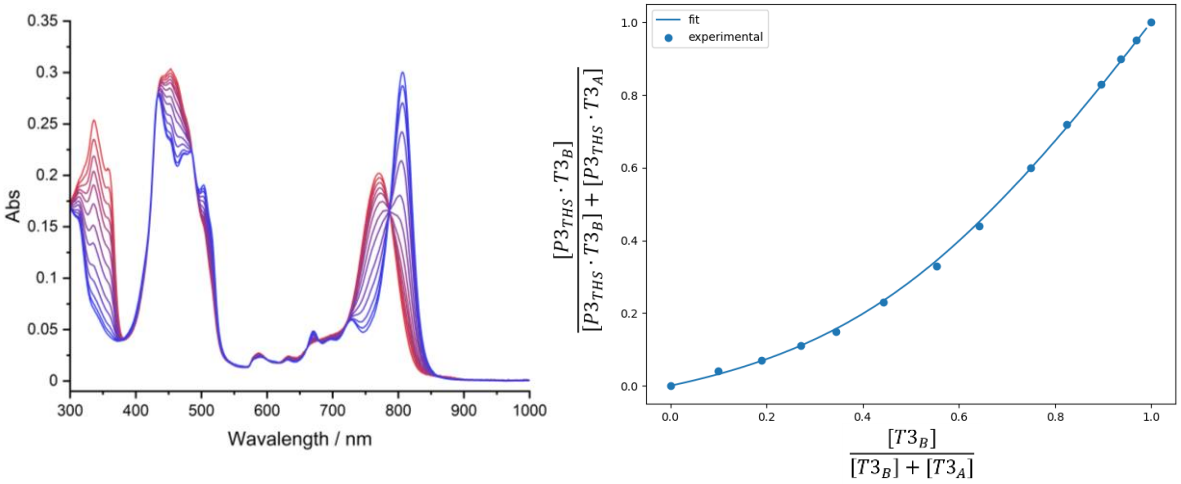

Figure 3.48. (left) Raw competition titration between **T3$_A$** and **T3$_B$** for **P3$_{THS}$(C$_2$CPDIPS)$_2$** (Red trace is pure **P3$_{THS}$·T3$_A$**, Blue trace is pure **P3$_{THS}$·T3$_B$**). (right) Processed raw data and fit to the competition binding model used to determine K_B/K_A (x-axis is the mole fraction of **T3$_B$**, y-axis is the mole fraction of **P3$_{THS}$(C$_2$CPDIPS)$_2$·T3$_B$**).

In the competition experiment, a cuvette was filled with 2,000 uL of a 2:1 solution of **T3$_A$** : **P3$_{THS}$(C$_2$CPDIPS)$_2$**. Throughout the titration aliquots were removed from the cuvette and replaced with an equal volume of 2:1 solution of **T3$_A$** : **P3$_{THS}$(C$_2$CPDIPS)$_2$**, which allows for the measurement of varying **T3$_A$** : **T3$_B$** rations (from 2:0 to 0:2) at constant concentration of

P3$_{THS}$(C$_2$CPDIPS)$_2$. We processed this data to determine K_B/K_A by fitting the experimental data to the equilibrium shown in Figure 3.49 and Eq 3.5, where [BP] and [AP] are the

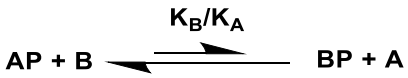

Figure 3.49. Equilibrium between complexes AP/BP and free templates A/B.

$$\frac{K_B}{K_A} = \frac{[BP][A]}{[AP][B]} \qquad \text{Eq 3.5}$$

The fitting process was conducted using the following workflow:

1. The UV-Vis spectra from the start and end of the titration were taken as they represent either a 1:1 mix of **T3$_A$**: **P3$_{THS}$·T3$_A$** or a 1:1 mix of **T3$_B$**: **P3$_{THS}$·T3$_B$**. These spectra were then used to produce a series of calibration curves representing the different ratios of **P3$_{THS}$·T3$_A$** : **P3$_{THS}$·T3$_B$** in 1% increments from 100% **P3$_{THS}$·T3$_A$** + 0% **P3$_{THS}$·T3$_B$**, to 0% **P3$_{THS}$·T3$_A$** + 100% **P3$_{THS}$·T3$_B$.**

2. Each spectrum from the competition titration experiment was compared to the calibration curves to determine the ratio of **P3$_{THS}$·T3$_A$** : **P3$_{THS}$·T3$_B$** present at that point in the titration. Using this value and the known amount of total **T3$_A$** and **T3$_B$** in solution at that point in the titration, we were able to plot the experimental data points as mole fraction of total **T3$_B$** in solution (χ_{T3B}) vs mole fraction of **P3$_{THS}$·T3$_B$** ($\chi_{P3THS\cdot T3B}$) (Figure 3.48, right, data points).

3. Next, consider a single experimental data point in Figure 3.48 (right). From the known mole fraction of total **T3$_B$** in solution (χ_{T3B}) there are many potential mole fractions of free **T3$_B$** possible, each of which correspond to a specific mole fraction of **P3$_{THS}$·T3$_B$** and therefore a specific value of K_B/K_A. This is based on the assumption that all **P3** in solution is complexed, therefore for a given mole fraction of total **T3$_B$** and chosen value of free **T3$_B$** we can calculate the absolute values of free **T3$_A$**, free **T3$_B$, P3$_{THS}$·T3$_B$** and

P3THS·T3A which when used in Eq 3.5 give K_B/K_A. It may be easier to understand this by considering the following three equations which always hold true for any 2:1 mix of **T3A/B:P3THS**, assuming all **P3THS** is bound:

$$[Total\ P3] = [P3_{THS} \cdot T3_A] + [P3_{THS} \cdot T3_B] \qquad \text{Eq 3.6}$$

$$[Total\ P3] = [Free\ T3_A] + [Free\ T3_B] \qquad \text{Eq 3.7}$$

$$[Total\ T3_B] = [Free\ T3_B] + [P3_{THS} \cdot T3_B] \qquad \text{Eq 3.8}$$

4. Using the relationships established in 3., for each experimental data point we can calculate the mole fractions of **P3THS·T3B** corresponding to all potential values of free **T3B**. Essentially these data points look like the orange points in Figure 3.50. Each of these orange points corresponds to a different value of K_B/K_A. We then find the calculated point with the smallest root mean square difference to the experimental data, which we assign as the K_B/K_A value for that experimental data point.

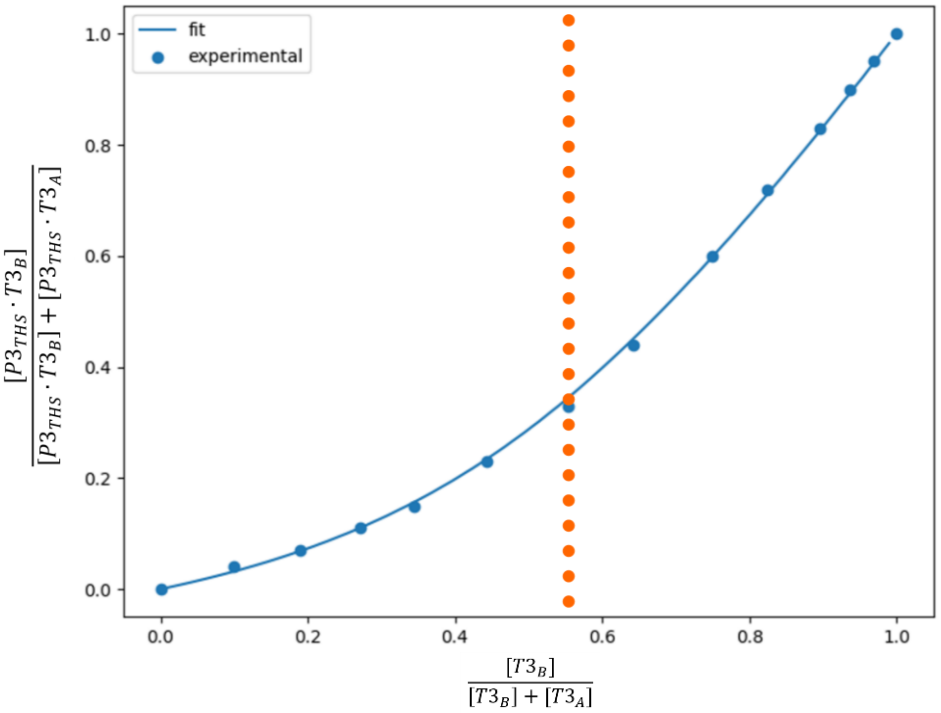

Figure 3.50. For a given mole fraction of total **T3B**, there are many potential values of free **T3B,** each of which corresponds to a different value for the mole fraction of **P3THS·T3B**, and therefore K_B/K_A. Examples of these values are shown as orange points.

5. The process in 4. is repeated for all experimental data points to obtain their respective values of K_B/K_A which are then averaged to determine the value of K_B/K_A which best represents the entire dataset. This calculated value of K_B/K_A was then finally used to calculate the fit curve shown in Figure 3.50.

3.7.2.3 Calculation of Complex Abundances at Equilibrium

From the competition binding experiments we have calculated the values of K_B/K_A for both the **T3$_{A/B}$** and **T18$_{A/B}$**. From these values we can calculate the absolute abundances of the A and B complexes in a 1:1:1 mixture of A template : B template : porphyrin species. First, again consider the equilibrium in Figure 3.49, where A is free template A, B is free template B, AP is complex A and BP is complex B. This equilibrium is formed from a 1:1:1 mix of A:B:P where P is the porphyrin species. K_B/K_A can be written as in Eq 3.9.

At equilibrium [A] + [B] = 1, [AP] + [BP] = 1 and [B] = 1 – [PB], so we can rewrite Eq 3.5 as:

$$\frac{K_B}{K_A} = \frac{[AP]^2 - 2[AP] + 1}{[AP]^2} \qquad \text{Eq 3.9}$$

Using Eq 3.6 and with known values of K_B/K_A we can form and solve a quadratic equation for [AP]. For the **T3** competition titration where K_B/K_A is 0.16, we obtain a value of [PA] = 0.71, therefore [BP] = 0.29. For the **T18** competition titration where K_B/K_A is 1.69, we obtain a value of [AP] = 0.43, therefore [BP] = 0.57.

3.7.3 Automated Deconvolution

In an attempt to automatically deconvolute the oxidative NMR titration data, we wrote a piece of code in R with the assistance of ChatGPT[27] which takes the raw ^{19}F NMR spectra as an input and follows the following procedure to output a deconvoluted version of each spectrum:

(1) For each ^{19}F spectrum (cut to a range of -56 to -62 ppm) the code uses the nls.lm function (non-linear least squares by modification of the Levenberg-Marquardt algorithm[19]) to

find the optimum fit using 1, 2, 3, 4, 5 and 6 Lorentzian peaks. In this process the ppm position, height and width of each peak can be varied to optimize the fit.

(2) The code calculates the Bayesian Information Criteria value (BIC)[18] for each fitting (1-6 Lorentzians) and identifies the fitting with the smallest value. Typically, the BIC is calculated using Eq 3.10, however this model always overfits the data, by selecting 6 Lorentzians every time, or even more if we calculated fits for >6 Lorentzians. We found that altering the BIC calculation to apply a more severe penalty to overfitting produced more reasonable results for our data (usually fits 3-5 Lorentzians). This altered BIC is shown in Eq 3.11 and was used for the deconvolution shown in Figure 3.51. (k = number of variables, which here is the number of Lorentzian peaks in the model * 3 (peak height, peak width and median peak value). n = number of data points in the experimental data (Effectively a constant value). The ln(likelihood) component adds a contribution which measures how well the model fits the experimental data.)

(3) The fit with the lowest BIC value was selected and plotted alongside the selected deconvolutions for the other ^{19}F spectra.

$$BIC = 3k\big(ln(n)\big) - \ln\,(likelihood) \qquad \text{Eq 3.10}$$

$$BIC = k^3\big(ln(n)\big) - \ln\,(likelihood) \qquad \text{Eq 3.11}$$

Using this process on the -40 °C NMR titration data of ***c*-P18$_{THS}$·T18$_{B}$** we get the deconvoluted spectra shown below (Figure 3.51) and discussed in detail in Section 3.4.3.4.

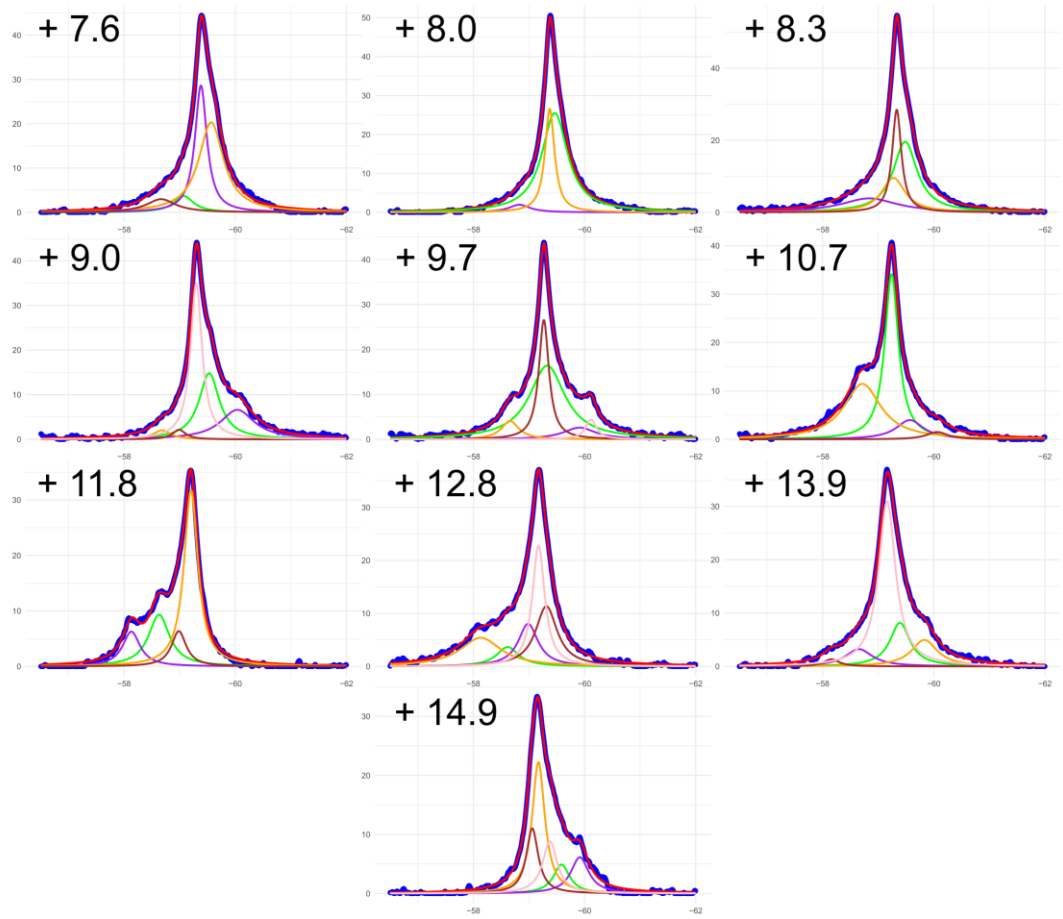

Figure 3.51. Automatically deconvoluted oxidative titration data of ***c*-P18$_{THS}$·T18$_{B}$** acquired at -40 °

3.7.3.1 R Code used for Automated Deconvolution

```
library(readxl)
library(ggplot2)
library(reshape2)
library(minpack.lm)

# Adjust the path to your file and read the data
file_path <- “Filepath.csv"
header_row <- colnames(read_xlsx(file_path, range = cell_rows(1)))
data <- read_xlsx(file_path, skip = 1)
colnames(data) = c("x", header_row)

# Reshape data and plot
data_long <- melt(data, id.vars = "x",
                  variable.name = "series", value.name = "value")
p1 <- ggplot(data_long, aes(x = x, y = value, color = series)) +
  geom_line() +
  scale_x_reverse() +  # Invert x-axis
  labs(title = "Plot of all series", x = "X-axis", y = "Values") +
  theme_minimal()
print(p1)

x <- data[[1]]  # x-axis values
y <- data[[12]]  # pick a column for y-values

########### Step 1: model selection with BIC to pick the best number of peaks

fit_gaussian_peaks <- function(k, x, y) {
  lorentzian_sum_k <- paste0("a", 1:k, " / (1 + ((x - b", 1:k, ")^2 / (c", 1:k, "^2)))",
collapse = " + ")
  fit_formula <- as.formula(paste("y ~", lorentzian_sum_k))

  start_lists <- list(
    as.list(rep(1, 3 * k)),  # Initial guess for a = 1
    as.list(rep(0.3, 3 * k)), # Initial guess for a = 0.5
    as.list(rep(2, 3 * k)) # Initial guess for a = 0.5
```

```
 )

 names(start_lists[[1]]) <- unlist(lapply(1:k, function(i) paste0(c("a", "b", "c"), i)))
 names(start_lists[[2]]) <- unlist(lapply(1:k, function(i) paste0(c("a", "b", "c"), i)))
 names(start_lists[[3]]) <- unlist(lapply(1:k, function(i) paste0(c("a", "b", "c"), i)))

 for (i in 1:k) {
  start_lists[[1]][[paste0("b", i)]] <- mean(x)
  start_lists[[1]][[paste0("c", i)]] <- 1
  start_lists[[2]][[paste0("b", i)]] <- mean(x)
  start_lists[[2]][[paste0("c", i)]] <- 1
  start_lists[[3]][[paste0("b", i)]] <- mean(x)
  start_lists[[3]][[paste0("c", i)]] <- 1
 }

 lower_bounds <- rep(-Inf, 3 * k)
 lower_bounds[seq(1, 3 * k, by = 3)] <- 0

 for (start_list in start_lists) {
  fit <- tryCatch({
   nlsLM(fit_formula, data = data.frame(x, y), lower = lower_bounds,
         control = nls.lm.control(maxiter = 500), start = start_list)
  }, error = function(e) {
   message("Fitting failed: ", e$message)
   return(NULL)
  })

  if (!is.null(fit)) {
   return(fit)  # Return the successful fit
  }
 }

 return(NULL)  # Return NULL if both attempts fail
}

# Iterate over different numbers of peaks and calculate BIC
bic_values <- sapply(1:10, function(k) {
 fit <- fit_gaussiangaussgagian_peaks(k, x, y)
 log(length(y)) * (k^3) - 2 * logLik(fit)
})

bic_values
p2 <- ggplot(data.frame(x = 1:10, BIC = bic_values), aes(x = x, y = BIC)) +
 geom_line() +
 scale_x_reverse() +  # Invert x-axis
 labs(title = "BIC for Number of Peaks", x = "Number of Peaks", y = "BIC") +
 theme_minimal()
print(p2)

# Find the best k value
min_bic <- min(bic_values, na.rm = TRUE)
k_within_threshold <- which(bic_values <= min_bic + 0)
best_k <- min(k_within_threshold)
best_fit <- fit_gaussian_peaks(best_k, x, y)
y_fit <- predict(best_fit, list(x = x))

# Plot the real data and the fitted Gaussian mixture
p3 <- ggplot() +
 geom_point(aes(x = x, y = y), color = "blue", alpha = 0.6, size = 2) +
 geom_line(aes(x = x, y = y_fit), color = "red", size = 1.2) +
 scale_x_reverse() +  # Invert x-axis
 labs(title = paste("Fitted Sum of Gaussian Peaks with", best_k, "Components")) +
 theme_minimal()
print(p3)

########### Step 2: viewing the K different peaks separately on a plot

plot_gaussian_peaks <- function(best_fit, best_k, x, y) {
 coef_values <- coef(best_fit)
 print(coef_values)

 # Update peak function to reflect inverted x-axis
 peak_func <- function(x, i) {
  inverted_x <- max(x) + min(x) - x  # Invert x-values
  coef_values[paste0("a", i)] / (1 + ((inverted_x - coef_values[paste0("b", i)])^2 / (coef_values[paste0("c", i)]^2)))
 }

 x_range <- seq(min(x), max(x), length.out = 1000)
 y_fit <- predict(best_fit, list(x = x))
```

```
  peak_values <- lapply(1:best_k, function(i) peak_func(x_range, i))


  p <- ggplot() + theme_minimal() +
    labs(title = paste("Fitted Sum of", best_k, "Lorentzian Peaks")) +
    geom_point(aes(x = x, y = y), color = "blue", alpha = 0.6, size = 2) +
    geom_line(aes(x = x, y = y_fit), color = "red", linewidth = 1.2) +
    scale_x_reverse()  # Invert x-axis
  colors <- c("green", "purple", "orange", "brown", "pink", "cyan",
"gray","yellow","black","magenta")


  for (i in 1:best_k) {
    p <- p + geom_line(aes(x = x_range), y = peak_values[[i]],
                       color = colors[i], linetype = "solid", size = 1.0)
  }
  print(p)
}


plot_gaussian_peaks(best_fit, best_k, x, y)
```

4

Single Molecule Spectroscopy of *c*-P18·T18$_{A/B}$

Contents

Chapter 4 - Single Molecule Spectroscopy of *c*-P18·T18$_{A/B}$

4.1 Single-Molecule Spectroscopy

4.1.1 Introduction

To further investigate the properties of ***c*-P18$_{THS}$·T18$_{A/B}$**, we initiated a collaboration with the group of Dr Gordon Hedley at the University of Glasgow, which aims to use single molecule spectroscopy to probe the time-dependent size and motion of excitons in our complexes. The experimental work presented in this chapter was completed by Natalie Miller, a PhD student in the Hedley group.

As a brief introduction, electrons in an organic π-conjugated molecule can be excited to higher electronic states by the absorption of UV-Vis light; a process that occurs on the femtosecond time scale.[1] This generates an excited negatively charged electron and a positively charged hole, which are bound by coulomb attractive forces typically an order of magnitude stronger than the accessible thermal energy at room temperature. Because of this, full separation of the charges cannot be achieved and the electron-hole pair are tightly bound into a quasi-particle termed an exciton.[1] Once formed, the exciton can return to the ground state via numerous different pathways, all of which occur on different time scales and are dependent on the molecular framework. Some key examples of the processes involved in this (with typical time scales) are: fluorescence (10^{-13} - 10^{-5} s), phosphorescence (10^{-7} – 1 s), intersystem crossing (10^{-13} - 10^{-3} s), internal conversion (10^{-14} - 10^{-11} s), exciton localization (10^{-14} - 10^{-12} s) and exciton delocalization (10^{-12} - 10^{-11} s).[1]

Organic π-conjugated molecules typically form Frenkel excitons[1] which are localized to a single molecular framework. From studies on previous porphyrin-based oligomers and nanorings,[2, 3] we understand that immediately after their formation, excitons in these molecules are delocalized over most of the framework. However, fast C-C vibrations lead to a geometric relaxation of the excited state that localizes the exciton on particular parts of the molecule; a

process which occurs on the picosecond time-scale (~1 x 10^{-12} s). This is known as "exciton self-trapping" and has been demonstrated in other π-conjugated organic molecules.[4] On a much slower time scale (~1 x 10^{-10} s), rotation of the porphyrin-porphyrin dihedral angle towards 0° increases inter-porphyrin π-conjugation, which has been shown to increase the size of the exciton by facilitating its delocalization over more porphyrin units.[2] Our collaboration seeks to explore these localization/delocalization dynamics and the motion of the exciton in our large ***c*-P18** nanoring. We additionally aim to study the effect binding the **T18** templates has on these properties.

4.1.2 Photon Antibunching

The first experiments performed in this project were focused on determining the number of emitting sites present in the **c-P18** nanoring, which we anticipated should be one, if the exciton is fully delocalized over the nanoring, or if it moves quickly around the nanoring, inhibiting the formation of a second exciton. To explore this, we performed photon antibunching experiments which are capable of quantifying the number of emitting sites in a molecule of interest.[5] To take these measurements, a small sample of the compound is dissolved in a toluene solution which contains 1% by weight PMMA. This solution is then spin coated onto a glass slide and placed onto an inverted confocal microscope. A scanning piezo stage then allows specific locations on the slide to be irradiated and the stream of emitted photons from the excitation pulses to be detected, which enables the photophysics of single molecules to be investigated.

In the photon antibunching experiments, single molecules are identified and irradiated at the λ_{max} of their respective Soret bands with pulses of light (120 fs long pulses, spaced 25 ns apart over a 60s acquisition time). For each pulse, the target molecule may be excited, after which it can radiatively decay to emit a photon. These photons are collected (termed the photon stream) by a high numerical aperture objective and reflected through a pinhole to a 50/50 beam splitter, which randomly directs the photons onto one of two orthogonal detectors. This experimental set up is termed a Hanbury Brown and Twiss geometry,[6, 7] which here allows for photon-

detection events to be correlated to their respective excitation pulse. Figure 4.1 and 4.2 demonstrate how these data can be used to determine the number of emitting sites on a molecule of interest.[5]

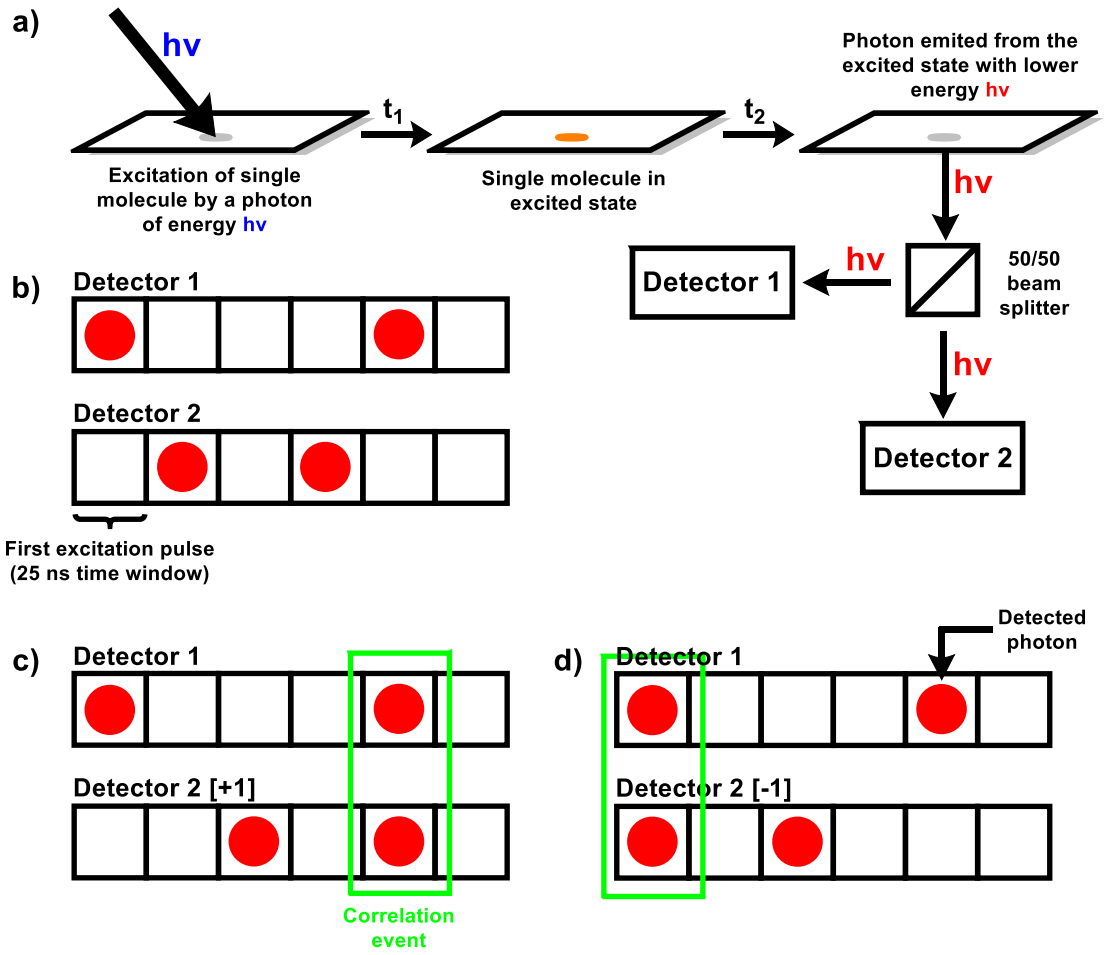

Figure 4.1. (a) Scheme illustrating excitation of a single molecule, then emission from the excited state, which is randomly sent to one of two orthogonal detectors by a 50/50 beam splitter. (b-d) An example of the detector responses when only one exciton can be formed on the molecule, portioned by excitation pulse. (a) at zero-shift (b) when detector 2 has been shifted by +1 excitation pulse (c) when detector 2 has been shifted by -1 excitation pulse.

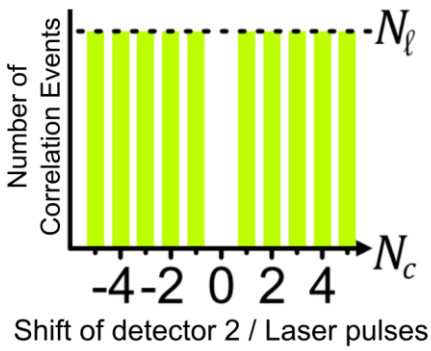

Figure 4.2. Theoretical photon antibunching result for an ideal molecule with 1 emitting site. Reproduced from reference.[5]

First, consider the ideal case in which there can only be one exciton formed on the single molecule. Upon radiative decay, this exciton can only emit one photon, which is randomly sent to either detector 1 or detector 2 by the 50/50 beam splitter, as a single photon cannot be split (Figure 4.1a). Figure 4.1b presents an example response from each detector portioned by excitation pulse. In this example, the response from the detector is binary, either it detects a photon (could be 1, 2, 3 … photon/s) or it doesn't. With only 1 emitting site per molecule, for a given laser pulse, there are 0 instances where detectors 1 and 2 both detect a photon; therefore, we say there are 0 correlation events. If we were to shift the data set of detector 2 forward by 1 excitation pulse, we see that we now have 1 correlation event (Figure 4.1c); the same is true if we shift it back by one excitation pulse (Figure 4.1d). The number of correlation events at varying shifts of detector 2 (e.g. from +5 to -5) can be used to produce a plot such as Figure 4.2, which for our ideal case of a single emitter has a perfect value of 0 correlations at 0 shift (N_c), and a consistently high number of correlations at all non-zero shifts (N_l is the average number of correlation events at non-zero shift).[5] It is important to note that even for molecules that are known to contain only a single emitter, N_c values of exactly 0 are never observed in this experimental set up, as some correlation events are always observed at 0 shift over the many excitation pulses measured in a typical experiment.

Now consider a molecule that possesses two independent emitting sites. Upon excitation from the pulse (multiple photons sent per pulse, therefore multiple excitations can occur if the molecule can support it) this molecule can form 0, 1 or 2 excitons. In the case of 0 excitons, there is no response from either detector. With 1 exciton, the detector response is as described in the previous example. However, for 2 excitons we have 3 possible detector responses: (1) Both photons are sent to detector 1, therefore it records a positive response and detector 2 has no response. (2) Both photons are sent to detector 2, therefore it records a positive response and detector 1 has no response. (3) One photon is sent to each detector, so they both record positive responses. Response (3) leads to this molecule having greater than 0 correlation events at zero

time-lag, as seen in Figure 4.3. The number of emitting sites (E) in the molecule can then be calculated using Eq 4.1.[5]

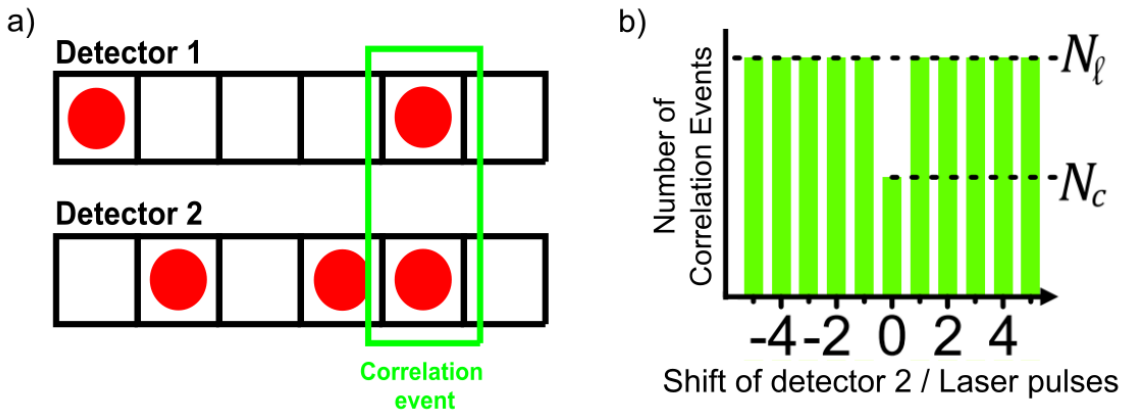

Figure 4.3. (a) Example detector response from a molecule with two independent emitting sites. (b) Example photon antibunching plot from this theoretical molecule showing non-zero N_c at zero-shift.

$$E = \frac{1}{1-\frac{N_c}{N_l}} \qquad \text{Eq 4.1}$$

For this study, we examined 5 molecules of interest **P6$_{THS}$(C$_2$CPDIPS)$_2$**, **P18$_{THS}$(C$_2$CPDIPS)$_2$**, ***c*-P18$_{THS}$** and ***c*-P18$_{THS}$·T18$_A$** and ***c*-P18$_{THS}$·T18$_B$**. Figure 4.4 presents the photon antibunching plots of these compounds (excluding ***c*-P18$_{THS}$·T18$_B$**) with the calculated number of emitters obtained using Eq 4.1. As all emitter values are very close to 1, we can conclude that all of the molecules studied are capable of supporting only a single exciton (emitter values of precisely 1 are never observed experimentally). Due to the large size of the molecules, these single excitons are either delocalized over the whole molecular framework, or rapidly move across the framework, preventing the formation of a second exciton.

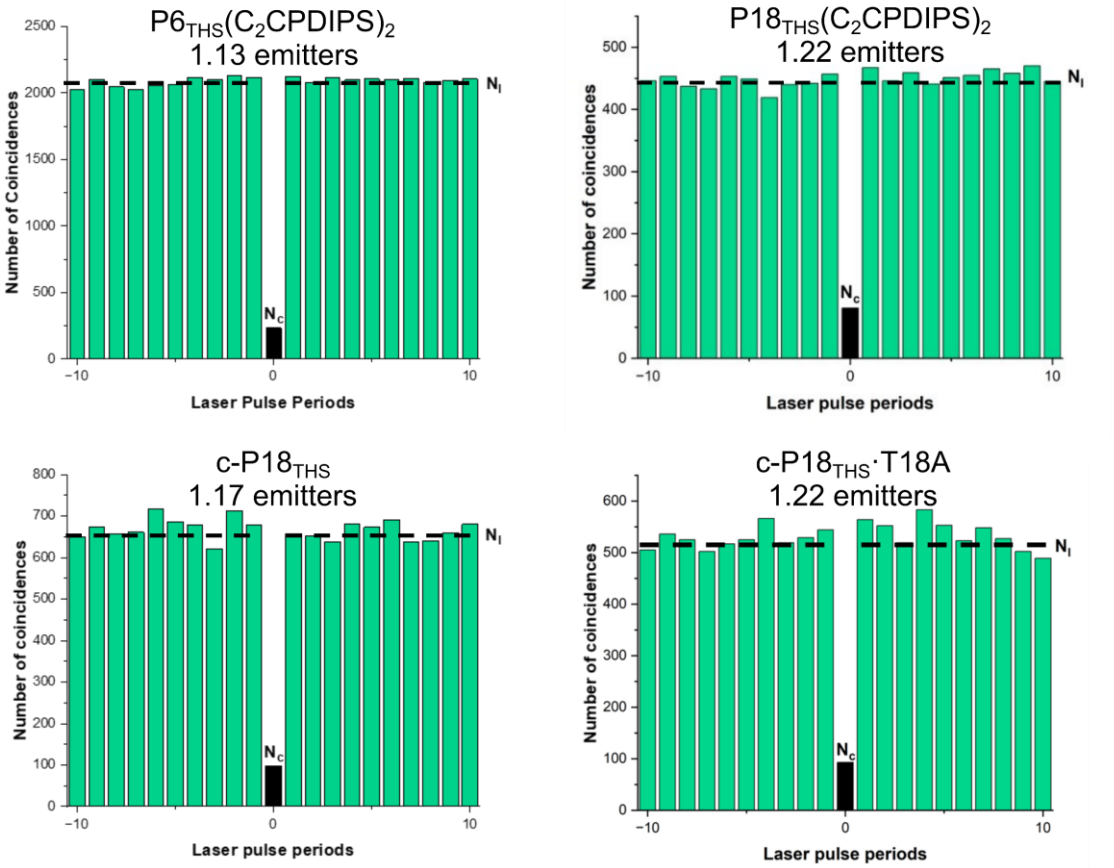

Figure 4.4. Results from photon antibunching measurements on various porphyrin-based oligomers and nanoring complexes.

4.1.3 Linear Dichroism

The linear dichroism (LD) of the photons emitted from our single molecules can be used to gain information on the transition dipole moment accompanying the transition from the excited to ground state. A change in the LD of emission over time implies a change in the transition dipole moment accompanying emission, which in turn means there is some change in the size, shape or motion of the exciton with time. To explore this, we used a similar experimental set up to the photon antibunching experiment, with the following changes: (1) the excitation source emits circularly polarized (CP) light, which unbiasedly excites the single molecules. (2) The emitted photon stream is passed through a polarizing beam splitter which sends perpendicular polarized light ($I_{\perp}$) to detector 1 and parallel polarized light ($I_{\parallel}$) to detector 2. (3) Using Eq 4.2, we can determine the LD value for a batch of 100 emitted photons. This value is then added to a histogram corresponding to the time period after excitation that the emitted photons came from.

$$LD = \frac{I_{\parallel} - I_{\perp}}{I_{\parallel} + I_{\perp}} \qquad \text{Eq 4.2}$$

Figures 4.5 and 4.6 present the time-resolved LD histograms for **P6$_{THS}$(C$_2$CPDIPS)$_2$** and ***c*-P18$_{THS}$·T18$_A$**. The first key point to note in these plots is the difference in overall shape between the two sets of histograms, as this informs us about the number of sites our single exciton can radiatively decay from. In the case of the linear oligomer **P6$_{THS}$(C$_2$CPDIPS)$_2$** the peaks towards LD values of ±1 and a minimum at 0 indicates that the exciton formed emits preferentially from one site. Emission from this single site, on a particular single molecule leads to a biased LD value depending on the orientation of that specific molecule with respect to the detectors. As we sample many single molecules, with many different orientations, it may be expected that the LD histogram show equal instances of all LD values from -1 to +1. However, under our specific experimental set up, we are less likely to observe LD values the closer they are to 0, so we instead see a valley like trend from -1 to +1 for the linear oligomer.[8]

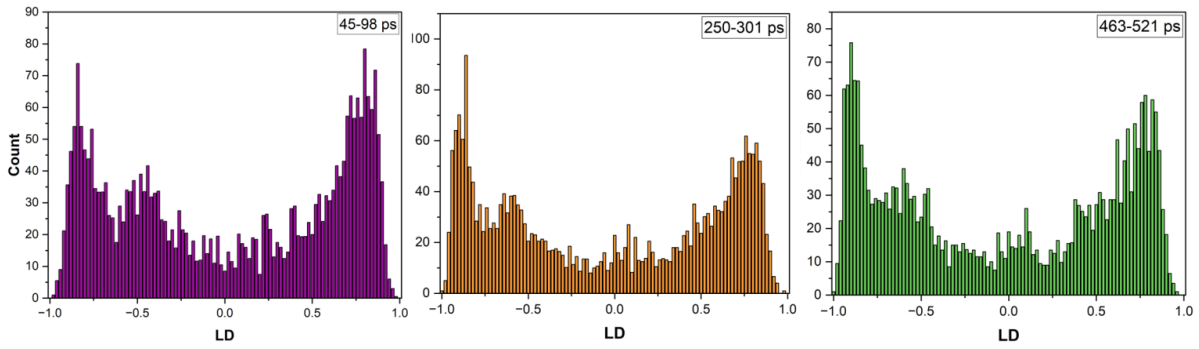

Figure 4.5. Selected time-resolved histograms showing LD values of **P6$_{THS}$(C$_2$CPDIPS)$_2$**. (CP excitation source at λ_{max} of porphyrin species Soret band. 120 fs excitation pulse, 25 ns between pulses over 60 s acquisition time per single molecule. Emission photons filtered for energy > 700 nm)

In contrast to the linear hexamer, ***c*-P18$_{THS}$·T18$_A$** has a distribution of LD values centred about 0 (Figure 4.6). This type of distribution indicates that the single exciton formed on this molecule can emit from numerous sites on the ring. This is not surprising given the high symmetry of the ***c*-P18$_{THS}$** nanoring. Our expectations from these measurements on ***c*-P18$_{THS}$·T18$_A$** is that we can observe some change in the shape of the LD histograms with respect to time, as a result

of the localisation, delocalisation and movement of the exciton. We hope our analysis of the time dependant LD will inform us about the timescale of these processes and reveal some quantitative information on the size, shape and movement of the exciton. Current work on this project is focused on collecting more data, so that we can draw firmer conclusions from the more substantial data set.

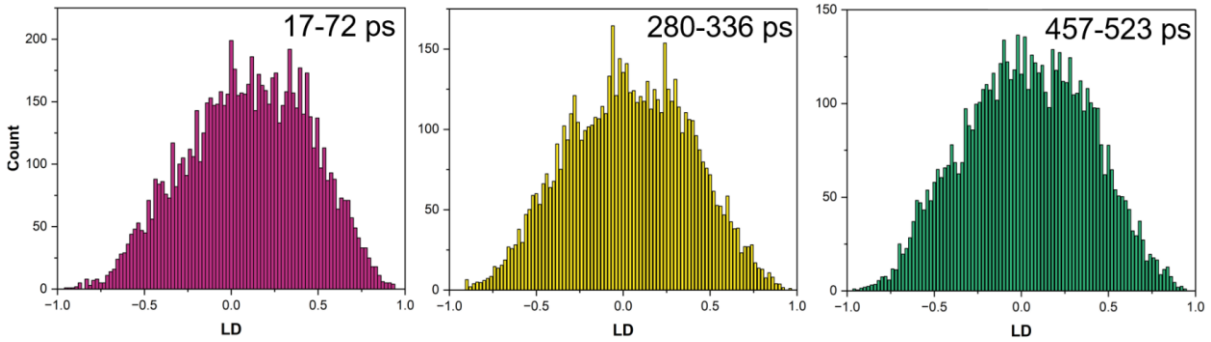

Figure 4.6. Selected time-resolved histograms showing LD values of ***c*-P18$_{THS}$·T18$_{A}$**. (CP excitation source at λ_{max} of porphyrin species Soret band. 120 fs excitation pulse, 25 ns between pulses over 60 s acquisition time per single molecule. Emission photons filtered for energy > 700 nm)

Finally, Figure 4.7 presents the LD histograms for all of the porphyrin species that we measured. From this figure we can see that **P18$_{THS}$(C$_2$CPDIPS)$_2$** has a distribution with a higher contribution from values closer to 0 when compared to **P6$_{THS}$(C$_2$CPDIPS)$_2$**, indicating that it has more potential sites for the exciton to decay from. This implies that the exciton in **P18$_{THS}$(C$_2$CPDIPS)$_2$** is not fully delocalized across the whole molecular framework and can instead emit from multiple sites along the oligomer. We also note that both the untemplated ***c*-P18$_{THS}$** and ***c*-P18$_{THS}$·T18$_{B}$** have wider distributions than for ***c*-P18$_{THS}$·T18$_{A}$**. In the case of ***c*-P18$_{THS}$** this could be attributed to some the untemplated nanorings laying in distorted, non-circular geometries, which preferentially emit from one site, leading to biased LD values closer to ±1, as in the linear oligomers. In the case of ***c*-P18$_{THS}$·T18$_{B}$** the slightly distorted geometry may have preferential emission sites, which bias the LD values away from 0.

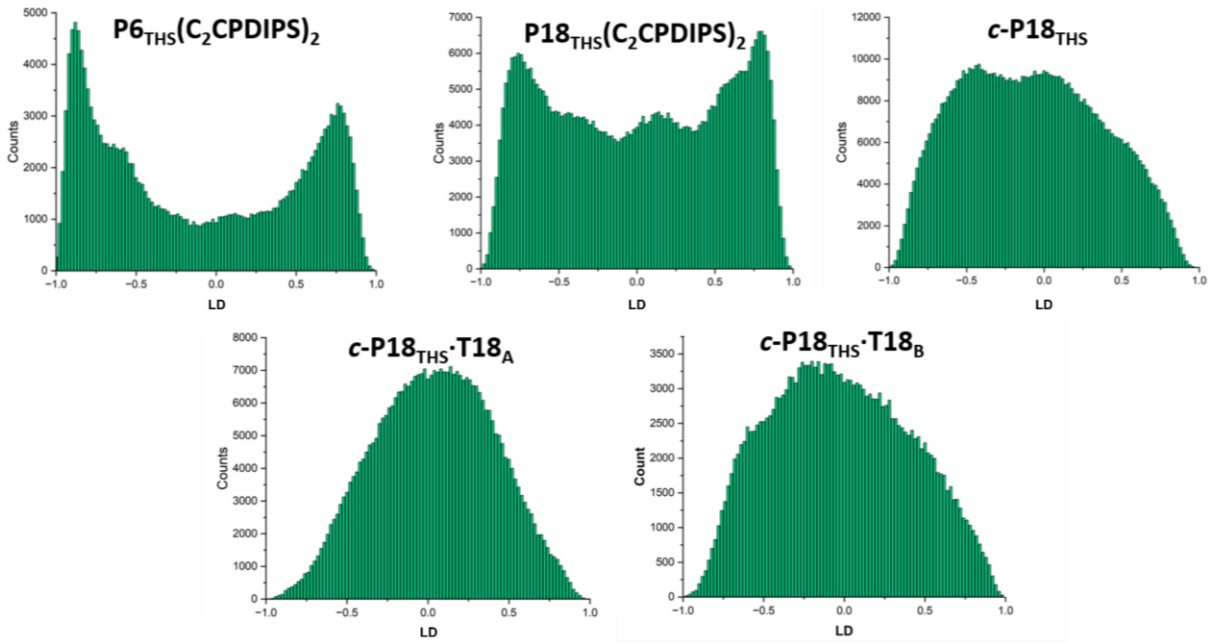

Figure 4.7. LD histograms for various porphyrin species. Each histograms represents data from many single molecule measurements, each of which was measured over a 60s acquisition period. (CP excitation source at λ_{max} of porphyrin species Soret band. 120 fs excitation pulse, 25 ns between pulses. Emission photons filtered for energy > 700 nm. Each count of LD is obtained from a bin of 100 photons.)

4.1.4 Dark States

Another observation from our study of the ***c*-P18$_{THS}$** nanoring (with and without **T18$_{A/B}$**) is the existence of long-lived dark states. Figure 4.8 presents a 60s long acquisition of a single molecule of ***c*-P18$_{THS}$·T18$_{A}$** which has periods of low emission (blue/purple sections), followed by periods of relatively high emission (pink section). This behaviour is surprising when we consider that these experiments are run under ambient conditions, with no exclusion of O_2. The presence of O_2 ensures that any long-lived triplet states are quenched, so the presence of such long-lived dark states is intriguing. Our current experiments aim to explore this by examining the effects of using alternative triplet scavengers and how changing the polarity of our matrix effects the dark state.

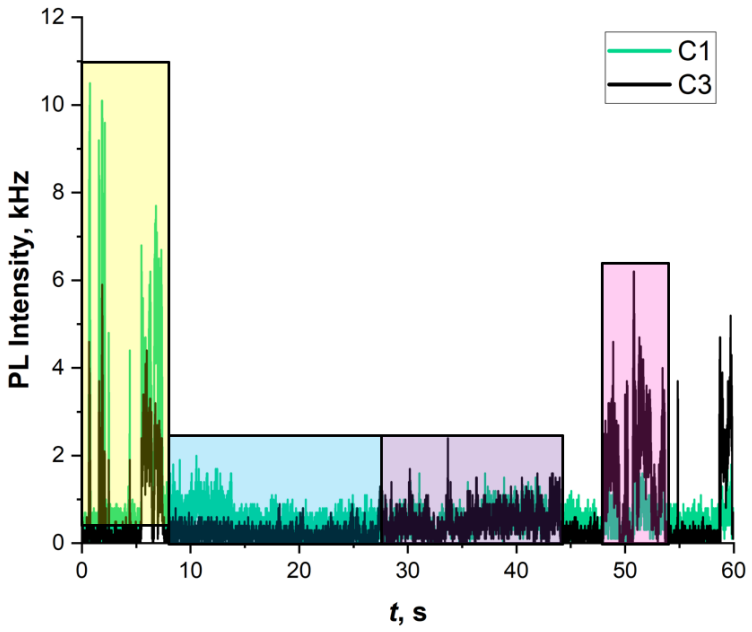

Figure 4.8. PL intensity over a 60s acquisition of a single molecule of ***c*-P18$_{THS}$·T18$_{A}$** (excitation at λ_{max} of the Soret band, pulse length 120 fs, 25 ns between pluses) (C1 and C3 are the responses from the detectors measuring orthogonally polarised light).

4.2 Summary and Outlook

To summarize this chapter, our ongoing collaboration using single molecule spectroscopy to study the size, shape and motion of excitons in ***c*-P18$_{THS}$** has revealed that the free nanoring and templated complexes with either **T18$_{A}$** or **T18$_{B}$** support the formation of only a single exciton, as confirmed by photon antibunching measurements. Our results show that the linear oligomers **P6$_{THS}$(C$_2$CPDIPS)$_2$** and **P18$_{THS}$(C$_2$CPDIPS)$_2$** also support only a single exciton, however there is evidence that the longer 18-mer may in some cases support an additional exciton, which we attribute to its longer framework and varied geometry in the spin coated sample. We also examined the LD of the emitted photons from our samples and can conclude the following: (1) **P6$_{THS}$(C$_2$CPDIPS)$_2$** emits preferentially from one site. (2) **P18$_{THS}$(C$_2$CPDIPS)$_2$** emits from a limited number of sites, but certainly more than one. (3) ***c*-P18$_{THS}$** with and without **T18$_{A/B}$** is a generally isotropic emitter, with many potential sites radiative decay can occur from. (4) ***c*-P18$_{THS}$** untemplated and ***c*-P18$_{THS}$·T18$_{B}$** have slightly broader LD distributions, indicating that they have a slight bias to particular emitting sites. (5)

***c*-P18$_{THS}$·T18$_{A}$** is the most isotropic emitter, so the exciton in this complex has the most potential sites that it can decay from. Future work in this collaboration seeks to draw more firm conclusions about the size, shape and movement of excitons in ***c*-P18$_{THS}$** and to further explore the long-lived dark states observed in these measurements.

4.3 References

1. O. P. Dimitriev, *Chemical Reviews*, 2022, **122**, 8487-8593.
2. M.-H. Chang, M. Hoffmann, H. L. Anderson and L. M. Herz, *Journal of the American Chemical Society*, 2008, **130**, 10171-10178.
3. C.-K. Yong, P. Parkinson, D. V. Kondratuk, W.-H. Chen, A. Stannard, A. Summerfield, J. K. Sprafke, M. C. O'Sullivan, P. H. Beton, H. L. Anderson and L. M. Herz, *Chemical Science*, 2015, **6**, 181-189.
4. K. H. Park, W. Kim, J. Yang and D. Kim, *Chemical Society Reviews*, 2018, **47**, 4279-4294.
5. G. J. Hedley, T. Schröder, F. Steiner, T. Eder, F. J. Hofmann, S. Bange, D. Laux, S. Höger, P. Tinnefeld, J. M. Lupton and J. Vogelsang, *Nature Communications*, 2021, **12**, 1327.
6. R. Hanbury Brown and R. Q. Twiss, *Nature*, 1956, **178**, 1046-1048.
7. R. H. Brown and R. Q. Twiss, *Nature*, 1956, **177**, 27-29.
8. J. T. Fourkas, *Opt. Lett.*, 2001, **26**, 211-213.

5

Helical Porphyrin Complexes

Contents

Chapter 5 - Helical Porphyrin Assemblies

5.1 Introduction: Chiral Porphyrin-based Materials

In Chapter 1 Section 1.3, we discussed a range of chiral π-conjugated materials, their synthesis, chiroptical activity and applications, in addition to discussing the CISS effect and spin polarization of electrical currents by chiral materials. Here I will provide an overview of a selection of published chiral porphyrin-based materials and their properties, as these materials are more directly related to the complexes we have produced and studied in this project.

5.1.1 Spin Filtering in Twisted Porphyrin-based Molecular Wires

The most closely related publication to work in this project is the report by Naaman and Therien, in which they explore the spin filtering capabilities of ethynyl linked porphyrin wires that have been forced into a twisted geometry by the coordination of chiral bidentate ligands (Figure 5.1 and 5.2).[1]

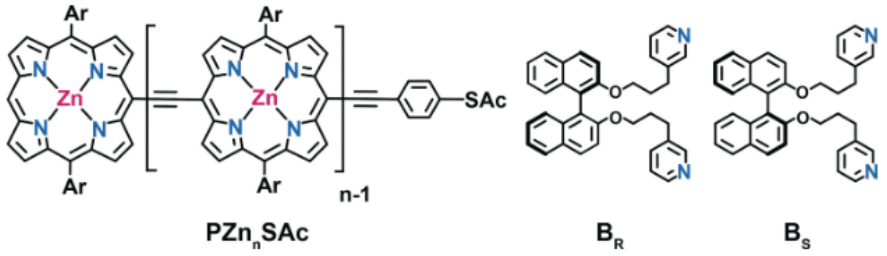

Figure 5.1. Chemical structure of the ethynyl linked porphyrin oligomers and chiral bidentate ligands used by Naaman and Therien. Reproduced from reference.[1]

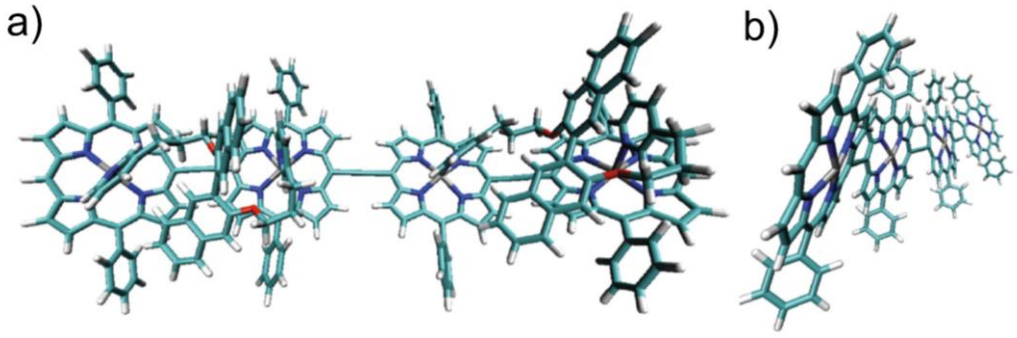

Figure 5.2. DFT optimized geometry of **PZn$_4$SAc·(B$_R$)$_2$** (B3LYP/def2-SVP) (a) Front view with SAc group omitted. (b) Side view with **B$_R$** groups omitted for clarity. Reproduced from reference.[1]

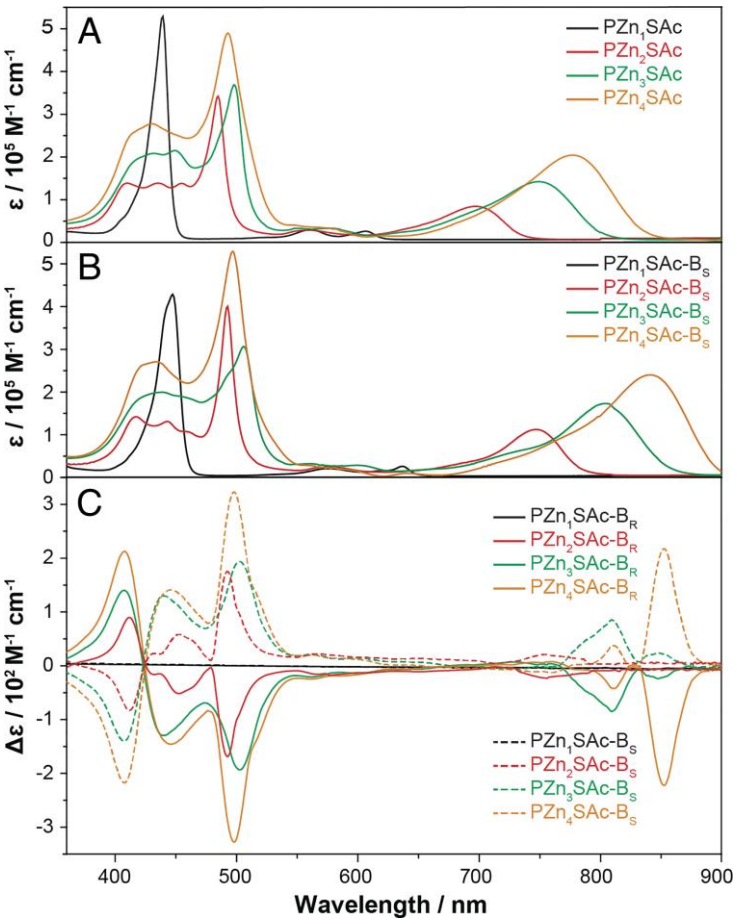

Figure 5.3. (a) UV-Vis spectrum of porphyrin species. (b) UV-Vis spectrum of porphyrin species in the presence of 10 Eq $\mathbf{B_{R/S}}$. (c) CD spectrum of the samples in (b). Reproduced from

In the presence of 10 equivalents of either ligand $\mathbf{B_R}$ or $\mathbf{B_S}$, $\mathbf{PZn_nSAc}$ with n = 2, 3 and 4 all produced CD spectra with moderate absorption intensities and maximum g_{ABS} values of the order 10^{-3} (Figure 5.3) across the wavelength range 350 – 900 nm, in which the porphyrin species strongly absorbs ($\mathbf{B_{R/S}}$ absorbs < 360 nm). This includes a strong CD response from the Q-band of the porphyrin species (650 – 900 nm, dependent on oligomer length). The monomer $\mathbf{PZn_1SAc}$ displayed no chiroptical activity in the presence of either $\mathbf{B_R}$ or $\mathbf{B_S}$. From these measurements the authors confirm that binding either $\mathbf{B_R}$ or $\mathbf{B_S}$ twists the porphyrin framework into a chiral geometry, in which the chirality of the bidentate ligand is imposed onto the oligomer.

Following these measurements, the ability of the chiral complexes to spin polarize currents was investigated using magnetic-conductive atomic force microscopy (mC-AFM); a technique which was developed by Naaman to quantify the spin filtering capabilities of chiral materials.[1-3] The setup of this experiment (Figure 5.4) has been varied across publications to suit the molecule of interest, but for the measurements on $\mathbf{PZn_nSAc{\cdot}(B_{R/S})}$, a substrate surface was first prepared with layers of Ti/Ni/Au with thicknesses of 10/120/8 nm respectively. A monolayer of the thiol functionalized $\mathbf{PZn_nSAc{\cdot}(B_{R/S})}$ was then self-assembled onto the Au layer (forming

a self-assembled monolayer (SAM)). During the measurements, a magnetic field of 0.75 T is applied either parallel or antiparallel to the substrate, which orients the magnetisation of the Ni layer either up or down.[1] Finally to measure the current, a platinum AFM tip is directed to the SAM with a controlled contact force of 5 nN. The current through the sample is measured over a potentiometric window of -2.0 to 2.0 V, which the authors show is dependent on the direction of the magnetic field and the chirality of the porphyrin-based oligomer (Figure 5.4). This observation provides evidence that electrons of opposing spin are transmitted with differing conductivity depending on the chirality of the conducting oligomer. The spin polarization of the currents for a given material can be calculated using Eq 5.1, where I_{up} and I_{down} are the currents measures for a particular material with the magnetic field orientated up or down, relative to the substrate surface. For **$PZn_nSAc{\cdot}(B_{R/S})$** this value was reported as ~32%.[1]

$$Spin\ Polarization = 100\% \times \frac{I_{up} - I_{down}}{I_{up} + I_{down}} \qquad \text{Eq 5.1}$$

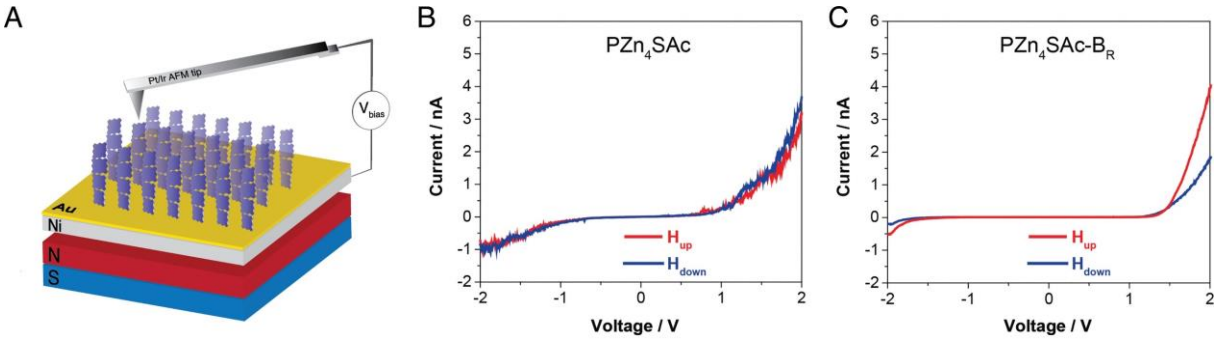

Figure 5.4. (a) mC-AFM experimental set-up used for the analysis of **$PZn_nSAc{\cdot}(B_{R/S})$**. (b) unbiased current observed when **PZn_4SAc** is used in the experiment. (c) Biased current recorded when **$PZn_nSAc{\cdot}B_R$** used in the experiment. Reproduced from reference.[1]

In comparison to other chiral spin filtering materials, the authors of this study emphasize the unique properties of these porphyrin-based materials as their low resistivity and relatively large NIR g_{ABS} values compared to other strongly NIR ECD absorbing materials.[4] The low resistivity, resulting from the high charge carrier mobility of the ethynyl linked porphyrin oligomers,[5] in

combination with the strong chiroptical response demonstrate that these porphyrin based oligomers are capable of generating large-magnitude spin-polarized currents.

5.1.2 Chiral Meso-meso Linked Porphyrin Oligomers

Another set of publications relevant to this chapter are the reports of the synthesis of chiral meso-meso linked porphyrins by Osuka.[6-8] In this work, asymmetric porphyrins substituted with differing aryl groups at the 10 and 20 positions were meso-meso linked using $AgPF_6$ mediated oxidative coupling. The resulting dimer-length oligomers can adopt two enantiomeric forms (R or S), and the trimer-length can form either the *dl*-pair RR/SS isomer or the meso RS/SR isomer. For a trimer-length oligomer with Ar_1 = 3,5-di-tert-butylphenyl and Ar_2 = 2,6-dimethoxyphenyl (Figure 5.5), Osuka has demonstrated that isolated samples of the *dl*-pair and meso isomers show no evidence of interconversion even when heated to 420 K for 3 hours. This study establishes that the chirality locked into the structures by the meso-meso bond is incredibly resistant to racemization and can be considered permanent under ambient conditions. This makes the meso-meso connection valuable in the synthesis of chiral porphyrin-based materials.

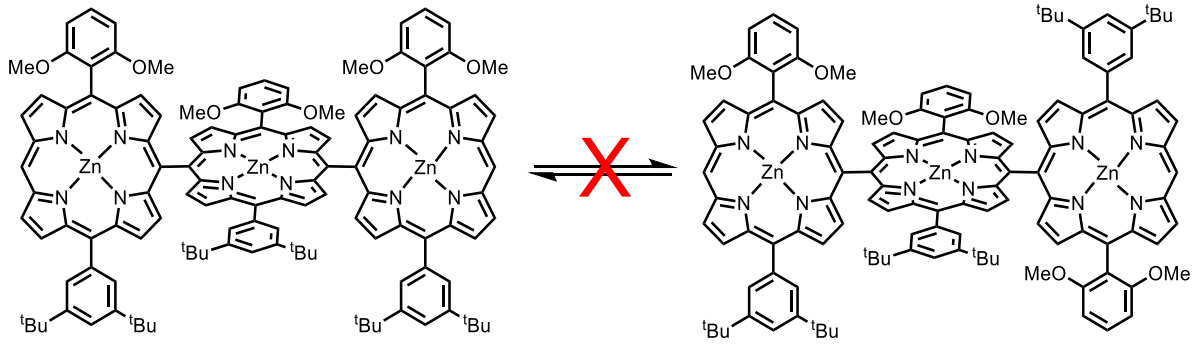

Figure 5.5. (left) meso isomer of meso-meso linked trimer synthesised by Osuka. (right) one enantiomer of the *dl*-pair of isomers.

A later paper in this series of publications focuses on the synthesis of chiral pyridyl-containing meso-meso linked porphyrin oligomers and their self-assembly into tetrameric boxes.[7] Figure 5.7 presents the oligomers used in this project and Figure 5.6 presents an example of the self-assembled boxes. Two key synthetic findings in this study were the chiral resolution of the homochiral R and S forms of the box formed from **MM-P2$_{PhPyOOct}$Zn** by chiral HPLC, and the separation of the dl-pair from the meso form of **MM-P3$_{PhPyOOct}$FB** on silica. Both of these findings provide literature precedence for the separation of chiral meso-meso linked porphyrin oligomers. No investigation into the spin filtering capabilities of these materials was reported.

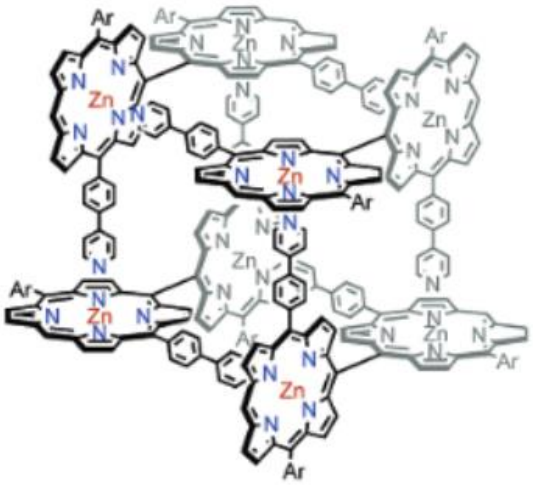

Figure 5.6. Homochiral self sorted porphyin boxes.

Reproduced from reference.[XX]

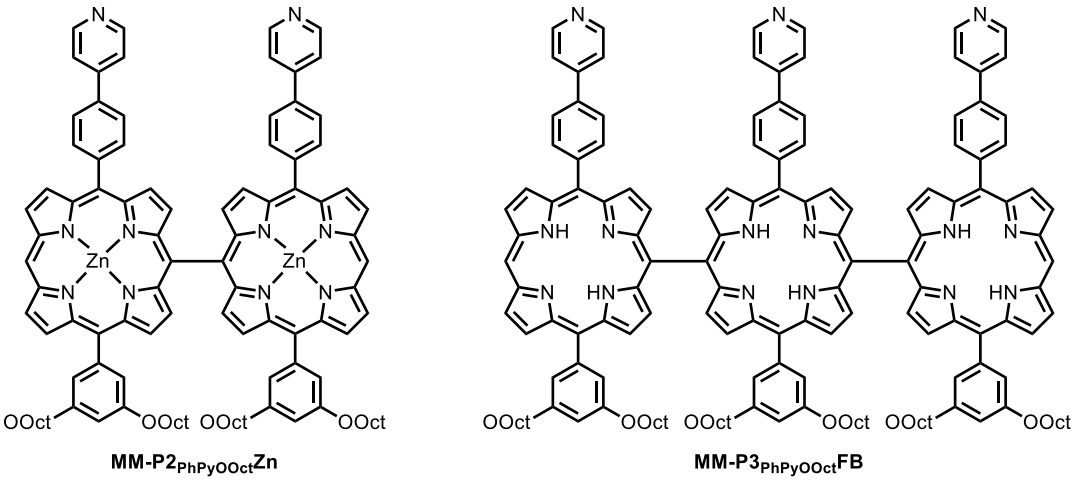

Figure 5.7. Meso-meso linked pyridyl-containing oligomers synthesised by Osuka.[7]

5.1.3 Chiral Porphyrin-based Nanographene

Aside from the work described in Sections 5.1.1. and 5.1.2. there are few examples in the literature of chiral porphyrin based molecular wires. The work in 5.1.1. induces chirality through the coordination of a chiral ligand, whereas in 5.1.2. the chirality of the structure is generated by the locked meso-meso bond. One final example to note is the recent work by

Anderson and coworkers that produced porphyrin-based nanorgraphenes which posess chirality similar to the structures in 5.1.2, as a result of steric hindrance preventing racemisation of the structure.[9] Figure 5.8 presents the synthsis of the these nanographenes, which were achieved by the Yamamoto coupling and fusion monomeric porphyrin species, bearing one or two nanographene precursor units.

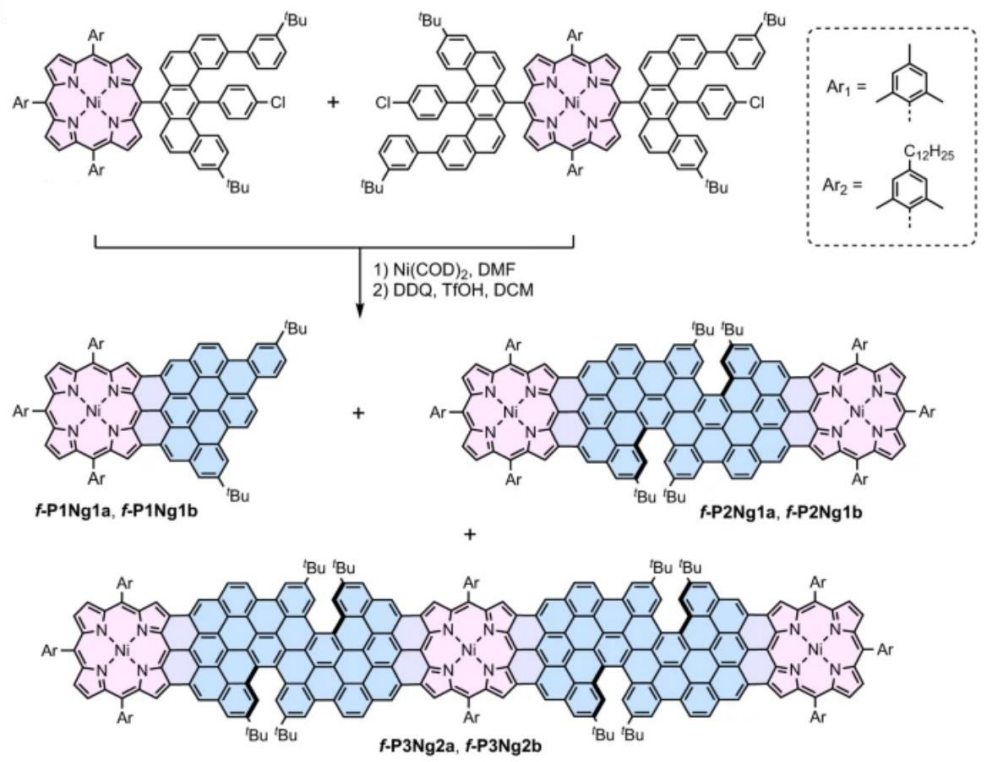

Figure 5.8. Synthesis of poprhyrin-based nanorgraphenes by Anderson. Reproduced from reference.[9]

Of particular interest to the work in this chapter is the chiral resolution and chiroptical measurements of the fused porphyrin dimer **f-P2Ng1a**, which has enantiomeric forms of either **f-P2Ng1a-MM** or **f-P2Ng1a-PP**. Figure 5.9a presents the CD spectrum of these materials along with the calculated CD spectrum of the two isomers, which were obtained from TD-DFT calculations on the energy minimised geometries using the LC-ωHPBE (ω = 0.1) functional (6-31G(d,p) used for C, H and N, and LanL2DZ used for Ni). Finding a functional that closely reproduces the experimental CD results can be reasonably well achieved for small molecules,[10] however, for large molecules such as **f-P2Ng1a** which possess many features in the experimental CD spectrum, this can be challenging. Figure 5.9b demonstrates this by presenting

the calculated CD spectra of **f-P2Ng1a-MM** using different functionals. Though all of the functionals screened struggle to exactly reproduce the experimental spectrum, LC-ωHPBE (ω = 0.1) produces the closest fit. These results are of relevance to the work in this chapter, as they emphasise how functional choice for TD-DFT calculations on such large π-conjugated materials must be carefully considered. This work provides further evidence that the range corrected functional LC-ωHPBE (ω = 0.1) describes these large porphyrin-based systems well, which matches our conclusions from the NICS calculations completed for ***c*-P18** in Chapter 3, section 3.3. If good agreement is found between experimental and calculated CD spectrum, the absolute stereochemistry of a sample can be assigned.[10] The calculated CD spectra presented in this work do not exactly match the experimental data, but the general trends observed across the spectra do line up. In the absence of crystallographic data, which is challenging to obtain with such small quantities of these large complex molecules, this is the most reasonable approach to assign the absolute stereochemistry.

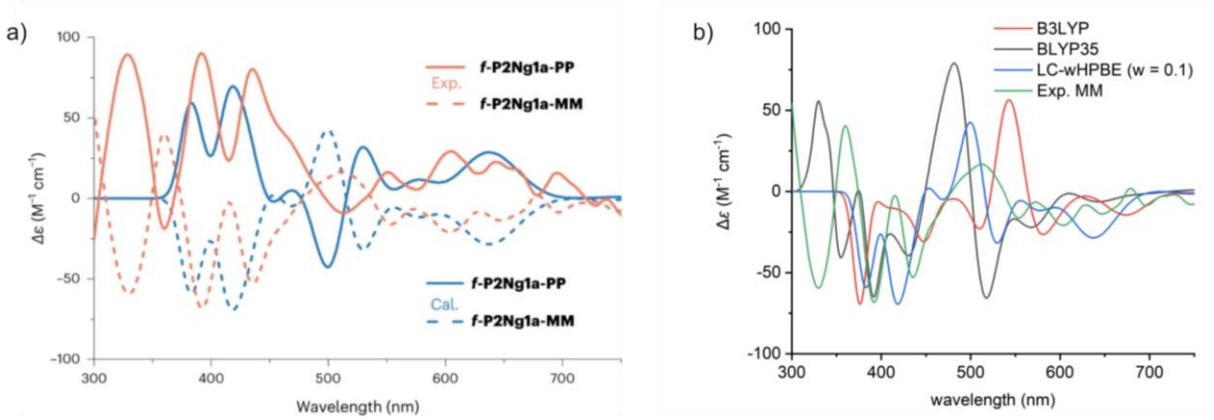

Figure 5.9. (a) Experimental CD spectrum of **f-P2Ng1a-MM/PP** alongside calculated spectrum obtained from TD-DFT calculations (LC-ωHPBE (ω = 0.1)). (b) Functional screening for TD-DFT calculations of the CD spectrum of **f-P2Ng1a-MM**. Reproduced from reference.[9]

Finally, the reported experimental g_{ABS} values of **f-P2Ng1a-PP** are interesting to note as they provide more context to the values of the work described in Section 5.1.1. and of those for our compounds reported later in this chapter. At 604 nm, g_{ABS} of **f-P2Ng1a-PP** is reported as 1.3 x 10^{-3} and at 695 nm as 5.6 x 10^{-4}. These values are roughly of the same magnitude as the

structures in Section 4.1.1 (~10^{-3}) which may reflect the similar twist of the materials. Qualitatively **PZn$_4$SAc·(B$_R$)$_2$** in Section 5.1.1 has about a ~20° twist from end to end of the oligomer, whereas **f-P2Ng1a-PP** has a twist of around ~22°.

5.2 Design of Helical Assemblies

5.2.1 Design and Computational Modelling

The primary aim of this research was to design and synthesize a template capable of holding a butadiyne-linked linear porphyrin oligomer in a helical conformation. The simplest approach to this seemed to be a linear axle containing coordinating groups pointing radially out from the axle (Figure 5.10). This presents a particular synthetic challenge to the template design, as there are not many structural motifs that allow for the 90° angle between the template axle and the pyridyl groups. Furthermore, for the axle to induce a helical conformation, there needs to be a mismatch between the Zn-Zn distance on the butadiyne-linked oligomer and the distance between pyridyl nitrogen groups on the axle. Specifically, the Zn-Zn distance needs to be larger to induce a helical conformation (Figure 5.10a).

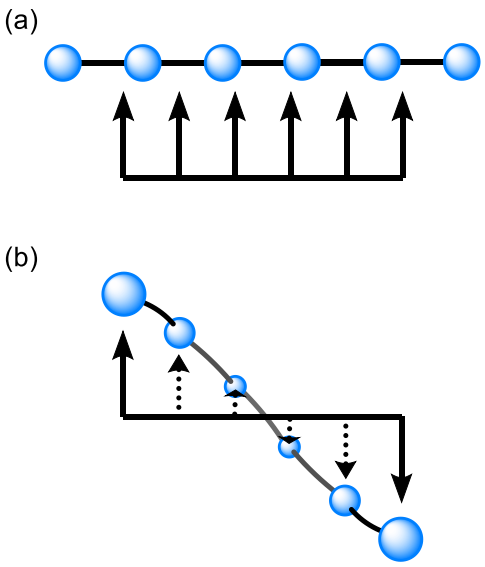

Figure 5.10. (a) Linear axle and oligomer, each with 6 binding sites. (b) Helical conformation adopted to bind all 6 sites.

Our first template designs relied on the phthalimide group, as it is one of the few organic structural motifs that possess 90° bond angles. Figure 5.11 presents two designs using this group, either directly linked or with a bridging butadiyne group. In both cases, we expected that the template designs would be achiral and that only the complexes with butadiyne-linked oligomers would possess chirality. Isolation of the chiral complexes would therefore require

the racemization rate to be very slow, which we were uncertain about, so we instead decided to explore chiral template designs, as these can only form helices of a single handedness.

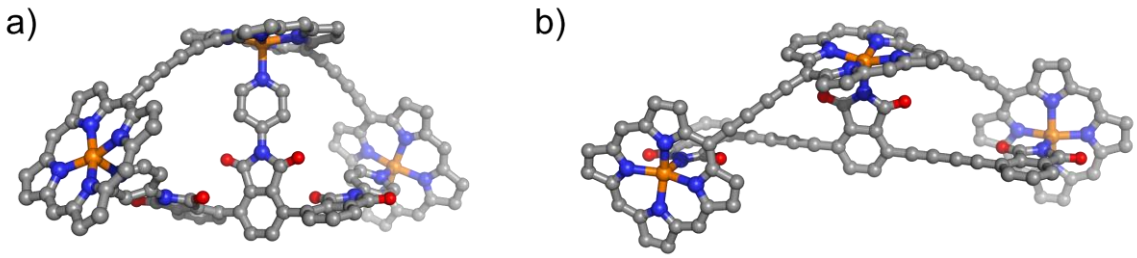

Figure 5.11. Meso-meso and butadiyne-linked phthalimide based template designs. (Optimized in MOPAC with the PM7 method).

After completing the above described modelling, we discovered that the phthalimide group has been successfully utilized in the synthesis of helical oligomers by Mayor (Figure 5.12).[11] Crucially however, his work produced structures in which the axle and helical oligomer were covalently bound and therefore not able to racemise due to steric clashing of the carbonyl groups. Additionally, this publication highlights that the design criteria we independently identified (90° angle between axle and binding site + mismatch in axle and helical oligomer length) are appropriate for preparing these kinds of helical structures.

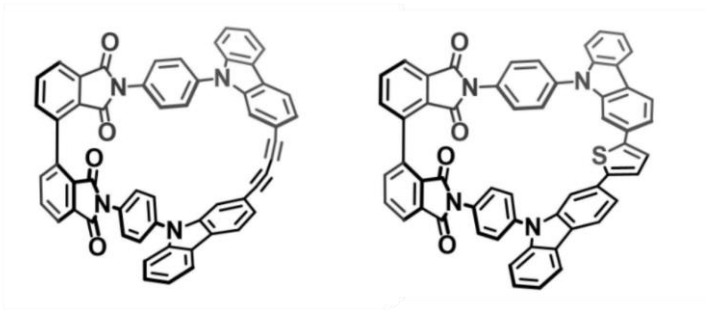

Figure 5.12 Covalently bound helical structures based on phthalimide produced by Mayor. Reproduced from reference.[11]

The requirement that the template be chiral adds an additional constraint to the design, however, we realized that directly meso-meso linked porphyrin units may satisfy all of these requirements. Firstly, porphyrin is one of the few building blocks with 90° bond angles, so a linear oligomer could be formed with pyridyl groups positioned orthogonal to the length of the

axle. Secondly, the meso-meso link is known to be stable to racemization, with chiral samples heated to 120 °C for 3 hours showing no sign of racemization.[8] Thirdly, the meso-meso link ensures that there is a mismatch between the pyridyl spacing and Zn-Zn distance on the butadiyne linked oligomer. In combination, these effects produced a very promising template design, as shown in the DFT (B3LYP/6-31g(d)) optimized geometry of the chiral hexameric template (**MM-P6$_{Py}$FB**) bound to **P6(C$_2$)$_2$** (Figure 4.13).

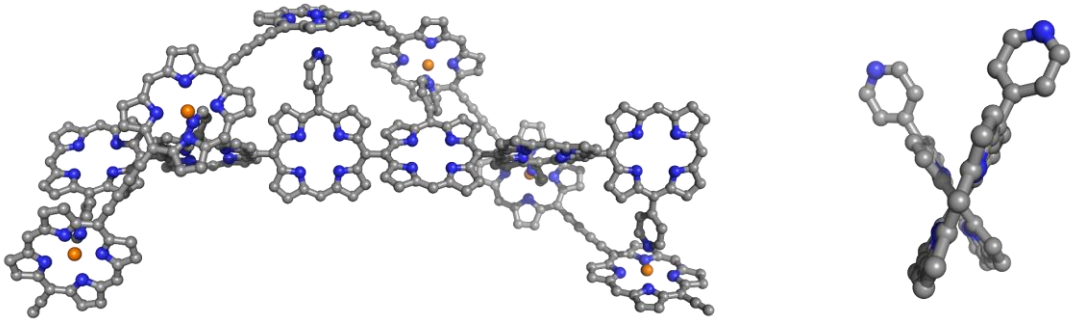

Figure 5.13 (left) DFT (B3LYP/6-31g(d)) optimized model of **P6(C$_2$)$_2$·MM-P6$_{Py}$FB**. (right) Central meso-meso link of **MM-P6$_{Py}$FB** from the complex.

One key point to note in this design (Figure 5.13) is that the meso-meso linked axle must be in the freebase form or have a 4-coordinate metal in the porphyrin units. Using zinc for example would enable the axle to bind to itself. Furthermore, we know that the meso-meso linked porphyrin units have a preference for laying orthogonal to one another.[12] In order to bind **P6** this dihedral angle has to be constrained from the ideal of 90° to 71°/69° as seen in the DFT model (Figure 5.13). Our hope was that the binding would be strong enough to compensate for the constraint of this dihedral angle.

Our DFT model demonstrates how 6 porphyrin units are required in each oligomer to complete one full helical pitch, however, this value can also be easily calculated using the simple relationship between the length of **one pitch** of a helix (L), the length of the axle it wraps around (P) and the radial distance between these two species (R) (Eq 5.2).

$$L^2 = P^2 + (2\pi R)^2 \qquad \text{Eq 5.2}$$

We can define L = NB, where N is the number of porphyrin units in a porphyrin oligomer and B is the distance between the Zn atoms in adjacent porphyrin units of a butadiyne-linked porphyrin oligomer, when the oligomer is perfectly flat. Additionally, we can define P = NM, where M is the distance between the center of adjacent porphyrin units in a meso-meso linked porphyrin oligomer. In our structure N in both of these equations must be identical.

Eq 5.2 can be rearranged to solve for N:

$$N = \sqrt{\frac{(2\pi R)^2}{B^2 - M^2}} \qquad \text{Eq 5.3}$$

Known distances from the crystal structures of porphyrin oligomers can be used to determine B (13.53 Å), M (8.35 Å) and R (10.25 Å). Inputting these values into Eq 5.3 outputs N = 6.05, which agrees well with the DFT model that 6 porphyrin units are required to complete one full helical pitch.

This calculation estimates the dihedral angle to be ~60° which is reasonably smaller than the DFT model. This can be rationalized by close analysis of the DFT model (Figure 5.13, right), which shows some minor distortion to the freebase porphyrin units in the meso-meso linked axle. This distortion increases the dihedral angle between adjacent porphyrin units and presumably occurs to minimize strain in the structure.

As discussed in Section 5.1.1 the spin selectivity of chiral materials can be measured using mc-AFM experimental techniques in which the AFM tip is magnetised parallel and antiparallel to the substrate surface.[1] Conducting these experiments on the helical complexes outlined in this section would further our understanding of the CISS effect and we believe these particular complexes offer a unique opportunity to probe the structure property relationship of this effect. By functionalising one of the terminal acetylenes of **P6(C$_2$)$_2$** with a thioacetate group, we can enable the butadiyne-linked porphyrin oligomer to bind to the gold-plated substrate surface used in these experiments. Measurement of the spin filtering capabilities of just the achiral

butadiyne-linked oligomer would provide a reference to compare the helical complexes to, which should easily be formed by coordination of enantiopure **MM-P6$_{Py}$FB**. After these measurements, analysis of shorter or longer oligomers would provide information on the length dependence of spin filtering. Whereas lengthening the distance between the pyridyl group and axle (e.g. adding an ethynyl spacer) would increase the pitch length and allow investigation of this parameters effect. We could also explore binding ethynyl or phenyl linked porphyrin oligomers to the meso-meso linked axle, which have stronger and weaker interporphyrin π-conjugation respectively and a shorter Zn-Zn distance, so are expected to form helices with longer pitches.

The spin filtering experiments discussed above require specialist equipment to perform, however, it is understood that there is a strong correlation between the chiroptical activity of a material (as measured by CD spectroscopy) and its spin filtering capabilities.[13] Measuring CD spectra is far more accessible to the average synthetic organic chemist, so will be used in this project as a preliminary assessment of the chiroptical activity of the complexes.

5.3 Single Helical Complexes

5.3.1 Synthesis of Enantiopure Single Helical Template

5.3.1.1 Meso-meso Coupling Approaches

The primary target of the single helical project was the 6-porphyrin long complex shown in Figure 5.13 (Solubilising groups omitted in the DFT model shown). To form this complex we require a butadiyne-linked porphyrin hexamer **P6$_{THS}$(C$_2$CPDIPS)$_2$** and an enantiopure meso-meso linked porphyrin hexamer axle **MM-P6$_{PyTHS}$FB-R** (Figure 5.14). The butadiyne linked oligomer was synthesized for the 18-ring project (Chapters 2, 3 and 4) so will not be further discussed. Instead, we turn our attention to the synthesis of the enantiopure meso-meso linked hexamer axle.

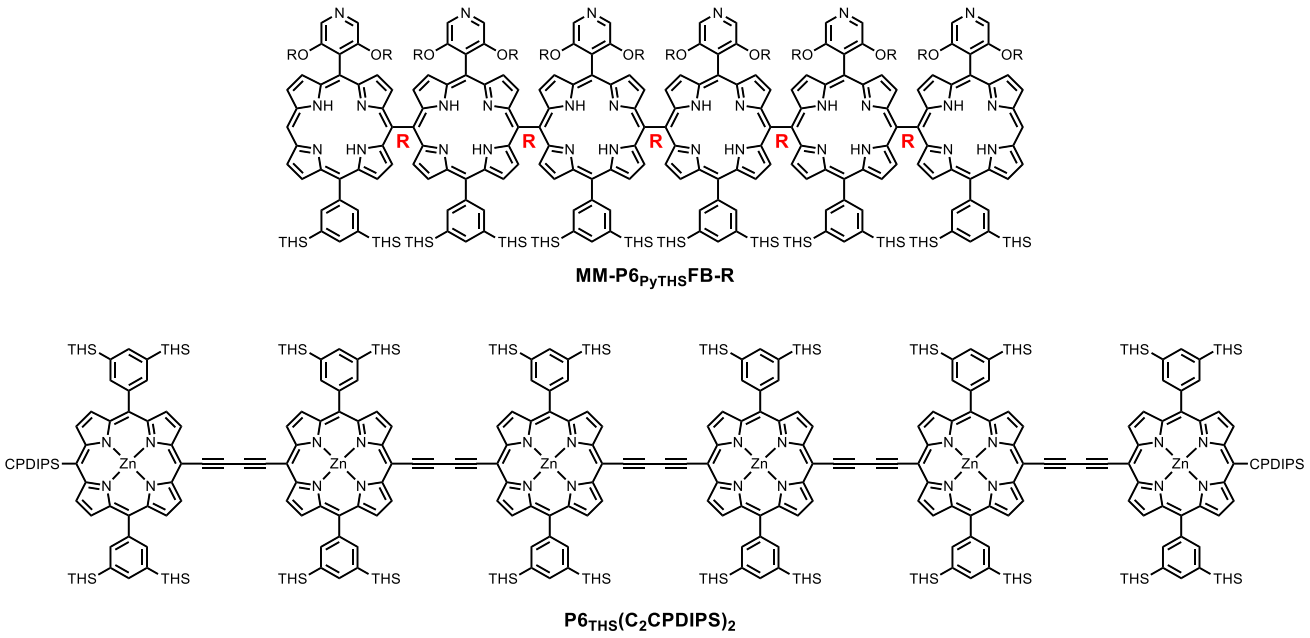

Figure 5.14. Chemical structures of **MM-P6$_{PyTHS}$FB-R** and **P6$_{THS}$(C$_2$CPDIPS)$_2$**. R = $OC_{12}H_{25}$.

As previously discussed, Osuka has reported the synthesis of chiral dimer and trimer length meso-meso linked porphyrin oligomers, bearing pyridyl groups orthogonal to the length of the oligomer, which were prepared by oxidative coupling of the respective porphyrin monomers with $AgPF_6$.[7] In this work, the porphyrin oligomers were complexed with zinc (II), which resulted in homochiral self-sorting of the dimers into tetrameric boxes containing a single enantiomer (Figure 5.15). Chiral HPLC of this racemate was able to effectively separate the boxes.

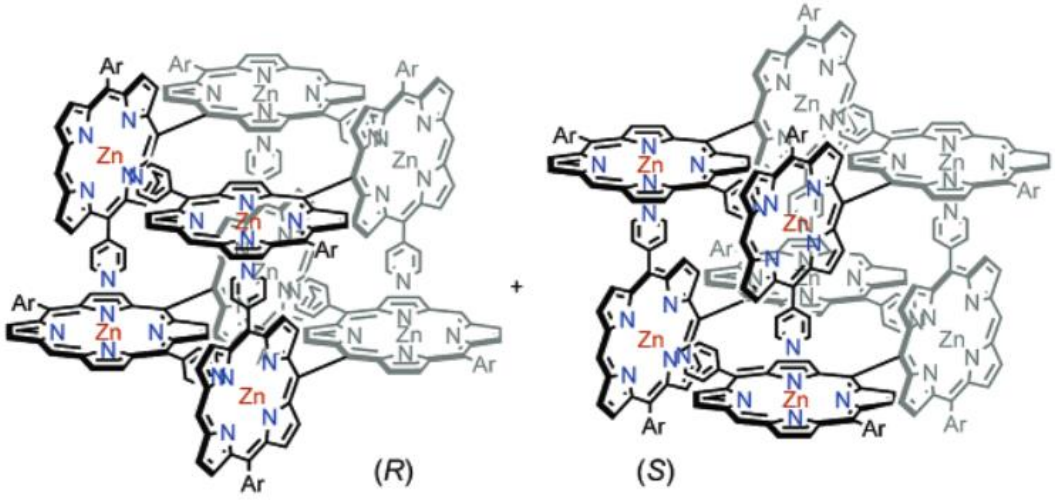

Figure 5.15 Homochiral self-sorted boxes reported by Osuka. Reproduced from reference.[7]

Osuka also reported that at the trimer length, three distinct species are formed. These are the *meso* form (*RS/SR*, 50%) and chiral enantiomers with *RR* (25%) or *SS* (25%) stereochemistry at the *meso* connections. Silica column chromatography on the free-base form of these oligomers was able to separate the *meso* form from this mix, however chiral resolution of the *RR* and *SS* enantiomers was not demonstrated.[7]

Previous projects in the Anderson group have also worked with pyridyl porphyrin oligomers, however these materials were not chiral and were also prepared with long alkyl groups, to ensure good solubility of the compounds.[14] As we aimed to target hexamer length meso-meso complexes in this work, we decided to combine the approaches by Anderson and Osuka to prepare long length, yet highly soluble meso-meso linked oligomers (Figure 5.16).

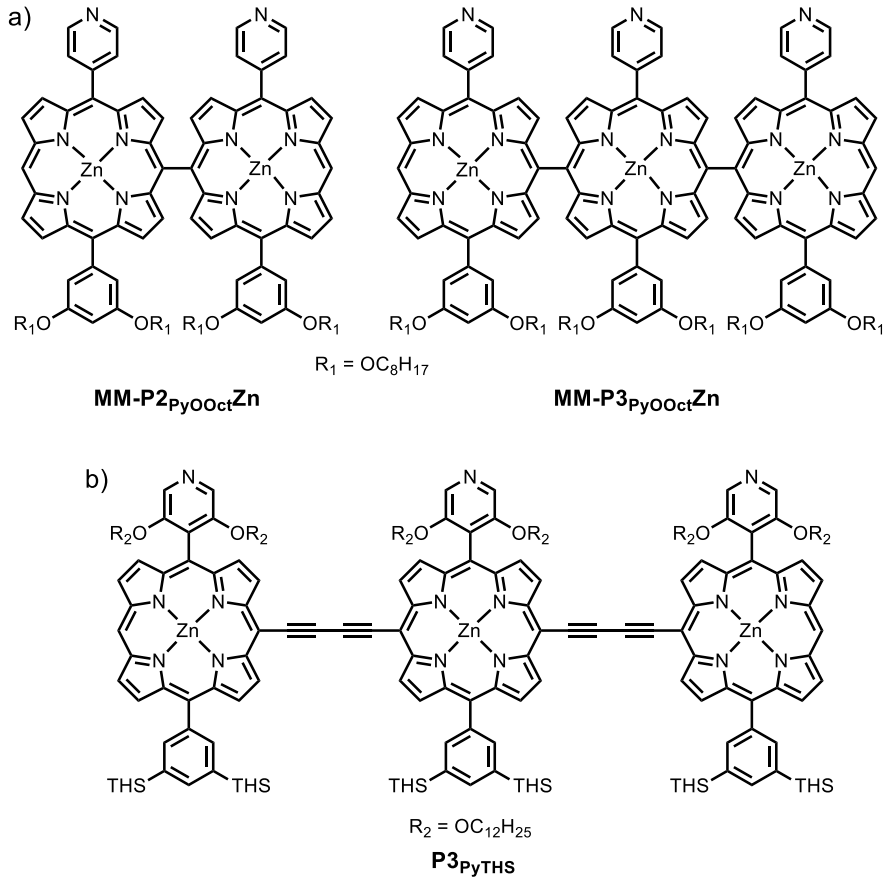

Figure 5.16. (a) Chemical structures of meso-meso linked pyridyl-containing porphyrin oligomers prepared by Osuka.[7] (b) Chemical structures of butadiyne-linked pyridyl-containing porphyrin oligomers prepared by Anderson.[14]

A key consideration in the synthesis of the enantiopure hexamer length axle is how best to set all 5 chiral centres. A straight oxidative coupling from the monomer **P1$_{PyTHS}$-Zn**, such as that used by Osuka, to a hexamer length oligomer would yield a completely scrambled mix of all possible combinations of the chiral centres (Figure 5.17, **MM-P6$_{PyTHS}$R/S**). Instead, we planned to complete this synthesis in a stepwise manner, by first isolating the enantiopure trimer (e.g. *RR*), then coupling this to itself (Figure 5.18). Using the *RR* timer as an example, this reaction would yield hexamer length material with only two diastereomers: *RRSRR* and *RRRRR*. We anticipated that these may be separable on silica, if not, then by chiral HPLC.

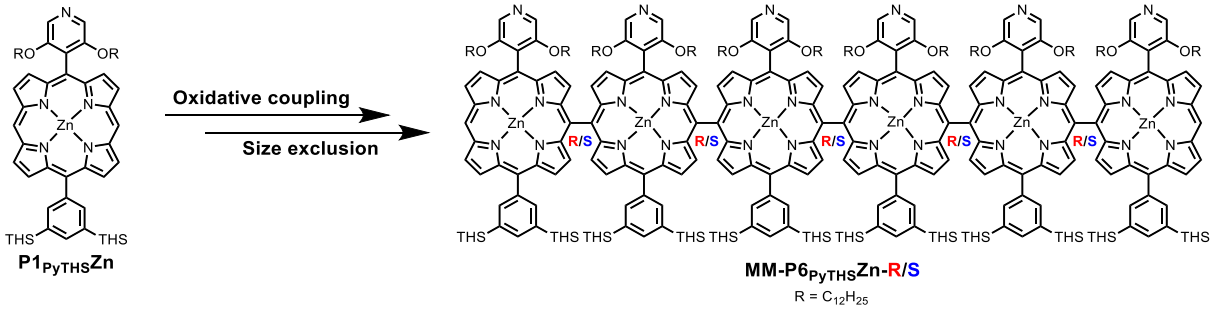

Figure 5.17. Oxidative coupling of **P1$_{PyTHS}$Zn** directly to hexamer length meso-meso linked oligomer leads to a complex mix of isomers.

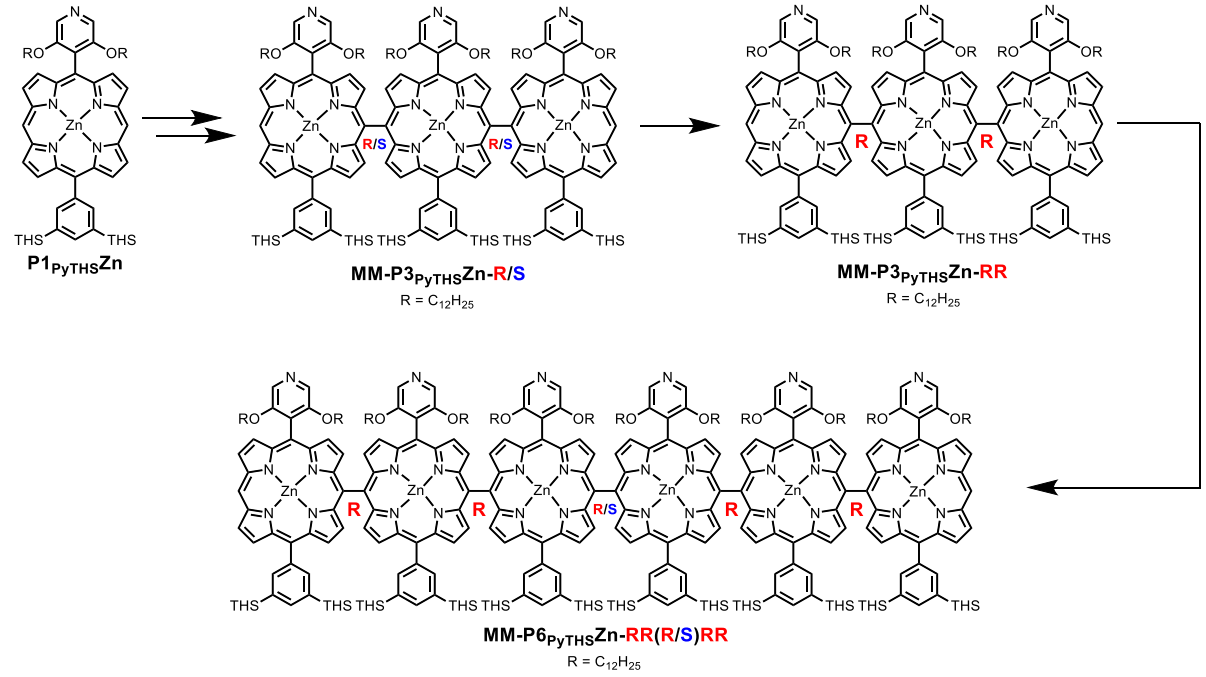

Figure 5.18. Stepwise approach to the synthesis of enantiopure meso-meso linked hexamer length templets **MM-P6$_{PyTHS}$-RRRRR**.

Porphyrin monomer **P1$_{PyTHS}$-Zn** was first prepared as reported by Anderson,[14] then subjected to the $AgPF_6$ mediated oxidative coupling conditions reported by Osuka (Figure 5.19).[7] This oligomerization unfortunately yielded a negligibly small amount of the desired trimer length material (Figure 5.20), even when the coupling was forced with additional $AgPF_6$ or by heating over multiple days.

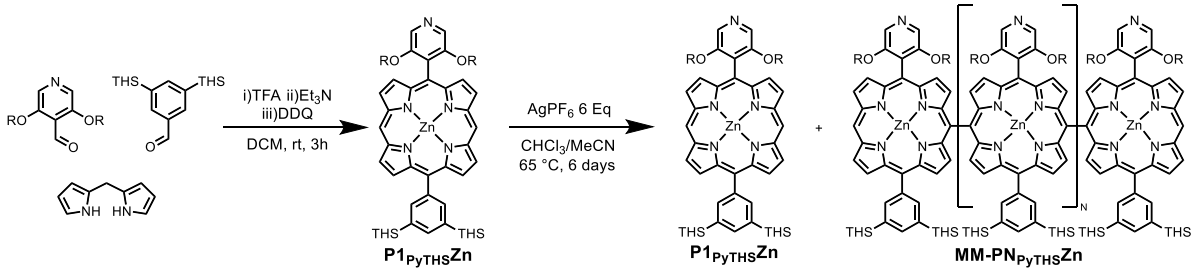

Figure 5.19. $AgPF_6$ mediated oxidative coupling of **P1$_{PyTHS}$Zn**.

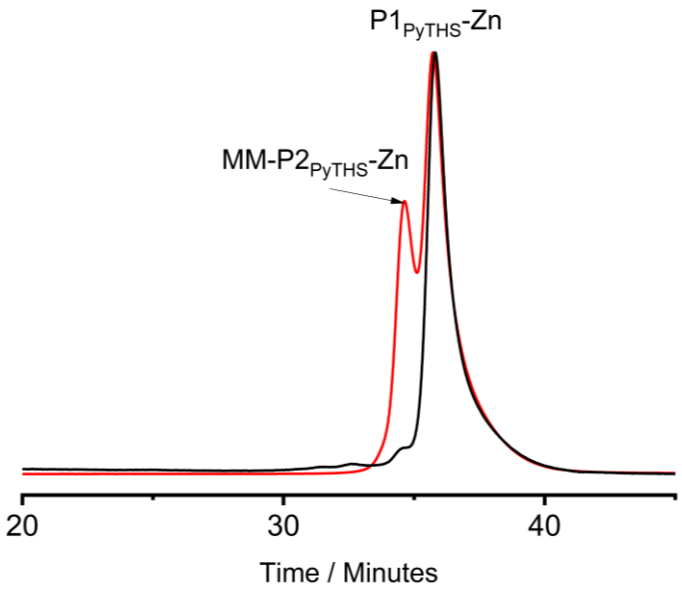

Figure 5.20. Analytical GPC trace of a typical crude reaction mixture from conditions in Figure 5.19. (THF + 1% pyridine as an eluent with a flow rate of 1.0 mL/min)

We were, however, able to obtain a significant amount of the dimer length **MM-P2$_{PyTHS}$-Zn** from this reaction. ^{1}H NMR (Figure 5.21, top) of this material indicates that it may self-coordinate into a tetrameric box, as it has a complex, yet sharp and defined spectrum. Dissociation of the aggregate by the addition of pyridine, or by removing the zinc (Figure 5.21, middle and bottom) significantly simplifies the spectrum. Confirmation of box formation in

Osuka's work primarily came from crystal structure analysis of the complexes[6] but evidence can also be obtained from the ^{1}H NMR spectrum (Figure 5.22). Specifically, shielding of coordinated pyridyl groups is observed, due to the local aromatic ring current of the porphyrin they are bound to. In our dimer, we have only two pyridyl protons, which are more electron rich than the analogous ortho protons in Osuka's compound, due to the electron donating inductive effect of our $OC_{12}H_{25}$ groups. It is likely that when bound into a box, these protons are more shielded than those in Osuka's box, which positions them more upfield and therefore under the broad THS peaks (2.5 – 0 ppm).

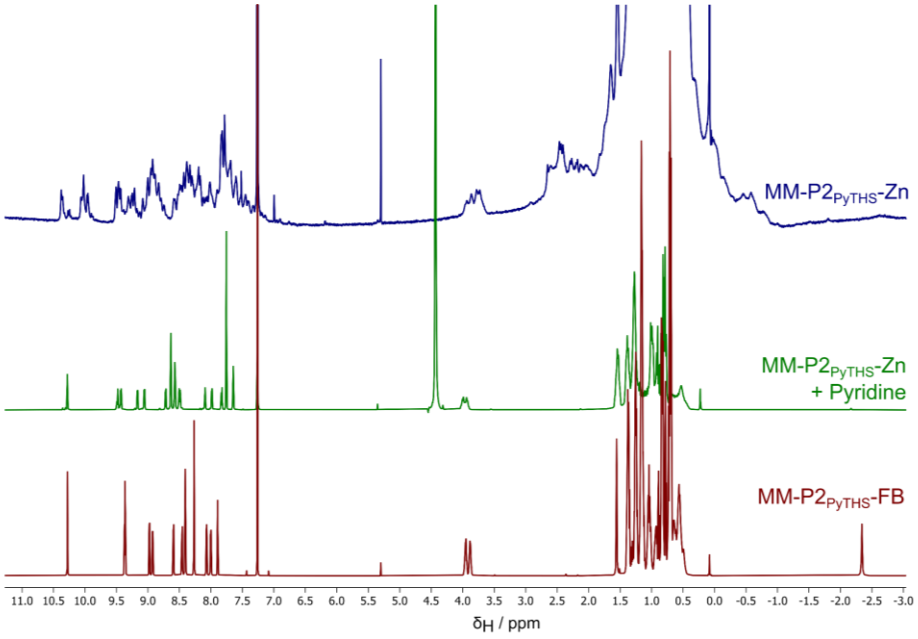

Figure 5.21. ^{1}H NMR of various **MM-P2$_{PyTHS}$** species ($CDCl_3$, 298 K, 400 MHz)**.** (Top) Complexed to zinc (II), therefore allows for self-coordination. (Middle) Complexed to zinc (II), but with 1% d_5-pyridine added to prevent self-coordination. (Bottom) Free-base, no self-coordination possible.

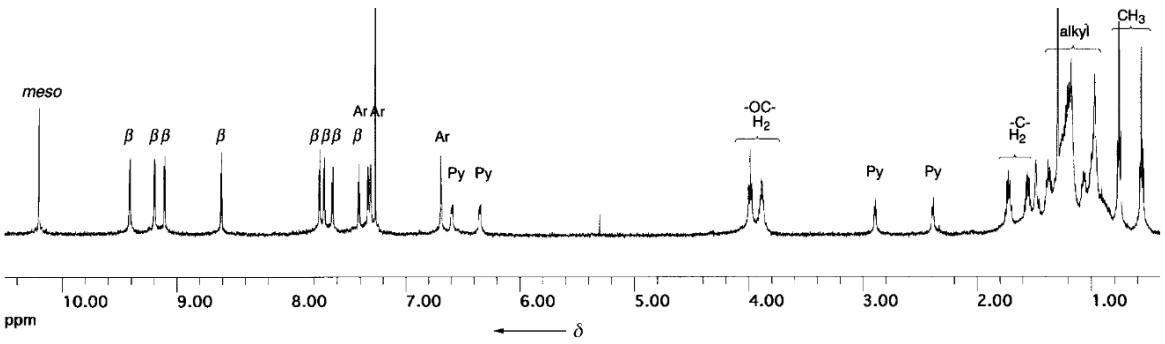

Figure 5.22 ^{1}H NMR spectrum of **MM-P2$_{PyOOct}$Zn** (Figure 5.16a) produced by Osuka ($CDCl_3$, 298 K, 400 MHz). Py denotes the pyridyl group in **MM-P2$_{PyOOct}$Zn**, not added pyridine. Reproduced from reference.[6]

We expect that the complicated ^{1}H NMR of our self-assembled box is a result of the steric interactions of the bulky $OC_{12}H_{25}$ groups that we included in our design for better solubility. Figure 5.23 presents a PM7 optimized model of Osuka's design (left) and the same model with OC_6H_{13} groups added post optimization (right). From this basic modelling, it is clear that the OC_6H_{13} groups are substantially crowded, particularly in the core of the box, which may inhibit self-coordination. Quantitative analysis of binding constant of this box could be obtained from UV-Vis formation titrations (s presented in Chapter 3), however this is outside the scope of this work.

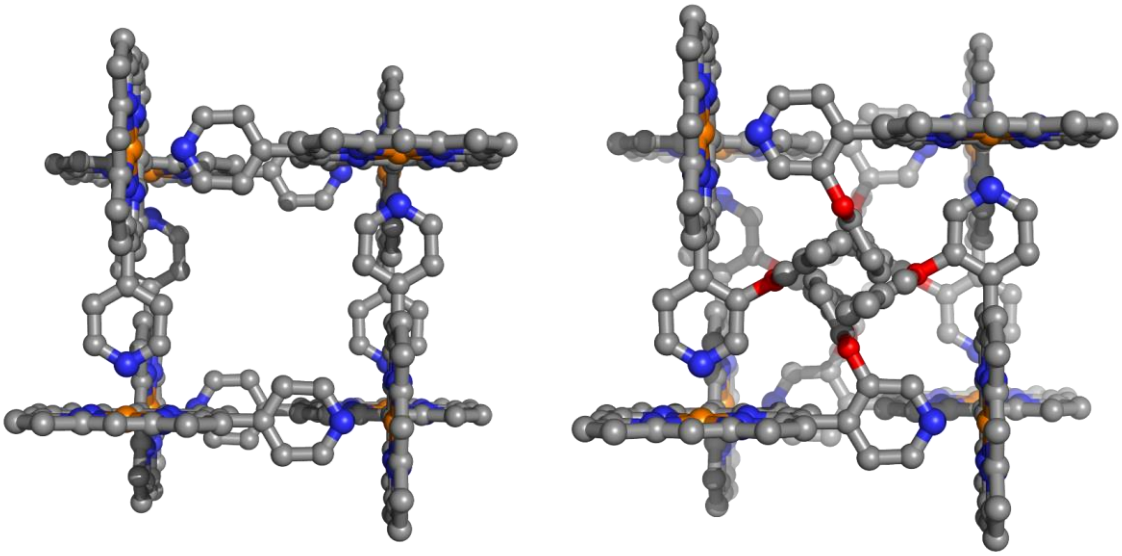

Figure 5.23. (left) PM7 optimized geometry of Osuka's **MM-P2$_{PyOOct}$Zn** box (Ar-OOct solubilising group omitted). (right) Model from left with OC_6H_{13} chains added at meta positions post optimisation to illustrate crowding.

In an effort to accelerate the meso-meso coupling we next turned to Bis(trifluoroacetoxy)iodo)benzene (PIFA), which has been used in multiple reports for the meso-meso coupling of porphyrin species.[15-17] Addition of PIFA to a solution of **P1$_{PyTHS}$-Zn** in $CHCl_3$ at room temperature (Figure 5.24) led to rapid oligomerization, which stalled after 10 minutes. This oligomerization produced a distribution centred about trimer (Figure 5.25), demonstrating a significant increase in the extent of oligomerization. However, upon isolation

of the oligomers formed under these conditions by recycling GPC, we found that all oligomers (including the recovered monomer) had mass peaks +30 higher than their expected value, as obtained by MALDI spectrometry.

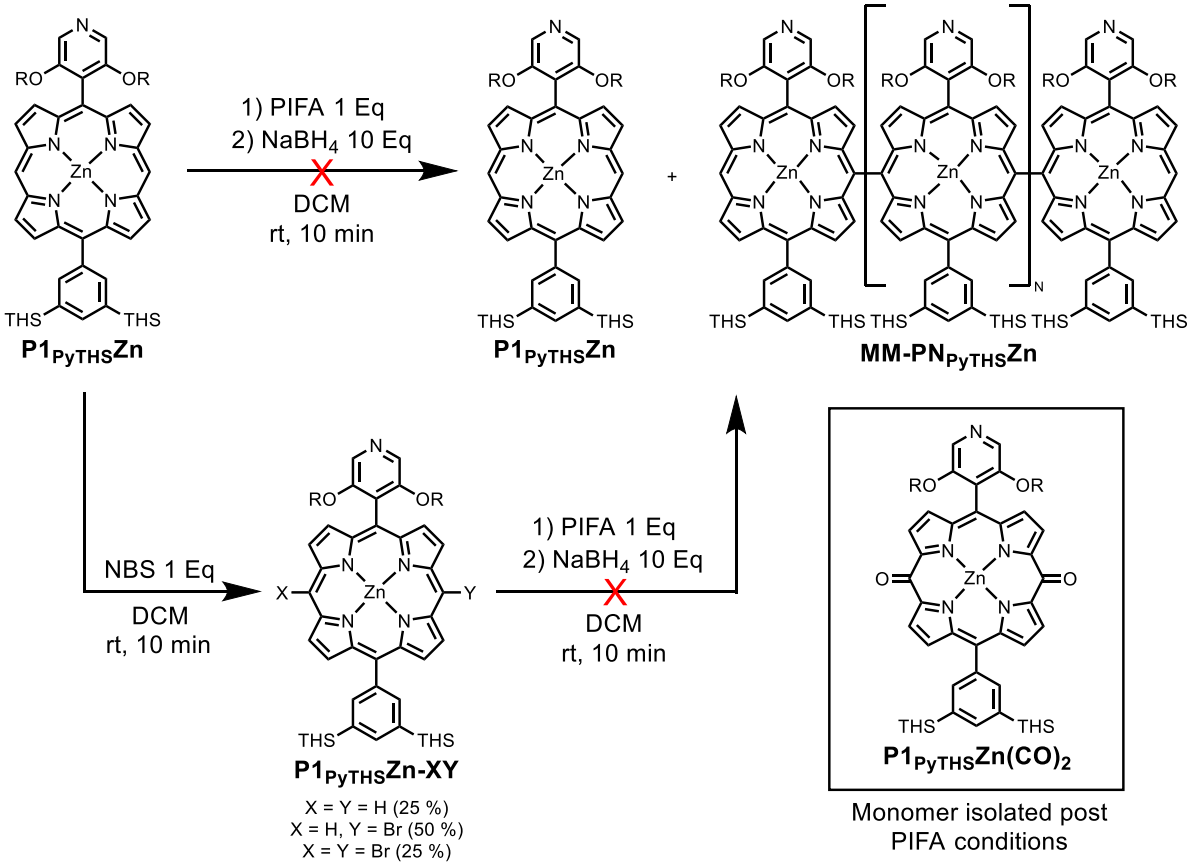

Figure 5.24. PIFA mediated oxidative coupling approaches to the synthesis of **MM-PN$_{PyTHS}$Zn** (R = $C_{12}H_{25}$).

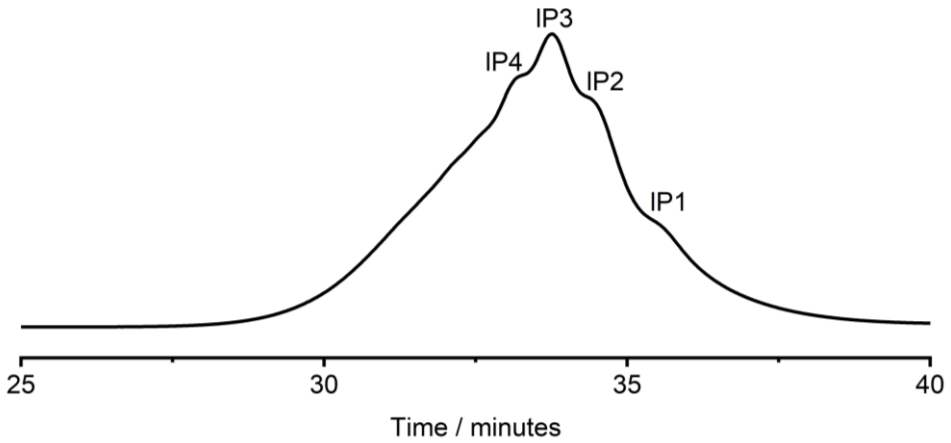

Figure 5.25. Analytical GPC trace of a typical crude reaction mixture from the conditions shown in Figure 5.24 (top). (THF + 1% pyridine as an eluent with a flow rate of 1.0 mL/min).

^{1}H NMR of the recovered monomer (Figure 5.26) indicates that carbonyl groups may have formed at the meso positions, as the meso protons are no longer visible and the β-protons of the porphyrin framework are shielded, as a result of the local ring current of the porphyrin being broken by the installation of the carbonyl groups (Figure 5.24). TLC comparison of the monomer recovered from the $AgPF_6$ conditions (right mass and ^{1}H NMR) and from the PIFA conditions, show that the PIFA product is drastically more polar and highly retained on the TLC plate (70/30, THF/Hexane). Attempting this PIFA coupling under inert conditions, with a reductive work up (addition of ferrocene) and on the nickel and free-base forms of the porphyrin monomer did not improve upon these results. We also attempted to block the terminal positions of these oligomers with bromine atoms by first statistically brominating **P1$_{PyTHS}$-Zn** then PIFA coupling this mixture (Figure 5.24, bottom route). Unfortunately, the PIFA conditions appear to debrominate this particular porphyrin, as we again only saw di-carbonylated products by MALDI spectrometry.

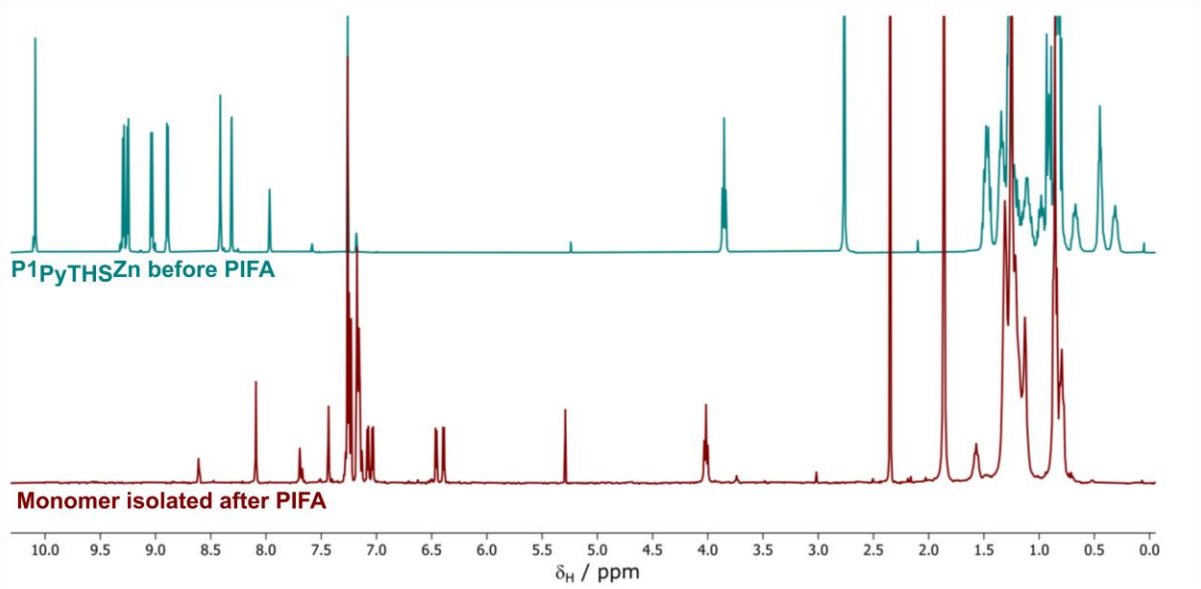

Figure 5.26. (top) ^{1}H NMR of **P1$_{PyTHS}$Zn** before addition of PIFA ($CDCl_3$, 298 K, 400 MHz). (bottom) ^{1}H NMR of isolated monomer length material after PIFA coupling reaction ($CDCl_3$, 298 K, 400 MHz).

A method of coupling that is defect free and reliable is essential for reaching the target compound **MM-P6$_{PyTHS}$Zn**, as this reaction first needs to produce **MM-P3$_{PyTHS}$Zn** in good yield, then also work for the coupling of enantiopure **MM-P3$_{PyTHS}$Zn** to make **MM-P6$_{PyTHS}$Zn**. We next explored using nickel mediated Yamamoto coupling for this reaction, as this has also previously been used for meso-meso coupling porphyrin species.[18] In these reactions **P1$_{PyTHS}$Zn** was first statistically brominated with NBS to yield a mixture of **P1$_{PyTHS}$Zn,** **P1$_{PyTHS}$Zn-HBr** and **P1$_{PyTHS}$Zn-Br$_2$**. ^{1}H NMR of this mixture could be used to reliable identify the relative proportions of each compound as they present distinct proton environments (Figure 5.27).

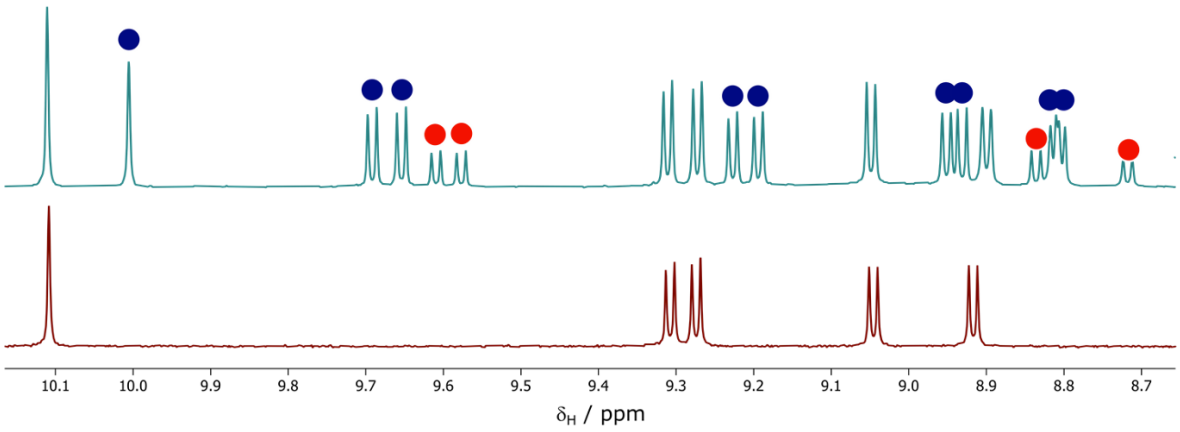

Figure 5.27. (bottom) ^{1}H NMR spectrum of spectrum of **P1$_{PyTHS}$Zn**. (top) ^{1}H NMR spectrum of statistically brominated **P1$_{PyTHS}$Zn** with peaks from monobrominated highlighted in blue and dibrominated in red. ($CDCl_3$ + 1% d_5-pyridine, 298 K, 400 MHz)

The statistically brominated mixture was then subjected to the nickel mediated Yamamoto coupling conditions outlined in Figure 5.28.[19] This reaction is particularly sensitive to oxygen, moisture and light, so all reactions were conducted with thoroughly degassed dry solvents in a fume hood with light switched off (see experimental section). Thankfully, these conditions effectively oligomerize the porphyrin monomer, with distributions that can be tuned by the degree of bromination of the starting monomer, with no carbonyl defects. Using this approach,

we were able to obtain racemic **MM-P3$_{PyTHS}$Zn** in 15% yield and **MM-P2$_{PyTHS}$Zn** in 23% yield. A preparative scale recycling GPC trace for a typical oligomerization is shown in Figure 5.29.

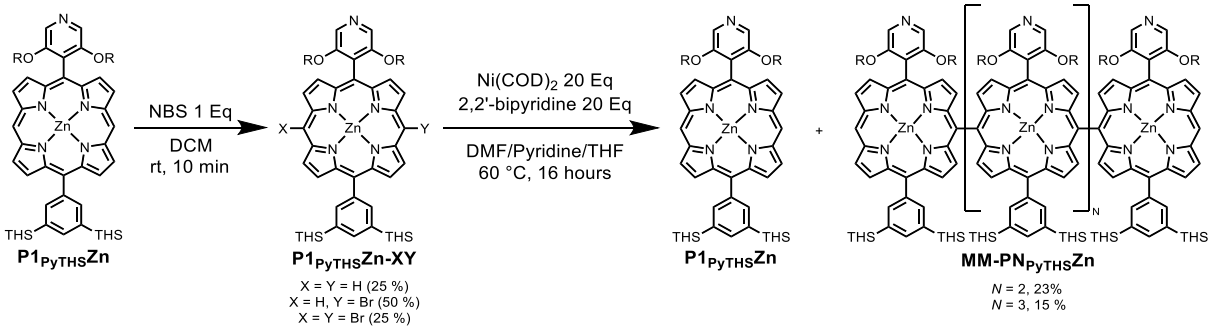

Figure 5.28. Nickel mediated Yamamoto coupling to produce **MM-P*N*$_{PyTHS}$Zn**.

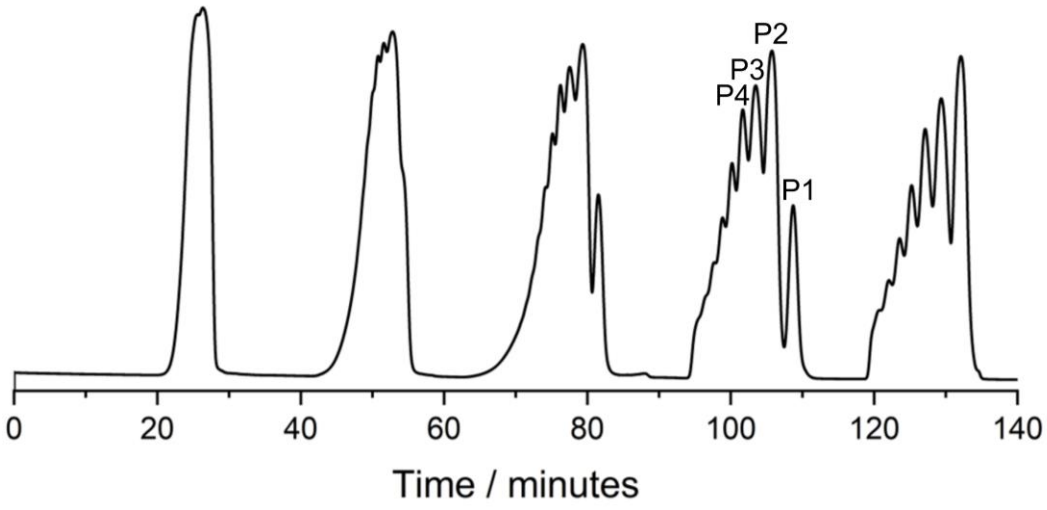

Figure 5.29. Recycling GPC trace of **MM-P*N*$_{PyTHS}$FB** oligomer mixture. (Toluene + 1% pyridine, rt, 400nm)

Demetallation of the **MM-P3$_{PyTHS}$Zn** racemate by treatment with TFA produces **MM-P3$_{PyTHS}$FB** in quantitative yield, from which the diastereomers can be separated by silica gel column chromatography using an eluent mix of THF/hexane (30/70) (Figure 5.30). After column chromatography, the fractions containing the pair of enantiomers (*RR/SS*) and the *meso* form (*RS/SR*) were identified by chiral HPLC, as discussed in the following section.

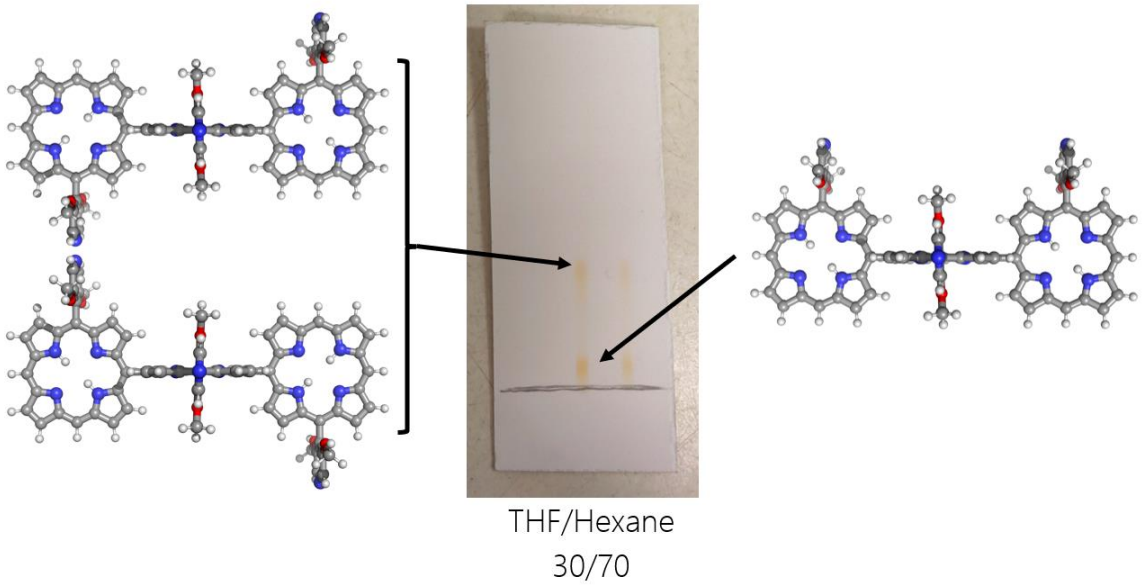

Figure 5.30 (centre) TLC of **MM-P3$_{PyTHS}$FB** racemate showing separation of the *meso* form (right) from chiral *RR* and *SS* forms (left). (THF/Hexane, 30/70)

5.3.1.2 Chiral Resolution of Enantiomers

With enantiomeric mixtures of **MM-P3$_{PyTHS}$FB** (RR/SS) and **MM-P2$_{PyTHS}$FB** (R/S) in hand, I next turned my attention to the chiral resolution of these enantiomers. Our laboratory does not have any chiral HPLC columns, however, I was generously granted permission to use the analytical chiral HPLC equipment in the group of Professor Stephen Fletcher. This instrument was not equipped with the SUMICHIRAL OA-3100 column used by Osuka in his chiral separation of the self-sorted chiral boxes, but instead had the full suite of CHIRALPAK columns produced by Daicel. I began my investigation by focusing on zinc (II) complex **MM-P2$_{PyTHS}$Zn**, as this compound was most similar to the boxes Osuka was able to separate. Unlike with Osuka's boxes, regardless of the column used, in non-coordinating solvent systems this material showed no separation. However, when small percentages of a coordinating solvent such as THF or pyridine were included, some separation of the enantiomers was observed. This was most apparent when using two CHIRALPAK-IC columns in series. Using pyridine as a model example, at low pyridine concentrations we see a dramatic shift in the retention of the material from 3 minutes in neat hexane to 22 minutes in hexane + 2% pyridine (Figure 5.31).

Furthermore, the material is now split into two peaks, one for each enantiomer. Increasing the pyridine concentration further only accelerates the elution of the material and leads to poorer separation of the enantiomers. We expect that the added pyridine dissociates the box formation, which allows the pyridyl group on **MM-P2$_{PyTHS}$-Zn** to interact with the chiral stationary phase, increasing the retention and allowing for discrimination between the two enantiomers. Unfortunately, higher loadings of **MM-P2$_{PyTHS}$-Zn** into this solvent system does not replicate the separation observed on an analytical scale. This is likely a reflection of the altered ratio of pyridine:**MM-P2$_{PyTHS}$-Zn** leading to less dissociation of the box and therefore a weaker interaction with the chiral stationary phase. Increasing the pyridine concentration of the stationary phase does not counteract this and instead leads to rapid elution of the injected material. Finally, no significant increase in enantiomer separation was achieved when using a chiral pyridine additive (e.g. 2% nicotine).

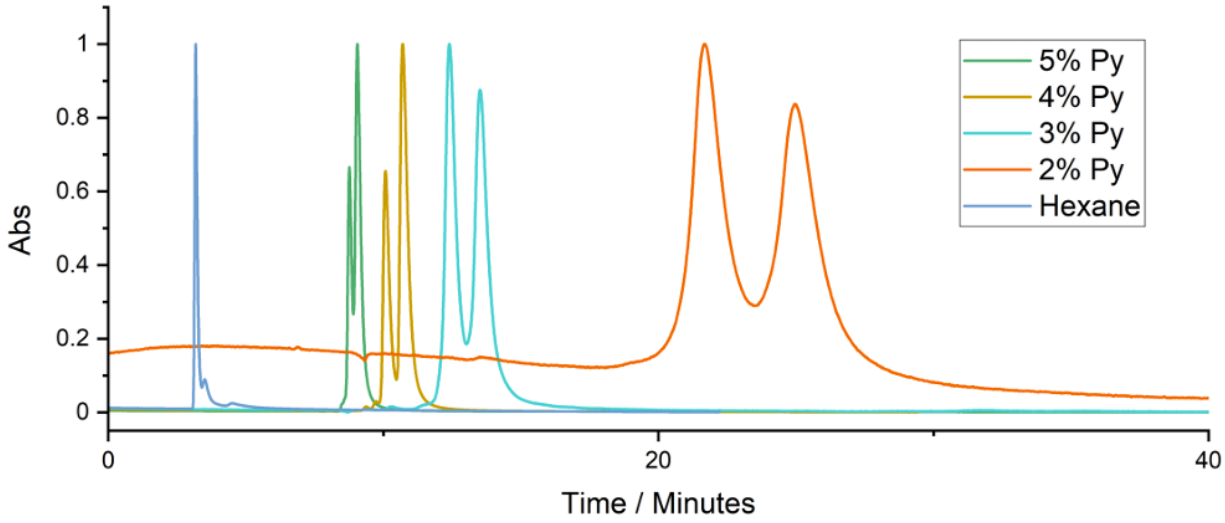

Figure 5.31. Analytical scale chiral HPLC trace of **MM-P2$_{PyTHS}$-Zn** racemate using two CHIRALPAC-IC columns in series and hexane + X % pyridine as the eluent (λ = 400 nm).

I next explored chiral HPLC of the free-base form dimer **MM-P2$_{PyTHS}$FB**. This material is significantly more polar that the boxes formed by **MM-P2$_{PyTHS}$Zn**, due to the ability of the free pyridyl groups in **MM-P2$_{PyTHS}$FB** to interact with the chiral stationary phase. In hexane **MM-P2$_{PyTHS}$FB** is entirely retained on the CHIRALPAK-IC column, however this material can be

eluted by using neat toluene as an eluent. This behaviour indicated that some ratio of toluene:hexane may allow the material to elute whilst still interacting with the stationary phase. By investigating mixtures of these solvents, I was able to identify that 70:30 toluene:hexane was optimal for separating the enantiomers of **MM-P2$_{PyTHS}$FB**. The apparatus I was using had no semi-prep or preparative columns, so I relied on loading as much material as possible onto the analytical column, then utilizing the autosampling and fraction collecting capabilities of the system to separate the enantiomers on a preparative scale (Figure 5.32a). This approach of separating the free-base form using a mix of toluene and hexane also worked well for separating the RR and SS forms of **MM-P3$_{PyTHS}$FB** on a semi-preparative scale (Figure 5.32c and d).

Until the absolute stereochemistry of the enantiomers can be definitively assigned (by comparison to TD-DFT calculations) I have differentiated between the pure enantiomers with a superscript in the compound codes indicating the order that they elute from the CHIRALPAK-IC column. For example, the peak shown in Figure 5.32b is the second to elute, so is labelled as **MM-P2$_{PyTHS}$FB^{2}**.

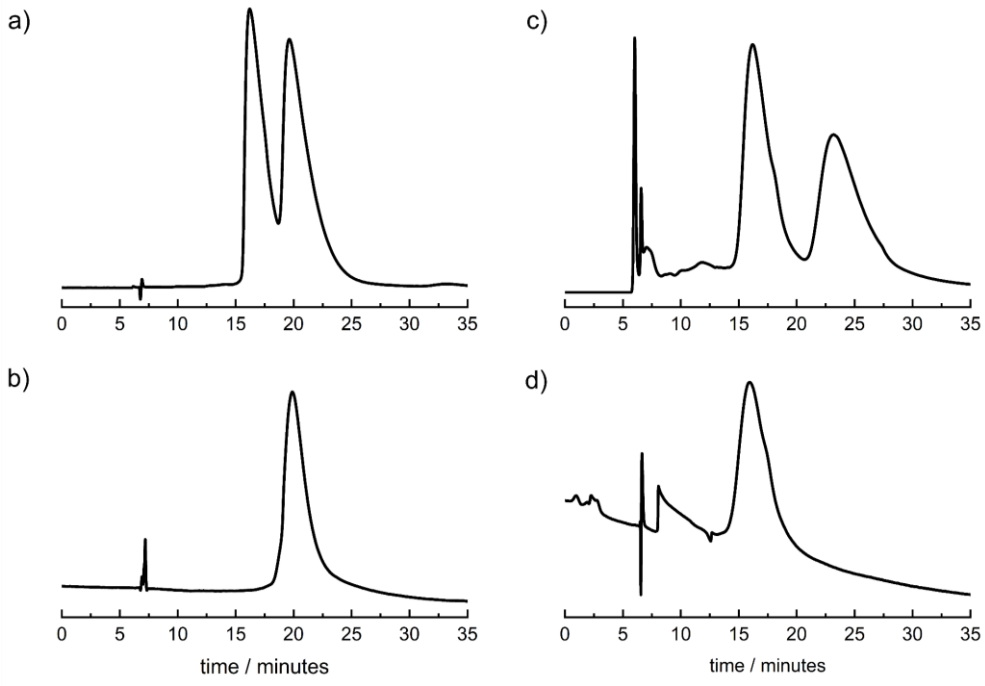

Figure 5.32. Chiral HPLC traces of: (a) **MM-P2$_{PyTHS}$FB** racemate (0.5 mg) (b) **MM-P2$_{PyTHS}$FB^{2}** (Analytical) (c) **MM-P3$_{PyTHS}$FB** racemate (0.5 mg) (d) **MM-P3$_{PyTHS}$FB^{1}** (Analytical) (Traces obtained using two CHIRALPAK-IC columns in series with 1 ml/min flow rate of toluene/hexane (70/30))

This method was used to isolate 4 mg of enantiopure **MM-P3$_{PyTHS}$FB^{1}**, which I subsequently complexed with zinc (II), statistically brominated and Yamamoto coupled (Figure 5.33). Unfortunately, the Yamamoto coupling of this material failed, which I expect was due to the relatively small scale this reaction was set up on due to the limited material available. Work on this project is currently focused on scaling up the route to enantiopure **MM-P3$_{PyTHS}$FB^{1}** described in this thesis, for eventual conversion into enantiopure **MM-P6$_{PyTHS}$FB**. The following sections will therefore focus on the information gained from the enantiopure samples of **MM-P2$_{PyTHS}$FB^{1}** and **MM-P3$_{PyTHS}$FB^{1}** isolated so far.

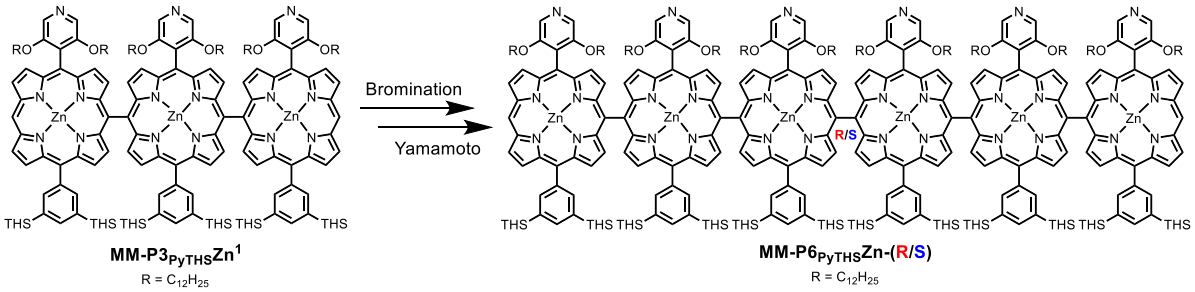

Figure 5.33. Final Yamamoto coupling to access enantiopure **MM-P6$_{PyTHS}$FB**.

5.3.2 Formation of Single Helical Complexes

With enantiopure **MM-P2$_{PyTHS}$FB^{1}** and **MM-P3$_{PyTHS}$FB^{1}** in hand, I next investigated the binding of these materials to their respective lengths of butadiyne-linked oligomer **P2$_{THS}$(C$_2$CPDIPS)$_2$** and **P3$_{THS}$(C$_2$CPDIPS)$_2$**.

From the binding work in the 18-ring project, we know that pyridine binds to **P1$_{THS}$(C$_2$CPDIPS)$_2$** with a formation constant of (1.47 ± 0.05) x 10^4 M^{-1}. Titration of **MM-P2$_{PyTHS}$FB^{1}** into **P2$_{THS}$(C$_2$CPDIPS)$_2$** (in $CDCl_3$ filtered over AlO_3) and analysis of the UV-Vis data with the 1:1 binding model (Chapter 3, Section 3.2) resulted in a binding constant of (1.91 ± 0.08) x 10^5 M^{-1} (Figure 5.34).

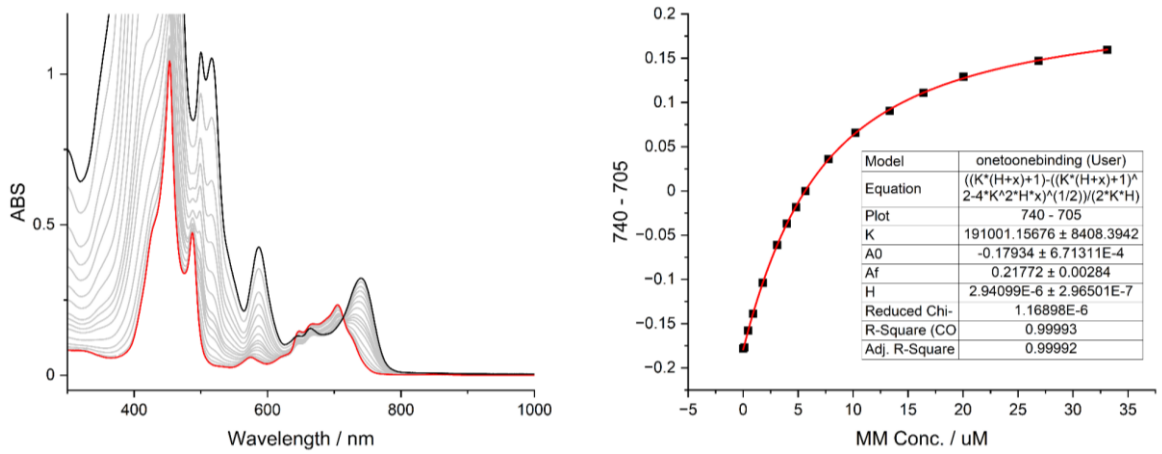

Figure 5.34. (left) UV-Vis binding titration of **MM-P2$_{PyTHS}$FB^{1}** into **P2$_{THS}$(C$_2$CPDIPS)$_2$.** Start in red, end in black. (right) Data fit to the 1:1 binding model. (Titration completed in $CDCl_3$ that was filtered over Al_2O_3 prior to use).

Repeating this process with **MM-P3$_{PyTHS}$FB^{1}** and **P3$_{THS}$(C$_2$CPDIPS)$_2$** reveals a binding constant of (3.97 ± 0.15) x 10^6 M^{-1} (Figure 5.35). This binding constant being stronger than that of the dimer complex indicates that all three sites do indeed bind and that we have begun forming partially helical structures.

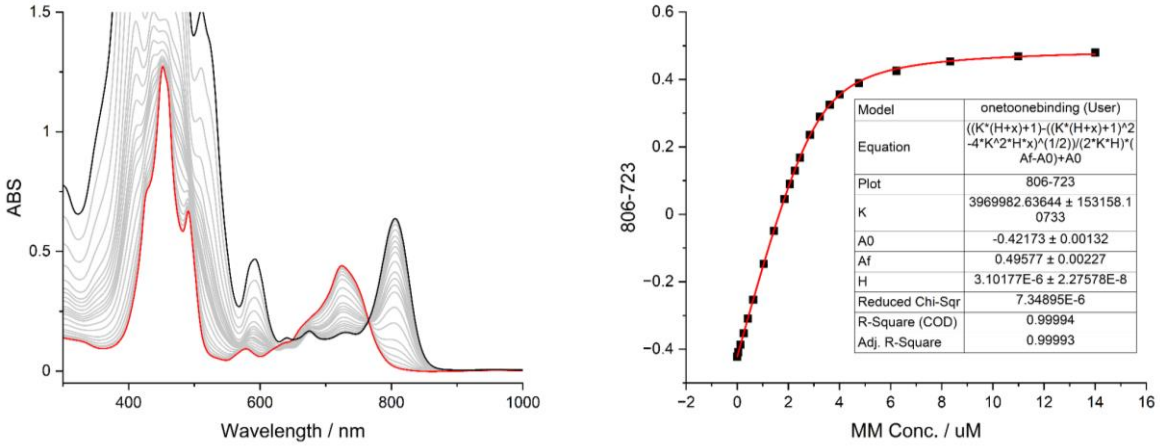

Figure 5.35. (left) UV-Vis binding titration of **MM-P3$_{PyTHS}$FB^{1}** into **P3$_{THS}$(C$_2$CPDIPS)$_2$.** Start in red, end in black. (right) Data fit to the 1:1 binding model. (Titration completed in $CDCl_3$ that was filtered over Al_2O_3 prior to use).

The trimer length *meso* form, **MM-P3$_{PyTHS}$FB^{MESO}**, has a binding constant of (4.70 ± 0.21) x 10^6 M^{-1} which is similar to that of the enantiopure trimer **MM-P3$_{PyTHS}$FB^{1}**. However, the meso form complex has a notably different UV-Vis spectrum with a partially split Q-band (Figure 5.36).

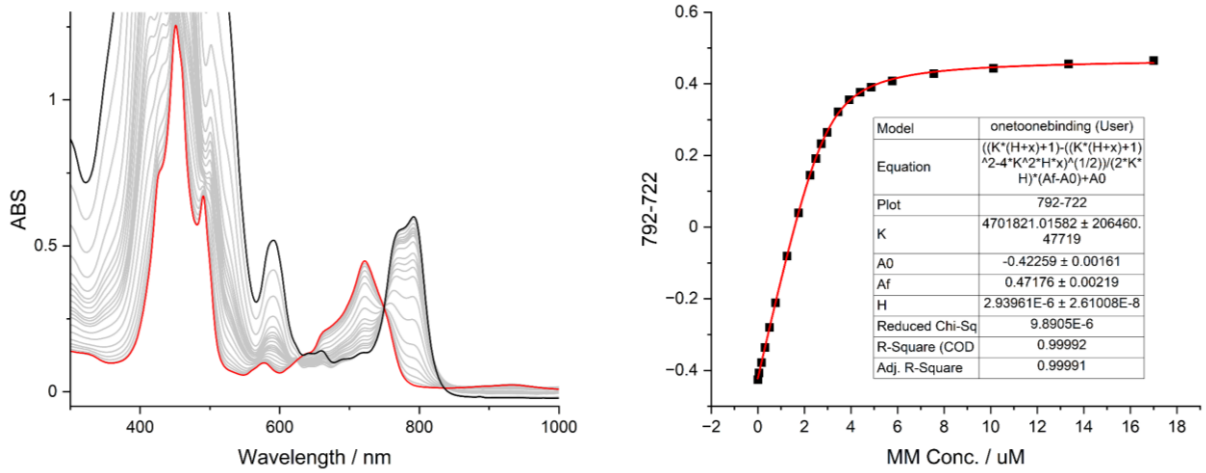

Figure 5.36. (left) UV-Vis binding titration of **MM-P3$_{PyTHS}$FB^{MESO}** into **P3$_{THS}$(C$_2$CPDIPS)$_2$**. Start in red, end in black. (right) Data fit to the 1:1 binding model. (Titration completed in $CDCl_3$ that was filtered over Al_2O_3 prior to use).

This partially split Q-band may be a consequence of Davydov splitting (Figure 5.37), which occurs when the electric transition dipole moments of two closely spaced chromophores couple.[20] This coupling results in a spilt band for the electronic transition, with one peak corresponding to the in-phase coupling and one for the out-of-phase coupling of the transition dipole moments.

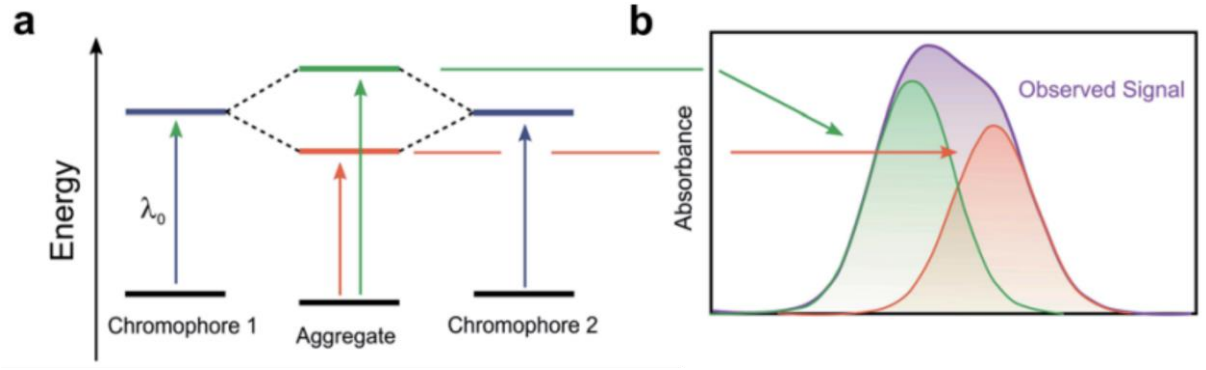

Figure 5.37. (a) Energy level diagram demonstrating how the excited states of two chromophores can couple. (b) A theoretical UV-Vis absorbance spectrum of an aggregate with Davydov splitting. Reproduced from reference.[20]

Figure 5.38 demonstrates how one equivalent of **MM-P3$_{PyTHS}$FB^{MESO}** cannot bind all three zinc centres of **P3$_{THS}$(C$_2$CPDIPS)$_2$**. For Davydov splitting to the cause the split Q-band of the complex, two molecules of **P3$_{THS}$(C$_2$CPDIPS)$_2$** must be close in space. Figure 5.39 demonstrates how a 2:2 complex of **MM-P3$_{PyTHS}$FB^{MESO}** and **P3$_{THS}$(C$_2$CPDIPS)$_2$** can position

two **P3$_{THS}$(C$_2$CPDIPS)$_2$** close in space, for the potential coupling of the Q-band electric transition dipole moments. The formation of a 2:2 complex would also explain the surprisingly strong binding of the *meso* form, as if only two sites bind (as in Figure 5.38) we would expect a similar binding strength to the dimer **MM-P2$_{PyTHS}$FB^1**.

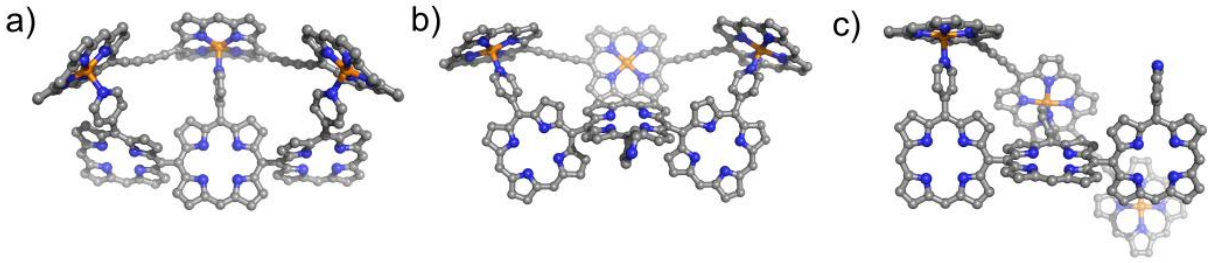

Figure 5.38. Different PM7 optimized binding geometries of **P3$_{THS}$·MM-P3$_{PyTHS}$FB^{MESO}**.

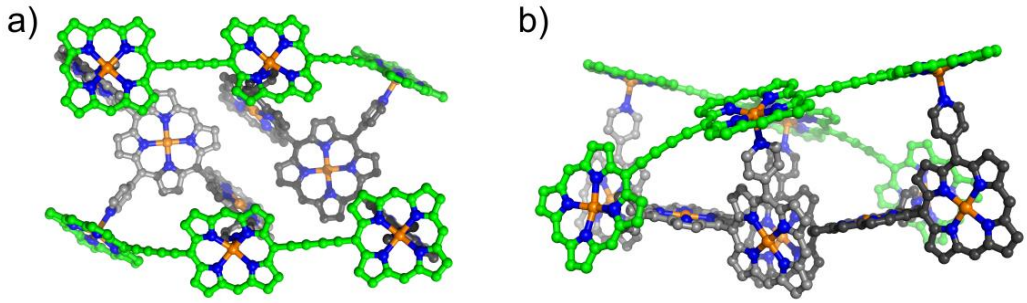

Figure 5.39. PM7 optimized geometry of a 2:2 complex of **P3$_{THS}$:MM-PN$_{PyTHS}$-Zn^{MESO}.**

5.3.3 Circular Dichroism of Single Helical Complexes

As discussed in Chapter 1, the dissymmetry factor (*g*) derived from the CD spectrum of chiral π-conjugated materials has been shown to be a good indicator of the spin polarization capabilities of such materials.[13] The dissymmetry factor (*g)* can be calculated using Equation 5.4, where I_{LH} and I_{RH} are the absorbances of LCP and RCP light respectively. The measurement of this value will therefore give us some insight into the potential chiroptical properties of our materials. We focused this analysis on the trimer length complex, as it constitutes roughly one half of a full helical pitch, so it is therefore an interesting sample to compare the target hexamer length complex to once synthesized.

$$g = \frac{2\times(I_{LH}-I_{RH})}{I_{LH}+I_{RH}} \qquad \text{Eq 5.4}$$

In this analysis we measured the CD spectra of the linear butadiyne-linked oligomer **P3$_{THS}$(C$_2$CPDIPS)$_2$**, the enantiopure first eluting meso-meso linked oligomer **MM-P3$_{PyTHS}$FB^1**, and a 1:1 mixture of these two materials which forms **P3$_{THS}$(C$_2$CPDIPS)$_2$·MM-PN$_{PyTHS}$FB^1**. All spectra shown are an average of three scans which were background corrected for the $CHCl_3$ solvent used (Figure 5.40).

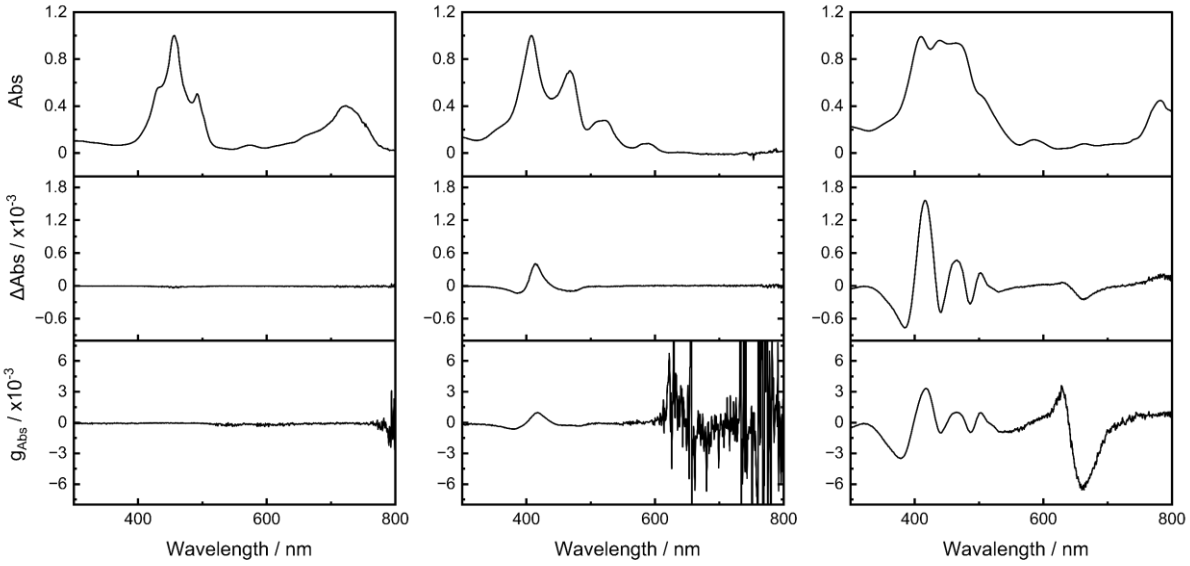

Figure 5.40 Absorbance spectrum (Top row), CD spectrum (Middle row), Dissymmetry factor g_{Abs} (Bottom row). **P3$_{THS}$(C$_2$CPDIPS)$_2$** (Left column), **MM-P3$_{PyTHS}$FB^1** (Middle column), **P3$_{THS}$(C$_2$CPDIPS)$_2$·MM-P3$_{PyTHS}$FB^1** (Right column). All samples were measured in $CDCl_3$ that had been stored over K_2CO_3 and filtered over Al_2O_3 prior to use.

Firstly, for **P3$_{THS}$(C$_2$CPDIPS)$_2$** we observe no significant features in the CD or dissymmetry factor plots, as expected for this completely achiral material. Moving to **MM-P3$_{PyTHS}$FB^1** we observe negative cotton effects at 386 nm and 468 nm, and a positive effect at 414 nm in the CD spectrum of this material. These effects are maintained in the dissymmetry factor plot which has a maximum value of g_{ABS} = 9.82 x 10^{-4} and 417 nm. Finally, in the complex **P3$_{THS}$(C$_2$CPDIPS)$_2$·MM-P3$_{PyTHS}$FB^1** we observe multiple oscillations of positive and negative cotton effects in the CD spectrum. In the 300 nm to 450 nm range these oscillations match those in **MM-P3$_{PyTHS}$FB^1**, but additional features are observed across the whole spectrum. Notably, only a weak CD signal was found in the Q-band region (> 700 nm), which corresponds to excitations with a transition dipole moment aligned with the long axis of **P3$_{THS}$(C$_2$CPDIPS)$_2$**. We anticipated that the semi-helical geometry of this oligomer in our

complex would induce a significant CD signal for this particular transition, but perhaps a more complete helix is required for this (such as in **P6$_{THS}$(C$_2$CPDIPS)$_2$·MM-P6$_{PyTHS}$FB^1**). Calculation of the g_{ABS} for **P3$_{THS}$(C$_2$CPDIPS)$_2$·MM-P3$_{PyTHS}$FB^1** reveals that this particular complex has non-zero values of g_{ABS} across the entire measured range (300 nm – 800 nm). The abundance of new CD and g_{Abs} features observed in **P3$_{THS}$(C$_2$CPDIPS)$_2$·MM-P3$_{PyTHS}$FB^1** compared to **MM-P3$_{PyTHS}$FB^1** confirms that we have induced chirality onto the **P3$_{THS}$(C$_2$CPDIPS)$_2$** unit.

5.3.4 Comparison of Single Porphyrin-based Single Helices to Previous Work

As discussed in the introduction, a study by Therein and coworkers reports the induction of chirality in a series of ethynyl linked porphyrin oligomers by binding bidentate chiral ligands, which generates complexes that are capable of producing spin polarized currents at room temperature.[1] This study is a useful reference to compare our complexes to as they reported both the CD spectra (Figure 5.3) of these compounds and quantified their spin filtering capabilities. The most impressive properties came from the tetramer length complex **PZn$_4$SAc·B$_{R/S}$** (Figure 5.41) which demonstrated a spin polarization of 32% at 2V, with key g_{ABS} values of ±1.3 x10^{-3} at 500nm and ±1.8 x 10^{-3} at 850nm. The most direct comparison we can make is between the g_{Abs} values of **P3$_{THS}$(C$_2$CPDIPS)$_2$·MM-P3$_{PyTHS}$FB^1** of 3.33 x 10^{-3} at 418nm and of -6.23 x 10^{-3} at 661nm. These values indicate that **P3$_{THS}$(C$_2$CPDIPS)$_2$·MM-P3$_{PyTHS}$FB^1** has stronger chiroptical activity, therefore may generate more strongly spin-polarized currents.

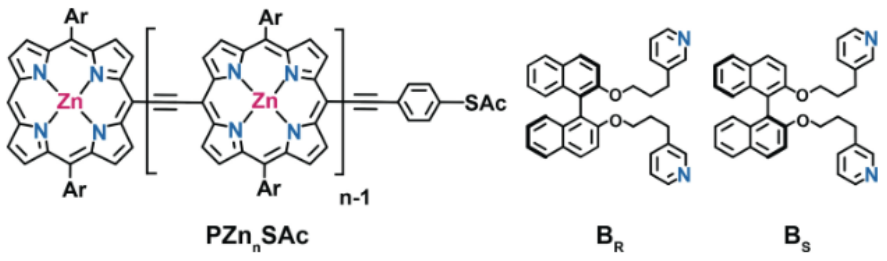

Figure 5.41. Chemical structures of compounds synthesized by Therein (Ar = 2′,6′-bis(3,3-dimethyl-l-butyloxy)phenyl). Reproduced from reference.[1]

One key point to note however is that **P3$_{THS}$(C$_2$CPDIPS)$_2$·MM-P3$_{PyTHS}$FB^1** does not exhibit any significant CD or g_{Abs} signals for its Q-band, whereas **PZn$_4$SAc·B$_{R/S}$** does. In both samples, this band corresponds to a transition dipole moment aligned with the long axis of the oligomer, so presumably is important for charge transport along this axis. The current in the mc-AFM measurements of spin polarization (discussed in 5.1.1) are measured along this axis, so the chiroptical activity of this band is likely an important factor for the generation of spin polarized currents. We were surprised to observe this weak Q-band activity in **P3$_{THS}$(C$_2$CPDIPS)$_2$·MM-P3$_{PyTHS}$FB^1** given its partially helical geometry. Isolation and measurement of the hexamer length **P6$_{THS}$(C$_2$CPDIPS)$_2$·MM-P6$_{PyTHS}$FB^1** will provide greater insight into the effect of the helical geometry on the chiroptical activity of these compounds, and quantification of the spin polarized currents will teach us more about the structure-property relationships of these materials.

5.3.5 TD-DFT of Single Helical Trimer-length Complex

Advances in TD-DFT mean that CD spectra of chiral complexes can often be computed with relative ease and are accurate enough to be used to determine the absolute stereochemistry of chiral materials.[10] As with many of the porphyrin-based materials described in this thesis, the synthetic design of the oligomers in this helical project contain many long aliphatic solubilizing groups, which make obtaining crystal structures challenging. Therefore, to determine the absolute stereochemistry of our complexes, TD-DFT was performed on the trimer length complex (**P3$_{THS}$·MM-P3$_{PyTHS}$FB**) (Figure 5.42).

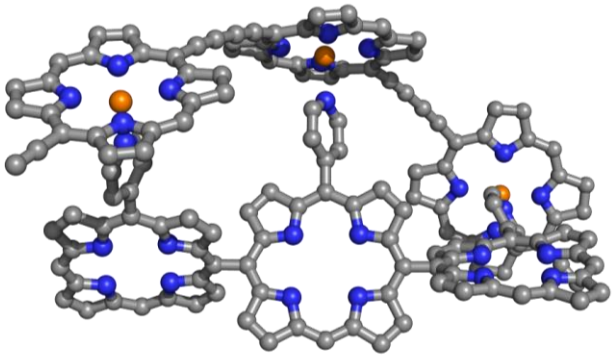

Figure 5.42. DFT (B3LYP/6-31g(d)) optimized model of **P3$_{THS}$·MM-P3$_{PyTHS}$FB**.

The geometry of the complex was first optimised using B3LYP/6-31g(d) then TD-DFT calculations were completed using the following functionals: B3LYP, LC-ωHPBE (ω = 0.1) and CAM-B3LYP. The predicted UV-VIS and ECD spectra using each functional, alongside the experimental data for the trimer length complex are presented in Figure 5.43.

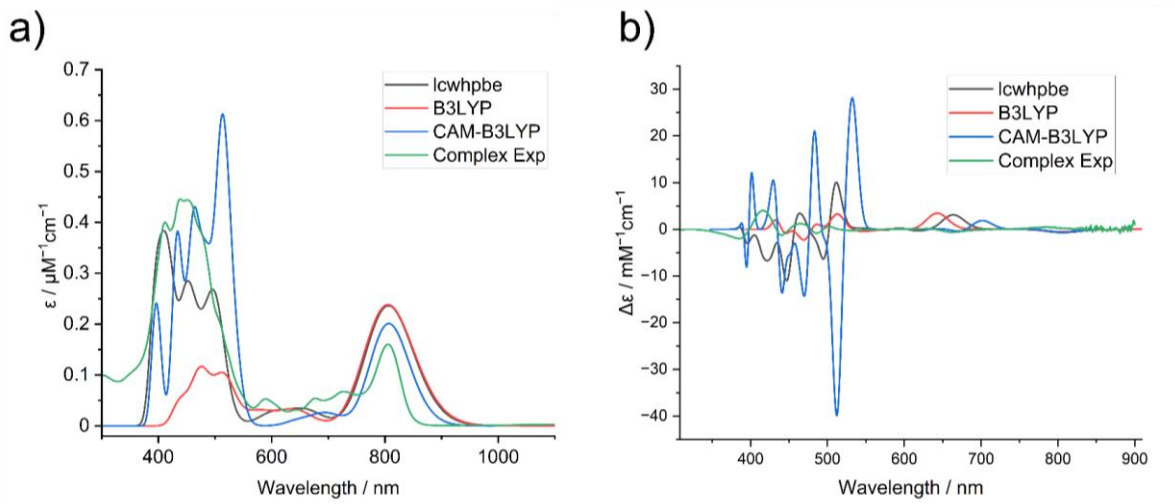

Figure 5.43. (a) Experimental UV-Vis spectrum and predicted UV-Vis spectra from TD-DFT calculations on the trimer-length complex. All predicted spectra were shifted to align the λ_{max} of the Q-band with the experimental data (B3LYP (+4 nm), LC-ωHPBE (+22 nm) and CAM-B3LYP (+95 nm)). (b) Experimental ECD spectrum and predicted ECD spectrum from TD-DFT calculations. Predicted ECD spectra are shifted by the same amount as for the UV-Vis spectrum.

From Figure 5.43 we firstly see a wide variance in the spectra produced by each functional. In the UV-Vis spectra (Figure 5.43a), we see that all functionals fail to reproduce the exact shape of the Soret band, and that B3LYP in particular significantly underestimates the Soret band intensity. Conversely, all functionals predict reasonably similar Q-Band shapes which match the experimental data, despite all predicting stronger intensity absorptions in this region. It is noteworthy that B3LYP and LC-wHPBE exhibit almost identical UV-Vis spectra above 600 nm.

Figure 5.43b presents the experimental and predicted ECD spectrum, which unfortunately show poor agreement regardless of the choice of functional. CAM-B3LYP notably overestimates the absorption intensities, whereas B3LYP and LC-wHPBE produce spectra more closely matching the magnitude of the experimental results. Due to the poor agreement, we cannot use these results to assign the absolute stereochemistry.

We may rationalise these poor results by considering them in the context of the binding titrations previously discussed. The experimental data shown in Figure 5.43 was obtained from a 1:1 sample of **P3$_{THS}$(C$_2$CPDIPS)$_2$** and **MM-P3$_{PyTHS}$FB^1** in $CHCl_3$. From our binding study of these two materials, we observe strong binding, but not strong enough to yield a sharp endpoint to the titration at the 1:1 stoichiometry. Instead, we observe a continual change in the UV-Vis spectrum, which eventually plateaus at high concentrations of **MM-P3$_{PyTHS}$FB^1**. This tells us that at the 1:1 stoichiometry in our CD measurements, we have a number of compounds in solution: Free **P3$_{THS}$(C$_2$CPDIPS)$_2$**, Free **MM-P3$_{PyTHS}$FB^1,** and the complex **P3$_{THS}$(C$_2$CPDIPS)$_2$·MM-P3$_{PyTHS}$FB^1**. In contrast to this, the TD-DFT calculations are performed on a single molecule of the exact 1:1 complex, which therefore does not account for the other species in solution in the CD measurements.

In Therin's work, this issue is resolved by taking CD measurements with a large excess of the chiral ligand which ensures that all of the porphyrin species is complexed. In this particular case this is a viable solution, as their ligand only absorbs below 360 nm, so an excess does not affect the spectrum of the porphyrin species. With our complex this approach is less ideal, because **MM-P3$_{PyTHS}$FB^1** absorbs strongly in the 300 nm – 600 nm region, so an excess of the ligand would dominate the CD spectrum of this complex.

5.4 Double Helical Complexes

5.4.1 Synthesis of Double Helical Template

With minor changes to the porphyrin synthesis, we were also able to prepare the achiral oligomers **MM-PN$_{Py}$FB** (Figure 5.44), which are interesting as templates for the double helical complex shown in Figure 5.45. This complex is somewhat unique as both components are achiral yet should bind to form a chiral complex. We hoped that these complexes would be bound strongly enough that they would form sharp 1:2 complexes, and that racemization would be slow relative to the time required to separate the two enantiomers. Due to the achiral nature

of the **MM-PN$_{Py}$FB** templates the synthesis and yields of these materials is far higher than for the chiral enantiopure templates previously discussed in this thesis.

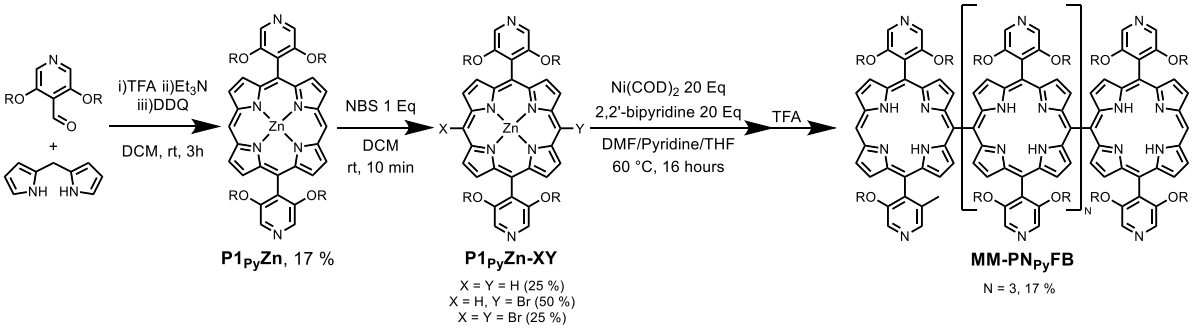

Figure 5.44. Synthesis of bipyridyl meso-meso linked oligomers.

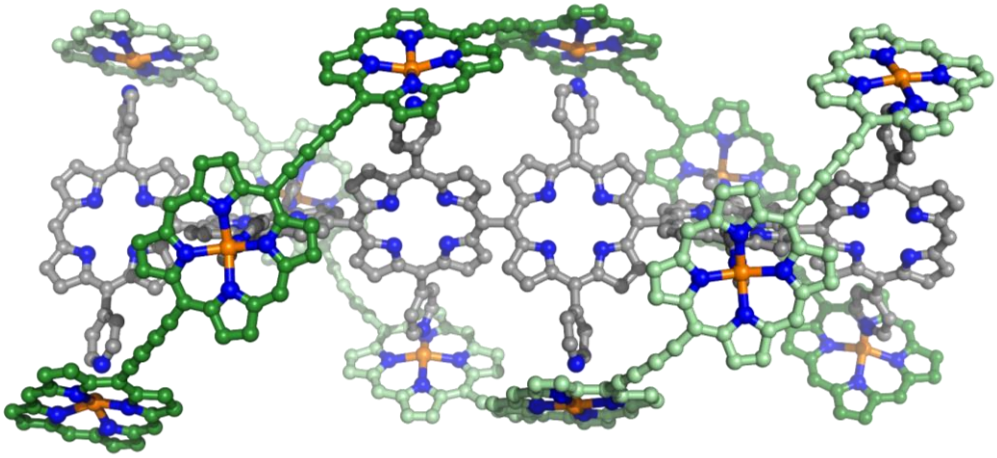

Figure 5.45. Model of the double helical complex formed from **MM-P6$_{Py}$FB** and **P6$_{THS}$** (Optimised in MOPAC with the PM7 method).

5.4.2 Formation of Double Helical Complexes

With **MM-P3$_{Py}$FB** in hand we initially focused our attention on the formation of the trimer length helical complex **(P3$_{THS}$(C$_2$CPDIPS)$_2$)$_2$·MM-P3$_{Py}$FB.** Figure 5.46 presents data from the UV-Vis titration used to monitor the binding. Here we first see the build up of a red-shifted Q-band with a λ_{max} of 816 nm, which peaks in intensity at the 2:1 stoichiometry (black trace). However, as additional **MM-P3$_{Py}$FB** is added, we see this band blue-shift and plateau at high **MM-P3$_{Py}$FB** concentrations. We expected that in this titration we were first observing the formation of the 2:1 complex, then the breakdown to the 1:1 complex at high **MM-P3$_{Py}$FB** concentrations.

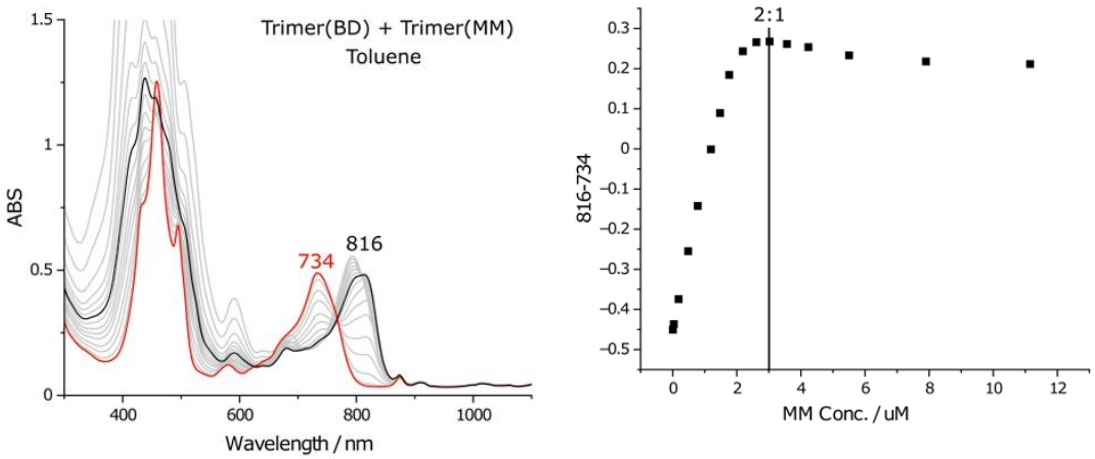

Figure 5.46. (left) UV-Vis data from a titration of **MM-P3$_{Py}$FB** into **P3$_{THS}$(C$_2$CPDIPS)$_2$**. (right) Change in Q-band absorbance with increasing **MM-P3$_{Py}$FB** concentration.

To further examine this binding, we decided to analyse our UV-Vis data with Musketeer.[21] In this analysis we assumed the equilibrium shown in Figure 5.47. In order to reasonably fit the data, we had to provide an estimation of K_1 for which we used the value obtained for the binding of **P3$_{THS}$(C$_2$CPDIPS)$_2$·MM-P3$_{PyTHS}$FB^1** (3.97×10^6 M^{-1}). This analysis (Figure 5.48) matches our expectations that the 2:1 **(P3$_{THS}$(C$_2$CPDIPS)$_2$)$_2$·MM-P3$_{Py}$FB** complex forms at early **MM-P3$_{Py}$FB** concentrations and is then completely broken down into the 1:1 complex at high **MM-P3$_{Py}$FB** concentrations (Speciation plot, Figure 5.48 right). We were initially surprised at the high molar absorbance value of the deconvoluted 2:1 complex (Figure 5.48, middle) however this spectrum is reasonable, as this species contains two equivalents of the **P3$_{THS}$(C$_2$CPDIPS)$_2$** component that contributes to absorption at this wavelength. In this analysis, Musketeer outputs a value for K_2 of 2.70×10^5 M^{-1}, therefore, there is negative cooperativity for the binding of **P3$_{THS}$(C$_2$CPDIPS)$_2$**.

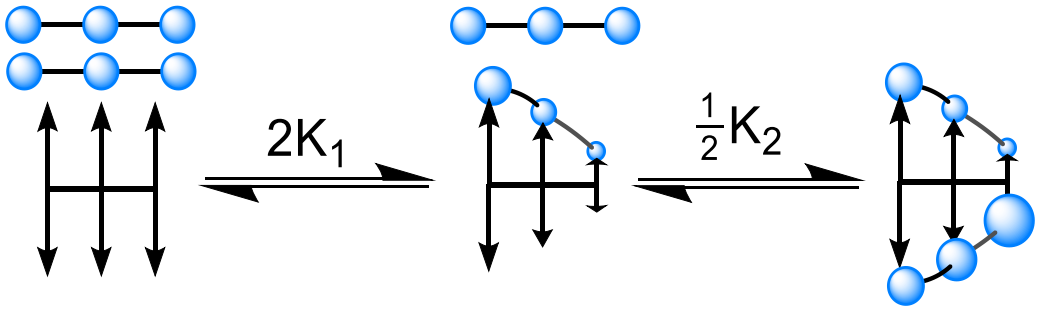

Figure 5.47. Equilibrium constants involved in the binding of **MM-P3$_{Py}$FB** to into **P3$_{THS}$(C$_2$CPDIPS)$_2$**

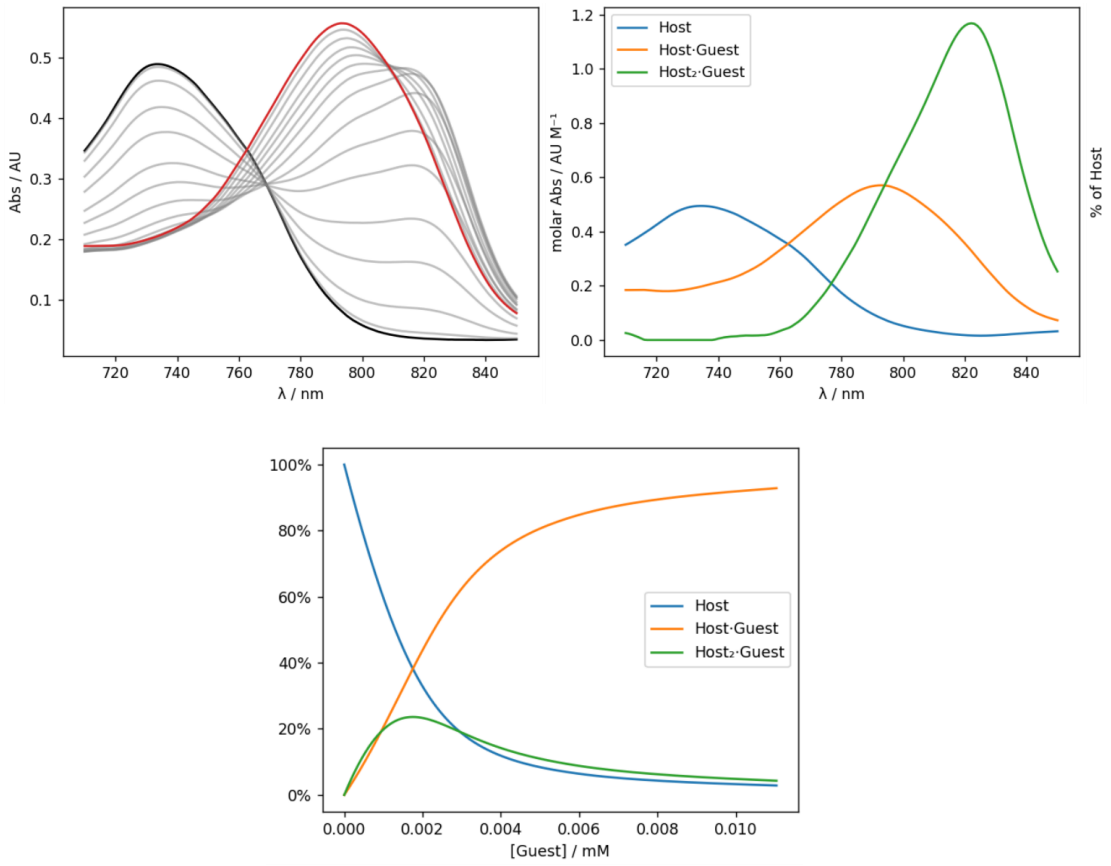

Figure 5.48. Deconvolution of the binding in **(P3$_{THS}$(C$_2$CPDIPS)$_2$)$_2$·MM-P3$_{Py}$FB** using Musketeer.[21] (top left) raw UV-Vis titration data as **MM-P3$_{Py}$FB** (guest) is added to **P3$_{THS}$(C$_2$CPDIPS)$_2$** (host) in $CDCl_3$. (top right) Deconvoluted UV-Vis spectra of species present. (bottom) speciation curve of species present. Deconvolution obtained with the constraint that equilibrium constant K_1 (Figure 5.47) is 3.97 x 10^6 M^{-1}.

The titration in Figure 5.46 was relatively quick, with additions taking place roughly 2 minutes apart. Due to the low concentration of the 1:1 and 2:1 complexes, this may not have given the system time to reach equilibrium, which we hoped at stoichiometric concentrations of **MM-P3$_{Py}$FB** should be biased towards the 2:1 complex. Our rationale for this is best demonstrated by the model in Figure 5.49 (left), which shows how formation of the 1:1 complex preorganises the unbound pyridyl units in **MM-P3$_{Py}$FB** for binding a second unit of **P3$_{THS}$(C$_2$CPDIPS)$_2$**. To explore this process, we measured the UV-Vis spectrum of a 2:1 mixture of **P3$_{THS}$(C$_2$CPDIPS)$_2$:MM-P3$_{Py}$FB** over 30 minutes. Figure 5.49 (right) presents the spectra obtained from this experiment, which shows very little change with time. Heating the sample after the 30 minutes to 50 °C leads to almost complete dissociation of the formed complex, as

seen by the dramatic blue shift of the Q-band. Together these results indicate that the 2:1 complex is relatively unstable with respect to conversion to the 1:1 complex and is not bound very tightly as a small increase in temperature fully dissociates the complex.

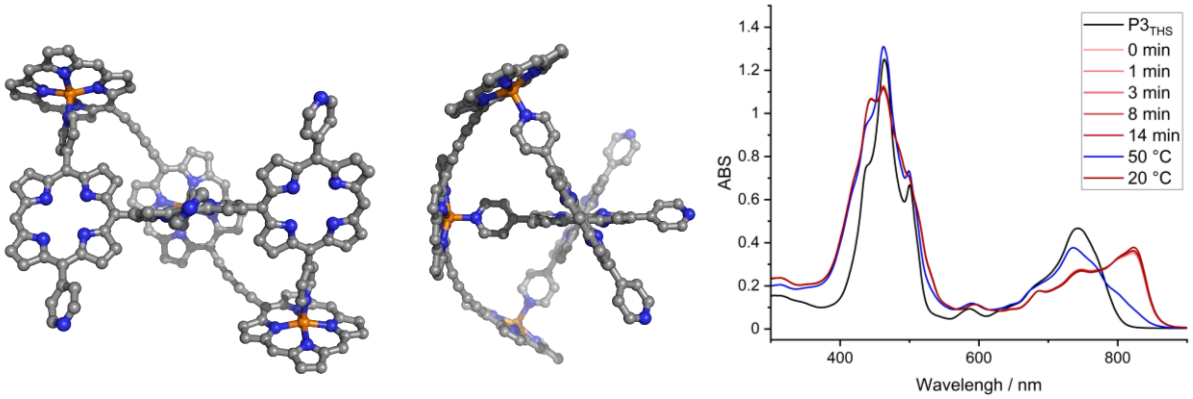

Figure 5.49. (left) 1:1 complex of **P3$_{THS}$(C$_2$CPDIPS)$_2$:MM-P3$_{Py}$FB.** (right) Time and temperature dependent UV-Vis spectrum of a 2:1 mixture of **P3$_{THS}$(C$_2$CPDIPS)$_2$** and **MM-P3$_{Py}$FB** ($CDCl_3$). (Time is after the addition of MM-P3$_{Py}$FB).

Isolation of the chiral double helices will require very tight binding, with slow racemization rates relative to the time required to separate the enantiomers. We anticipate that the formation of hexamer, 9-mer or 18-mer length double helical complexes may be stronger and more selective for the 2:1 complexes due to the increased number of binding sites. Current work on this project is focused on synthesizing and exploring the properties of these materials, with the hope of isolating the enantiomers of the longer complexes and measuring their spin polarisation capabilities.

5.4.3 Planned Extension into a Helical Nanoring 3-Catenane

Another approach to isolating chiral double helical complexes is to covalently lock in the chirality of the double helix once it has formed. We have explored some ambitious options for this, with the most promising candidate being the synthesis of a nanoring 3-catenane. This idea is heavily inspired by current unpublished work in the Anderson group, which has successfully prepared meso-meso linked porphyrin nanorings using the nickel mediated Yamamoto coupling of nickel porphyrins (Figure 5.50). If this reaction were to be successfully used on **P1$_{Py}$Ni** it would produce meso-meso linked porphyrin nanorings with pyridine units coming of the 10

and 20 positions of each porphyrin (Figure 5.51). From our molecular modelling, we have determined that an 18 porphyrin nanoring with this structure is the ideal template to attempt the formation of the helical nanoring 3-catenane (Figure 5.52), which is formed first by the coordination of 2 equivalents of **P18$_{OOct}$(C$_2$)$_2$**, then Glaser coupling of the free acetylene end groups to lock the structure.

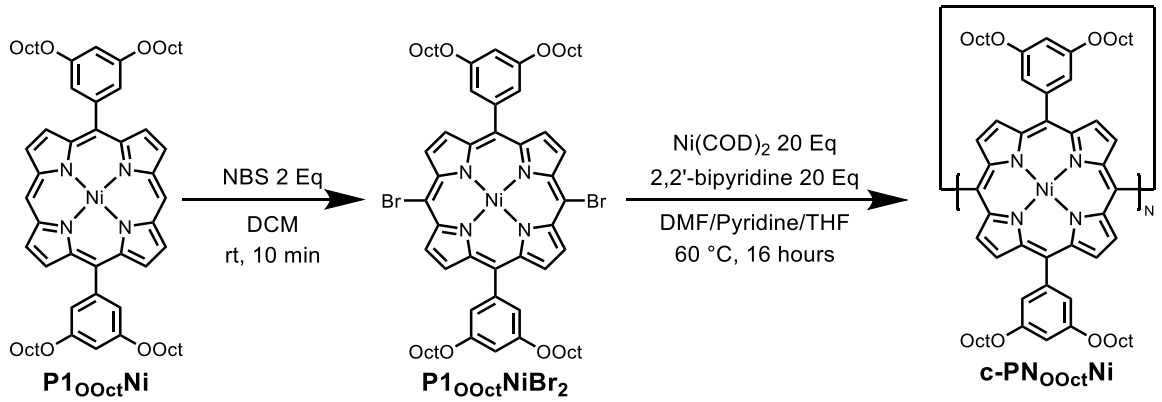

Figure 5.50. Unpublished route to meso-meso linked porpyrin nanorings discovered in the Anderson group.

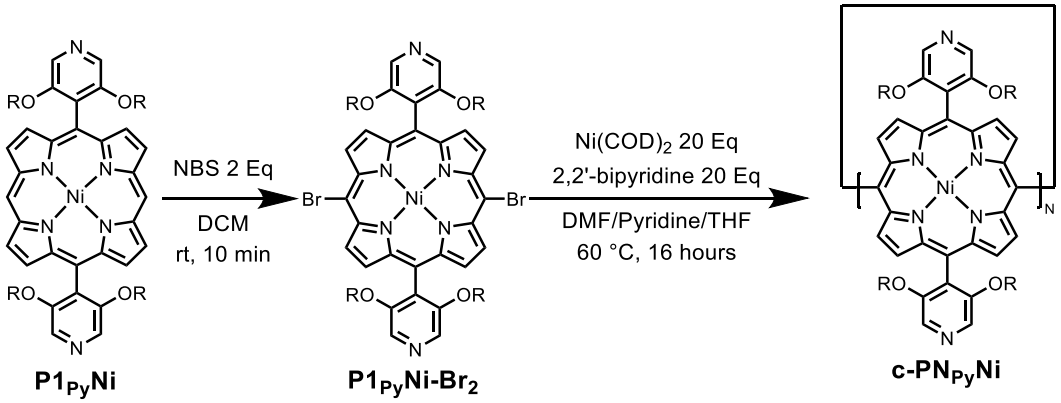

Figure 5.51. Proposed route to pyridyl containing meso-meso linked porphyrin nanoring.

From our studies of the single and double helical complex we understand that one full helical pitch of a butadiyne-linked porphyrin around a meso-meso linked axle requires 6 porphyrin units. Therefore, cyclic templates with 6N porphyrin units in the meso-meso linked ring seemed the most reasonable designs to attempt, as this ensures the ends of the butadiyne linked oligomer meet up with one another (Figure 5.52b). From the model of the 18-porphyin helical catenane (Figure 5.52a) we see a reasonable amount of crowding in the center of the ring, but no direct clashes of the porphyrin units or solubilizing groups. In the smaller 12-ring, this clashing was

more apparent, which we anticipated would make formation of the complex more challenging. Finally, though the coordination of such a complex is challenging, we hope that the large number of N-Zn binding interactions will make the complex relatively stable, long enough for the Glaser coupling to lock in the chirality. Exploring the binding of the longer linear double-helical complexes will be incredibly informative for this process (e.g. **MM-P18$_{Py}$FB** + **P18$_{OOct}$(C$_2$THS)$_2$**).

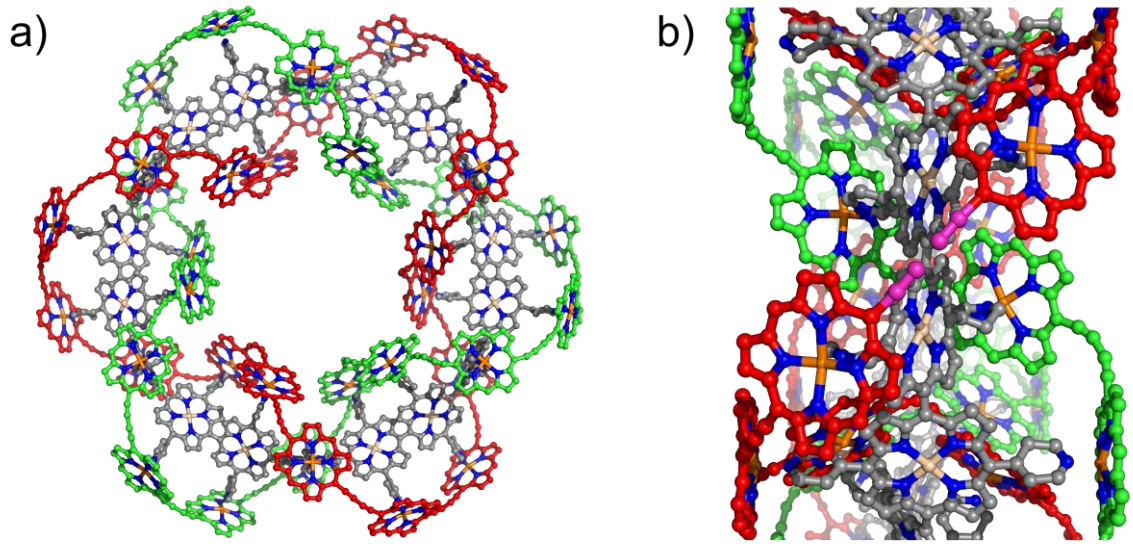

Figure 5.52. (a) Model of the proposed helical nanoring 3-catenane **MM-*c*-P18$_{Py}$Ni·(*c*-P18Zn)$_2$**. (b) Fragment of the model from (a) showing how the terminal acetylenes on **P18** would align once bound to **MM-c-P18$_{Py}$Ni**.

Immediately after the submission of this thesis we will attempt the synthesis of the meso-meso lined 18-porphyrin nanoring template and the subsequent binding and Glaser coupling of the catenate structure. Isolation of the enantiomers and conformation of the helical structure by STM would mark the first synthesis of an all porphyrin nanoring catenane, and the study of the chiroptical properties of the canenane would teach us more about the structure property relationships of these materials.

5.5 Summary of Results and Outlook

With the synthesis and chiral resolution of the single helical templates established, the current position of this project is promising. We have established that with an enantiopure trimer-length meso-meso linked template (**MM-P3$_{PyTHS}$-FB^{1}**), we can induce chirality in an achiral butadiyne-linked trimer (**P3$_{THS}$(C$_2$CPDIPS)$_2$**) upon the binding of these species, as CD spectroscopy of the complex shows additional features that are not seen in the spectrum of **MM-P3$_{PyTHS}$-FB^{1}**. Comparison of this spectrum to the TD-DFT calculated spectrum does not yet allow us to unambiguously assign the absolute stereochemistry of **P3$_{THS}$(C$_2$CPDIPS)$_2$·MM-P3$_{PyTHS}$FB^{1}**, but future work aims to refine these calculations to do so.

The synthesis of the enantiopure meso-meso linked axel is hindered by losses to longer undesired oligomers and unproductive diastereomers. However, our work on the double helical template (**MM-PN$_{Py}$-FB**) reinforces the benefits of having a chiral template. Despite its simpler synthesis, the achiral **MM-P3$_{Py}$-FB** template does not selectively form a 2:1 complex with **P3$_{THS}$(C$_2$CPDIPS)$_2$**. Instead, we observe a significant abundance of the 1:1 complex and unbound **P3$_{THS}$(C$_2$CPDIPS)$_2$** at low concentration of **MM-P3$_{Py}$-FB**. Because of this, isolation of the chiral **(P3$_{THS}$(C$_2$CPDIPS)$_2$)$_2$·MM-P3$_{Py}$FB** complex is not possible. In this context, the added synthetic effort required to produce the enantiopure single-helical template **MM-P3$_{PyTHS}$-FB^{1}** is valued as it is does allow for the formation and study of helical butadiyne-linked oligomers.

Current work on this project is focused on the synthesis of the enantiopure hexamer-length single-helical template **MM-P6$_{PyTHS}$-FB^{1}**, which we plan on using to study the chiroptical properties of **P6$_{THS}$(C$_2$CPDIPS)$_2$** in a conformation that encompasses one full helical pitch. After the preparation of the enantiopure trimer and hexamer length single-helical complexes, we hope to initiate a collaboration to measure the ability of these complexes to spin polarize currents, as reported for similar porphyrin oligomers by Naaman and Therien.[1] Additionally, we hope to explore coordination of porphyrin oligomers with different connection (e.g. ethynyl)

to our chiral templates and to explore the circularly polarized emission of these complexes. The complexes described in this chapter have various parameters we can vary (e.g. oligomer length, helix pitch, solubilizing group, distance from helix to template, metal centers used) so we hope though our systematic study of the various combinations that we can learn a lot about the structure property relationships of these materials.

Finally, upon submission of this thesis I will continue exploring the synthesis and binding of longer bipyridyl substituted meso-meso linked oligomers and their function as templates for double helical complexes in a short postdoctoral stay in the group. I also plan on expanding this work to explore the synthesis of the meso-meso linked 18-porphyrin nanoring **MM-*c*-P18$_{Py}$Ni** and its ability to template the helical nanoring 3-catenane in Figure 5.52. The successful synthesis of this 3-catenane will mark the first synthesis of an all porphyrin nanoring based catenane. Furthermore, despite the lack of terminal groups in the catenane where anchors for AFM based spin filtering measurements could be placed, there is literature precedent that we could still perform these measurements on the enantiopure nanoring catenane. This is based on another report by Naaman which quantifies the spin filtering capability of topologically chiral trefoil knots using magnetic conductive probe atomic force microscopy.[22]

5.6 References

1. C.-H. Ko, Q. Zhu, F. Tassinari, G. Bullard, P. Zhang, D. N. Beratan, R. Naaman and M. J. Therien, *Proceedings of the National Academy of Sciences*, 2022, **119**, e2116180119.
2. G. Bullard, F. Tassinari, C.-H. Ko, A. K. Mondal, R. Wang, S. Mishra, R. Naaman and M. J. Therien, *Journal of the American Chemical Society*, 2019, **141**, 14707-14711.
3. Z. Xie, T. Z. Markus, S. R. Cohen, Z. Vager, R. Gutierrez and R. Naaman, *Nano Letters*, 2011, **11**, 4652-4655.
4. J. Bosson, G. M. Labrador, C. Besnard, D. Jacquemin and J. Lacour, *Angewandte Chemie International Edition*, 2021, **60**, 8733-8738.
5. J. Rawson, P. J. Angiolillo and M. J. Therien, *Proceedings of the National Academy of Sciences*, 2015, **112**, 13779-13783.
6. A. Tsuda, T. Nakamura, S. Sakamoto, K. Yamaguchi and A. Osuka, *Angewandte Chemie International Edition*, 2002, **41**, 2817-2821.
7. I.-W. Hwang, T. Kamada, T. K. Ahn, D. M. Ko, T. Nakamura, A. Tsuda, A. Osuka and D. Kim, *Journal of the American Chemical Society*, 2004, **126**, 16187-16198.
8. N. Yoshida and A. Osuka, *Tetrahedron Letters*, 2000, **41**, 9287-9291.
9. Q. Chen, A. Lodi, H. Zhang, A. Gee, H. I. Wang, F. Kong, M. Clarke, M. Edmondson, J. Hart, J. N. O'Shea, W. Stawski, J. Baugh, A. Narita, A. Saywell, M. Bonn, K. Müllen, L. Bogani and H. L. Anderson, *Nature Chemistry*, 2024, **16**, 1133-1140.
10. G. Pescitelli and T. Bruhn, *Chirality*, 2016, **28**, 466-474.
11. A. D'Addio, J. Malinčik, O. Fuhr, D. Fenske, D. Häussinger and M. Mayor, *Chemistry – A European Journal*, 2022, **28**.
12. S. Richert, B. Limburg, H. L. Anderson and C. R. Timmel, *Journal of the American Chemical Society*, 2017, **139**, 12003-12008.
13. B. P. Bloom, Y. Paltiel, R. Naaman and D. H. Waldeck, *Chemical Reviews*, 2024, **124**, 1950-1991.
14. P. Parkinson, C. E. I. Knappke, N. Kamonsutthipaijit, K. Sirithip, J. D. Matichak, H. L. Anderson and L. M. Herz, *Journal of the American Chemical Society*, 2014, **136**, 8217-8220.
15. H. Gotfredsen, J.-R. Deng, J. M. Van Raden, M. Righetto, J. Hergenhahn, M. Clarke, A. Bellamy-Carter, J. Hart, J. O'Shea, T. D. W. Claridge, F. Duarte, A. Saywell, L. M. Herz and H. L. Anderson, *Nature Chemistry*, 2022, **14**, 1436-1442.
16. Q. Ouyang, Y.-Z. Zhu, C.-H. Zhang, K.-Q. Yan, Y.-C. Li and J.-Y. Zheng, *Organic Letters*, 2009, **11**, 5266-5269.
17. W. Stawski, J. M. Van Raden, C. W. Patrick, P. N. Horton, S. J. Coles and H. L. Anderson, *Organic Letters*, 2023, **25**, 378-383.
18. H. Zhu, G. Wen, W. Zheng, N. H. Rees, W. Stawski, H. I. Wang, M. Bonn and H. L. Anderson, *Angewandte Chemie International Edition*, 2025, **64**.
19. T. Yamamoto, S. Wakabayashi and K. Osakada, *Journal of Organometallic Chemistry*, 1992, **428**, 223-237.
20. J. L. Greenfield, J. Wade, J. R. Brandt, X. Shi, T. J. Penfold and M. J. Fuchter, *Chemical Science*, 2021, **12**, 8589-8602.
21. D. O. Soloviev and C. A. Hunter, *Chemical Science*, 2024, **15**, 15299-15310.
22. D.-Y. Zhang, Y. Sang, T. K. Das, Z. Guan, N. Zhong, C.-G. Duan, W. Wang, J. Fransson, R. Naaman and H.-B. Yang, *Journal of the American Chemical Society*, 2023, **145**, 26791-26798.
23. P. Parkinson, N. Kamonsutthipaijit, H. L. Anderson and L. M. Herz, *ACS Nano*, 2016, **10**, 5933-5940.

5.7 Experimental

Contents

5.7.1 Synthesis of Single and Double Helical Templates

5.7.1.1 $P1_{PyTHS}Zn$

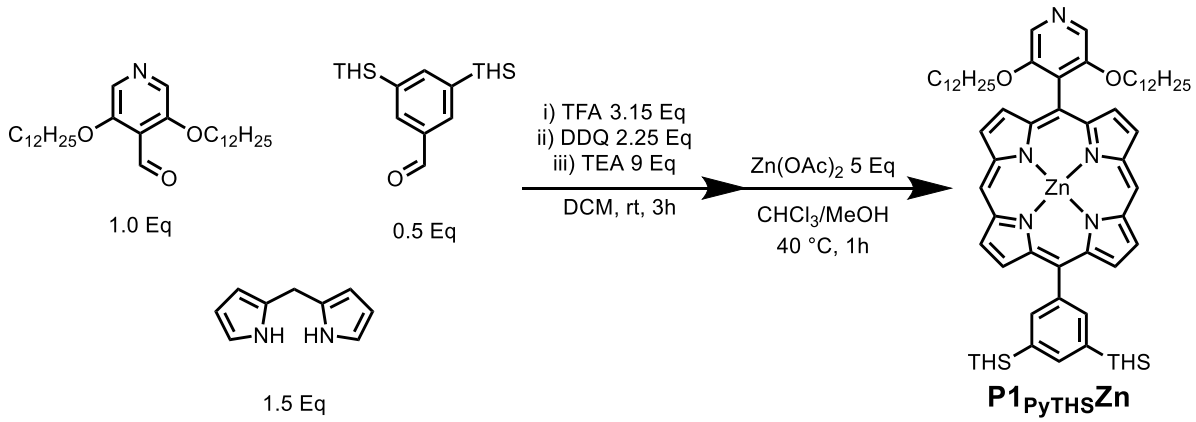

The procedure used to access the free-base porphyrin was conducted as previously reported[23]:

To a 2L round bottomed flask containing N_2 purged DCM (500 mL) was added 3,5-bis(dodecyloxy)isonicotinaldehyde (1080 mg, 1 Eq, 2.27 mmol), 3,5-bis(trihexylsilyl)benzaldehyde (762 mg, 0.5 Eq, 1.14 mmol) and DPM (498 mg, 1.5 Eq, 3.41 mmol). The solution was stirred in the dark for 30 minutes, then TFA (815 mg, 547 µL, 3.15 Eq, 7.15 mmol) was added over 5 minutes. After stirring in the dark for 3 hours, DDQ (1.160 g, 2.25 Eq, 5.11 mmol) was added. After a further 40 minutes stirring, TEA (2.85 mL, 9 Eq, 20.43 mmol) was carefully added over 5 minutes. The mixture was stirred fror a final 30

minutes, then concentrated in vacuo and purified by silica gel column chromatography (SiO_2, DCM/MeOH 99:1, DCM).

The crude reaction mixture was redissolved in $CHCl_3$ (55 mL) then a solution of $Zn(OAc)_2$ (707 mg, 5 Eq, 3.22 mmol) in MeOH (7.7 mL) was added. The solution was stirred at 40 °C for 1 hour then concentrated in vacuo and purified by silica gel column chromatography (SiO_2, DCM/PE 1:1, then DCM/PE 1:9 + 1% pyridine) to afford a red oil (920 mg, 27 %).

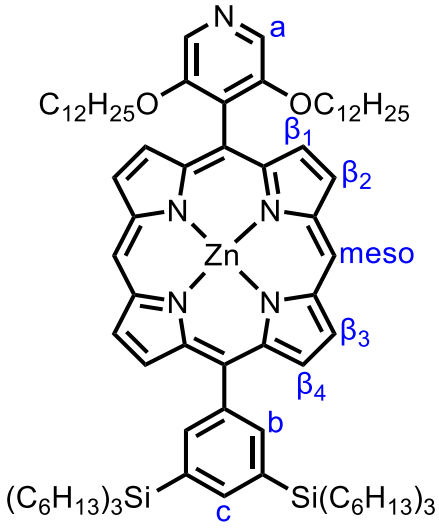

Characterisation matches previous report.[14]

^{1}H NMR (400 MHz, $CDCl_3$ + 1% d_5-pyridine) δ 10.10 (s, 2H, **H_{meso}**), 9.30 (d, *J* = 4.4 Hz, 2H, **β_2**), 9.26 (d, *J* = 4.4 Hz, 2H, **β_3**), 9.04 (d, *J* = 4.4 Hz, 2H, **β_1**), 8.90 (d, *J* = 4.4 Hz, 2H, **β_4**), 8.45 (s, 2H, **H_a**), 8.31 (s, 2H, **H_b**), 7.97 (s, 1H, **H_c**), 3.87 (t, *J* = 6.4 Hz, 4H, **OCH_2**), 1.86–0.27 (m, 124H, **alkyl**).

MALDI-ToF *m/z* 1459.80 (calculated for $[C_{91}H_{143}N_5O_2Si_2Zn]^{\bullet+}$ = $(M)^{\bullet+}$: 1459.01).

5.7.1.2 MM-PN$_{PyTHS}$FB

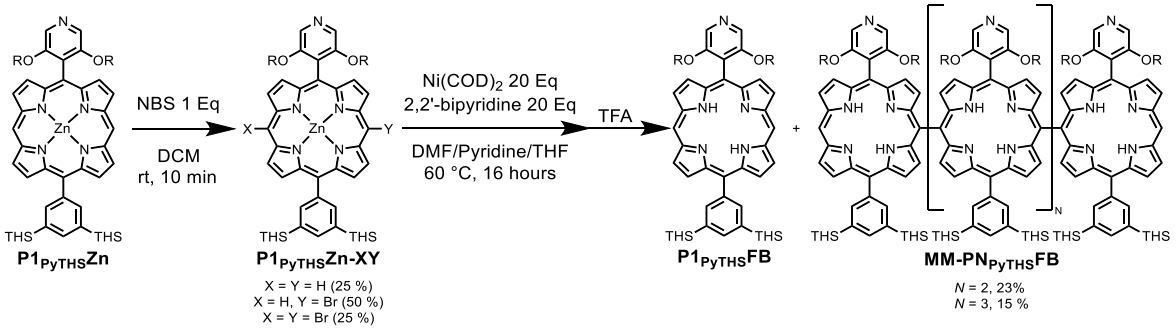

To a stirring solution of **P1$_{PyTHS}$Zn** (263 mg, 1 Eq, 0.18 mmol) in $CHCl_3$ (90 mL) at rt was added NBS (48 mg, 1.5 Eq, 0.27 mmol). After 10 minutes, the reaction was quenched by the addition of acetone (20 mL) and reduced in vacuo. The resulting residue was passed through a short silica plug using an eluent mix of DCM + 1 % pyridine and the collected fraction concentrated and used without further purification in the next step.

The crude material from the first step was transferred into an oven dried Schlenk tube which was then dried under high vacuum and placed under an argon atmosphere. To this material was added degassed dry THF (22.3 mL) and dry pyridine (1.1 mL). The solution was then degassed by three freeze/pump/thaw cycles. To a second oven dry Schlenk tube was added 2,2-bipyridine (564 mg, 20 Eq, 3.61 mmol) and under a positive flow of argon, $Ni(COD)_2$ (993 mg, 20 Eq, 3.61 mmol). Immediately after the addition of $Ni(COD)_2$ the Schlenk tube was stoppered and evacuated. The tube was then subjected to 3 vacuum/argon cycles, before being placed under a positive pressure of argon. The fume hood light was then switched off and DMF (67 mL) was added to the Schlenk tube. The resulting solution was then freeze pump thaw degassed for 3 cycles, then under a positive pressure of argon, stirred at 60 °C for 1 hour. During this time the solution turns a deep purple colour.

The porphyrin solution was then transferred by cannula to the active nickel catalyst solution, and the resulting mixture stirred at 60 °C for two hours. After cooling to rt, the crude mixture was passed through a short silica gel plug in DCM + 2% pyridine and concentrated in vacuo. The resulting residue was purified by column chromatography (SiO_2, DCM + 2% pyridine).

The crude material was then dissolved in DCM (60 mL) and TFA (50 uL) was added. After stirring at rt for 1 hour a saturated solution of $NaHCO_3$ (30 mL) and DCM (30 mL) were added. The separated

organic layer was washed with H_2O (3 x 30 mL), concentrated in vacuo, then purified by silica gel column chromatography (SiO_2, DCM + 2% pyridine), size-exclusion chromatography (Bio-Beads, S-X3, toluene + 1% pyridine) and preparative GPC (toluene + 1% pyridine) to yield a range of free-base form oligomer lengths: **MM-P2$_{PyTHS}$FB** (57 mg, 23 %) and **MM-P3$_{PyTHS}$FB** (38 mg, 15 %).

As described in section 4.3.1.2, the enantiomers of **MM-P2$_{PyTHS}$FB** are separable by chiral HPLC using a CHIRALPAK-IC column with a flow rate of 1 ml/min of toluene/hexane 70/30. Additionally, the diastereomers of **MM-P3$_{PyTHS}$FB** are separable by silica gel column chromatography using a mix of THF/hexane 30/70, giving one faster eluting fraction containing the RR/SS enantiomer pair, and a slower eluting second fraction containing the meso RS/SR isomer. The RR/SS enantiomer pair can be separated using the same chiral HPLC setup as for **MM-P2$_{PyTHS}$FB.**

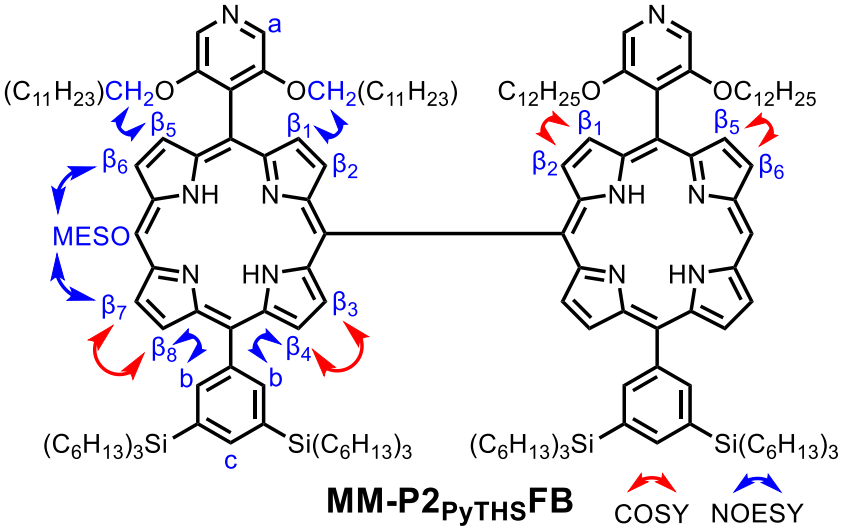

^{1}H NMR (600 MHz, $CDCl_3$) δ 10.28 (s, 2H, **H_{MESO}**), 9.38 – 9.35 (m, 4H, **β$_6$ + β$_7$**), 8.98 (d, *J* = 4.9 Hz, 2H, **β$_8$**), 8.93 (d, *J* = 4.6 Hz, 2H, **β$_5$**), 8.60 (d, *J* = 4.9 Hz, 2H, **β$_4$**), 8.46 (d, *J* = 4.8 Hz, 2H, **β$_1$**), 8.40 (s, 4H, **H$_a$**), 8.26 (s, 4H, **H$_b$**), 8.07 (d, *J* = 4.8 Hz, 2H, **β$_3$**), 8.00 (d, *J* = 4.8 Hz, 2H, **β$_2$**), 7.90 (s, 2H, **H$_c$**), 3.99 – 3.92 (m, 4H, **OCH$_2$-In/Out**), 3.92 – 3.85 (m, 4H, **OCH$_2$-In/Out**), 1.51 – 0.37 (m, 248H, H_{Alkyl}), -2.34 (s, 4H, **$H_{Freebase}$**).

MALDI-ToF *m/z* 2791.46 (calculated for $[C_{182}H_{288}N_{10}O_4Si_4]^{\bullet+}$ = $(M)^{\bullet+}$: 2792.18).

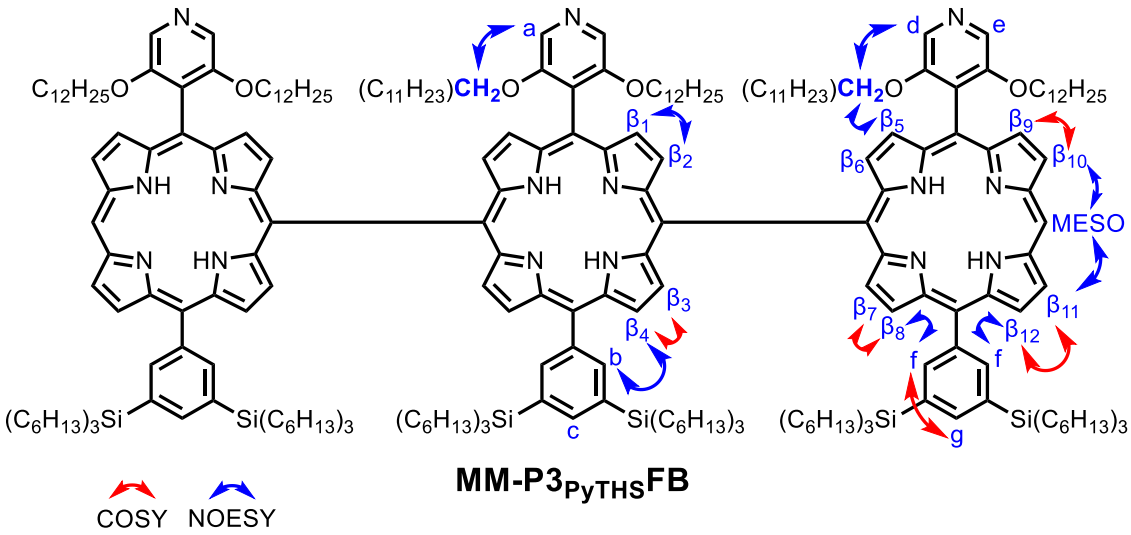

Characterisation data from the *dl*-pair enantiomer that elutes first by chiral HPLC.

^{1}H NMR (600 MHz, $CDCl_3$) δ 10.29 (s, 2H, **H_{MESO}**), 9.38 (m, 4H, **β10 + β11**), 8.99 (d, *J* = 4.5 Hz, 2H, **β12**), 8.95 (d, *J* = 4.5 Hz, 2H, **β9**), 8.68 (d, *J* = 4.7 Hz, 2H, **β8**), 8.54 (m, 4H, **β4 + β5**), 8.47 (d, *J* = 5.4 Hz, 2H, **β1**), 8.44 (d, 4H, **Hd + He**), 8.30 (s, 4H, **Hf**), 8.29 (s, 2H, **Ha**), 8.22 (d, J = 4.7 Hz, 2H, **β7**), 8.21 (s, 2H, **Hb**), 8.16 (d, *J* = 4.7 Hz, 2H, **β6**), 8.11 (d, *J* = 4.9 Hz, 2H, **β3**), 8.06 (d, *J* = 4.9 Hz, 2H, **β2**), 7.93 (s, 2H, **Hg**), 7.76 (s, 1H, **Hc**), 4.01 – 3.95 (m, 4H, **OCH_2-Side$_{In/Out}$**), 3.94 – 3.89 (m, 4H, , **OCH_2-Side$_{In/Out}$**), 3.89 – 3.84 (m, 4H, , **OCH_2-Central**), 1.63 – 0.39 (m, 372H, H_{Alkyl}) -1.58 (s, 2H, **$H_{FreebaseCentral}$**), -2.31 (s, 4H, **$H_{FreebaseSide}$**).

MALDI-ToF *m/z* 4186.43 (calculated for $[C_{273}H_{431}N_{15}O_6Si_6]^{\bullet+}$ = $(M)^{\bullet+}$: 4187.26).

5.7.1.3 P1PyZn

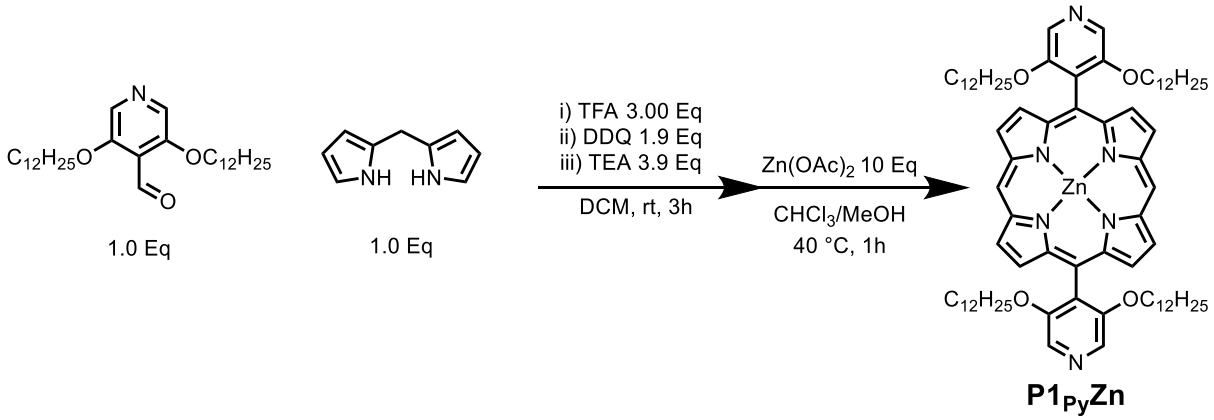

The procedure used to access the free-base porphyrin was conducted as previously reported[14].

To a 2L round bottomed flask containing N_2 purged DCM (500 mL) was added 3,5-bis(dodecyloxy)isonicotinaldehyde (2.18 g, 1 Eq, 4.59 mmol) and DPM (671 mg, 1.0 Eq, 4.59 mmol). The solution was stirred in the dark for 30 minutes, then TFA (1.57 g, 1.06 mL, 3.00 Eq, 13.8 mmol) was added over 5 minutes. After stirring in the dark for 3 hours, DDQ (1.98 g, 1.9 Eq, 8.72 mmol) was added. After a further 40 minutes stirring, TEA (2.5 mL, 3.9 Eq, 17.9 mmol) was carefully added over 5 minutes. The mixture was stirred fror a final 30 minutes, then concentrated in vacuo and purified by silica gel column chromatography (SiO_2, PE:DCM:Pyridine, 60:40:2).

The crude reaction mixture was redissolved in $CHCl_3$ (33 mL) then a solution of $Zn(OAc)_2$ (822 mg, 10 Eq, 0.37 mmol) in MeOH (4.7 mL) was added. The solution was stirred at 40 °C for 1 hour then concentrated in vacuo and purified by silica gel column chromatography (SiO_2, DCM + 2% pyridine) to afford a red oil (474 mg, 17 %).

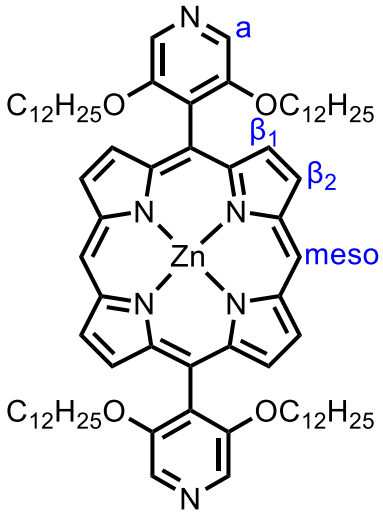

Characterisation data matches previous report.[14]

^{1}H NMR (400 MHz, $CDCl_3$ + 1% d_5-pyridine) δ 10.03 (s, 2H, **H_{meso}**), 9.24 (d, *J* = 4.4 Hz, 4H, **β_2**), 8.92 (d, *J* = 4.3 Hz, 4H, **β_1**), 8.49 (s, 4H, **H_a**), 3.92 (t, *J* = 6.6 Hz, 8H, **OCH_2**), 1.35–0.39 (m, 92H, **alkyl**)

MALDI-ToF *m/z* 1264.73 (calculated for $[C_{78}H_{114}N_6O_4Zn]^{\bullet+}$ = $(M)^{\bullet+}$: 1262.82).

5.7.1.4 MM-P3$_{Py}$FB

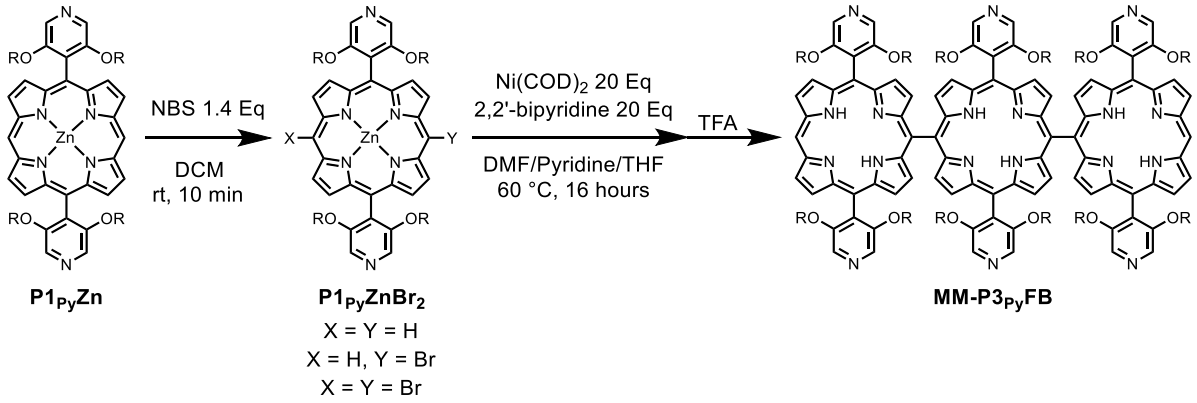

To a stirring solution of **P1$_{Py}$Zn** (200 mg, 1 Eq, 0.16 mmol) in $CHCl_3$ (40 mL) at rt was added NBS (39 mg, 1.4 Eq, 0.22 mmol). After 10 minutes, the reaction was quenched by the addition of acetone (20 mL) and reduced in vacuo. The resulting residue was passed through a short silica plug using an eluent mix of DCM + 1 % pyridine and the collected fraction concentrated and used without further purification in the next step.

The crude material from the first step was transferred into an oven dried Schlenk tube which was then dried under high vacuum and placed under an argon atmosphere. To this material was added degassed dry THF (20 mL) and dry pyridine (1 mL). The solution was then degassed by three freeze/pump/thaw cycles. To a second oven dry Schlenk tube was added 2,2-bipyridine (247 mg, 10 Eq, 1.58 mmol) and under a positive flow of argon, $Ni(COD)_2$ (435 mg, 10 Eq, 1.58 mmol). Immediately after the addition of $Ni(COD)_2$ the Schlenk tube was stoppered and evacuated. The tube was then subjected to 3 vacuum/argon cycles, before being placed under a positive pressure of argon. The fumehood light was then switched off and DMF (59 mL) was added to the Schlenk tube. The resulting solution was then freeze pump thaw degassed for 3 cycles, then under a positive pressure of argon, stirred at 60 °C for 1 hour. During this time the solution turns a deep purple colour.

The porphyrin solution was then transferred by cannula to the active nickel catalyst solution, and the resulting mixture stirred at 60 °C for two hours. After cooling to rt, the crude mixture was passed through a short silica gel plug in DCM + 2% pyridine and concentrated in vacuo. The resulting residue was purified by column chromatography (SiO_2, DCM + 2% pyridine).

The crude material was then dissolved in DCM (60 mL) and TFA (50 uL) was added. After sitirring at rt for 1 hour a saturated solution of $NaHCO_3$ (30 mL) and DCM (30 mL) were added. The separated organic layer was washed with H_2O (3 x 30 mL), concentrated in vacuo, then purified by silica gel column chromatograhy (SiO_2, DCM + 2% pyridine), size-exclusion chromatography (Bio-Beads, S-X3, toluene + 1% pyridine) and preparative GPC (toluene + 1% pyridine) to yield **MM-P3$_{Py}$FB** (23 mg, 12 %).

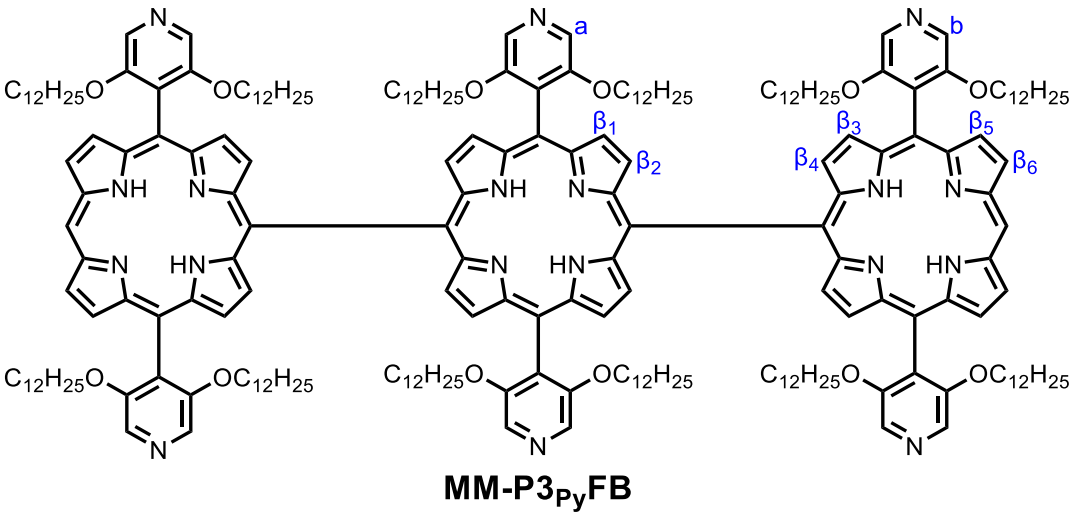

MM-P3$_{Py}$FB

^{1}H NMR (400 MHz, $CDCl_3$) δ 10.26 (s, 2H, **H$_{MESO}$**), 9.37 (d, *J* = 4.5 Hz, 4H, **β**), 8.96 (d, *J* = 4.6 Hz, 4H, **β**), 8.55 (d, *J* = 5.0 Hz, 4H, **β**), 8.47 – XXX (m, 4H, **β**), 8.45 (s, 8H, **H$_b$**), 8.30 (s, 4H, **H$_a$**), 8.19 (d, *J* = 4.9 Hz, 4H, **β**), 8.10 (d, *J* = 4.9 Hz, 4H, **β**), 4.05 – 3.95 (m, 8H, **OCH$_2$-Central**), 3.95 – 3.84 (m, 16H, **OCH$_2$-Side**), 1.36 – 0.57 (m, 276H, H$_{Alkyl}$), -1.65 (s, 2H, **H$_{FreebaseCentral}$**), -2.38 (s, 4H, **H$_{FreebaseSide}$**).

MALDI-ToF *m/z* 3601.43 (calculated for $[C_{234}H_{344}N_{18}O_{12}]^{\bullet+}$ = $(M)^{\bullet+}$: 3600.69).